Rijksuniversiteit Groningen

MSc Astronomy

Detectability of biosignatures in nearby terrestrial exoplanetary atmospheres with the ELT

Author:
A. H. Corporaal

Supervisor:
Prof. dr. F. F. S. van der Tak
Dr. M. Min

August 19, 2019

Abstract

Biosignatures, features in planetary atmospheres that can be related to life and may be detected remotely in atmospheres of potential habitable planets, play a key role in our current search for life beyond Earth. Using the knowledge of life to create these signatures, the possible abiotic origin and the sources and sinks in the atmosphere of these signatures, it can be deduced whether a planet may host life. Moreover, for characterisation of atmospheres, the concept of the habitable zone (HZ), the shell around a star where the planetary temperature could be such that liquid water could exist on the surface of a terrestrial planet, was used. Planets located in this region around the host star have preference in future studies related to the search of life beyond Earth. In this thesis it was investigated whether frequently proposed biosignatures gases oxygen (O_2), ozone (O_3), nitrous oxide (N_2O), methane (CH_4), ethane (C_2H6), ammonia (NH_3), and methyl chloride (CH_3Cl) are detectable with planned instruments for the Extremely Large Telescope (ELT). We included the detectability of the habitability marker water (H_2O) in our analysis. This was realised by building atmospheres using the exoplanet modelling code 'ARtful Modelling code for exoplanet Science' (ARCiS) written by Michiel Min. Synthetic spectra for potentially inhabited planets are created using opacity tables at the high resolutions at which the instruments for the ELT will operate. Synthetic reflection- and transmission spectra for the Mid-infrared E-ELT Imager and Spectrograph (METIS) and the High Resolution Spectrograph (HIRES) respectively are created assuming clear atmospheres. For investigating the detectability of biosignatures, the transmission of the atmosphere of the Earth is considered. We consider a hypothetical Earth-Sun analogue at 10 pc, Trappist-1 d, Trappist-1 e, Trappist-1 f, Trappist-1 g, LHS 1140 b, and K2-18 b as examples. It was concluded that METIS may be able to detect the O_3 3.6 μm band, the N_2O 3.7 μm band and H_2O features in the wavelength range of 3.5-4.3 μm within 27 observation nights for Earth at 10 pc, Trappist-1 d, Trappist-1 e, Trappist-1 f, and Trappist-1 g. The other spectral features in the mid-infrared will be blocked by Earth's atmosphere. For the wavelength range of HIRES, the optical and near-infrared, it was concluded that features will not be detectable.

Acknowledgements

Foist of all, I would like to thank my thesis supervisors, Floris van der Tak and Michiel Min, for their assistance during this thesis. You were available for questions when I needed help with concepts, analysis or understanding codes. Thank you for giving opportunities to develop myself with oral presentations and with research skills. I would like to acknowledge Migo Müller as the second reader of this thesis. Thanks for willing to read this thesis. I would like to thank the master students from room 0134 for the fruitful (related and unrelated) discussions, the motivation and the scientific support in good times and in tougher times.

I would like to thank the Kapteyn Astronomical Institute in general for educating me, for a great ambiance and for being a place were I could develop myself scientifically.

Last but not least, I want to thank my mom, my brother and my neighbours from number 64 for providing continuous encouragement and emotional support. Not only throughout this thesis but during my years of study, during my whole life, you have always been there for me. This thesis would not have been possible without you.

Contents

Chapter 1

Introduction

The concept of life beyond Earth has been around for centuries. This has led to the hope of finding inhabited extrasolar planets and identifying whether we are alone. This interest has brought us to find and characterise exoplanets around nearby stars. The first scientific paper related to the search of alien life was published halfway the twentieth century. In their paper Cocconi and Morrison (1959) suggested to look for radio signals around the 21 cm line of neutral hydrogen to hunt for intelligent life forms on planets orbiting nearby stars (within 15 light years). In that way, they suggested, we would be able communicate with those civilisations.

Remotely detecting life was first proposed in the 1960s for Solar System planets (Lederberg, 1965). It was realised that the environment, including the atmosphere, on Earth is altered by the presence of life. This could therefore also have happened on other planets. A mature biosphere may change both atmospheric and surface properties of a planet and these may be remotely detectable because of the influence life may have on the atmospheric composition (Lovelock, 1965, 1975). To date, telescopes are planned and designed such that a biosphere may be remotely detectable. Before these telescopes are used to observe planetary systems outside the Solar System, a theoretical framework for interpreting the data is needed (Lovelock, 1975).

One of the interesting questions that is tried to be answered in the exoplanet community is whether exoplanets host life. Not necessarily intelligent life is considered to hunt for but signs of all life forms are subject of modern studies. The first proof of planets around other stars than the Sun came in 1995 when 51 Pegasi b, a hot-Jupiter orbiting around the main-sequence star 51 Pegasi, was discovered by Mayor and Queloz (1995). The first discovery of an exoplanet, however, came three years earlier when Wolszczan and Frail discovered exoplanets orbiting the pulsar PSR 1257+12 (Wolszczan & Frail, 1992). The first Earth-sized planet located at such a distance from the star that it is located in the Habitable Zone (HZ) of that star was discovered in 2014 (Quitana et al., 2014). They reported the discovery of Kepler-186f transiting an M-dwarf.

1.1 Exoplanets

The search for and characterisation of extrasolar planets, or exoplanets, planets orbiting other stars than our Sun, are of importance for the goal and interest of finding life elsewhere. Finding life goes beyond the detection of exoplanets. With 4106 confirmed exoplanets identified in August 2019[1], the field is moving from the detection of exoplanets to the characterisation of exoplanets. Fig. (1.1) shows the year of the planetary detection versus the planetary mass in units of Jupiter masses. The black horizontal line indicates the mass of Earth (1 $M_{\oplus}$). It can be seen that roughly 1% of the planets has

[1] exoplanet.eu

a mass of 1 $M_\oplus$ or less. This subset of all planets are discovered in the last decade. The distribution of masses also shows that there are planets more massive than Jupiter (i.e. >1 M_{jup}, roughly 300 $M_\oplus$). Most of these gaseous planets are orbiting close (within 0.01 AU) to their host star (hot Jupiters). Moreover, some of the newly discovered worlds have masses between the masses of Neptune and Earth (Super-Earths). These planets are only categorised by their mass. Super-Earths masses between 1 $M_\oplus$ and 10 $M_\oplus$ where the upper limit is somewhat arbitrary. At 10 $M_\oplus$ a planet can either be rocky or gaseous. To infer a first estimate of the composition of the planet, both the planetary mass and the radius need to be known (Kaltenegger, 2017). The discovery of these hot Jupiters and Super-Earths reveal that there are populations of planets without a Solar System counterpart. The diversity of exoplanets exceeds the planetary environments known from our own Solar System.

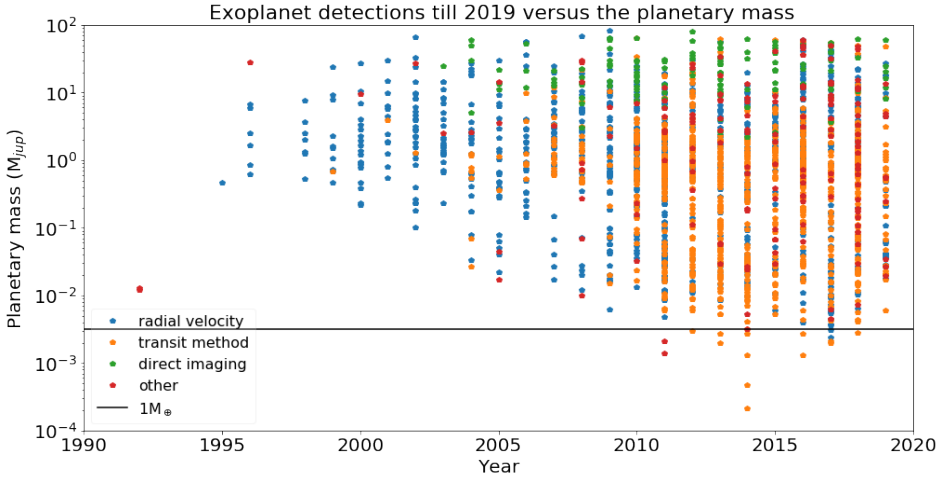

Figure 1.1: Exoplanetary mass in Jupiter masses versus year of discovery. Colour coding indicate discovery method (see legend). Other techniques are for example timing and astrometry. Data taken from exoplanet.eu. The black line indicates the mass of the Earth.

In Fig. (1.1) the coloured dots indicate the discovery method of the planets. Most of these planets known to date are detected via indirect techniques where the most successful have been the radial velocity (RV) method before Kepler and the transit method since Kepler. With the RV method the presence of a planet is deduced from Doppler shifting lines in the host star's stellar spectrum along the line of sight resulting in a determination of the minimum mass of a planet and the parameters of the planet's orbit can be inferred (see e.g. Lovis and Fischer, 2010 for more details). The other successful method for detecting exoplanets is the transit method. A transit occurs when a planet passes in front of the star from our line of sight causing a dimming in the starlight. From the depth of the resulting dip in the light curve, the radius of the planet relative to the radius of the host star can be determined. Since the stellar radius is known for those nearby stars, the planetary radius can be inferred. Combining the radial velocity method and the transit method provides an estimate of the density, and therefore the composition to first order, of the planet. This estimate of the composition is important for the search for life. Only mass and radius provide us with estimates of divisions between terrestrial planets and gas planets. Planets that have densities consistent with a rocky composition are of interest for our search for life.

There are planets that are discovered via a direct imaging: deriving planetary properties directly from imaging the planet. It can be seen that only planets with masses ∼10 M_{jup} are discovered via the direct imaging technique at this moment. This technique is not in its mature phase yet but is expected to be the most useful technique in the future for both detecting and characterising exoplanets. Other techniques to detect exoplanets include astrometry (detecting a change in the position of the planet)

and timing (e.g. pulsar timing by Wolszczan & Frail (1992)).

The field of searching for planets continues with the Transiting Exoplanet Survey Satellite (TESS[2], Ricker et al., 2015), Gaia[3], the Automated Planet Finder (APF[4], Vogt et al., 2014), the Anglo-Australian Planet Search (AAPS[5]), High Accuracy Radial Velocity Planet Searcher (HARPS[6]), and many more. In the meantime, the field of characterising exoplanets matures. In this thesis the focus is on the characterisation of exoplanetary atmospheres rather than on the detection of exoplanets. In particular, the study of exoplanet atmospheres is a way within technological reach to address a fundamental question: is there life on other planets? However, there are a lot of hurdles in the search for signs of life that can be remotely detectable. Technology for detecting signals is planned but not yet operating. Besides the observational part, we also do not understand what life really is (e.g. Walker & Davies, 2013) since we only have one example: life on planet Earth.

1.2 Life

1.2.1 Definitions of life

With our small subset of a range of possibilities for life to exist, there is not one particular definition of life. However, a definition of life is necessary to be able to recognise it if we find it on other planets. Life as we know it is carbon based and needs water (H_2O) as a solvent. On Earth biochemical reactions need liquid H_2O as a solvent. H_2O is the only solvent we know at the moment that can mediate biochemical reactions (Cockell et al., 2016). Moreover, both the hydrogen atom and the oxygen atom are in the top three of most abundant species in the universe. Alternative solvents have been discussed where the use of liquid ammonia (NH_3), methane (CH_4), ethane (C_2H_6) and other organic solvents, formanide and sulfuric acid are speculated (Benner et al., 2004; Schlulze-Makuch and Irwin, 2006). Since we do not know life forms that can use alternative solvents, we do not consider these solvents in this thesis.

Carbon based life seems to be favoured since the element carbon (C) is an abundant element in the universe, and it can form highly complex molecules. On Earth, C is embedded into life forms. However, alternative biochemical life may exist, and it is only based on life as we know it. Of course, we should not limit ourselves to life as we know it but it is a good first step in the search for extraterrestrial life. Referring to the universality of the laws of chemistry and physics three requirements for life can be noted (e.g. Cockell et al., 2016; Schwieterman et al., 2018): (1) a liquid solvent to mediate metabolic reactions, (2) an energy source that can drive metabolic reactions, and (3) a suite of nutrients in order to build enzymes that can function as a catalyst and to build biomass.

1.2.2 Habitability and the habitable zone

In this thesis, habitability is defined as a measure of the ability of the environment to support and maintain the activity of one or more organisms (e.g. Cockell et al., 2016). An habitable environment is therefore an environment which is suitable for the activity of at least one form of life. Note that it is possible to have on uninhabitable environment on part of the planet. For example, on Earth, such an environment is found in fresh lava flows (Cockell, 2014). A world or environment can either be instantaneously habitable or continuously habitable. Instantaneous habitability refers to the set of conditions on a planet or environment that can support life on the planet for a part of the geological

[2] tess.mit.edu
[3] sci.esa.int/gaia
[4] apf.ucolick.org
[5] newt.phys.unsw.edu.au/ cgt/planet/AAPS_Home.html
[6] eso.org/sci/facilities/lasilla/instruments/harps.html

time period (i.e. Archean, Proterozic and Phanerozoic, therefore millions of years, see Fig. (1.2) for an overview of these eons) (Cockell et al., 2016). Continuous habitability refers, however, to the ability of the planet in general to support life, or at least habitable conditions, somewhere on or in the planet over geological time scales (see Cockell et al., 2016 for a detailed description).

One of the first steps in the remote detection of extraterrestrial life is to find planets located at distances from the host star such that the planet has a temperature that liquid H_2O could exist on the surface. This forms the basis of the concept of the Habitable Zone (HZ). The concept of the HZ was first proposed by Huang (1959). The HZ, or more conveniently the circumstellar habitable zone, is a circular shell around a star where the planetary temperature could be such that the planet could support liquid H_2O on the surface of a terrestrial planet (e.g. Kasting et al., 1993; Kopparapu et al., 2013). Rocky planets in the HZ have priority in follow-up observations for projects concerning the search for life on exoplanets since they are considered most likely to host life.

In recent work there are several limits used to constrain the HZ. These limits are set by climatic constrains. Limits that are generally used for the concept of habitability are the Conservative Habitable Zone (CHZ) and the Optimistic Habitable Zone (OHZ). For the CHZ, the outer edge is given by the maximum greenhouse limit: the limit beyond which atmospheric carbon dioxide (CO_2) addition cannot prevent oceans to freeze completely. The inner edge is given by the runaway greenhouse limit: the limit where surface H_2O of a planet can completely evaporate because the planet is unable to cool sufficiently to prevent the surface H_2O from evaporating. The critical temperature is 647 K for pure H_2O (Kasting et al., 2013). This may happen because greenhouse gases present in the atmosphere block thermal radiation from the planet to the surroundings. This restricts the cooling of the planet which leads to evaporating of surface H_2O.

The Optimistic Habitable Zone (OHZ) uses as boundaries the Recent Venus (RV) as an inner edge and Early Mars (EM) as an outer edge. This empirical HZ is based on evidence that both Mars and Venus had liquid H_2O on their surface in the past (e.g. Kasting et al., 1993). From observations of the D/H ratio (Donahue et al., 1982) it is estimated that Venus must have had liquid H_2O on its surface at the moment the Sun was less bright by $\sim 8\%$ of the total luminosity it has today (e.g. Kasting et al., 1993). The RV limit indicates that the inner edge of the HZ is at least 4% farther out than Venus orbital distance (Kasting et al., 2013). Based on the observation that Mars did not have surface H_2O after about 3.8 Ga ago, the EM limit was set. The limits are such that the HZ of the Sun excludes present day Venus at a distance of 0.723 AU from the Sun and it includes present day Mars. A planet located in the HZ does not imply that life is possible or exists on that planet but it is the region where liquid water is possible on the surface of a geologically active rocky planet.

For different stellar spectral types and different stellar ages, the spectral energy distribution (SED) changes: for cooler stars the peak of the radiation shifts toward longer wavelengths while for hotter stars this peak shifts to smaller wavelengths. The shift in the peak makes that a cooler star is more efficient in heating an Earth-like planet, partly because of Rayleigh scattering and partly because of near infrared (near-IR) H_2O and CO_2 absorption (Kaltenegger, 2017). The effect of Rayleigh scattering (i.e. elastic scattering of radiation by particles smaller than $\sim 1/10$ times the wavelength of this radiation) decreases at longer wavelengths. The other effect that occurs for a cooler star is that there is an increase in near-IR absorption by H_2O and CO_2. This leads to the finding that for the same incident stellar flux at a planet surrounding a cool star and a planet orbiting a hot star, the planet around the cool star will be heated more efficiently. The age of the main sequence star matters because as the stellar age increases, the luminosity of the star increases. Therefore, the limits of the HZ change with stellar age. Moreover, stellar activity such as stellar magnetic field evolution has effect of the stellar emission at ultraviolet (UV) and X-ray wavelengths (Catling et al., 2018). Since the HZ of M dwarfs are close to the host star, the planets in this region have to deal with intense radiation,

flares etc.

In Table 1.1 and Table 1.2 stellar effective temperature, the habitable zone distance (HZD) (Eq. (1.1)), the equilibrium temperature of the planet and the period in which the planet orbits its host star of F, G, K, and M stars for the CHZ and the OHZ respectively are shown. Both the inner edge properties and the outer edge properties are indicated. The properties are determined using the estimates of Kopparapu et al. (2013) and are shown as average values of the stellar spectral type. For each stellar spectral type there are 10 subclasses. These subclasses are based on the temperature of the star. Subclassses are not taken into account but average values for F, G, K, and M stars are shown. Kasting et al. (1993) argued that the CHZ should be used when considering the design for telescopes if they devoted to detecting planets in the HZ and the OHZ should be used when interpreting the data obtained from these telescopes.

The HZD is the distance from the planet's host star at which liquid H_2O could exists according to the concept of the HZ. The HZD has to be calculated such that both the inner and the outer edge could be determined. The HZD depends on the luminosity of the host star, L, and the effective stellar flux, $S_{\rm eff}$:

$$\mathrm{HZD} = \left(\frac{L/L_{\odot}}{S_{\rm eff}}\right)^{0.5} \tag{1.1}$$

The relation between the stellar effective temperature, $T_{*\rm eff}$, and $S_{\rm eff}$ is given by (Kopparapu et al., 2013):

$$S_{\rm eff} = S_{\rm eff_{\odot}} + aT_* + bT_*^2 + cT_*^3 + dT_*^4 \tag{1.2}$$

where $T_* = T_{eff} - 5780\mathrm{K}$ is the stellar effective temperature. For determining the limits of the HZ, the parameters of Eq. (1.2) are determined. We used the estimates of a, b, c and d from Kopparapu et al. (2013). The HZD may also be given with a number between -1 and 1. In those cases the HZD is scaled such that 0 represents to the middle of the HZ, -1 serves as the inner edge of the HZ and +1 represents the outer edge of the HZ. Therefore, if -1<HZD<1, the planet is within he HZ of the star.

$$\mathrm{HZD} = \frac{2r - r_o - r_i}{r_o - r_i} \tag{1.3}$$

where r is the distance between the host star and the planet, and r_i and r_o are the inner and outer boundary of the HZ respectively.

Whether it is possible that planets in the HZ of M stars are habitable or not, is a point of discussion. This discussion began in the late 1800's, when discussing the potential of life on Venus (e.g. Schiaparelli, 1891). With an inaccuracy in the measurement of the orbit of Venus it was stated that Venus was tidally locked. The HZ of M stars coincides with the region where planets are expected to be tidally locked because they are orbiting close to their host star. Tidal locking occurs when the planet's revolution period around the star equals the rotation period around the planet's axis. Since such tidally locked planets receive starlight on one hemisphere and no starlight on the other hemisphere, it is more difficult to infer habitability.

Stellar type	$T_{*\rm eff}$ (K)	Stellar Flux ($S_{\odot}$)		HZD (AU)		$T_{\rm eq}$ (K)		period (days)	
		inner	outer	inner	outer	inner	outer	inner	outer
F	6000-7500	1.05	0.38	1.56	2.60	257	199	621	1341
G	5200-6000	1.01	0.35	0.99	1.69	255	196	361	801
K	3700-5200	0.95	0.31	0.64	1.13	251	189	216	507
M	2400-3700	0.87	0.25	0.12	0.22	246	189	26	68

Table 1.1: The Conservative Habitable Zone limits

Stellar type	$T_{*\text{eff}}$ (K)	Stellar Flux ($S_\odot$)		HZD (AU)		T_{eq} (K)		period (days)	
		inner	outer	inner	outer	inner	outer	inner	outer
F	6000-7500	1.84	0.32	1.18	2.84	296	191	408	1529
G	5200-6000	1.78	0.29	0.75	1.84	294	187	237	913
K	3700-5200	1.67	0.26	0.48	1.23	289	181	142	578
M	2400-3700	1.53	0.21	0.09	0.24	283	171	17	77

Table 1.2: The Optimistic Habitable Zone limits

In this work only atmospheres dominated by N_2 and O_2 are considered. Note that habitability is not limited to these atmospheric compositions: H_2 dominated atmospheres could also be habitable (Stevenson, 1999; Pierrehumbert and Gaidos, 2011; Seager et al., 2013). Atmospheres of super-Earths are thought to consist in some cases of low-molecular-weight component (i.e. He and H_2), but not as massive as the H_2 envelopes of the giant planets.

1.3 Biosignatures

Biosignatures, or biomarkers, are "objects, substances and/or patterns whose origin specifically requires a biological agent" (Des Marais & Walter 1999; Des Marais et al., 2008). Biosignatures are therefore signatures that are predominately created by life and whose abiotic origin can be excluded to our best knowledge about the origin of these signatures. Therefore, not only the abilities for life to create these signatures are important but also the inabilities for abiotic processes are essential. In view of the analysis of biosignatures several aspects need to be taken into account in order to provide us with good biosignatures. Criteria taken into account are: (1) The signature is more likely to be produced by life than by abiotic processes on the planet, (2) the origin of abiotic sources of this signature on the planet are small and/or have a known source (i.e. photochemistry, geology or stellar activity), (3) the signature has a reasonable survivability such that the signature is present because it has avoided the sinks for the signature in the planetary environment, (4) the detectability of the signature with current or future instruments and, (5) the spectral features of the signature does not have overlap with spectral features of other molecules present in the atmosphere such that the signature can be identified (e.g. Meadows et al., 2018).

Biosignature detections can suffer from both false positives and false negatives. False positives are detections of a proposed biosignature in the exoplanetary atmosphere produced abiotically on the planet of interest. Abiotic processes are for example photodissociation and volcanic activity but also stellar activity can alter the atmosphere of the planet in such a way that a gas is produced by abiotic processes not happening at Earth. This is for example the case for atmospheric oxygen (O_2) of planets around M-dwarfs generated during the pre-main sequence, superluminous phase of M dwarfs (Luger and Barnes, 2015). False negatives are non-detections of proposed biosignatures in an exoplanetary atmosphere if the biosignature is present in the atmosphere. This is for example the case for early-Earth, when the O_2 rise had started but was not detectable (e.g. Meadows et al., 2018).

Life on Earth produces hundreds of thousands of chemicals but only a few of these are volatile enough to enter our atmosphere in more than trace amounts (Seager et al., 2016). The biosignatures that are commonly proposed (e.g. Des Marais et al., 2002; Meadows and Seager, 2010; Schwieterman et al., 2018) and discussed below are indicators of life present in the current atmosphere of the Earth. Since there is only one example known of a planet that supports life, the focus of research is on these biosignatures.

There is no universally accepted scheme for classifying potential biosignatures. Since currently Earth is the only example of an inhabited planet, there are many uncertainties about which signatures

can be signs of life on planets other than the Earth. One scheme is suggested by Meadows (2006, 2008) who proposed to group proposed biosignatures in how they will likely be revealed to the observer. This resulted in three kinds of biosignatures: gaseous-, surface-, and temporal biosignatures. Gaseous biosignatures are direct or indirect products of chemical processes that take place in bodies of living organisms that help to maintain life (Meadows, 2006; 2008). Gaseous biosignatures are based on gases being present in the atmosphere in thermodynamic disequilibrium (e.g., Lovelock, 1965; Lippincott et al., 1967; Meadows et al., 2018). Finding gaseous biosignatures in abundances inconsistent with thermodynamic equilibrium will be suggestive of life altering the planetary atmosphere. For an overview of how thermodynamic disequilibrium works and is maintained in Earth's atmosphere see Kleidon (2012).

Surface biosignatures are spectral features that can be related to radiation reflected or scattered by life forms. Temporal biosignature are time-dependent modulations of gases or other signatures that are present in measurable quantities that can be linked to biological activity and may be remotely observable (Meadows, 2006; 2008). These three kinds of biosignatures are discussed below. Indicated are the signatures that are related to the classes.

1.3.1 Gaseous biosignatures

1.3.1.1 Oxygen (O_2)

The strongest biosignature on modern Earth is O_2. Although on Earth most of the O_2 abundance has biotic origins, it was recently realised that it can also have abiotic origins in planets located in the HZ. O_2 is generally considered as a good sign of life on Earth because for Earth we do not know any mechanism that can produce O_2 in significant quantities (21% by volume in the Earth's atmosphere) that can remain in the atmosphere for a longer timespan (i.e. more than a few hours) and because animals and humans require it (Meadows et al., 2018). O_2 is very reactive and therefore it has to be produced continuously such that the atmosphere can sustain that amount of oxygen (e.g. Meadows et al., 2018). On Earth, almost all of the oxygen present in the atmosphere is produced by oxygenic photosynthesis (OP) which is arguably the most important biological change that has happened on Earth (Meadows et al., 2018):

$$CO_2 + 2H_2O + h\nu \rightarrow (CH_2O)_{\mathrm{org}} + H_2O + O_2(g) \tag{1.4}$$

OP used starlight to convert atmospheric CO_2 and liquid H_2O to glucose $(CH_2O)_{org}$) and O_2. On Earth, OP maintains a large part of the biomass available today.

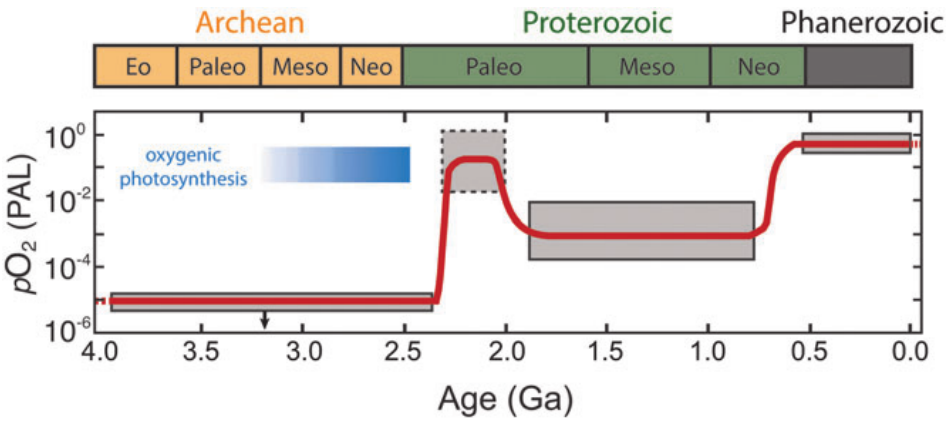

Figure 1.2: Evolution of the atmospheric O_2 concentration of Earth through time. The red line represents the trend of the evolution of the O_2 concentration while the grey areas indicate the approximate ranges of the O_2 concentration based on geochemical proxy records. Figure taken from Schwieterman et al., (2018) who adapted it from Reinard et al., (2017)

Thus, O_2 is present in detectable quantities in the atmosphere of Earth. O_2 and is considered as a remotely detectable sign of life for Earth. However, if O_2 is detected on a planet, it does not necessarily mean that O_2 has biotic origins. O_2 detections may suffer from false positives and false negatives. New insights in the production of O_2 both on other planets and on our own younger planet showed that the idea behind O_2 as a biosignature is quite complex. Advances in theoretical work in planet-star interactions for planets around other stars gave new insight in the atmospheric O_2 on early Earth and the potential false negatives related to these and relation between false positive O_2 detection and planets orbiting M-dwarfs. In the 4.6 billion years that the Earth exists, the planet has gone through different types of atmospheres. The evolution of the abundance of O_2 in the atmosphere of the Earth is illustrated in Fig. (1.2). It is suggested that life started very early on in the history of the Earth but the development of photosynthesis took place much later (Meadows et al., 2018). It seems likely from isotope measurements that OP had been developed on early Earth before the atmospheric abundance of O_2 was as significant as nowadays (e.g. Czaja et al. 2012; Riding et al., 2014). It was shown that between 3.0 and 2.65 Ga transient low levels of O_2 were present in the Earth's atmosphere which was likely produced by OP. However, the global accumulation of atmospheric O_2 occurred between 2.45 and 2.2 Ga (e.g. Farquahar, 2000; Canfield, 2005).

Proposed mechanics for the irreversible O_2 rise are the burial and removal of organic carbon from the surface of the Earth (Kasting, 2001; Lyons et al., 2014), hydrogen escape from the upper atmosphere (Catling et al., 2001), and the evolution of volcanic and tectonic processes at the surface of the planet over a longer time span (i.e. centuries). Abiotic production of O_2 is favoured for F and M stars through photochemical mechanisms (Domagal-Goldman et al., 2014).

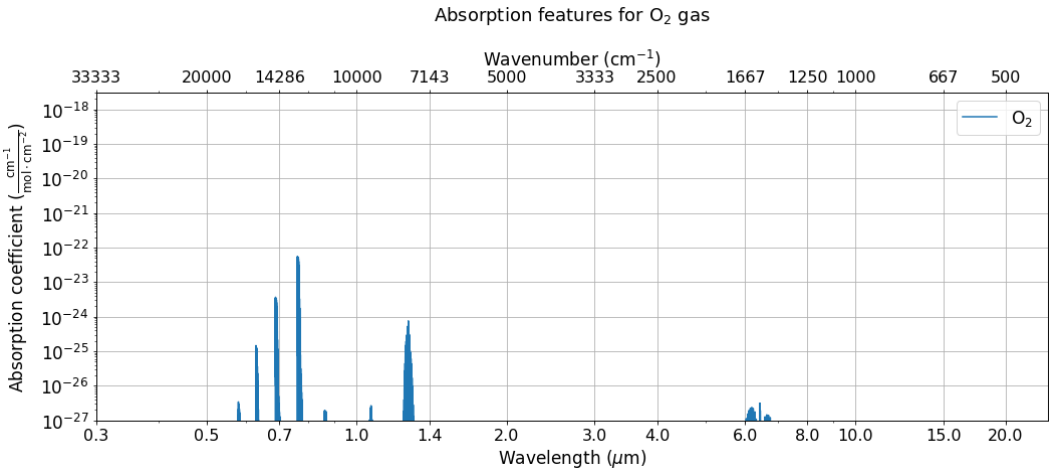

Figure 1.3: Absorption features of oxygen at optical and infrared wavelengths for a temperature of 296 K and a pressure of 1 bar. The line intensities are taken from the HITRAN 2016 database.

Spectroscopically, O_2 is one of the few biotic gases on Earth that has strong bands in the optical. Fig. (1.3) shows the optical, near-IR and mid-IR absorption as a function of wavelength. Since the Extremely Large Telescope (ELT) does not have instruments planned that can either go to lower or higher wavelengths, those wavelengths longer or shorter than the optical or mid-IR are not of interest for this thesis. In this wavelength range of interest, O_2 has the γ band at 0.628 μm, a band at 0.688 μm dubbed the B-band, the strong A-band at 0.762 μm, and the band at 1.269 μm called the $a\ ^1\delta_g$ (Gordon et al., 2017). Besides this region of interest, O_2 has strong bands at wavelengths $< 0.2\mu$m, i.e. in the far-ultraviolet (far-UV).

The detectability of the O_2 A-band has been explored several times. Snellen et al. (2013) and Rodler & López-Morales (2014) investigated this for nearby transiting planets orbiting around M

stars. These measurements can be of great importance for transiting rocky planets in the habitable zone of M dwarfs but it is only limited to transiting planets.

1.3.1.2 Ozone (O_3)

Ozone, or O_3, is considered as a biosignature since it indicates the presence of photosynthetically generated O_2 (Leger et al., 1993; 2011; Des Marais et al., 2002). On Earth the presence of atmospheric O_3 is the result of photochemical reactions in the stratosphere. Formation and destruction of O_3 was proposed by Chapman (Chapman, 1930):

$$\begin{aligned} O_2 + h\nu(\lambda_{O_2} < 240\text{ nm}) &\rightarrow O + O \\ O + O_2 + M &\rightarrow O_3 + M \\ O_3 + h\nu(\lambda_{O_3} < 340\text{ nm}) &\rightarrow O_2 + O \\ O + O_3 &\rightarrow O_2 + O_2 \end{aligned} \tag{1.5}$$

where λ_{O_2} and λ_{O_3} are the minimum wavelengths for photodissociation of O_2 ($\lambda = 0.24\mu$m) and O_3 ($\lambda = 0.34\mu$m) respectively. M is a non-reactive molecule that can take away excess vibrational energy. N_2 is one of the molecules that can fulfill this role.

O_3 can be used as a proxy for O_2 if the abundance of O_2 is small. Features of O_3 are seen in spectra for much lower abundances than O_2 because of the strength of the absorption features (Rugheimer et al., 2013). Another advantage of O_3 over O_2 is that O_3 has absorption bands in the near-IR and mid-IR as demonstrated in Fig. (1.4) whereas O_2 only has strong bands in the optical. O_3 has bands in UV where Hartley-Huggins bands absorb UV radiation. These bands extend from 0.15 μm to 0.35 μm. In Earth's spectrum, these bands are saturated and overlap with other molecules. In the optical absorption regions the Chappuis bands extend from 0.5 to 0.7 μm. This band is too weak to appear in Fig. (1.4). In the near-IR, O_3 has bands at 2.05 μm, 2.15 μm, 2.5 μm, 3.3 μm, 3.6 μm, 4.6 μm, and 4.8 μm. These bands are, however, relatively weak. The most well studied and strongest band is at a wavelength of 9.65 μm. This band is therefore also considered as the most promising band for examining O_3 abundances (Des Marais et al., 2002). However, the 9.65 μm band of O_3 has overlap with the CO_2 9.4 μm band (see Fig. (2.3c)). Moreover, around that wavelength, methyl chloride (CH_3Cl) (discussed below, see Fig. (1.8)) and some sulfur bearing molecules absorb and produce overlapping features (Pilcher, 2003). The band at 14.08 μm is completely overlapping with the 15 μm band of CO_2. Therefore, inferring the presence of atmospheric O_3 requires observations in different wavelength regions and cannot be inferred from only IR, optical or UV observations.

There is no one-to-one relation between the O_2 concentration and the O_3 concentration. The concentration of O_3 in the atmosphere depends on the incident UV photon flux, the stellar type, flaring, the temperature structure of the atmosphere and sources and sinks of O_3 due to environmental influences (Grenfell et al., 2007; Rugheimer et al., 2013). The higher the incident UV photon flux, the more absorptions and therefore the higher the concentration of O_3. Far-UV ($\lambda < 0.2\mu$m) photons drive both CO_2 and O_2 photolysis (top reaction Eq. (1.5)) and therefore cause an increase in O_3 concentration. Mid-UV ($0.2 < \lambda < 0.3\mu$m) and near-UV ($0.3 < \lambda < 0.4\mu$m) photons are, however, the primary drivers for O_3 destruction. Flares can attenuate the O_3 abundance. In the Earth's atmosphere the temperature increases if the concentration of O_3 is higher, i.e. in the ozone layer (Stathopoulou et al., 2008). Thus for higher atmospheric temperatures, the O_3 concentration is increased.

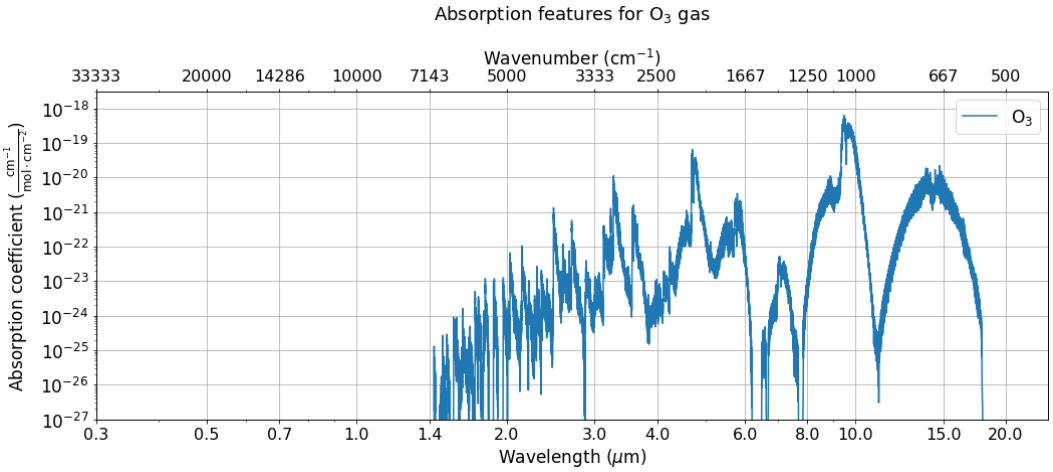

Figure 1.4: Absorption features of O_3 at optical and infrared wavelengths for a temperature of 296 K and a pressure of 1 bar. The line intensities are taken from the HITRAN 2016 database.

Abiotic production of O_3 results, like for O_2, from photochemical mechanisms. The study by Domagal-Goldman et al. (2014) demonstrated that this abiotic production is favoured around M- and F-dwarfs.

1.3.1.3 Nitrous oxide (N_2O)

Nitrous oxide, or N_2O, is considered as a strong biosignature if it is present in terrestrial planet atmospheres in combination with O_2. It is considered as a biosignature because it is present in Earth's atmosphere at high disequilibrium abundances, it has only small abiotic sources on modern Earth, and it has potentially detectable spectral features (e.g. Sagan et al., 1993; Segura et al., 2005). Biotic sources of N_2O include algae and bacteria producing N_2O via an incomplete conversion of soil and oceanic NO_3^- to N_2 gas (Sagan et al., 1993, Schwieterman et al., 2018). A simplified reaction can be described by:

$$NO_3^- \rightarrow NO_2^- \rightarrow NO + N_2O \rightarrow N_2 \tag{1.6}$$

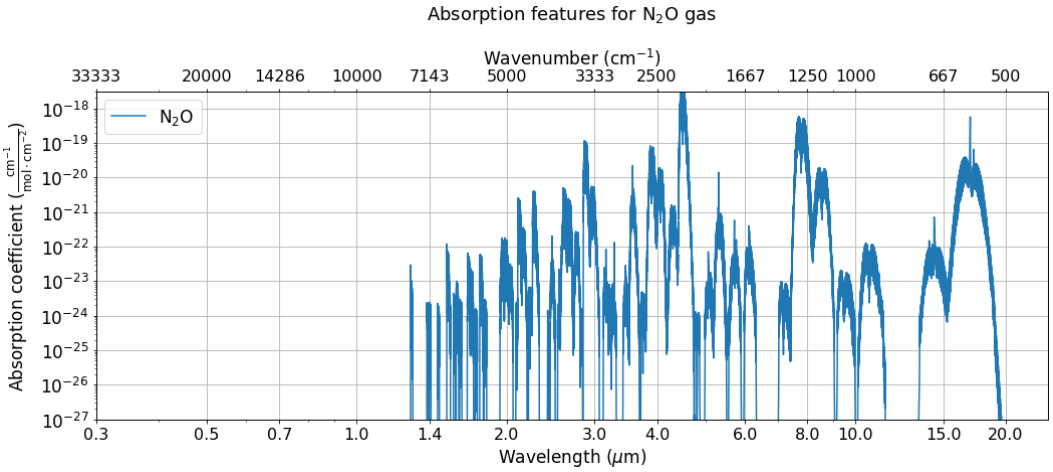

Figure 1.5: Absorption features of N_2O at optical and infrared wavelengths for a temperature of 296 K and a pressure of 1 bar. The line intensities are from the HITRAN 2016 database.

The preindustrial abundance of N_2O was about 270 ppb (Myhre et al., 2013). During portions of the Proterozoic epoch (i.e. between 2.5 and 0.5 Ga) H_2O that was both anoxic and sulphuric

(i.e. euxinic, deplete with hydrogen sulfide) ensured that the last step in denitration was facilitated (i.e. reduction of $N_2O \rightarrow N_2$) (Schwieterman et al., 2018). This in turn allowed N_2O to build up in Earth's atmosphere in concentrations that could impact the climate (Roberson et al., 2011). From photochemical modelling of rocky planets orbiting around M stars it was shown that N_2O would be able to build up to higher concentrations than an Earth-Sun analogue due to lack of UV photons of those cool stars (e.g. Segura et al., 2005).

Sinks for N_2O include photodissociation with an atmospheric lifetime of about half a century. Abiotic sources on Earth include lightning (Levine et al., 1979) and chemodenitrification happening in Antarctica. For the latter the available NO_3^- needed for this requires O_2 from OP (Samarkin et al., 2010). After all, this abiotic source is coming from biological activity on Earth.

N_2O has spectral features at wavelengths between 1.3 μm and 20 μm as shown in Fig. (1.5). The strongest bands are centered at 3.7 μm, 4.5 μm, 7.8 μm, 8.6 μm, and 17 μm while weaker bands are between 1.3-2.2 μm and 9.5-10.7 μm. At Earth-like abundances most bands are weak and overlap with H_2O (see Fig. (2.3a)), carbon dioxide (see Fig. (2.3c)) and/or methane (see Fig. (1.6)).

1.3.1.4 Methane (CH_4)

Methane, or CH_4, is considered as a biosignature since is enhances the confidence that the observed O_2 in a planetary atmosphere is indeed produced by biological agents (Hitchcock & Lovelock, 1967). On Earth, biotic CH_4 is produced in single-celled organisms (i.e. methanogens) that produce CH_4 as a waste product. These biotic methogens are the dominant source of CH_4 of the modern atmosphere. Therefore, CH_4 is considered as a biosignature. Another biotic source of CH_4 results from degradation of organic matter in sedimentary rocks (Etiope & Sherwood Lollar, 2013). CH_4 can either be produced by respiring (i.e. exchange of gases between life and the atmosphere) CO_2 or by simultaneously oxidising (i.e. O_2 enriching) and reducing (i.e. prevented to build up because of removal of gas, here of O_2) acetic acid (CH_3COOH). The net reaction of oxidation of CH_4 is given by:

$$CO_2 + 4H_2 \rightarrow CH_4 + 2H_2O$$

The multi step process is used by micro organisms to produce energy. The second reaction, for disproportionating acetic acid to CO_2 and CH_4, is given by:

$$CH_3COOH \rightarrow CH_4 + CO_2$$

Abiotic sources of CH_4 arise form gas-water-rock reactions. For an overview of these abiotic sources see Etiope & Sherwood Lollar (2013). Additionally, abundances of CH_4 in planet forming material are relatively high. Planets that are formed in this CH_4 enriched region may be expected to have abiotic, atmospheric CH_4. For example, Titan has a CH_4 concentration of 5% by volume because of this material. Since it is not yet fully understood if observed exoplanets has formed at its current location (i.e. planet migration), CH_4 is considered as a companion biosignature. Observed together with a strongly oxidising gas indicates thermodynamic disequilibrium. CH_4 can be considered a habitability marker when observed together with CO_2 since CO_2 indicates that the atmosphere is oxidising (i.e. oxygen rich, Schwieterman et al., 2018). Sinks for CH_4 concern oxidation of CH_4 by radical species (Schwieterman et al., 2018).

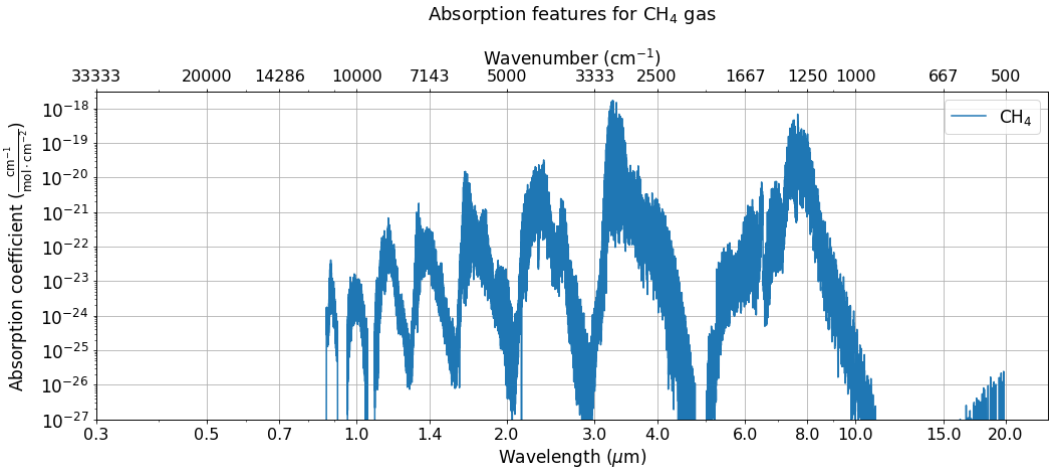

Figure 1.6: Absorption features of CH_4 at optical and infrared wavelengths for a temperature of 296 K and a pressure of 1 bar. The line intensities are taken from the HITRAN 2016 database.

Fig. (1.6) shows the optical and IR absorption features of CH_4. The strongest absorption bands of CH_4 can be found at 1.65 μm, 2.4 μm, 3.3 μm, and 7.5 μm. These bands all overlap with H_2O features (see Fig. (2.3a)). Weaker absorption bands of CH_4 are at 0.7, 0.8. 0.9, 1.0, 1.1, and 1.4 μm. Further, the strongest band, around a wavelength of 7.5 μm, overlaps with the N_2O band around 8 μm. For detections of CH_4 in the atmosphere, high resolutions are needed to distinguish H_2O absorptions from CH_4 features.

1.3.1.5 Ethane (C_2H_6)

Ethane, or C_2H_6, is a proposed biosignature because it is the most detectable molecule of the organic sulphur gases that can indirectly be used to infer a sulphur dominated atmosphere (Schwieterman et al., 2018). These sulfur gases are produced by bacteria in wetlands, inland soils, and oceanic environments (Rasmussen, 1974; Schwieterman et al., 2018). A study done by Domagal-Goldman et al. (2011) found that radials from a sulfuric gases catalysed the photochemical build-up of C_2H_6 beyond the level of the concentration of C_2H_6 expected from the atmospheric concentration of CH_4 (discussed below). This resulted in considering C_2H_6 as a potential biosignature for sulphur dominated atmospheres.

C_2H_6 is a photochemical product of other carbon bearing molecules, such as CH_4. If the ratio of C_2H_6 to CH_4 is larger than one, there is an overabundance of C_2H_6 compared to what is expected based on photochemical equilibrium reactions. An overabundance would reveal the likelihood of other sources to produce C_2H_6 such as dimethyl sulfide (DMS). Therefore, to infer the biosignature nature of C_2H_6, both C_2H_6 and other carbon bearing molecular abundances are needed. Moreover, modelling of the chemistry from the stellar spectrum and the temperature structure of the planet is needed to compare the abundances.

The absorption as function of wavelength for optical and infrared wavelengths for ethane is shown in Fig. (1.7). C_2H_6 has strong bands at 6-7 μm and 11-13 μm and a weaker spectral signature at 3.3 μm.

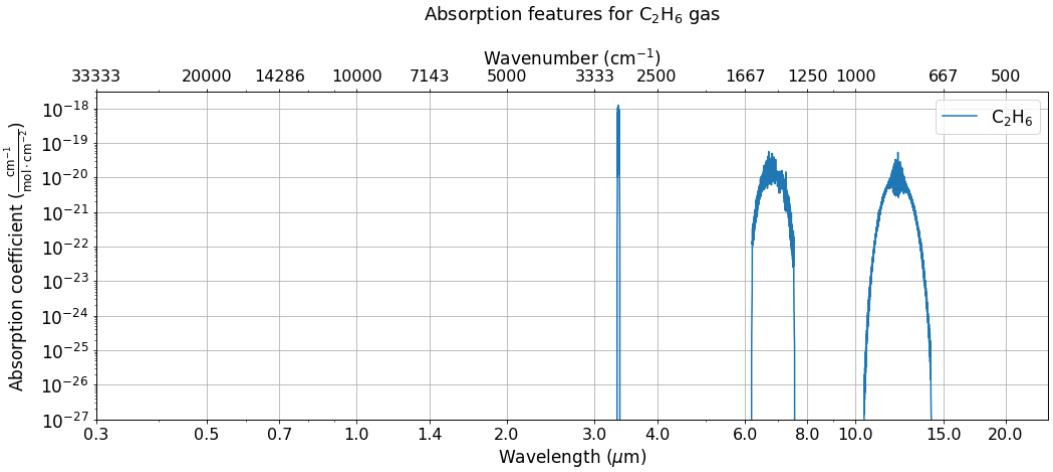

Figure 1.7: Absorption features of C_2H_6 at optical and infrared wavelengths for a temperature of 296 K and a pressure of 1 bar. The line intensities are taken from the HITRAN 2016 database.

1.3.1.6 Methyl chloride (CH_3Cl)

Methyl chloride, or chloromethane, is known by the chemical formula CH_3Cl and has a variety of biological sources on Earth causing it to be referred as a biosignature: (sub)tropical plants (Yokouchi et al., 2002; Saito and Yokouchi, 2006), algae in oceans (Singh et al., 1983; Khalil and Rasmussen, 1999), terrestrial plants (Saini et al., 1995; Rhew et al., 2014), fungi (Harper, 1985; Watling and Harper, 1998), decay of organic matter (Keppler et al., 2000; Hamilton et al., 2003), biomass burning (Lobert et al., 1999), and industrial processes involving organic matter (Kohn et al., 2014; Thornton et al., 2016).

Volcanoes are an example of abiotic origin of CH_3Cl (Schwandner et al., 2004; Frische et al., 2006). Additionally, Fayolle et al. (2017) detected CH_3Cl in the envelop of a low-mass protostar and in the coma of a comet. They concluded that a part of CH_3Cl found in atmospheres of rocky planets could have been originating from the planetary formation period.

The pathway to produce CH_3Cl is not unique and not well understood yet. CH_3Cl can be created via biosynthesis in various organisms, decay and combustion of organic matter, and gas-phase reactions of volcanoes (Schwieterman et al., 2018).

Spectral absorbance features in the wavelength range of interest are around 3.3 μm and other wavelength bands are at 7, 9.7 μm, and around 13.7 μm. Sinks occur if it reacts with hydroxyl (OH) radical (Schwieterman et al., 2018). For M stars, the stellar near-UV flux is low causing OH formation to be suppressed and therefore CH_3Cl could potentially be present in planets around M stars in detectable levels. Spectral features of CH_3Cl overlap with other molecules (H_2O, CO_2, O_3, and CH_4) which means that some difficulty arises when interpreting data (Segura et al., 2005). According to Rugheimer et al. (2015) CH_3Cl would best be detectable at 13.7 μm .

1.3.1.7 Ammonia (NH_3)

Ammonia, known by the chemical formula NH_3, can be considered as a signatures in hydrogen (H_2) and N_2 dominated atmospheres via the reaction (Seager et al., 2013):

$$N_2 + 3H_2 \rightarrow 2NH_3$$

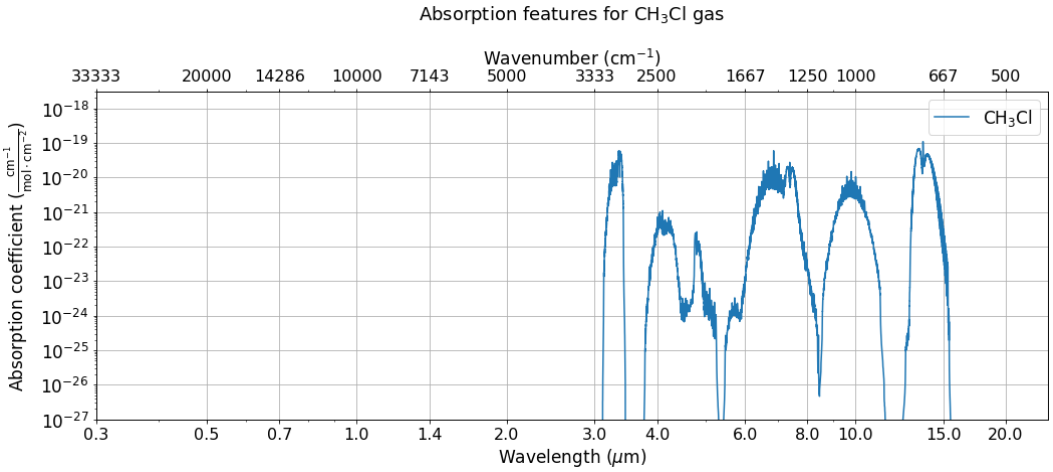

Figure 1.8: Absorption features of methyl chloride at optical and infrared wavelengths for a temperature of 296 K and a pressure of 1 bar. The line intensities are taken from the HITRAN 2016 database.

This is an exothermic reaction and therefore is considered as a biological source. Abiotic sources include outgassing from primordial material in the planet, comet impacts, and chemical equilibrium reactions (Schwieterman et al., 2018). Spectral features occur at bands near 2.0 μm, 2.3 μm. 3.0 μm, 5.5-6.5 μm, and 9-13 μm as can be seen in Fig. (1.9).

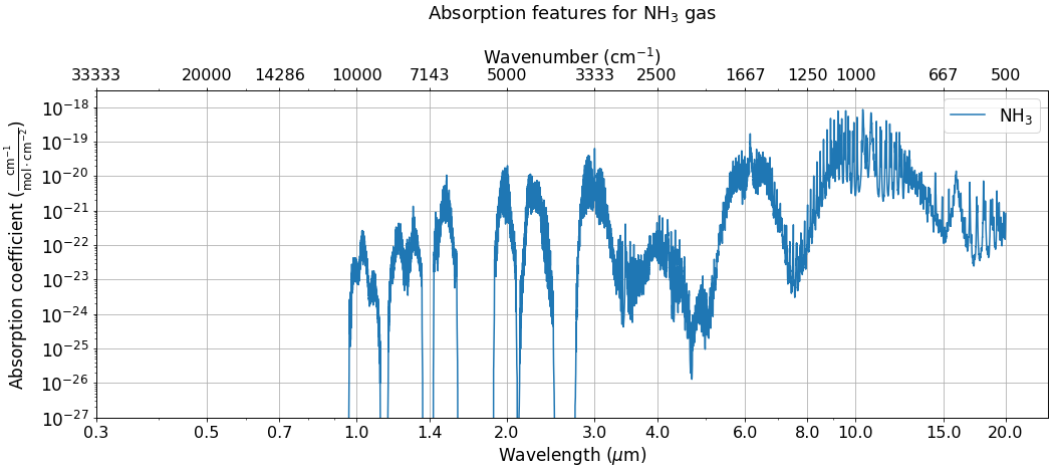

Figure 1.9: Absorption features of NH_3 at optical and infrared wavelengths for a temperature of 296 K and a pressure of 1 bar. The line intensities are taken from the HITRAN 2016 database.

1.3.2 Surface biosignatures

Besides searching for molecules in exoplanetary atmospheres, some surface features can also hint at the existence of life on exoplanets. Surface biosignatures results from life leaving a spectral or polarisation feature on the spectrum of reflected, transmitted or scattered light (Schwieterman, 2018). Two of these surface biosignatures are found on Earth: the Vegetation Red Edge (VRE) and circular polarisation which are both signs of OP on the planet. These type of biosignature is not modelled in this thesis and presented to give an overview of the proposed biosignatures.

1.3.2.1 Vegetation Red Edge (VRE)

The VRE is a feature in the reflection spectrum of the Earth caused by OP of plant leaves. The VRE is characterised by a sharp increase in the reflection spectrum of the Earth around 0.7 μm, near the

boundary between optical and near-IR wavelengths. The VRE originates because there is a change in chlorophyll absorption at wavelengths between $\sim 0.65 - 0.70\mu$m and between $\sim 0.75 - 1.10\mu$m wavelengths. Photosynthetic plants are developed in such a way that they absorb effectively optical light, but reflect IR light. A plant leave is reflective at the latter wavelength range because of the layered structure of leaves (Seager et al., 2005). This results in an change in index of refraction between cells walls. Light can refracts through the cell walls and simultaneously reflect off of the cell walls (Seager et al., 2005).

For Earth, the VRE was detected in observations of Earth from the Galileo spacecraft (Sagan et al., 1993), and in the Earth-shine spectrum obtained from observations of reflected light from the moon (Arnold et al., 2002; Woolf et al., 2002; Turnbull et al.,2006). From knowledge about the reflectively of deserts, oceans, ice, forests etc. it was possible to assign this rise in reflection observed to the vegetation.

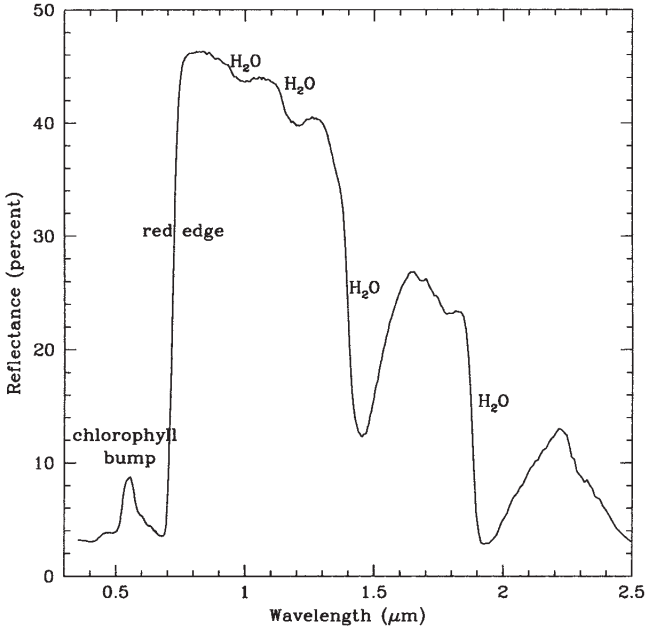

Figure 1.10: Reflection spectrum of a short-lived leaf with data from Clark et al., 1993. The chlorophyll bump near 0.5 μm results from chlorophyll absorption causing the leave to appear green. The red edge around 0.7 μm is the sharp rise in reflection between absorption in the optical and reflection in the near-IR of chlorophyll. Some water absorption bands of the leave are shown around 1.4 μm and 1.9 μm (Seager et al., 2005).

The VRE is much more significant in strength than the chlorophyll bump near 0.5 μm. The chlorophyll bump at visible wavelengths is caused by chlorophyll absorption. This absorption gives plants a green colour and the plant uses this absorbed chlorophyll for OP. The VRE and the chlorophyll bump are illustrated in Fig. (1.10) (Clark et al., 1993). Also some H_2O absorption bands in the near-IR are shown. Plants contain H_2O and therefore have those absorption bands. The strength of these bands depends on the H_2O content of the plant, the plant type, and the weather (Seager et al., 2005). These H_2O bands are, however, not useful for characterising life on other planets since they will likely not be unique because of interference of at-

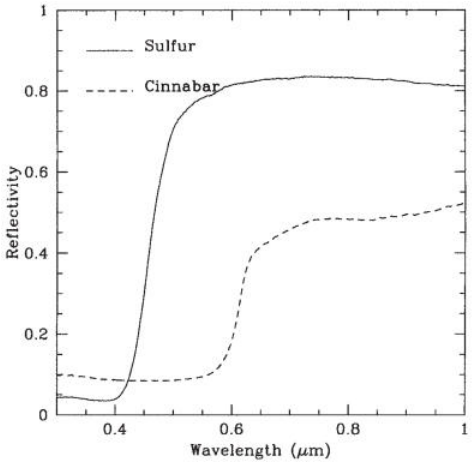

Figure 1.11: Reflectance spectra of sulfur (continuous line) and cinnabar (dotted line) with data from Clark et al. (1993) to illustrate possible false positives for the Vegetation Red Edge (Seager et al., 2005).

mospheric H_2O vapour.

As for the gaseous biosignatures, the VRE may also suffer from false positives. Seager et al. (2005) indicated that semiconductor crystals such as sulfur and cinnabar have similar reflectance edges at 0.45 μm and 0.6 μm respectively (see Fig. (1.11)). Therefore, also surface biosignatures must be examined with care and other planetary observables need to be taken into context.

1.3.2.2 Circular polarisation

Measurements of both linear and circular polarisation can be used to characterise planetary atmospheres (Schwieterman, 2018). Polarisation is the propagation of light as a transverse wave. The direction of polarisation is defined by the direction of the electric field vector. Linearly polarised light has an electric field vector oscillating in one plane. Circular polarisations refer to the case when the magnitude of the factor is constant but the direction of the vector rotates as a function of time. Circular polarisation is a proposed surface biosignature that relies on remotely detecting chirality (or handedness) of organic molecules (Sparks et al., 2009). Amino acids and sugars both are chiral compounds: asymmetric molecules that have a certain handedness. That means that a mirror image of these compounds cannot be superimposed on one another. Both amino acids and sugars are optically active in the UV. Chiral compounds prefer to absorb either right handed or left handed circularly polarised light. Circular polarisation of vegetation has a direct relation to the absorption spectra of vegetation. However, surfaces without any biotic origin do not have such a relation (Spark et al., 2009). In this way, circular polarisation can be used to infer the presence of liquid H_2O on the surface (Schwieterman et al., 2018).

1.3.3 Temporal biosignatures

Temporal signs of life are time-dependent modulations of e.g. the concentration of a certain gas or the planetary albedo that can be linked to biological activity and may be remotely observable (Meadows, 2006; 2008). These modulations can be seasonal, daily or stochastic in such a way that they can be linked to the presence of life on a planet. Temporal biosignatures are not modelled in most studies, including this thesis, since these signatures are more complex to understand than gaseous- and surface biosignatures. This is partially because additional planetary properties need to be taken into account. Examples of such properties include the axial tilt of the planet, its eccentricity, the distribution of continents and oceans on the planetary surface, and the presumed response of life on these processes (Schwieterman, 2018). For now, with only one proven example of a planet hosting life available, modulations of atmospheric gases on Earth is taken as an example as a proof of concept.

1.3.3.1 Modulation of atmospheric gases

Both CO_2 and CH_4 show seasonal changes in the Earth's atmospheric abundance. For CO_2 gas this oscillation is due to the growth of vegetation in spring and summer and decay in autumn and winter (Hall & Kauffmann, 1975). This trend for CO_2 obtained with data taken at Mauna Loa, Hawaii from 2000 to 2019[7] is shown in Fig. (1.12). The rise in CO_2 abundance over the years is not concerned in this thesis. Besides the seasonal change in CO_2 concentration, the oscillations are also location dependent: the northern hemisphere has a larger fraction of land than the southern hemisphere. Therefore, the oscillations are more significant in the northern hemisphere (Keeling et al., 1996). For CH_4 the seasonal variation at Mauna Loa, Hawaii from 2000 to 2019 is shown in Fig. (1.13). When it is summer in the

[7] https://www.esrl.noaa.gov/

northern hemisphere, the CH_4 concentration shows a deep minimum. In spring and autumn the CH_4 concentration reaches a maximum and in the winter there is a small minimum. This is partly because of interactions with OH (Schwieterman, 2018).

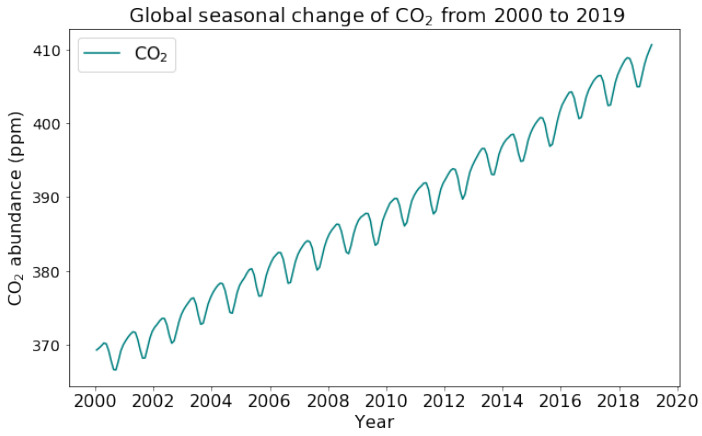

Figure 1.12: Temporal variation in the CO_2 concentration for the years 2000 till 2019. Data taken from the United States National Oceanic and Atmospheric administration's Earth System Research Laboratory.

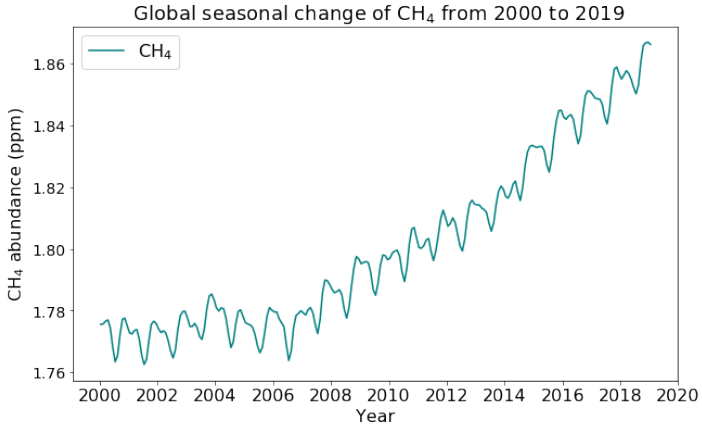

Figure 1.13: Temporal variation in the CH_4 concentration for the years 2000 till 2019. Data taken from the United States National Oceanic and Atmospheric administration's Earth System Research Laboratory.

Detecting seasonal modulations of atmospheric gases are challenging because it requires observations at different times of the year and disk-averaged spectra will likely be observed such that the variation per location will not be inferred. The peak-to-though of CO_2 is about 6.5 ppm, which corresponds to $\sim 2\%$ (Zhao & Zeng, 2014). The maximum change in the CO_2 abundance will be on the order of 2% as derived from Beer's law considering small optical depths ($\tau \ll 1$). Beer's law, also known as the Beer–Lambert law, is a relation between the attenuation of light, A, and the properties of the travelling material. It can be stated as:

$$A = \epsilon b c \tag{1.7}$$

where ϵ is the absorbtivity of the material, b is the path length and c is the concentration of the material. However, strength of the absorbance may be lower depending on the strength of the CO_2 bands of the planet (Des Marais et al., 2002; Schwieterman, 2018). Seasonal variations of CH_4 are also on the order of 2% at maximum and are not always biogenic (Khalil & Rasmussen, 1983). Both variations in concentrations of CO_2 and CH_4 are not likely to be observed at spectra taken with near-future technology.

1.3.4 Antibiosignatures

Besides searching for evidence of biological activity on a planet, evidence against the presence of life can also be helpful in the search for life and the understanding of habitability. These remotely detectable signatures are called antibiosignatures. Antibiosignatures can be useful to direct the search to more promising targets and to avoid a false positive claim for the detection of life (Schwieterman et al., 2019). Also, finding uninhabited planets can inform us about the origin of life. An antibiosignature is evidence that there is currently no life that uses the chemical free energy. Detection of an antibiosignature in an atmosphere does not imply that a planet is not inhabitable but rather that there is currently no life on the surface of the planet.

One proposed antibiosignature is carbon monoxide (CO). The presence of CO suggests that there is a source of unexploited chemical free energy present in the atmosphere and reduced carbon (e.g. Ragsdale 2004; Gao et al., 2015; Catling et al., 2018, Schwieterman et al., 2019). Moreover, CO is able to build up in an atmosphere in the absence of water vapour. Identifying exoplanetary atmospheres including antibiosignatures are beyond the scope of this thesis.

1.4 Temperatures of planets

Besides the physical temperature of a planet, the equilibrium temperature is an important concept related to the concept of planetary habitability. Temperature in general is a balance between all heating and cooling mechanisms present in the system. Heating of a planet results from absorption of radiation from the host star and internal heating if available. The stellar radiation a planet receives depends on the distance between the star and the planet and the luminosity of the host star. Cooling mechanisms are emission of thermal IR radiation which depends on the atmospheric composition and the ability of the planet to effectively distribute the heat. The atmospheric composition in turn depends on the sources and sinks of the constituent gases and photochemical reactions happening in the planetary atmosphere. The sources and sinks are linked to the crust material of the planet, whether or not it has oceans, geological activity, and biological processes if present (Kaltenegger, 2017). The physical temperature of the planet is the surface temperature a planet has on average. This temperature is hard to determine for exoplanets with current technology because the physical temperature depends on multiple quantities which cannot be determined with current instruments. Examples include internal heating, clouds (and therefore the albedo) and rotations.

The equilibrium temperature is the temperature that a planet would have if it is in thermal equilibrium assuming the planet behaves as a blackbody. The equilibrium temperature, T_{eq}, can be determined from the balance between incoming stellar radiation from its host star and the amount of radiation it re-radiates outwards and is given by:

$$T_{eq} = T_s(1-a)^{1/4}\sqrt{\frac{R_s}{2D}} \tag{1.8}$$

Where T_s is the host star's effective temperature, a is the bond albedo of the planet, R_s is the stellar radius, and D is the semi-major axis. For Earth, T_{eq}=255 K, compared to the surface temperature of 288 K. This difference results from greenhouse gases which are present in Earth's atmosphere. This results in a higher surface temperature compared to the equilibrium temperature.

1.5 Goals and outline of this thesis

This thesis builds up a model for exoplanetary atmospheres with the intention to investigate whether the biosignature gases O_2, O_3, N_2O, CH_4, C_2H_6, NH_3, and CH_3Cl are detectable with the ELT. Included in the analysis is the detectabilility of H_2O in planetary atmospheres. Moreover, a determination of the optimal resolution for detecting biosignatures in exoplanetary atmospheres and an estimation of the photon noise will be made. Steps taken include investigating multiple atmospheric temperature and pressure structures and the effect of changing abundances of biosignatures. This will be done considering a hypothetical Earth-Sun analogue located at a distance of 10 pc. Moreover, planets that are detected in previous observations that may be Earth-like and are lying in the HZ are considered. In Chapter 2 the details of the characterisation of planetary atmospheres will be outlined: the detection techniques used and planned for exoplanetary atmospheres and a description of which instruments on the ELT can be used for characterisation of exoplanetary atmospheres. In Chapter 3 the method is outlined where after the results are described in Chapter 4. In Chapter 5 these results are interpreted with reference to previous studies and in Chapter 6 the conclusions are outlined.

Chapter 2

Characterisation of planetary atmospheres

2.1 Detection techniques for exoplanetary atmospheres

To reach the goal of finding life beyond Earth, a step that needs to be taken is characterising (exo)planetary atmospheres. With current technology this is difficult, because of the extremely low amplitude signals that an exoplanetary atmosphere provides and the current instrumental limitations. The detection of spectral lines from the atmosphere and knowledge about sources and sinks of molecules are important for science of biosignatures. However, measurements of spectral lines from atmospheres are only possible with present day instrumentation for two kinds of planets. (1) For young planets still glowing from their formation that are orbiting far from their host star using direct imaging techniques and (2) for hot Jupiters orbiting closely their host star using the transit method. These methods are discussed below.

2.1.1 Transit method, secondary eclipses and phase curves

The most successful technique for the characterisation of exoplanetary atmospheres and for detecting exoplanets to date has been the transit method. A planet can transit its host star from our point of view such that light is transmitted at different wavelengths according to the wavelength dependent opacities of atmospheric chemical species. A transit obscures the light of the host star by an amount equal to the ratio of planet-to-star area. Using this area and the assumption that both the star and the planet are spherical bodies, this can be translated to a ratio of planet-to-star radius (see Eq. (2.1)). From previous stellar observations the radius is already known for nearby stars and therefore the planetary radius can be determined. One advantage of the transit method is that the technique does not depend on the planet-star contrast, but it depends rather on the radii of both the planet and the star:

$$\Delta F = F_s \frac{R_p^2}{R_s^2} \tag{2.1}$$

where R_s and R_p are the stellar and planetary radii respectively, ΔF is the transit depth, and F_s is the stellar flux. To use the transit method to detect a planet or characterise a planetary atmosphere, a planet has to transit the star from our line of sight in the first place. The probability, p, to transit to first order is given by:

$$p = \frac{R_s + R_p}{a} \tag{2.2}$$

where a is the orbital semi-major axis of the planet (Borucki & Summers, 1984). From Eq. (2.1) it can be estimated that the probability that an Earth-sized planet orbiting an G2 star at a distance of 1 AU will be 0.47%. The probability for Trappist-1 e ($R = 0.918 \quad R_\oplus$) transiting its host star Trappist-1 ($R = 0.117 \quad R_\odot$) at a distance of $a = 0.02812$ AU is, however, about 2%. Therefore, Trappist-1 e is much more favourable for observing using transit photometry as compared to an Earth-Sun analogue.

Besides the transit depth the amplitude of the transit, δ,is an important characteristic of a transit. The amplitude of spectral features is given by:

$$\delta = \frac{(R_p + nH)^2}{R_s^2} - \frac{R_p^2}{R_s^2} \approx \frac{2nR_pH}{R_s^2} \tag{2.3}$$

where n is the number of scale heights crossed at wavelengths with higher opacity and H is the atmospheric scale height: the change in altitude at which the pressure decreases by a factor of e. Assuming an ideal gas law and hydrostatic equilibrium, the scale height can be expressed as:

$$H = \frac{kT}{\mu m_h g} \tag{2.4}$$

where k is the Boltzmann constant, T is the planetary surface temperature (or if not known the equilibrium temperature), μ is the mean molecular weight of the constituents of the atmosphere, m_h is the mass of the hydrogen atom, and g is the gravitational acceleration of the planet. Therefore, planets with a high temperature, relatively small host stars, a small gravitational acceleration, and small molecular weight of the atmosphere (i.e. gas giants) will have a higher amplitude and will therefore be more favourable for characterising. Hot Jupiters are the ideal candidates but only have $\delta \sim 0.1\%$ (Kreidberg, 2017). Earth-sized planets around Sun-like stars have an amplitude of about 3 orders of magnitude smaller (Kreidberg, 2017). Therefore, studies to detect planets and characterise the atmospheres favours planets that have orbits of a relatively short amount of time (a few days) in order to be able to observe multiple transits and be able to extract the spectrum of the atmosphere. When such an event is captured by a telescope, a transmission spectrum can be obtained. Fig. (2.1) shows a transmission spectrum of the Earth as observed from lunar eclipse observations (Pallé et al., 2009). Studying the transmission spectrum of the Earth can be seen as a proxy for observations of a transit of Earth as seen from a planet outside our Solar System.

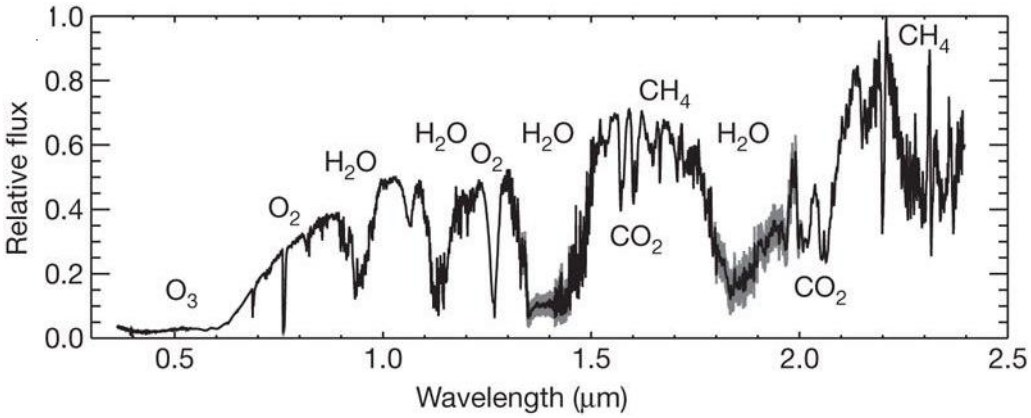

Figure 2.1: Transmission spectrum of Earth in the optical and near-infrared from observations of a lunar eclipse. Note that the vertical axis is in units of the relative flux of the star and the planet and not in the planet to stellar radii. Figure adapted from Pallé et al. (2009).

The above description is both important for the detection of planets and the characterisation of planetary atmospheres. For a detection a few transits are needed to conclude whether a planet is

transiting while characterisation takes more effort. With the wavelength dependent opacities it is possible to figure out which atoms and molecules are present in a planetary atmosphere. The planet blocks slightly more stellar flux at wavelengths where an atom or a molecule absorbs. The transit depth is therefore a function of wavelength which results in the transmission spectrum. Variations in absorption as a function of wavelength are measured by binning the light curve into spectrophotometric channels.

The geometry of the transit method, the secondary eclipse and the phase curve is illustrated in Fig. (2.2). The transit, the case that a planet passes in front of the star from our point of view, is also called the primary eclipse. The secondary eclipse can be observed if a planet passes behind the star from our point of view. During the secondary eclipse only the stellar spectrum is observed. By combining observations of the secondary eclipse and observations of the planet and star just after the secondary eclipse, the spectrum of the planet alone can be deduced. When observing the complete orbit or phase of the planet around its host star a phase curve can be inferred. A phase curve is therefore a spectrum with data taken during the complete orbit. In a phase curve also the primary and secondary eclipse will be prominent. By analysing a phase curve, not only the orbital parameters can be determined, but also the atmospheric composition can be inferred. Since all intermediate planetary temperatures can be determined, a phase curve contains information about the heat circulation in the planetary atmosphere. Since transits are more favourable for planets that orbit their host star close-in and these planets are mostly tidally locked (for both hot Jupiters and planets in the HZ of M-dwarfs (e.g. Barnes, 2017)), this spectrum corresponds to the day-side of the planet. For tidally locked planets both the day-side and the night-side temperature can be estimated when a phase curve is taken.

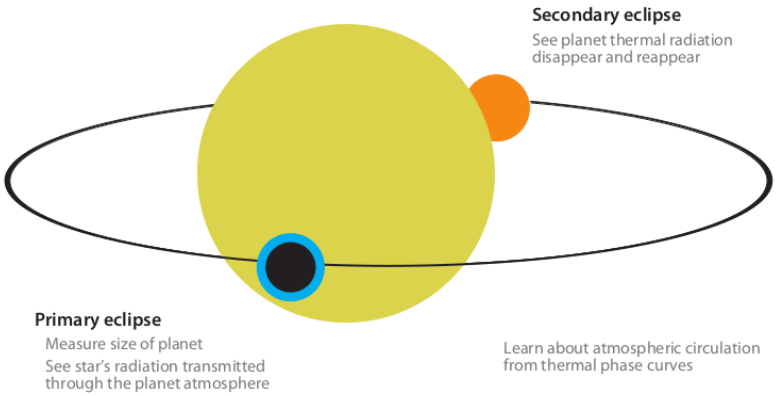

Figure 2.2: Schematic of the geometry of a transiting planet. The primary eclipse is also referred to as the transit. From observations following the complete orbit, represented here in black, a phase curve can be deduced. From observations of the secondary eclipse, the spectrum of the star alone can be made and compared to spectra taken from the star and the planet together to deduce the (day-side) spectrum of the planet. Figure taken from Seager & Deming, 2010.

2.1.2 Direct imaging

The method that will be most promising for future exoplanetary atmosphere characterisation is the direct imaging technique. In high contrast imaging, or direct imaging, the point spread function of a planet is attempted to be distinguished from the host star. The technique relies on the property that the planet reflects a portion of the light it receives from the host star. The reflected light from a planet is observed, which contains information about the composition of the atmosphere. Atmospheric properties that alter the amount of reflected light are the atmospheric constituents, the clouds, surface types, and aerosols. The latter three atmospheric properties result in the planetary albedo (Tinetti

et al., 2009). Direct imaging requires telescopes with a high resolution and a high contrast. High resolution can be obtained by a large telescope and extreme adaptive optics. High contrast is reached by including a coronagraph to reduce photon noise. For the high-resolution, high-contrast technique to be applicable, the star-planet system is spatially resolved and therefore the distance to the star plays a critical role. Exoplanets around stars which are located up to 10 pc away from us are best to consider using this technique (Traub & Oppenheimer, 2010).

To date, the direct imaging technique is used for young, massive planets on wide orbits. These planets are still glowing from their formation which gives them a high temperature and a large size. These properties result in planet-star flux ratios of about 10^{-7}. Because of the wide orbits, stellar light can be easier blocked allowing them to be detected. Mature planets have an effective temperature comparable to the equilibrium temperature derived from the stellar properties and the distance between the star and the planet. These planets will be fainter in the IR compared to young, massive planets. Moreover, those terrestrial planets in the HZ will be relatively close to their host star (see Table 1.1). Direct imaging is a promising technique for characterising exoplanetary atmospheres of terrestrial planets inside the HZ in the near future. However, because of the small semi-major axis, sub-arcsecond angular resolution is needed to distinguish the stellar light from the scattered light by the planet (Traub & Oppenheimer, 2010).

For some near-future instruments on the ELT the focus will be on reflected light measurements. The measureable quantity is the planet-to-star flux ratio (F_p/F_s). For reflected light measurements the flux ratio is given by Eq. (2.5).

$$\frac{F_p(\lambda,\alpha)}{F_s(\lambda)} = A_g(\lambda)g(\alpha)\Big(\frac{R_p}{a}\Big)^2 \tag{2.5}$$

where $F_p(\lambda,\alpha)$ is the reflected spectrum at phase angle α, $F_s(\lambda)$ is the stellar spectrum as function of the wavelength, $A_g(\lambda)$ is the geometric albedo spectrum which is defined by Eq.(2.7), R is the radius of the planet, a is the orbital semi-major axis and $g(\alpha)$ is the phase function. A Lambertian surface is defined as an absolute white, diffuse surface which reflects all radiation falling upon it isotropically. Therefore, for a Lambertian surface, the brightness is the same in all viewing directions. For a Lambertian surface, the phase function is given by:

$$g(\alpha) = \frac{\sin\alpha + (\pi-\alpha)\cos\alpha}{\pi} \tag{2.6}$$

The geometric albedo, A_g, is defined as the ratio of reflected flux of an object at full phase ($\alpha = 0°$), $F_p(\lambda,\alpha=0)$, to the flux from a perfect Lambertian disk, $F_{\odot,L}(\lambda)$:

$$A_g = \frac{F_p(\lambda,\alpha=0°)}{F_{\odot,L}(\lambda)} \tag{2.7}$$

The phase angle is defined as the angle between the incident light produced by the star and the radiation of the star that is received by the observer on Earth. In order to obtain reflection spectra, usually the radiance factor, I/F, is determined. I is the reflected intensity at a given wavelength and viewing angle, and πF is the incident stellar flux density upon the planet at a specific wavelength (de Pater and Lissauer, 2013). I/F equals the geometric albedo if the planet is observed at $\alpha = 0°$. A perfectly reflecting Lambertian surface would have $I/F = 0$ Reflection spectra can also be displayed with flux units. In that case the flux of the planet is plotted versus the wavelength of observation.

Observations of reflected starlight only reveal the product of the albedo and the radius of the planet and therefore there is a degeneracy. This degeneracy can be broken by doing more observations (Quanz et al., 2015).

Direct imaging has several advantages over the transit method for planets in the HZ. First, if the planet is farther away from their host star, the probability that the planet is transiting from our point of view is very small. Therefore, it can take years for characterising a planetary atmosphere. With direct imaging a planet can be observed not only during a transit, but over a great part of their orbit. Therefore, the direct imaging technique can characterise a planetary atmosphere in in less time. Moreover, the transit method is limited to a planet/star contrast of 10^{-5}. This contrast, C is calculated from:

$$C = \frac{F_p(\lambda)}{F_s(\lambda)} \tag{2.8}$$

where F_p and F_s are the wavelength dependent planetary and stellar fluxes respectively. In the visible, Earth has a contrast of about $C10^{-10}$ while Jupiter has a contrast of $C \sim 10^{-9}$ (Traub & Oppenheimer, 2010). This means that the achievable contrast level with the transit method is to high. For direct imaging, these contrast levels can be pushed down to 10^{-8} with current and planned technology and may be pushed lower because techniques to suppress starlight mature.

For the characterisation of exoplanetary atmospheres to search for biosignatures, large telescopes like the ELT are needed in order to collect enough photons while a high resolution (i.e. $R >\sim 30,000$) is needed in order to disentangle the observed planets spectral features from the Earth's spectrum. These telescopes therefore are ground-based because bringing a large telescope to space will be unfeasible. However, the Large UV Optical Infrared telescope (Luvoir[1]) and the Habitable Exoplanet Observatory (HabEx[2]) have been proposed as future space based telescopes. Both Luvoir and Habex have been proposed to be launched in mid 2030s with the science goal of characterising exoplanetary atmospheres using the direct imaging technique. While the 15-m and 8-m Luvoir has been proposed as a multi-discipline mission, the mission of 4-m HabEx will mainly be to directly image Earth-like exoplanets. Those have a smaller collecting area compared to the ELT but do not have noise from Earth's atmosphere. Because ground-based telescopes necessarily look through atmospheric water, observations of planets considered nowadays as potential habitable (i.e. with liquid H_2O on the surface and therefore likely also in the atmosphere), the Doppler shift needs to be large enough in order to distinguish telluric water lines from exoplanetary water lines. Doppler effects can be taken into account in Eq. (2.5) using the projected orbital velocity, v_r. The fluxes of both the planet and the star are Doppler-shifted by v_r:

$$\frac{F_p(\lambda, v_r, \alpha)}{F_s(\lambda, v_r)} = A_g(\lambda) g(\alpha, v_r) \Big(\frac{R_p}{a}\Big)^2 \tag{2.9}$$

For Luvoir and HabEx, doppler shifts will play not a significant role.

2.2 The Extremely Large Telescope (ELT)

The 39-m ELT is scheduled for first light in 2025 and is currently under construction on the top of Cerro Armazones in the Atacama desert located in the north of Chile. The ELT will be important for exoplanetary science at optical and mid-infrared wavelengths. Not only the characterisation of exoplanets is a major ELT science goal, also understanding the formation and evolution of planetary systems and galaxies is important. The focus of this thesis is on the characterisation of exoplanetary atmospheres. In particular, determining whether biosignatures can be detected and recognised in observations conducted with the ELT are subject of this thesis. Therefore, only instruments planned or proposed for the ELT that share this science case are discussed here.

[1] https://asd.gsfc.nasa.gov/luvoir/
[2] https://www.jpl.nasa.gov/habex/

2.2.1 Exoplanet Imaging Camera and Spectrograph (EPICS)

The Exoplanet Imaging Camera and Spectrograph (EPICS) will be an instrument for direct imaging and characterisation of atmospheres of rocky planets in the habitable zone around late type stars in systems that are not farther away from us than 4 pc (Kasper et al., 2010). Besides that, EPICS will be able to detect young planets close to the ice-line. This latter capability is important for the research on planet formation. EPICS will cover the wavelength range between 0.6 and 1.65 μm and will be able to characterise exoplanetary atmospheres of rocky planets with direct imaging, spectroscopy and polarimetry (Kasper et al., 2010). Diffraction polarimetry is provided by EPOL, a coronagraphic imaging polarimeter in EPICS which provides a field of view of 2"x2" in the wavelength range 0.6 μm to 0.9 μm (Kasper et al., 2010).

Spectral deconvolution is provided by an integral field spectrograph (IFS) which has a field of view of 0.8"x0.8" over a wavelength range 0.95 μm to 1.65 μm. In the main observing mode, the spectral resolution is 124.6. It also has two higher resolution modes, one with $R = 1,400$ and one with $R = 20,000$, which provide a field of view of 0.8"x0.014". At medium resolutions of $R = 3,000$ spectral analysis and analysis of exoplanet chemistry is provided.

Some analysis of the capacities of EPICS has already been done: the Parallel EPICS Simulation Codes and Applications (PESCA) and a Monte-Carlo code named MESS which compares the modelled stellar properties and planetary properties with the limits of detection have been developed (Kasper et al., 2010). With PESCA it was shown that EPICS will push the systemetic limits of the photon noise (photon noise limited contrast levels of about 10^{-9} at separations of 0.1"). MESS predicts that EPICS will be able to detect 6 and 4 exoplanets with $M_p < 10M_{Earth}$ with IFS and EPOL respectively.

2.2.2 Mid-infreared E-ELT Imager and Spectrograph (METIS)

One of the three first light instruments on the ELT will cover mid-IR wavelengths: the Mid-infrared E-ELT Imager and Spectrograph (METIS) (Brandl et al., 2014). It is the only instrument of the ELT that covers the wavelength range from 3-19 μm (L, M and N bands) (i.e. the mid-IR). METIS has three main observing modes: imaging, medium-resolution spectroscopy, and high-resolution spectroscopy. METIS has a combination of a high angular- and spectral resolution. With this unique combination, METIS will be an instrument that opens up observations in different areas of astrophysics: circum-stellar disks and planet formation, solar system formation, massive stars, star formation in galaxies, and exoplanet detection and characterisation (Brandl et al., 2014). Since this thesis is focused on the characterisation of exoplanets, the center of attention for the description of the science goals of METIS will be on the latter.

METIS will characterise exoplanetary atmospheres of planets that are already detected by previous missions with the radial velocity method, the transit method or astrometry using a combination of high contrast imaging (HCI) and High Resolution Spectroscopy (HRS) (e.g. Snellen et al., 2015). The combination of HCI and HRS is basically as follows: high resolution spectra can be cross-correlated with a template for planetary atmospheres. This comes down to comparing how well the line positions and the line depth of the observed planetary spectrum correspond with the template (Birkby, 2018). Using HCI (also: integral field unit spectroscopy (IFU)) at wavelengths between 2.9 to 5.3 μm METIS will not only be able to detect gas giants beyond 3 AU from their host star. The characterisation of rocky exoplanets is, however, also one of the science goals of METIS. Using the IFU it should be possible to measure the strength of individual lines coming from planetary atmospheres such that the temperature-pressure profile of the planetary atmosphere can be probed (Brandl et al., 2014). METIS has an IFU field of view of 0.4"x1.5". Observationally, METIS needs to have an Adaptive Optics (AO) with IFU because HRS combined with HCI requires that combination (Snellen et al., 2015).

The HCI modes cover both imaging and spectrospopy. Choronographs are used for high spectral resolution in the L and M bands IFU and for imaging in the L, M and N bands. With HCI molecular bands can be resolved into individual lines. Moreover, strong Doppler effects due to the orbital motion of a planet can be distinguished from the telluric lines and the stellar lines from the host star from the planet in question. Hereby it is usually assumed that the telluric- and stellar lines are stationary within the time of the observation. With the combination of HCI and HRS it is possible to search for the O_2 band in reflected light (Hawker et al., 2019). One advantage of this is that reflected light measurements do not require planets to transit from our point of view.

Quanz et al. (2015) already provided some estimates of which planet sizes, temperatures and host star properties will be possible to probe with METIS. Their analysis showed that cool planets ($T_{eq} = 255 - 300$ K) would be detectable in neither the L band nor the M band but will be detectable in the N band. It also shows that planets with $T_{eq} = 400 - 600$ K are best detectable in the L band.

2.2.3 High Resolution Spectrograph (HIRES)

The ELT High Resolution Spectrograph (E-ELT-HIRES, HIRES hereafter) is an instrument planned for the ELT that finished its phase A study at the end of 2018. HIRES is designed with the experience and success of the Very Large Telescope (VLT). Two previous concept instruments were proposed based on the VLT: CODEX ($\lambda = 0.37 - 0.61\mu$m, $R = 120,00$ and the Echelle SPectrograph for Rocky Exoplanets and Stable Spectroscopic Observations (ESPRESSO) ($\lambda = 0.84 - 2.5\mu$m, $R = 130,000$, AO-assisted). These were to specific individually and therefore were combined to one instrument: HIRES (Maiolino et al., 2013). The proposed science cases for HIRES are related to a number of astronomical research fields: the study of chemical composition of protoplanetary disks and accretion disks, chemical enrichment study of the first stars related to the epoch of reionisation, studying the evolution of massive early type galaxies at $z = 1-3$, advances in the field of fundamental physics related to the fine structure constant measurements of the deuterium abundance, and, most importantly for this thesis, the characterisation of exoplanetary atmospheres with the prospect of detecting signals of life on rocky planets (Maiolino et al., 2013). This variety of science cases results in a set of requirements such that a progress in all these fields can be made when HIRES will be used to observe with the ELT. One requirement is that there is a primary high spectral resolution observing mode with $R \sim 100,000$. For the characteristation of exoplanetary atmosphere, this resolution is proposed to disentangle telluric lines from features of the planet of interest, to trace different atmospheric layers, and to detect narrow bands such as those from O_2. Another requirements is the wavelength coverage: an instantaneous wavelength coverage of 0.37 μm to 2.5 μm with a wavelength accuracy of 10 cm s^{-1} for the exoplanet science case. For some science cases, including the study of galaxy evolution and extragalactic star clusters, a moderate spectral resolution ($R \sim 10,000 - 50,000$) mode is proposed such that the sky background can be more accurately subtracted.

For the characteristion of exoplanetary atmospheres, the focus of HIRES will be on planets with masses of Neptune and if possible to Earth-like masses (Maiolino et al., 2013). HIRES will provide characterisation of atmospheres in terms of chemical composition, stratification and weather with the ultimate goal to detect biosignatures. Moreover, a polarimetric mode is proposed to increase the chance to detect biosignatures.

2.3 The HITRAN molecular spectroscopic database

The *hi*gh-resolution *tran*smission molecular absorption database (HITRAN), edition HITRAN2016[3] is used to obtain line-by-line spectroscopic parameters for the molecules of interest (Gordon et al., 2017). The molecules of interest are the gaseous biosignatures O_2 O_3, CH_4, N_2O, CH_3Cl, NH_3, and C_2H_6 and the habitability markers N_2, H_2O, and CO_2. HITRAN contains line-by-line transitional data for 49 molecular species and uses a reference temperature of 296 K and a reference pressure of 1 atm of most significant isotopologues in the atmosphere of the Earth (Gordon et al. 2017). The line-by-line data are available for a large part of the electromagnetic spectrum: form microwave thought the UV and consists of pure rotational, ro-brational and electronic transition as much as possible. The line-by-line database is the main part of HITRAN. However, HITRAN also has data for cross sections, collision-induced absorption cross sections, and aerosol refractive indices which are not used in this thesis.

HITRAN gives the spectral line intensity in unis of $\mathrm{cm}^{-1}/(\mathrm{molecule} \cdot \mathrm{cm}^{-2})$ to emphasise that intensity is wavenumbers per unit column density, a unit used in atmospheric transmission and radiance codes. In HITRAN, the intensity is for the above reason defined per molecule per unit volume. HITRAN gives the positions of the lines in vacuum wavenumbers, k in units of cm^{-1}. The conversion from wavenumber to wavelength is given in Eq (2.10):

$$\lambda(\mu\mathrm{m}) = \frac{10^4}{k(\mathrm{cm})} \tag{2.10}$$

Fig. (2.3) shows the spectral line intensities as a function of wavelength for the habitability markers H_2O, N_2, and CO_2 for optical,near-IR and mid-IR wavelengths. While N_2 has no significant spectral features because it is a homonuclear molecule, H_2O have spectral band over almost the whole wavelength range and CO_2 has bands from 0.7-3.0 μm, 4.0-6.0 μm and 9.0-20.0 μm. As mentioned in section 1.3 both H_2O and CO_2 overlap with most of the gaseous biosignatures considered.

HITRAN line-by-line data have been downloaded using the HITRAN Application Programming Interface (HAPI) (Kochanov et al., 2016), a Python library to access molecular spectroscopic data of HITRAN. HAPI filters the data in SQL-like fashion and allows for high resolution spectra taking into account pressures, temperatures and optical path lengths. A Voigt line profile was chosen in this thesis but HAPI allows also for Doppler, Lorenzian, Voigt, and Rautian line profiles. Furthermore, HAPI can be used to simulate experimental spectra and allows for calculations of partition sums and apparatus functions.

The abundances of the isotopologues given in HITRAN for the atmosphere of the Earth are assumed to hold in other planetary systems, which is reasonable for nearby stars and therefore nearby planetary systems.

[3] http://hitran.org/

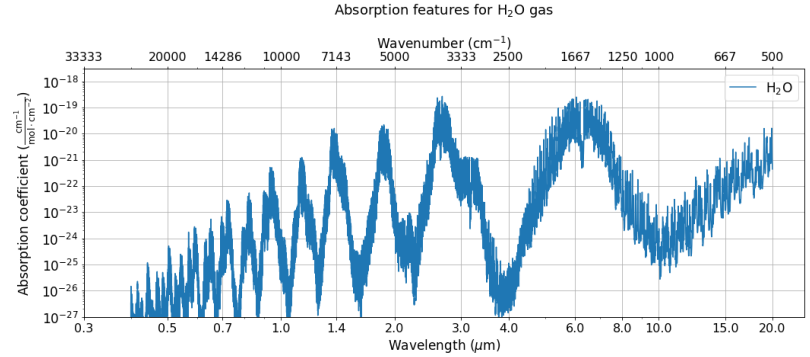

(a)

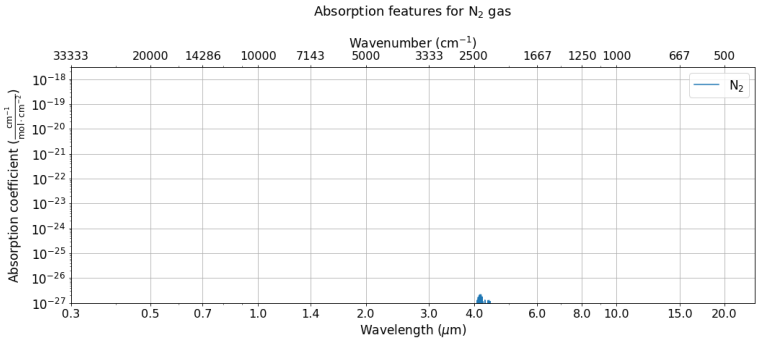

(b)

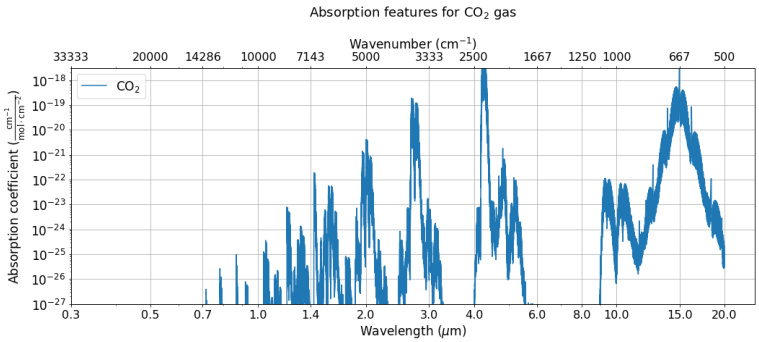

(c)

Figure 2.3: Absorption features of water (a), nitrogen (b) and carbon dioxide (c) at optical and infrared wavelengths for a temperature of 296 K and a pressure of 1 bar. The line intensities are taken from the HITRAN 2016 database.

Chapter 3

Method

3.1 ARtful Modelling Code for exoplanetary Science (ARCiS)

For modelling exoplanetary atmospheres with different molecules, abundances, pressures, and temperatures, the planetary atmosphere modelling code ARtful Modelling Code for exoplanetary Science (ARCiS) was used. ARCiS is written by Michiel Min and is only distributed to collaborators. Besides atmospheric properties, computations of radiative transfer and retrieval can be done using ARCiS. In particular, ARCiS was written for creating synthetic spectra for observing transiting hot Jupiters with space based telescopes. However, by calculating opacity tables at appropriate resolutions for the ELT, it was found that the code can also be used for colder rocky planets using both the transit method and the direct imaging technique. With ARCiS it is possible to calculate transmission spectra, emission spectra, and reflection spectra. To calculate opacity tables ARCiS uses the downloaded HITRAN tables and an user input with the following information: molecule for which the opacity table is calculated, the pressure range, the temperature range, the spectral resolution which also determines the number of wavelength elements, the number of temperature points in the temperature range for which the tables are calculated, NT, the number of pressure points for which the opacity is calculated in the given pressure range, NP, and the number of points per resolution element, NG. An example of an input file for calculating opacity tables in the wavelength range of METIS is given in Fig. (3.1) showing the input for calculating opacity tables for H_2O. NT and NP are chosen such that the system did not result in a memory error. For this low NT and NP, the calculations need to interpolate significantly for all intermediate values. The pressure range spans about 13 orders of magnitude meaning that a value is calculated for less than one order of magnitude. For the temperature, spanning about 2 orders of magnitude, the value of 10 temperature points is more reliable compared to the pressure. For calculating all opacity tables the spectral resolution is set to 50,000. This is different from the proposed resolution for both HIRES and METIS to be able to distinguish tellurlic lines from exoplanetary features. Creating the opacity tables at resolutions of 100,000 resulted in synthetic reflection spectra containing a significant number of calculated planetary flux that could not be calculated and a 'NaN' was reported. Therefore, the

```
H2O=100d-2



lmin=2.8d0
lmax=5.4d0

specres=50000

pmin=1d-12
pmax=90d0

Tmin=100d0
Tmax=750d0
NT=10
NP=10
NG=25


computeopac=.true.
opacitymode=.true.
```

Figure 3.1: Example input to calculate opacity tables. In this example an opacity table for H_2O is created for wavelengths appropriate for METIS at a spectral resolution of 50.000.

resolution of the opacity tables was set as high as possible to avoid this: R=50,000.

All opacity tables are created using a pressure range of 10^{-12} to 90 atm. The upper boundary of $P_{\max} = 90$ atm was chosen such that it would be able to model Venus like atmosphere since Venus has a surface pressure of 90 atm. Keeping in mind the concept of the HZ, properties of Venus, Earth and Mars can be seen as limits for habitability. The temperature range was chosen such that the temperature range of the atmosphere of Earth with and without temperature inversions is included and accounted for planets having a higher and lower surface temperature. Habitable planets probably do not have surface temperatures above 750 K because water would evaporate on those planetary surfaces. The limit of 750 K was chosen because Venus has a surface temperature of about 750 K.

To illustrate the minimum pressure and the minimum temperature choices, an Earth-like planet around a Sun-like star with an equilibrium temperature of 200 K is chosen. With $T_{eq} = 200$ K a planet can still be habitable since the equilibrium temperature is usually lower than the surface temperature, depending on the atmospheric content (e.g. Earth has $T_{eq} = 255$ K and $T_s = 288$ K on average). Fig. (3.2) shows the pressure temperature profile (P-T profile) for an Earth-like atmosphere with both the average surface temperature of the Earth and the example temperature of $T = 200$ K taking for both cases an atmospheric profile with the International Standard Atmosphere (ISA) as a reference (ISO, 1975). It can be seen that the minimum pressure for a planetary equilibrium temperature of 200 K goes down to about 10^{-10} bar while the temperature decreases to about 100 K in the mesosphere. To include this minimum pressure and temperature of a planet with $T = 200$ K and to go a little bit lower in surface temperature, the minimum pressure and temperature were set to 10^{12} bar and 100 K respectively.

The ISA is a static model of the Earth's atmosphere published by the International Organization for Standardization (ISO) to provide a consistent way to model the pressure, the temperature, the density, and the viscosity as a function of altitude in their document ISO 2533:1975 (ISO, 1975). In the ISA, the lapse rate for the troposphere is 6.5 K/km up to the tropopause at 11 km above the surface. In the pause the temperature remains constant. At a height of 20 km above the Earth's surface, the stratosphere begins. The lapse rate for the stratosphere is -1.0 K/km up to 32 km above the surface which means that there is a temperature inversion in this atmospheric layer. A temperature inversion in the atmosphere is a reversal of the normal behaviour of the atmosphere to decrease with temperature as a function of altitude. Then the temperature goes up more rapid as a function of temperature with a lapse rate of -2.8 K/km up to an altitude of 47 km, where the stratopause begins. In the stratopause the temperature of 270 K remains constant. At an altitude of 51 km the mesosphere beings. In the mesosphere the temperature goes down as a function of altitude with a lapse rate of 2.8 K/km up to 71 km and a lapse rate of 2.0 K/km up to a height of 80 km. At that height an isothermal point is reached which corresponds to a minimum temperature at the boundary of the mesosphere and the thermosphere: the mesopause. Above the thermosphere the atmospheric pressure and temperature profiles are not modelled in the ISA. In this thesis the boundary was chosen because for the search for biosignatures it is convenient to probe the lower atmosphere since life is more likely to alter the lower atmosphere compared to the upper atmosphere. In the ISA it is assumed that the air behaves as a perfect gas. The pressure profile in the ISA is exponentially dropping with altitude:

$$P = P_0 \exp\left(-z/H\right) \tag{3.1}$$

where P_0 is the surface pressure, z is the altitude and H is the atmospheric scale height given by Eq. (2.4).

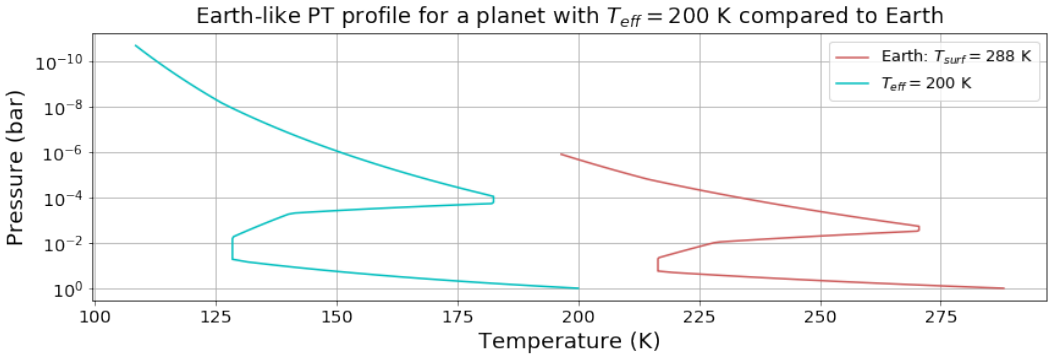

Figure 3.2: Pressure-Temperature profile of an Earth-like atmosphere for the average surface temperature of the Earth ($T = 288$ K) in red and a planetary equilibrium temperature of $T = 200$ K in blue taking the International Standard Atmosphere as a reference.

Fig. (3.3) shows an example input for an Earth-Sun analogue at a distance of 10 pc for calculating the transmission, emission and reflection spectra. The stellar surface temperature, *Tstar*, is 5777 K for the Sun, *Rstar* is given in solar radii, *Dplanet* is given in AU and *distance* is given in pc. The radius and mass of the planet, *Rp* and *Mp* respectively, are given in Jupiter radii and masses. The number of layers in which the atmosphere is divided, *nr*, is chosen to be 100 in order to have a new layer every 0.8 km. The TPfile consists of a grid of temperatures, pressures and abundances of one or more molecules present in an atmosphere. Setting gridTPfile to True ensures that the grid of temperatures and pressures provided by the TPfile is adopted. Setting mixratfile to True also ensures that the abundances as specified in the TPfile are used in the calculation. This specific input file uses HIRES as an instrument. Setting scattering of thermal radiation and scattstar (scattering of stellar light) to True is necessary for creating reflection spectra while scattering does not alter synthetic transmission spectra. Besides a TPfile it is also possible to set the pressure and temperature of the planet separately. In that case the maximum pressure (pmax), the minimum pressure (pmin), the temperature of the planet at 1 bar (Tp), a temperature gradient (dTp), and the atmospheric constituents with their abundances need to be specified in the input file. The temperature gradient is calculated using Eq. (3.2)

```
Tstar=5777d0
Rstar=1d0
Dplanet=1.0d0
distance=10d0


Rp=0.08921d0
Mp=0.003146d0


nr=100
gridTPfile=.true.
mixratfile=.true.
TPfile='PTlist_Earth_H_full.dat'


lmin=0.38d0
lmax=2.45d0

specres=100000

scattering=.true.
scattstar=.true.
```

Figure 3.3: Example input for ARCiS to create transmission, emission and reflection spectra for an Earth-Sun analogue at 10 pc. The stellar surface temperature in K, radius of the star in $R_\odot$, distance to the analysed planet in AU and the distance to the observer in pc are given as stellar and planet-star input parameters. The radius and the mass of the analysed planet are given in R_{jup} and M_{jup} respectively. Properties of the atmosphere itself are given in the temperature-pressure file (TPfile) containing the pressure and temperature throughout the atmosphere and the abundances of the molecules that are assumed to be present in the atmosphere of the analysed planet. The spectral resolution is set to 100,000 for all simulated spectra to match the spectral resolution of the HIRES and METIS. Scattering ensures that reflection spectra can be created by calculating the scattering of thermal radiation.

$$\log_{10}(T[\mathrm{K}]) = \log_{10}(T_p[\mathrm{K}]) + dT_p \log_{10}(P[\mathrm{bar}]) \tag{3.2}$$

For calculating reflection spectra ARCiS uses the Monte Carlo method in which the number of photons absorbed around the planet are counted. In order to simulate synthetic reflection spectra in which the photon noise is about equal to the noise ARCiS generates, the spectrum is averaged over 17 inclination angles close to 90°. 90° is chosen because in this thesis only planets that are detected both with the radial velocity method and the transit method are considered. Therefore, only planets that transit from our point of

view are taken into account.

Since the code is still under development and the primary goal for developing this code was creating synthetic spectra for transiting hot Jupiters using space-based telescopes, there are a few properties that are not modelled to reality. One property already discussed is that the opacity tables could not be created at resolutions of 100,000. The synthetic spectra simulating using these opacity tables are, however, calculated at a spectral resolution at 100,000 (see Fig. (3.3)). For some molecules however, some problems kept arising in simulating reflection spectra for METIS when the opacity tables were calculated at a resolution of 50,000. For N_2O the resolution was set to 20,000 because a higher abundance of N_2O than the abundance of the Earth otherwise gives a saturated band around 4.5 μm as can be seen from Fig. (3.4). Fig. (3.4) shows spectra of all molecules being in Earth abundances as presented in Fig. (4.25), decreasing the abundance of only N_2O by a factor of 10 while keeping the abundances of the other molecules constant and increasing the abundance of N_2O by a factor of 10. It can be seen that for 10 times the abundance of N_2O the strong 4.5 μm band becomes saturated as a result of numbers that become close to 0 arising from ARCiS since it was not developed for resolutions as high as 50,000. Note that this band is also strong (see Fig. (1.5)).

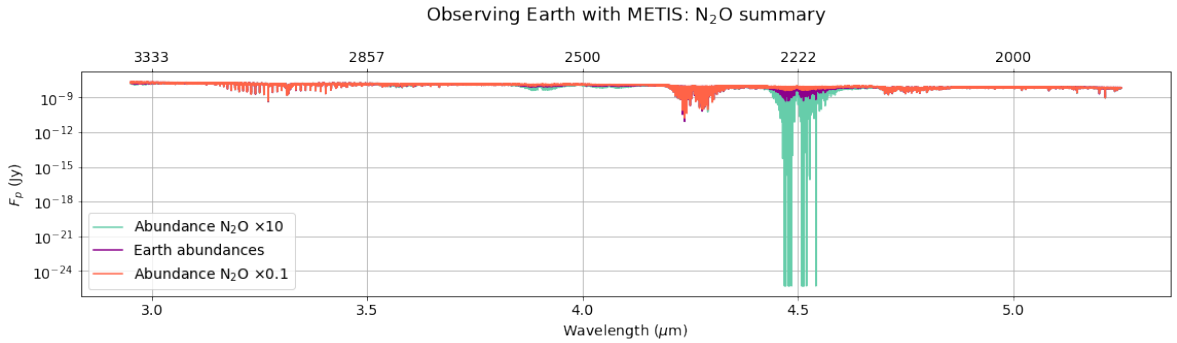

Figure 3.4: Synthetic reflection spectrum of an Earth-Sun analogue at 10 pc observed with METIS to illustrate the issue with the N_2O band around 4.5 μm. Purple indicates the the spectrum with all molecules having the abundance of Earth (see 4.25). Changing only the abundance of N_2O by a factor of ten results in the orange spectrum and the green spectrum for 10 times less and 10 times more atmospheric N_2O respectively.

Another problem that arose is the behaviour of the strong CO_2 band around 4.3 μm (see Fig. (2.3c). Fig. (3.5) shows how different CO_2 abundances affect the overall spectrum of Earth around a G2V star at a distance of 10 pc from the Earth. The overall spectrum is the spectrum including N_2, O_2, CO_2, O_3, N_2O, H_2O, and CH_4. It can be seen that for the atmospheric abundance of Earth (i.e. $4.09 \cdot 10^{-4}$) the 4.3 μm of CO_2 is saturated. Also for a 10 times lower abundance the band is saturated. For both a 100 and 1000 times lower abundance compared to the Earth abundance the band is unsaturated. The CO_2 abundance for simulating spectra for METIS was therefore set to 0.01 times the CO_2 abundance known for the Earth.

Another assumption in ARCiS is that the surface of the planet is always a diffuse (i.e. Lambertian) surface. Therefore, in ARCiS planets are modelled close to a planet covered with fresh snow. However, for terrestrial planets the surface can be covered with water, water-ice and/or continents. The continents can be sand-like or forest like etc. Therefore, surface biosignatures such as the VRE cannot be modelled using ARCiS. Moreover, these surface biosignatures are also not features of planetary atmospheres in general which is the subject of this thesis. Also temporal biosignatures cannot be modelled since the calculated synthetic spectra are all disk-averaged.

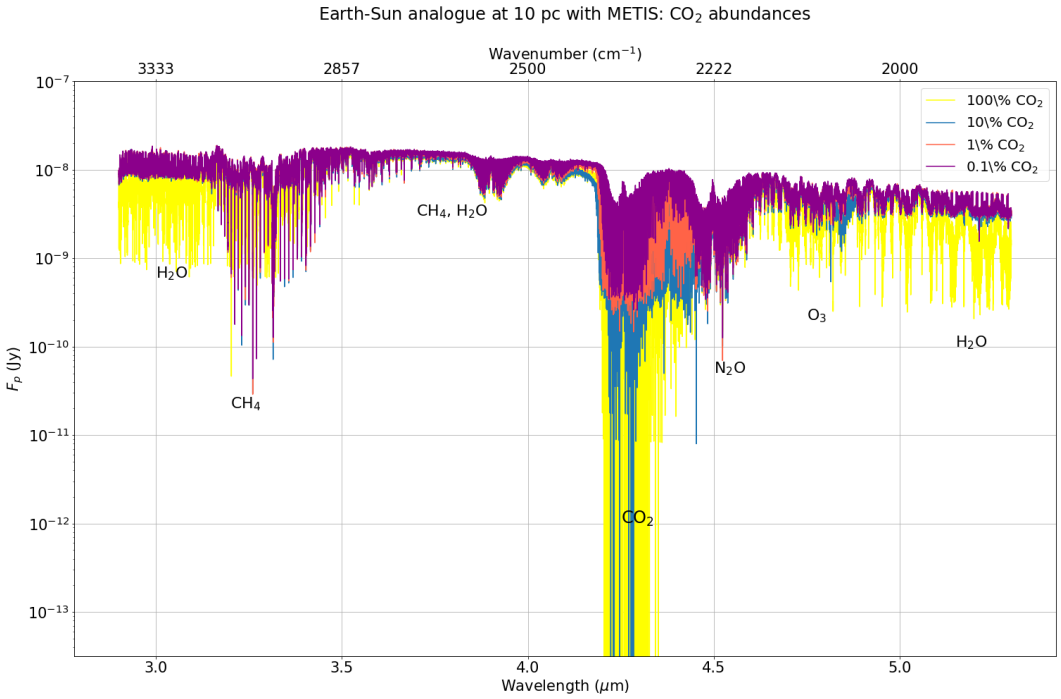

Figure 3.5: Synthetic reflection spectrum of an Earth-Sun analogue at 10 pc to illustrate the issue with the CO_2 band around 4.3 μm. The overall reflections spectrum of this Earth-Sun analogue is shown which includes the biosignature gases present in concentrations more than trace amounts (O_2, O_3, N_2O, and CH_4, and the habitability molecules N_2, H_2O, and CO_2, The abundance of the Earth (4.09 $\dot{1}0^{-4}$) is represented in yellow, while 10 times less, 100 times less and 1000 times less this abundance are represented in blue, yellow and purple respectively. The regions where molecules absorb are indicated.

3.2 The Habitable Exoplanets Catalog

To make a prediction about the detectability of biosignatures for some of the known exoplanets, some planets of the the Habitable Exoplanet Catalog (HEC)[1] are analysed. The HEC is an online catalogue of potentially habitable planets managed by the Planetary Habitability Laboratory (PHL). The PHL is a laboratory led by the University of Puerto Rico that focuses its research on studying the habitability of both planets in our Solar System and exoplanets. As of June 2019 the HEC consists of 52 potentially habitable exoplanets. The HEC is divided in two lists: a Conservative Sample of Potentially Habitable Exoplanets and an Optimistic Sample of Potentially Habitable Exoplanets. The first group lists exoplanets that have likely a rocky composition derived from the planetary mass and/or radius and the criterion that the planet is within the CHZ of the host star such that it can sustain liquid water on the surface. If both the mass and radius are known the composition is derived from the density, were it is usually assumed that a rocky composition density is between 0.7 and 1.5 $\rho_\oplus$ (4.4-8.3 g cm^{-3}) (Schulze-Makuch et al.; 2011, PHL, 2019)). If either the planetary radius or the minimum planetary mass is known the radius and mass corresponding to Earth-like values are taken. For the conservative sample the criterion used for the planetary radius is that the value is between 0.5 $R_\oplus$ and 1.5 $R_\oplus$. For the minimum planetary mass the boundaries are 0.1 $M_\oplus$ and 5 $M_\oplus$. The optimistic sample classifies exoplanets that have less likely a rocky composition and is orbiting at such a distance from the star that is does not lie in the conservative HZ but orbits in the optimistic HZ. The density can only be determined if both planetary mass and radius are known. If only one of the two is known, the limits for the optimistic sample are 1.5 $R_\oplus < R_p <$ 2.5 $R_\oplus$ and 5 $M_\oplus <$ $\sin i \cdot M_p <$ 10 $M_\oplus$.

To determine which detected planets are habitable or not five metrics for habitability are used by

[1] http://phl.upr.edu/hec

the PHL: the Earth Similarity Index (ESI), the Habitable Zone Distance (HZD), the Habitable Zone Composition (HZC), the Habitable Zone Atmosphere (HZA) and the Standard Primary Habitability (SPH). Additionally, two classification systems are used: the Planetary Mass Classification (PMC) and the Planetary Thermal Classification (PTC) (PHL, 2019). All these are used to rank planets according to their probability of habitability.

3.2.1 The Earth Similarity Index (ESI)

The ESI is a quantity that measures how much a planet resembles the Earth (Schulze-Makuch et al., 2011; PLH, 2019). The ESI ranges from zero (no similarity) to one (indistinguishable from Earth). The simple version of the ESI is based on parameters that are generally known for exoplanets such as equilibrium temperature, radius and mass. The basic equation for ESI can be written as (Schulze-Makuch et al., 2011):

$$\mathrm{ESI_x} = \left(1 - \left|\frac{x - x_0}{x + x_0}\right|\right)^w \tag{3.3}$$

where x is a property of the planet of interest, x_0 is the value for the Earth used as a reference, w is a weighting exponent used to provide a sensitivity measurement solved using ESI=0.8 as a reference value (Schulze-Makuch et al., 2011). This reference value is chosen because for ESI$>$ 0.8 the planet can be considered to be Earth-like. Note that for $0.6 <$ ESI < 0.8 planets can still be habitable: habitability does not only depend on the ESI. Earth-like here does not only mean similar to Earth in bulk-composition but also surface properties can be estimated to be similar to Earth. Planets with ESI$<$ 0.6 are considered to be uninhabitable.

Since most parameters of exoplanets are not known yet for most exoplanets, there is a simple estimate for the ESI using the radius, density, escape velocity and the surface temperature of the planet (Schulze-Makuch et al., 2011):

$$\mathrm{ESI} = \prod_{i=1}^{n} \left(1 - \left|\frac{x_i - x_{i0}}{x_i + x_{i0}}\right|\right)^{w_i/n} \tag{3.4}$$

3.2.2 The Habitable Zone Distance (HZD)

In the HEC the HZD is given with a number between -1 and 1. See section 1.2.2 for a description of the limits. An analytic description of the HZD is given by Eq. (1.1). By analysing the HZD, the PHL limited themselves to the CHZ boundaries. Properties which determine the HZD are the luminosity and therefore effective temperature of the star to determine the boundaries of the HZ and the distance between the star and the planet. These are properties that can be determined from observations and therefore the HZD is the easiest proxy for habitability (PHL, 2019). Note that it is assumed that liquid H_2O is used as a solvent and life forms of other solvent may fall outside the definition.

3.2.3 The Habitability Zone Composition (HZC)

The HZC is a measure of the suitability of the bulk composition (i.e. rocky composition needed for habitability) of the planet for the habitability of the planet (PHL, 2019). This refers to the mixture of elements from volatiles to iron that life needs. Planets with compositions that can sustain life have densities between those densities corresponding to pure iron and pure water planets. The HZC is given by (PHL, 2019):

$$\mathrm{HZC} = \frac{2r - r_o(m) - r_i(m)}{r_o(m) - r_i(m)} \tag{3.5}$$

where m is the mass of the exoplanet with a specific composition, r_o is the outer limit for a pure water planet and r_i is the inner limit representing a planet composed of pure iron. As for the HZD, the HZC is normalised such that exoplanets with values -1<HZC<1 likely have a habitable composition. Planets that have HZC<-1 have very dense iron bodies while planets with HZC>1 are considered gas planets.

3.2.4 The Habitable Zone Atmosphere (HZA)

Besides the composition and the distance to the host star, the ability for the planet to have an atmosphere that can sustain life is also important. This is quantified with the HZA and is based on thermal escape. The HZA is given by (PHL, 2019):

$$\text{HZA} = \frac{2\sqrt{m/r} - v_{eH} - v_{eN}}{v_{eH} - v_{eN}} \tag{3.6}$$

where r is the radius of the planet and v_{eN} and v_{eH} are the escape velocities of nitrogen and hydrogen respectively given by:

$$v_{e_x} = \sqrt{\frac{zT_eq}{M_{w_x}}} \tag{3.7}$$

where the subscript x can be N or H for nitrogen and hydrogen respectively and $M_{WN} = 14$ g/mol and $M_{WH} = 1$ g/mol are the molecular weights of nitrogen and hydrogen atoms. There are many more processes regulating planetary atmospheres besides thermal escape and these are not taken into account in the calculation of the HZA. Examples include stellar wind erosion, the impact of weathering (i.e. the process in which rocks and minerals are dissolved naturally when coming in contact with the atmosphere or biomass) and sequestration (long term build up of e.g. C in biomass and oceans having potential to be found in the atmosphere in the long term as CO_2), and the presence of planetary magnetic fields.

3.2.5 The Standard Primary Habitability (SPH)

The Standard Primary Habitability (SPH) is a measure of the ability of the planet to support primary produces (e.g. vegetation) (PHL, 2019). The SPH ranges from 0 (nominal environment) to 1 (best environment for vegetation). The SPH is used by the PHL to evaluate the global climatic habitability of planets. For an estimate of the SPH two environmental variables are needed: the surface temperature, T, and the relative humidity, RH. The SPH is estimated by (PHL, 2019):

$$\text{SPH} = H_T(T) \cdot H_{RH}(RH) \tag{3.8}$$

where H_T and H_{RH} are habitability functions for temperature and relative humidity respectively. The habitability functions, H_x are given by:

$$\begin{cases} H_x = \left[\frac{(x-x_{min})(x-x_{max})}{(x-x_{min})(x-x_{max})-(x-x_{opt})^2}\right]^w & x_{min} < x < x_{max} and x_{min} < x_{opt} < x_{max} \\ 0, & \text{otherwise} \end{cases} \tag{3.9}$$

where the x can be replaced by either T or RH. The weighting exponent, w, is based on the global temperature and relative humidity measurements. x_{opt} is the optimum value of the parameter which is determined from SPH=1.

Planets with SPH=0 may not be able to sustain complex (i.e. multicelluar) life but such a planet may be able to support microbial life. Earth has SPH=0.33 meaning that planet Earth is not fully

able to support vegetation. On Earth, deserts and oceans take some space of vegetation.

3.2.6 Planetary Mass Classification (PMC)

The Planetary Mass Classification refers to the classification of planets into seven mass categories (mercurian, subterran, terran, superterran, neptunian, and jovian). The mass categories are illustrated in Fig. (3.6). Asteroidan are asteroid sized objects with masses <0.00001 $M_\oplus$ generally not considered as planets. The mecurian mass category is used for planets with masses between 0.00001 $M_\oplus$ and 0.1 $M_\oplus$ while planets with 0.1 $M_\oplus < M_p <$0.5 $M_\oplus$. Earth falls into the terran mass category with limits 0.5 $M_\oplus < M_p <$2 $M_\oplus$, while super-Earths fall into the category supertteran. The gas planets can be categories into neptunian and jovian depending on their planetary mass.

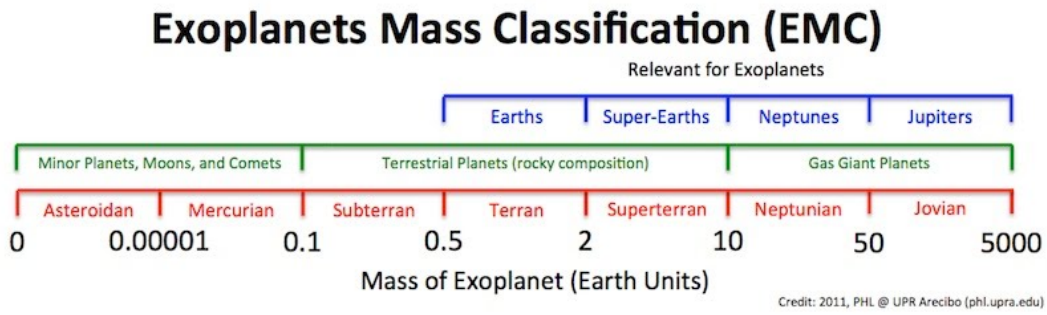

Figure 3.6: Scheme proposed the classify exoplanets according to their mass (HEC, 2019)

3.2.7 Planetary Thermal Classification (PTC)

The PTC is a planetary temperature division scheme for exoplanets. The thermal division is defined such that warm corresponds to planets inside the HZ and therefore hot and cold zones are outside the inner and outer boundary of the HZ respectively.Different forms of life need different temperatures. For example: microbial life has a wide thermal tolerance between temperatures of -15 °C and 121 °C while can tolerate temperatures between approximately 0 °C and 50 °C. To classify planets according to their temperature, the PHL uses terms well known in the field of microbiology. These names correspond to microbiological life that tolerates the temperatures. M-planets (mesoplanets) are planets that have an equilibrium temperature similar to Earth and are considered warm (0-50°). However, P-planets (psychroplanets) are cold (i.e. <0°C) and T-planets (thermoplanets) are hot (i.e. >50°C). Both P-planets and T-planets may only be habitable for microbial life. M-planets are considered to be more Earth-like planets compared to P-planets and T-planets.

Of the metrics presented above, the HZD and the ESI are the more uncertain metrics to infer habitability. However, the other metrics require additional information of the planet which cannot be obtained with observations today. The metrics do not take into account the possibility of life on planetary sub surfaces. Also estimates of the classification metrics can be given.

A selection of 6 planets of this catalogue was made based on the criterion that both mass and radius are known. These 6 planets are those planets of the HEC that have these two properties known as of June 2019. The 6 planets that are considered further are Trappist-1 d, Trappist-1 e, Trappist-1 f, Trappist-1 g, LHS1140 b, and K2-18 b. In Table 3.1 the ESI, the HZD, whether his planet is in the conservative sample or the optimistic sample, the PMC, and the PTC are presented for these 6 planets. 4 of the 6 planets have an ESI<0.8 and therefore not considered as Earth-like planets only based on their ESI. The Trappist-1 planets present in the HEC are all in the conservative sample (C)

while LHS 1140 b and K2-18 b are both in the optimistic sample (O).

Planet	ESI[(1)]	HZD	C/O[(1)]	PMC[(1)]	PTC[(1)]
Trappist-1 d	0.89	-0.80	C	subterran	warm
Trappist-1 e	0.87	-0.38	C	terran	warm
Trappist-1 f	0.70	0.19	C	terran	warm
Trappist-1 g	0.59	0.70	C	terran	warm
LHS 1140 b	0.69	0.41	O	superterran	warm
K2-18 b	0.71	-0.88	O	superterran	warm

Table 3.1: Selected planets based on the criteria that both planetary mass and planetary radius are determined from previous observations. The ESI, the PMC, and the PTC are taken from the HEC. Column 4 represents whether the planet is in the conservative sample (C) or the optimistic sample (O) in the HEC. The HZD (column 3) was calculated from Eq. (1.3).
(1) Parameters taken from PHL (2019)

3.3 Simulated noise

Since there is always instrumental noise the spectra obtained with ARCiS needs to be altered, or at least checked, for these noise sources such that the noise ARCiS generates is equal to the noise level of instruments of interest. Besides contributions from our own atmosphere when observing with ground based telescopes, there is also systematic noise, instrumental noise, photon noise etc. To take into account atmospheric contributions, it was checked at which wavelengths the Earth's atmosphere transmits light from other planets. The high resolution that is feasible for the considered instruments ensures that the planetary lines can be separated from telluric lines. This is especially important for water lines since water has absorption features that are strong in the optical, near-IR, and mid-IR.

The photon noise depends on the blackbody emission from the host star (B_λ), the telescope aperture size, the integration time, the distance to the target, and the radius of the star. The main parameter is the number of photons received at the telescope at each wavelength of interest.

The stellar blackbody, $B_\lambda(T)$, can be can be determined from:

$$B_\lambda(T) = \frac{2hc^2}{\lambda^5} \frac{1}{e^{\frac{hc}{\lambda k T}} - 1} \tag{3.10}$$

where T is the stellar temperature, h is Planck's constant, c is the speed of light, k is Boltzmann's constant, λ is the wavelength of interest. Using cgs units, the blackbody function has units of erg/s/cm^2/cm/steradian. Here 'cm' refers to the units of the wavelength of interest while the 'cm^2' refers to the units of the area of the emitting body. The units of time refer to the observation time and 'steradian' is the unit for the solid angle. For determining the photon noise the number of photons, it is necessary to multiply with units of 'cm', 'cm^2, 's', and 'steradian' to arrive be left with units of energy. The unit of wavelength can be eliminated by multiplying with the wavelength bin of the instrument. The telescope retrieves a flux value for a range of wavelengths defined by each wavelength bin. Since $R = \lambda/\Delta\lambda$, $\Delta\lambda$ can be determined from the known spectral resolution and the wavelength range of the considered instrument. Note that $\Delta\lambda$ is a function of wavelength. The disk area, A_*, of the emitting body is given by:

$$A_* = \pi R_*^2 \tag{3.11}$$

where R_* is the stellar radius. Since the planet only notices the radiation of one hemisphere of the host star, only that area is used. The integration time, t_{int}, was set to 10 hours, approximately the equivalent of 1 night of observations depending on the season. The solid angle, ϕ, can be calculated

by:

$$\phi = \frac{\pi(D/2)^2}{d^2} \tag{3.12}$$

where D is the telescope size and d is the distance between the observer and the target. The energy of the target received by the instrument can be calculated by:

$$E = B_\lambda(T) \cdot \Delta\lambda \cdot A_* \cdot t_{int} \cdot \phi \tag{3.13}$$

To convert this to a number of photons, the energy of a photon needs to be considered. Dividing this total energy by the energy per photon results in the number of photons, n:

$$n = \frac{E\lambda}{hc} \tag{3.14}$$

Notice that $n \propto \lambda^2$. The photon noise falls off as $1/\sqrt{n}$ (i.e. Poisson noise). Therefore, the larger the number of photons on the detector, the smaller the photon noise. The noise budget is estimated assuming that the total noise budget (i.e. including the systematic noises, the instrumental noises, and photon noises) are about 120% of the photon noise.

3.4 Detectability

The detectability of a gas in any exoplanetary atmosphere is a function of the abundance of that gas in the atmosphere of the planet, the distance between Earth and the planet of interest, the star-to-planet contrast, background noises, and instrumental noises. The signal to noise ratio (SNR), the ratio of the signal of interest and the background noises, is an important quantity for the detectability. The ELT receives a high level of radiation from the telescope, the instrument and the atmosphere of the Earth as it is a ground-based telescope. It is necessary to account for these effects when evaluating the detectability.

EPICS will not be sensitive enough to characterise the planets in either characterising the atmosphere of an Earth-Sun analogue at a distance of 10 pc or the planets listed in Table 3.1, since they all have a distance beyond 4 pc (Kasper et al., 2010). Therefore, EPICS data is not considered for these real planets The instruments that are considered here are METIS and HIRES.

Concerning the detectability of biosignatures with METIS, the performance calculation of Kendrew et al. (2010) were used. They calculated the sensitivity of the three main observing modes (i.e. imaging medium-resolution and the high-resolution IFU spectroscopy) of METIS for unresolved point sources at a SNR=10 for an exposure time of 1 hour. Only those for the IFU spectroscopy are used where properties of the atmosphere, the telescope and the instrument are taken into account. The analysis was done at the time the ELT was intended to be 42 m in diameter and when the location of the ELT was not decided yet. They did their analysis for three sites: Paranal at an altitude of 2.6 km, High and dry at an altitude of 5.0 km and the Armazones at an altitude of 3.064 km. The ELT will be build at the Armazones but sensitivity calculations to the IFS spectroscopy for this site are not performed. The sensitivities given for the low site and the high and dry sites are therefore the weighted averages of the sensitivities per altitude were taken. This resulted in sensitivity estimates of $4.3 \cdot 10^{-10}$ Jy at 2.9 μm, $5.7 \cdot 10^{-10}$ Jy at wavelengths of 3.8 μm, and $1.4 \cdot 10^{-8}$ Jy at 5.3 μm. The increase in sensitivity is because of the step between the M and L band. These are the sensitivities for a SNR of 10 for an exposure time of 1 hour. Considered planets are all considered transiting planets and therefore are not visible during the secondary eclipse. This duration is, however, short compared to the duration of an orbit of the planet around the host star and is not taken into account. Since the sensitivity increases

with $\sqrt{t}$, longer observing times will be able to probe atmospheres more effectively.

Since HIRES has just finish its phase A study, sensitivity calculations are not provided. Sensitivity calculations were done using the method in Rauer et al. (2013). The signal to noise ratio (SNR) for a spectral band or line in transmission is calculated by:

$$SNR_T = SNR_s \frac{f_A}{\sqrt{2}} = \frac{F_s \cdot t_{int} \cdot f_A}{\sigma_{tot}} \tag{3.15}$$

where σ_{tot} is the assumed noise, here 1.2 times the photon noise. SNR_s is the stellar signal to noise ratio. The stellar signal is given by:

$$F_s = \frac{1}{N} \frac{R_s^2}{d^2} I_s \cdot A \cdot q \cdot \Delta\lambda = \frac{\lambda}{hc} \frac{R_s^2}{d^2} I_s \cdot \pi R_{tel}^2 \cdot q \cdot \lambda / R \tag{3.16}$$

where $N = hc/\lambda$ is a conversion to the number of photons, A and R_{tel} are the collecting area and the radius of the telescope respectively, d is the distance between the Earth and the star, I_s is the spectral energy flux of the star, q is an efficiency factor (0.5 for the ELT), λ is the wavelength of interest and R is the spectral resolution. f_A is the additional transit depth:

$$f_A = \frac{(R_p + h_e(\lambda))^2}{R_s^2} - \frac{R_p^2}{R_s^2} \tag{3.17}$$

where h_e is the effective height of the atmosphere as function of wavelength. SNR_T is the transmission signal to noise ratio:

$$SNR_T = \frac{Rp^2}{R_s^2} \tag{3.18}$$

The factor of $1\sqrt{2}$ in Eq. (3.15) results from the consideration that the measurements of the difference in stellar flux transmitted to the planetary atmosphere if it is in and out of transit.

The integration time, t_{int}, is set equal to the transit duration, T_d, the time the planet of interest is in front of the star. Assuming the inclination is 90°, T_d can be derived from:

$$T_d = \frac{P}{\pi} \arcsin\left(\frac{R_s}{a}\right) \tag{3.19}$$

where P is the orbital period of the planet and a is the semi-major axis. Using T_d the planetary SNR can be calculated and the integration time can subsequently be calculated from:

$$t_i = T_D \left(\frac{SNR_{t_i}}{SNR_p}\right)^2 \tag{3.20}$$

Chapter 4

Results

The results for examining the detectability of biosignatures with the ELT are divided into several sections. The idea behind the structure is building a more and more realistic atmosphere in subsequent sections and subsections starting from very simple atmospheres. As a first example, an Earth-Sun analogue is simulated at a distance of 10 pc. It is assumed that the Earth-twin transits the Sun-twin from our point of view. Section 4.1 describes a simple atmosphere in which only one gas is present. The atmosphere is assumed to have a small pressure range and a single temperature throughout the atmosphere. In section 4.2 more realistic pressure-temperature structures are used for simulating simple atmospheres consisting of one gas. In section 4.3 the effect of a mixture of gases is discussed. This includes changing the abundances of the atmospheric gases by a factor of 10. In section 4.4 spectra are shown for the 6 planets taken from the HEC. This section also includes an analysis of molecular abundances. In section 4.5 the optimal resolution for the characterisation of exoplanetary atmospheres will be discussed using the design of the ELT.

4.1 Simple isothermal atmosphere consisting of one gas

In this section we assume simple atmospheres which have a small pressure range and are isothermal (i.e. have only one temperature throughout the atmosphere). This atmosphere is assumed to consist of one gas. The pressures and temperatures are varied to investigate the effect of different pressures and temperatures on the spectra. The pressures and temperatures are chosen such that a planet can be habitable. That is, because of our definition of life, a planet that can sustain liquid H_2O. See section (3.1) for a detailed explanation of the adopted limits. In short, for determining ranges for pressures and temperatures, the pressures and temperatures should be within the surface- pressure and temperature range of Mars-Earth-Venus. The effect of varying the temperature in an isothermal atmosphere is that the temperature in the whole atmosphere is changed. For investigating the effect of the surface pressure, however, the minimum pressure is set constant to $P = 10^{-2}$ bar and to study the effect of the surface pressure on both the transmission and the reflection spectrum, the maximum pressure is varied. The pressure varies linearly from the surface pressure to the pressure of 10^{-2} bar. For the different wavelength regions were HIRES and METIS are sensitive to, different gases are assumed to be present in the atmosphere for both instruments. For the wavelength range of HIRES, the optical and the near-IR, O_2 is used as an example. METIS is, however, sensitive to wavelengths in the mid-IR and O_3 is used as an example. These molecules are chosen taking into account the spectral lines of the molecules and the importance for habitability of these molecules on Earth. The spectra in this section are simulated by considering 100% O_2 and 100% O_3 atmospheres for HIRES and METIS respectively.

4.1.1 Effect of the surface pressure

Except for the terrestrial planets in our solar system, the surface pressure of other discovered terrestrial planets is not well determined. Therefore, investigating the effect of surface pressure is useful to investigate whether it might be possible to determine the surface pressure from near-future observations. Since this is dependent on the pressure profile of the atmosphere, investigating whether determining the surface pressure is possible with near-future technology is beyond the scope of this thesis. In this thesis, the effect of the surface pressure is shown to indicate why the spectrum changes with surface pressure. Fixing the surface temperature to 300 K, about the average surface temperature of the Earth and a surface temperature within the CHZ limits, the surface pressure is varied between 0.5 and 50 bar.

The effect of the surface pressure for an atmosphere consisting of 100% O_2 observed with HIRES is shown in Fig. (4.1). The differences between the various surface pressures and 1 bar are shown in the residual plot. The differences are represented in the same colours as the surface pressures other than 1 bar. Changing the pressure results in a difference in the ratio of the planetary radius versus the stellar radius from about a wavelength of 0.5 μm. Because of the assumption that the ideal gas law holds for gases in the atmosphere, it should be noted that changing only the pressure in the atmosphere and keeping the other parts constant causes the ideal gas law to be disobeyed.

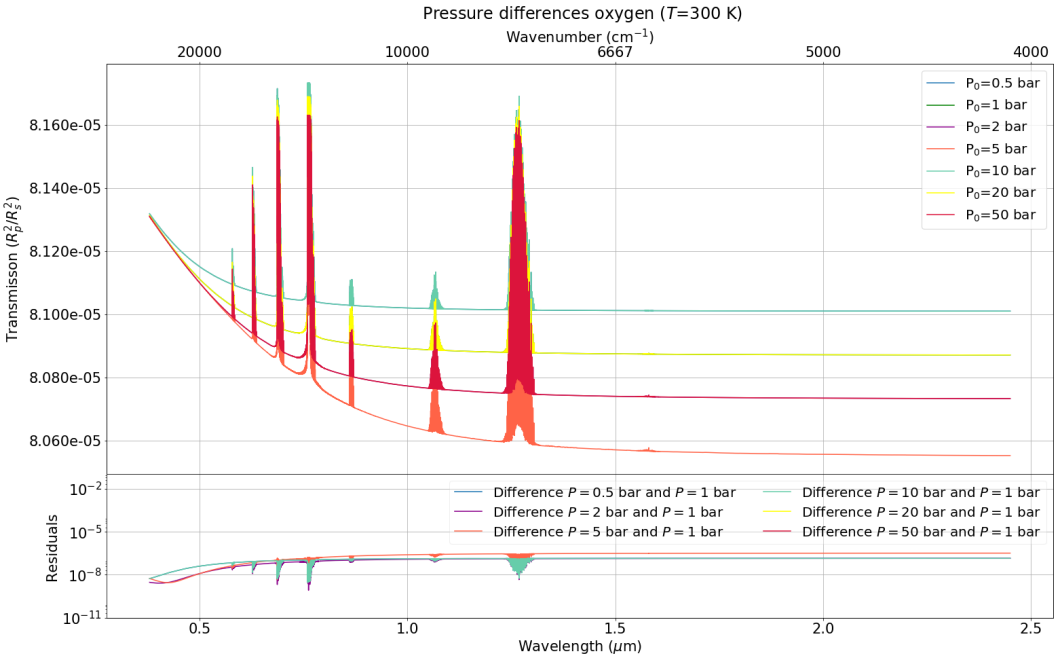

Figure 4.1: Synthetic transmission spectrum of an 100% O_2 atmosphere showing the effect of the the variation of the surface pressure for an Earth-Sun analogue located at a distance of 10 pc as simulated for HIRES assuming isothermal atmospheres ($T = 300$ K) with a minimum pressure of 10^{-2} bar. The variation in transmission of O_2 for surface pressures of 0.5 bar (blue), 1 bar (green), 2 bar (purple), 5 bar (orange), 10 bar (cyan), 20 bar (yellow), and 50 bar (red) are shown. The residual plot below shows the difference between the different pressures and the reference pressure of 1 bar as function of wavelength.

One result is that the width of the band at 1.3 μm increases slightly with increasing pressure as can be seen from the residual plot consistent with the concept of pressure broadening. This is also the case for the other spectral features but this broadening is less prominent for those lines. The effect of pressure broadening is not very notable for pressure range spanning two orders of magnitude.

Assuming an atmosphere consisting of only O_3 gas using METIS as an instrument and varying the surface pressures has a similar result. The reflection spectrum of such an atmosphere is shown in Fig. (4.2). It can be seen that there is a difference of at most $\sim 10^{-8.5}$ bar. This can be considered

as a small difference and can be caused either because of some uncertainties in the computation or that there is not a significant difference between these pressures. Nevertheless, the pressure range considered is two orders of magnitude and the spectrum for a pressure of 10 bar results in the most significant change in the spectrum not consistent with the concept of pressure broadening.

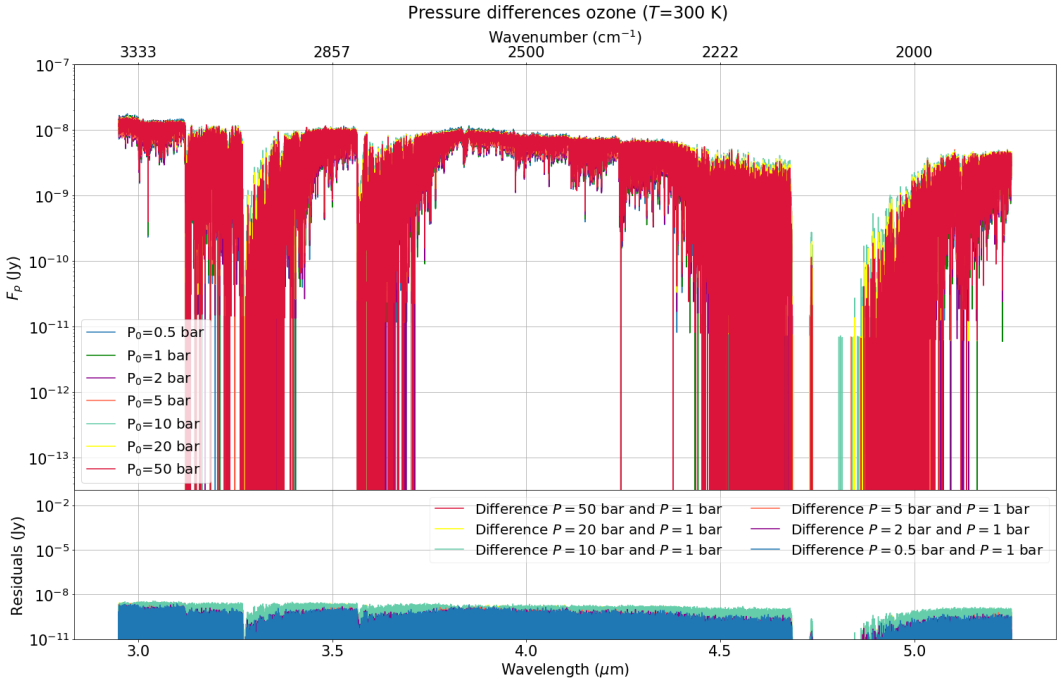

Figure 4.2: Synthetic reflection spectrum of an 100% O_3 atmosphere showing the effect of the the variation of the surface pressure for an Earth-Sun analogue located at a distance of 10 pc as simulated for METIS assuming isothermal atmospheres (T = 300 K) with a minimum pressure of 10^{-2} bar. The variation in planetary flux of O_3 for pressures of 0.5 bar (blue), 1 bar (green), 2 bar (purple), 5 bar (orange), 10 bar (cyan), 20 bar (yellow), and 50 bar (red) are shown. The residual plot below shows the difference between the different pressures and the reference pressure of 1 bar as function of wavelength.

Besides changing the maximum pressure in the atmosphere (i.e. the surface pressure), also the minimum pressure in the atmosphere can be changed. Physically, decreasing the minimum pressure in the atmosphere results in a thicker atmosphere. In this case the pressure is linearly decreases in the atmosphere up to 10^{-2} bar (as was chosen previously), 10^{-4} bar, 10^{-6} bar and 10^{-8} bar setting the boundary of the planetary atmosphere to 80 km. Effectively, of lower minimum pressures, the change in pressure is more rapid per km in altitude. For the example of an 100% O_2 and 100% O_3 atmosphere the results are shown in Fig. (4.3) and Fig. (4.4) respectively. For lower minimum pressures the transmission is larger compared to higher minimum pressures. Transmission spectra probe the upper atmosphere and therefore the pressure probed is lower for the cases a lower minimum pressure is assumed. The residual plot shows differences of about 10^{-7}. Compare this to the transmission of the order of $\sim 8 \cdot 10^{-5}$. Note also that the spectra for the different minimum pressures are split up to a wavelength of 0.5 μm instead of from 0.5 μm for the changing surface pressure. It can be seen that changing the minimum pressure does not result in a significant change in the reflection spectrum which probes more layers of the atmosphere compared to transmission spectra. Changing the minimum pressure mostly affects the upper atmosphere. A change in the minimum pressure is not relevant for the search for biosignatures since the upper atmosphere is not considered to be altered by life.

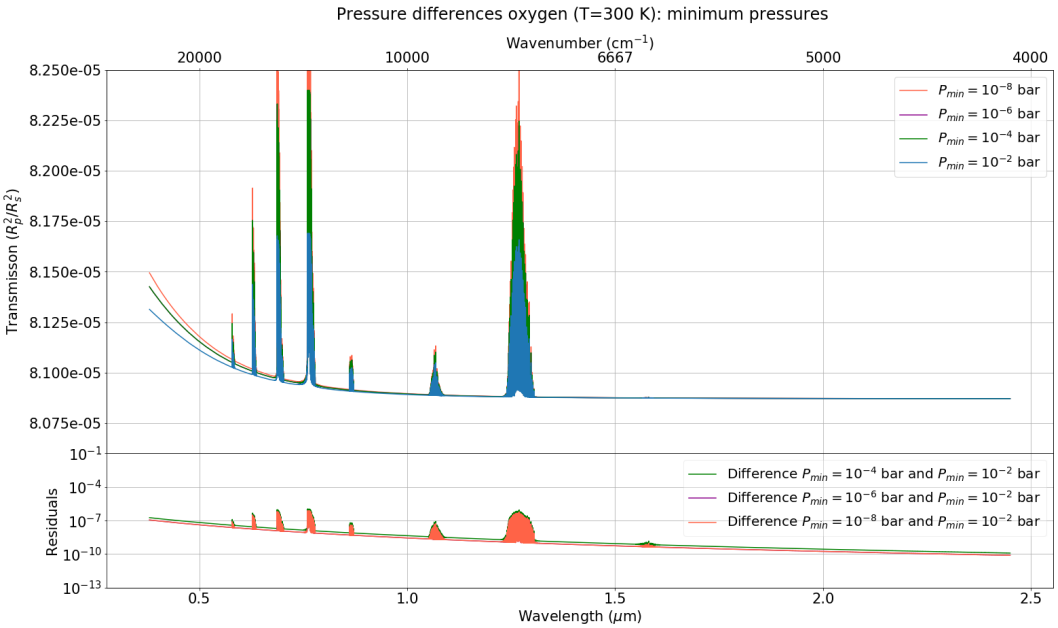

Figure 4.3: Synthetic transmission spectrum of an 100% O_2 atmosphere showing the effect of the the variation of minimum atmospheric pressure for an Earth-Sun analogue located at a distance of 10 pc as simulated for HIRES assuming an isothermal atmosphere ($T = 300$ K) with a maximum pressure of 1 bar. The variation in minimum pressure for pressures of 10^{-2} bar (blue), 10^{-4} bar (green), 10^{-6} bar (purple), and 10^{-8} bar (orange) are shown. The residual plot below shows the difference between the different pressures and the reference minimum pressure of 10^{-2} bar as function of wavelength.

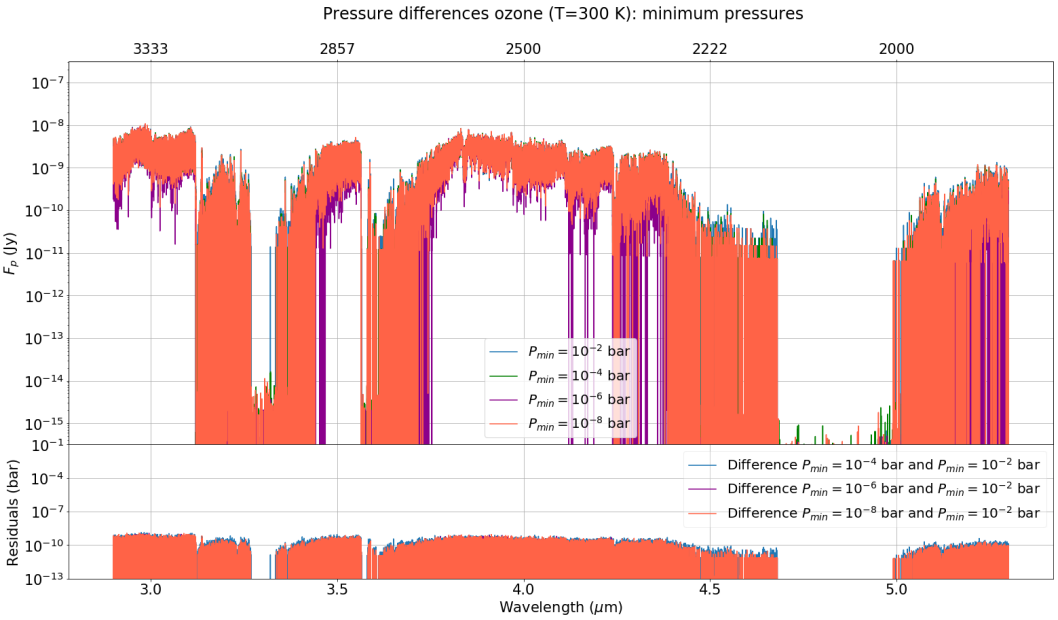

Figure 4.4: Synthetic reflection spectrum of an 100% O_3 atmosphere showing the effect of the the variation of minimum atmospheric pressure for an Earth-Sun analogue located at a distance of 10 pc as simulated for METIS assuming isothermal atmospheres ($T = 300$ K) with a maximum pressure of 1 bar. The variation in minimum pressures for pressures of 10^{-2} bar (blue), 10^{-4} bar (green), 10^{-6} bar (purple), and 10^{-8} bar (orange) are shown. The residual plot below shows the difference between the different pressures and the reference minimum pressure of 10^{-2} bar as function of wavelength.

4.1.2 Effect of the surface temperature

Although the surface temperature of most planets cannot be measured with current technology, an estimate of the temperature can be made using the equilibrium temperature. For this, an albedo needs

to be assumed. For Solar System planets, the albedo is known: it ranges between 0.1 for Mercury to 0.8 for Venus. The average albedo of Earth is 0.3 and is usually taken as a reference for other habitable planets. Fixing the surface pressure to 1 bar (i.e. the surface pressure of Earth) and the minimum pressure to 10^{-2} bar, the temperature of the atmosphere is varied between temperatures of 250 K and 500 K. The effect of the temperature for an 100% O_2 isothermal atmosphere is shown in Fig. (4.5). In the transmission spectrum of the 100% O_2 atmosphere it can be seen that the transmission (R_p^2/R_s^2) is higher for higher temperatures. This is because of the local scale height which changes linearly with T ($H \propto T$). The scale height is responsible for setting the depth of the absorption features in the transmission spectrum. It can be seen that the strength of O_2 lines is different for different temperatures. For higher temperatures, the features at a wavelength of 0.8 μm and 1.1 μm have higher strengths. Limiting ourselves to these temperatures, it can be deduced from the zoom around the O_2 A-band, Fig. (4.5b), that changing the temperature in an isothermal atmosphere has an effect on the transmission but not on the broadening of the bands.

The effect of changing the temperature for an 100% O_3 atmosphere for an Earth-Sun analogue at 10 pc results in the reflection spectrum shown in Fig. (4.6). The atmospheric pressure is assumed to be 1 bar at the planetary surface decreasing linearly to 10^{-2} at an altitude of 80 km. In this reflection spectrum it can be seen that the temperature effect of O_3 does not result in a change in the sharpness of bands. Around a wavelength of 4.8 μm the temperature has an effect of the location of the band. For lower temperatures the band starts at lower wavelengths while at higher temperatures the band is shifted to a wavelength of 5.0 μm. For higher temperatures the reflection spectrum is somewhat lower than for the lower temperatures. This results from the flux of the planet: $F_p \propto F_s \propto L \propto T^4$. Only the temperature of the atmosphere is changed and all other variables are kept constant. Therefore, the flux of the planet increases with increasing T^4.

4.2 Atmosphere with realistic P-T profile for one gas

In this section atmospheres with more realistic P-T profiles are considered. The atmosphere are assumed to have only one gas in their atmosphere. Again an 100% O_2 atmosphere is assumed for the wavelength range of HIRES and an 100% O_3 atmosphere is assumed for the wavelengths METIS is sensitive to.

The more realistic P-T profile is modelled taking the Earth's temperature profile as a function of altitude as a basis.There is a differentiation made between atmospheres with and without temperature inversions. The atmosphere of the Earth has one temperature inversion up to the height of 80 km to with the atmosphere was modelled. The temperature change as a function of altitude was described in section 3.1 where the ISA was specified. This P-T profile was used here to model an atmosphere with temperature inversions. When an atmosphere without temperature inversions is mentioned, it indicates that the temperature does not change with altitude above an altitude of 11 km. That means that the atmosphere is isothermal with a temperature of 216.5 K from 11 km above the planetary surface. Below 11 km, an atmosphere without temperature inversions is assumed to follow the Earth's tropospheric lapse rate of 6.5 K/km.

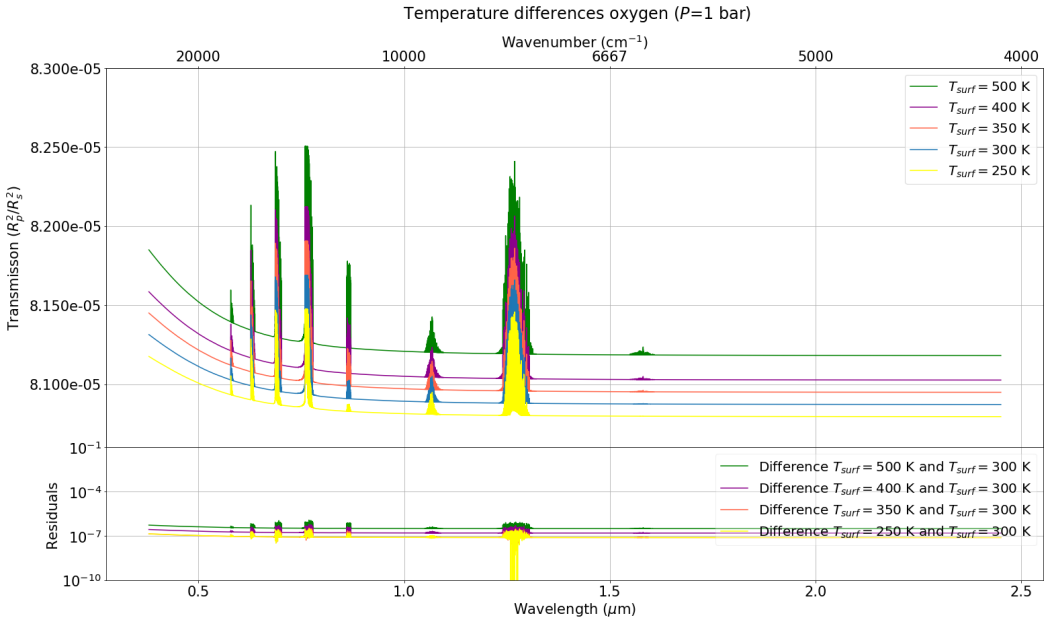

(a)

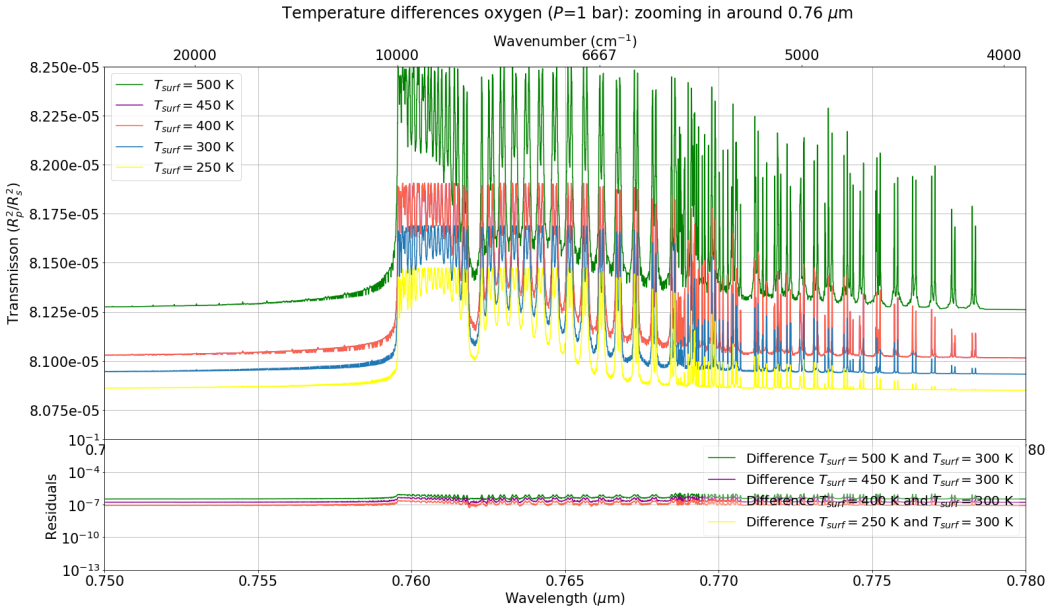

(b)

Figure 4.5: Synthetic transmission spectra of an 100% O_2 atmosphere showing the effect of the surface temperature for an Earth-Sun analogue located at a distance of 10 pc as simulated for HIRES assuming an isothermal atmosphere with a pressure range from 10^{-2} bar to 1 bar. The variation in transmission (R_p^2/R_s^2) of O_2 for temperatures of 250 K (yellow), 300 K (blue), 350 K (orange), 400 K(purple), and 500 K (green) is shown. The spectrum for the wavelength range of HIRES is shown in (a) while a zoom around the O_2 A-band is shown in (b). The residual plots below show the difference between the different temperatures and the reference temperature of 300 K as function of wavelength.

Modelling the troposphere similar as the pressure-temperature profile has a few reasons: since we only know life on planet Earth, modelling the troposphere with the same lapse rate and up to the same altitude makes sure that no additional assumptions are made. More importantly, it can be compared to the P-T profile with temperature inversions and results can give insight whether is would be possible to distinguish an atmosphere with and without temperature inversions for observations with HIRES and METIS. An atmosphere without temperature inversions is also modelled to end at an altitude of 80 km above the planetary surface for the reason that life is assumed to alter the lower atmosphere.

This atmosphere without temperature inversions is comparable to the structure of Mars which does not show any significant increases of temperature with altitude. Fig. (4.7) illustrates what is intended with a temperature with (red) and without (blue) temperature inversions for a planet with a surface temperature of 288 K.

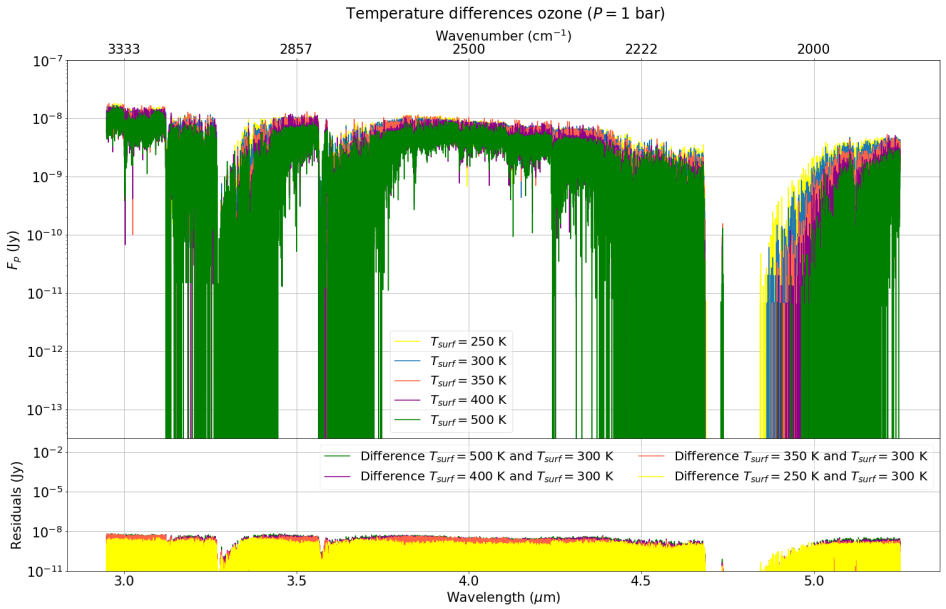

Figure 4.6: Synthetic reflection spectrum of an 100% O_3 atmosphere showing the effect of the surface temperature for an Earth-Sun analogue located at a distance of 10 pc as simulated for METIS assuming an isothermal atmosphere with a pressure range from 10^{-2} bar to 1 bar. The difference of the reflection of O_3 as a function of wavelength for temperatures of 250 K (yellow), 300 K (blue), 350 K (orange), 400 K (purple), and 500 K. The residual plot below shows the difference between the different temperatures and the reference temperature of 300 K as function of wavelength.

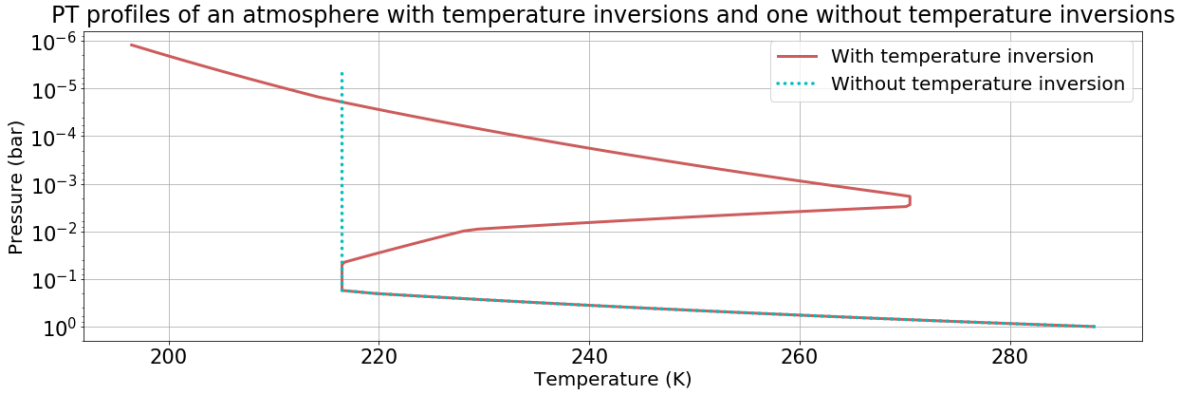

Figure 4.7: Pressure-Temperature profile of a planet with $T_{surf} = 288$ K assuming an atmosphere with (red) and without (blue) temperature inversions. In both cases the troposphere has the same lapse rate and ends at an altitude of 11 km. In case of an atmosphere with temperature inversions, the ISA up to 80 km is modelled whereas for the case of an atmosphere without temperature inversions the temperature does not change with altitude beyond 11 km.

4.2.1 Effect of surface pressure

The effect of the surface pressure of both an atmosphere without a temperature inversion and with a temperature inversion was investigated. The same pressures are taken for the case of an isothermal atmosphere with a small pressure gradient. The transmission spectra for an 100% O_2 atmosphere assuming both a temperature profile without temperature inversions and one with a temperature inversion are shown in Fig. (4.8b). It can be seen that there is no difference in the transmission

spectra for both cases. This is consistent with the idea that transmission spectra are not sensitive to the vertical temperature profile of the atmosphere since transmission spectra are pure absorption spectra (Kempton et al., 2016). The effect of the surface pressure is therefore the same for an atmosphere without temperature inversions and for one with a temperature inversion. The difference between transmission spectra and one for an isothermal atmosphere are only up to 0.5 μm. For the more realistic P-T profile, the pressure changes according to the scale height resulting in an overall change in transmission. Therefore, the spectra in Fig. (4.8b) do not have the same starting transmission.

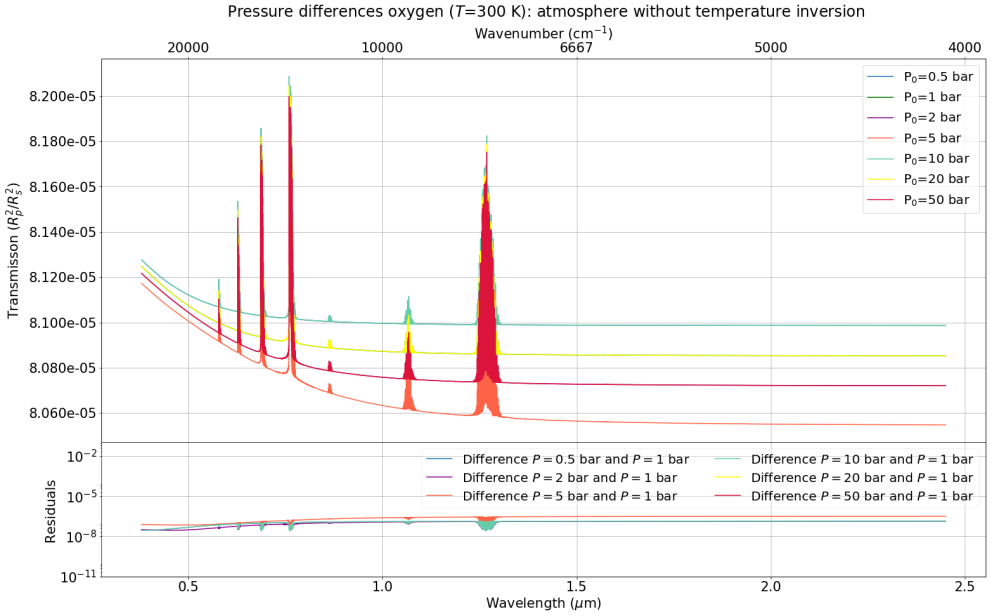

(a)

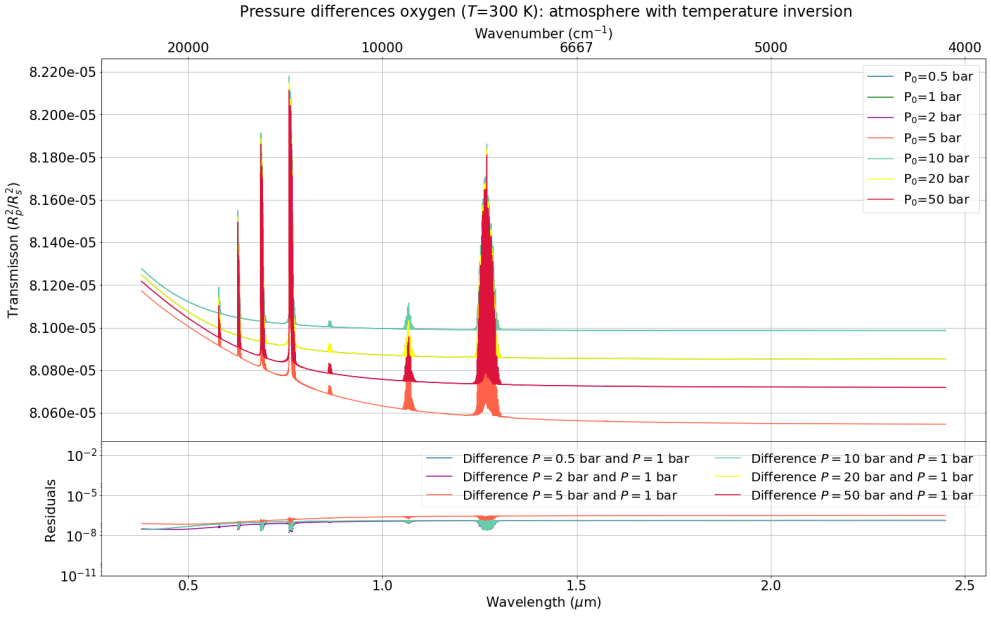

(b)

Figure 4.8: Synthetic transmission spectra of an 100% O_2 atmosphere showing the effect of the surface pressure for an Earth-Sun analogue located at a distance of 10 pc as simulated for HIRES assuming an atmosphere without temperature inversions (a) and an atmosphere with a temperature inversion (b). In both cases the surface temperature is assumed constant at 300 K while the pressure in the atmosphere drops exponentially. The variation in transmission of O_2 for pressures of 0.5 bar (blue), 1 bar (green), 2 bar (purple), 5 bar (orange), 10 bar (cyan), 20 bar (yellow), ad 50 bar (red) are shown. The residual plots below show the difference between the different pressures and the reference pressure of 1 bar as function of wavelength.

For the reflection spectra of atmospheres consisting of 100% O_3 there is, however, a significant difference between an atmosphere without any temperature inversion and one with a temperature inversion as shown in Fig. (4.9). For an atmosphere without temperature inversion it seems that for higher pressures the spectrum becomes saturated and the planetary flux drops to values $\sim 10^{-10}$ Jy while for lower pressures the reflection is between 10^{-8} and 10^{-9} as is the case for an atmosphere with a temperature inversion and an isothermal atmosphere. The reflection spectrum of the atmosphere with temperature inversions seems to be closest to the isothermal case except for the 10 bar spectrum. Differences seem to be because of computational errors of ARCiS.

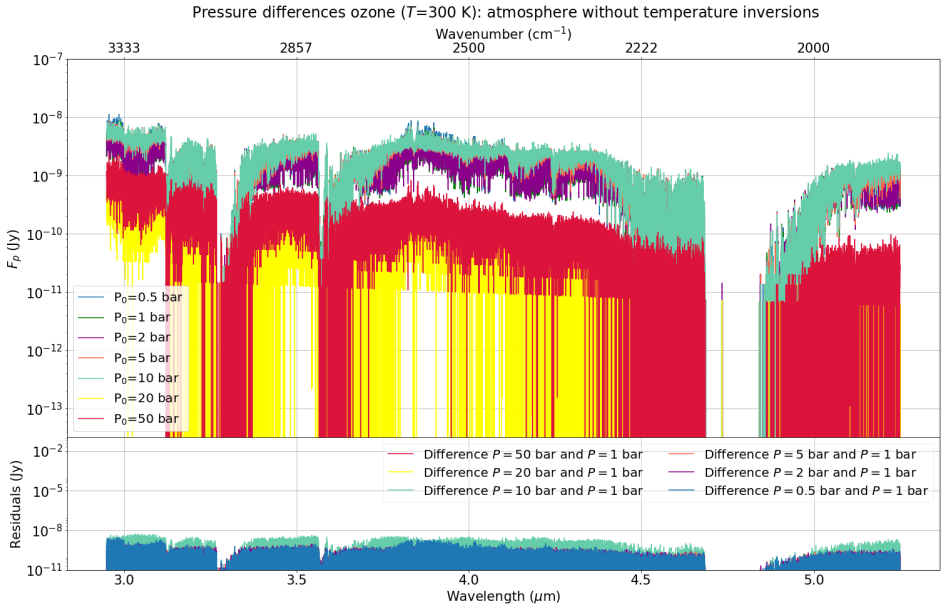

(a)

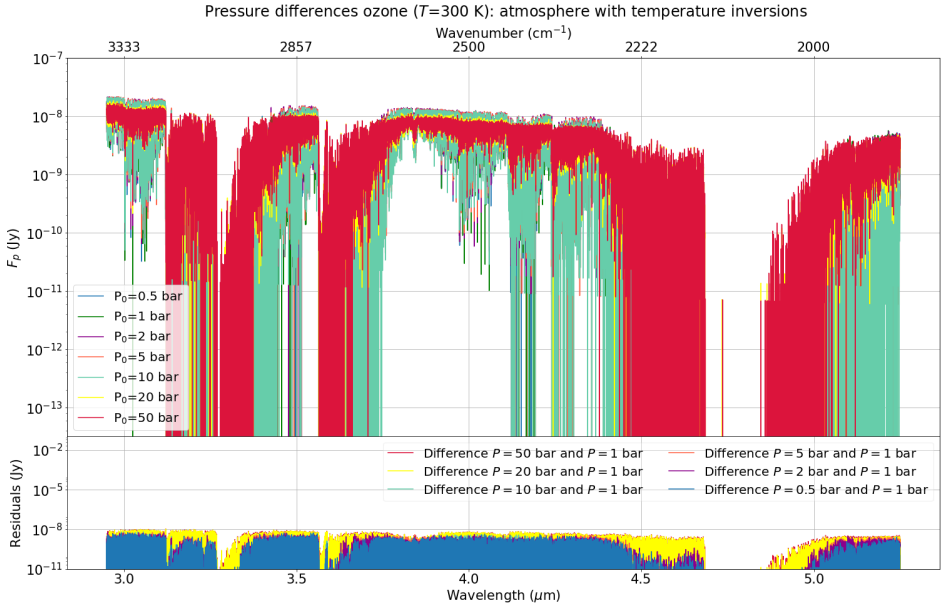

(b)

Figure 4.9: Synthetic reflection spectra of an 100% O_3 atmosphere showing the effect of the surface pressure for an Earth-Sun analogue located at a distance of 10 pc as simulated for METIS assuming an atmosphere without temperature inversions (a) and an atmosphere with a temperature inversion (b). In both cases the surface temperature is assumed constant at 300 K while the pressure in the atmosphere drops exponentially. The variation in planetary flux of O_3 for pressures of 0.5 bar (blue), 1 bar (green), 2 bar (purple), 5 bar (orange), 10 bar (cyan), 20 bar (yellow), ad 50 bar (red) are shown. The residual plots below show the difference between the different pressures and the reference pressure of 1 bar as function of wavelength.

4.2.2 Effect of surface temperature

The effect of the surface temperature for an Earth-Sun analogue at 10 pc on the transmission spectra for both an atmosphere without any temperature inversion and one with a temperature inversion with the instrumental characteristics of HIRES are shown in Fig. (4.10). Similar to the effect of the surface pressure, transmission spectra are not sensitive to the temperature profile and therefore the transmission spectra for an atmosphere without temperature inversion is indistinguishable from the transmission spectra for an atmosphere with a temperature inversion. However, there is a discrimination between the isothermal case and the ones with the more realistic P-T profile in terms of the strengths of the O_2 lines. The O_2-A band has a transmission of almost $8.3 \cdot 10^{-5}$ for $T = 500$ K for an atmosphere with more realistic P-T profile while the same band has a transmission of $8.25 \cdot 10^{-5}$ for $T = 500$ K in the case of an isothermal temperature profile with a linear pressure decrease.

Synthetic reflection spectra for varying the surface temperature that can be seen with METIS taking again an Earth-Sun analogue at 10 pc as an example for both an atmosphere without any temperature inversion and one with a temperature increase in the stratosphere is shown in Fig. (4.11). The reflection spectra assuming no temperature inversion is very dense: for $T = 500$ K the bands centered at 3.6 and 4.6 μm are hardly distinguishable. The reason for this may lie in the fact that the temperature remains constant for about 85% of the atmospheric extent. However, the effect of the isothermal case and the case where the atmosphere has an Earth-like tropospheric lapse rate followed by an isothermal profile are expected to be more similar than seen in this study. The spectra for an atmosphere with a temperature inversion and for an isothermal atmosphere are, however, more similar.

4.3 Atmosphere consisting of a mixture of gases

This section is divided in two parts: one in which the abundances of the molecules assumed to be present in the atmosphere do not change higher in the atmosphere and one in which these abundances do change with height above the planetary surface. Again an Earth-Sun analogue at a distance of 10 pc is chosen as an example. The detectability of the features themselves is discussed in section 4.4 where the integration times are compared to Trappist-1 d, Trappist-1 e, Trappist-1 f, Trappist-1 g, LHS 1140 b and K2-18 b.

4.3.1 Molecules with a constant mixing ratio throughout the atmosphere

In order to take a next step toward building a more and more realistic atmosphere, molecules are assumed to be present in the atmosphere in quantities that do not change with altitude, i.e. the vertical distribution of molecules is constant. The values for the atmospheric abundances used here are the mixing ratios of the Earth's troposphere. Also, some of the proposed biosignatures which are not present in the Earth's atmosphere in significant quantities (e.g. the mixing ratio of CH_3Cl is on the order of parts per trillion in the Earth's atmosphere) are added individually to the spectrum. For C_2H_6, CH_3Cl and NH_3 the mixing ratios are assumed to be between 10^{-5} and 10^{-7}. These values are chosen to cover the range of the mixing ratios for the molecules that are present in the Earth's atmosphere in more than trace amounts. The mixing ratios used for the assumed atmosphere without a vertical distribution of molecules throughout the atmosphere for N_2, O_2, CO_2, H_2O, CH_4, N_2O, O_3, C_2H_6, CH_3Cl, and NH_3 are displayed in Table 4.1.

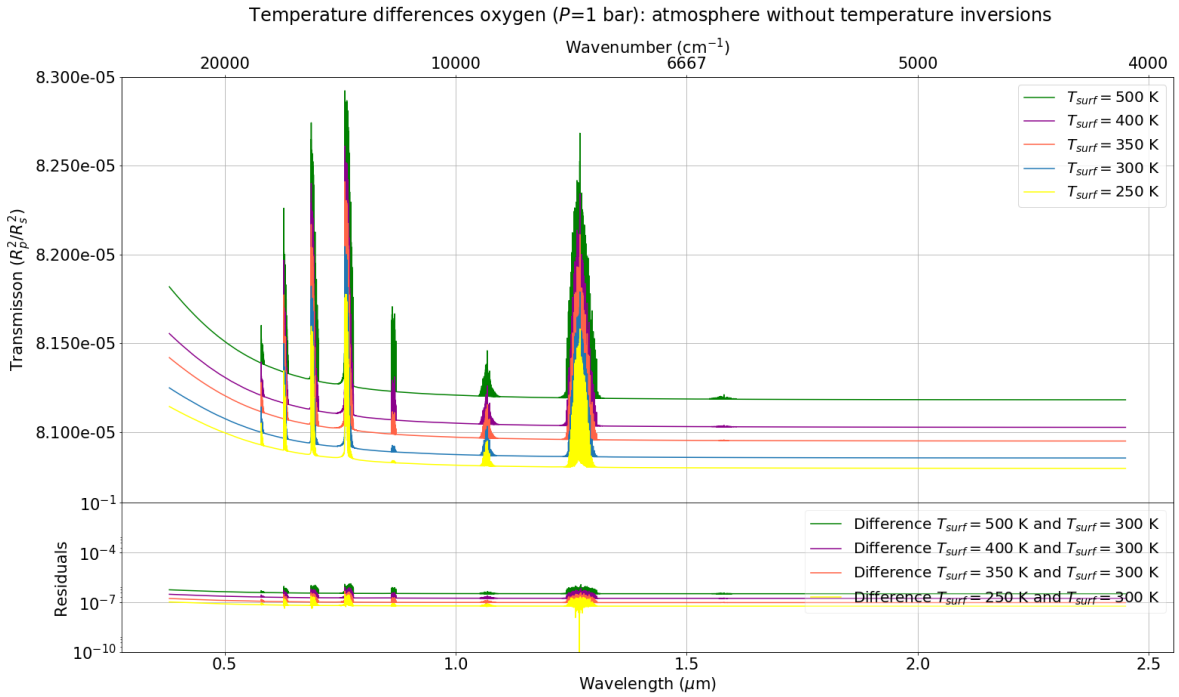

(a)

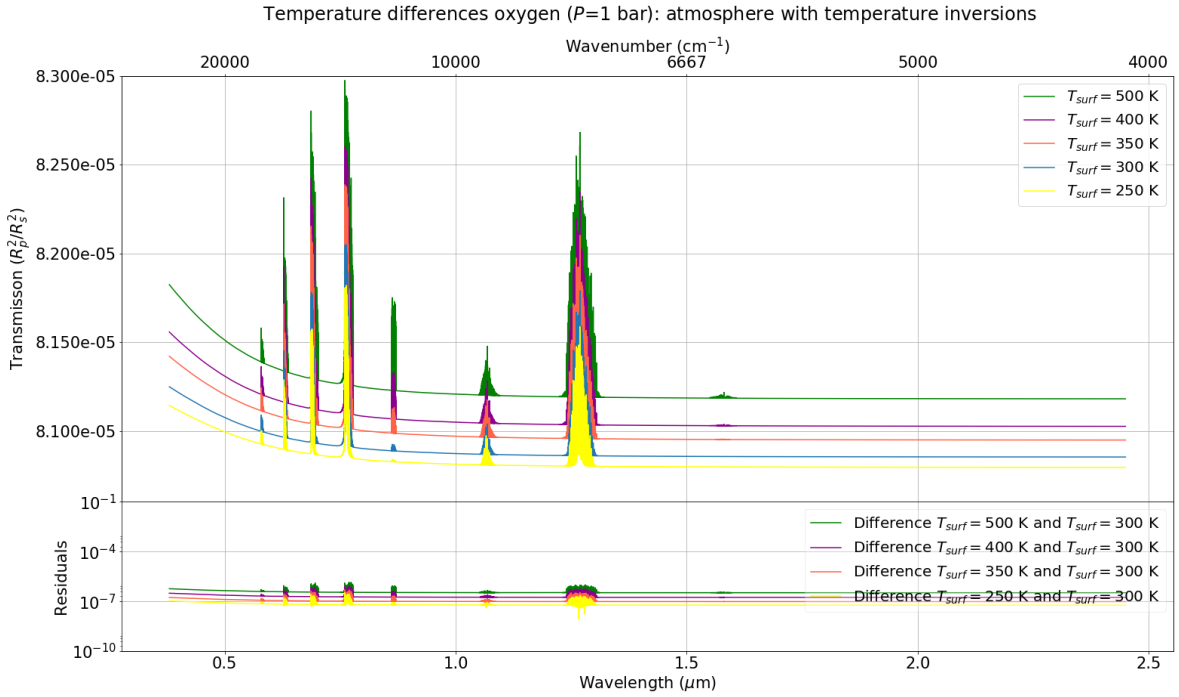

(b)

Figure 4.10: Synthetic transmission spectra of an 100% O_2 atmosphere showing the effect of the surface temperature for an Earth-Sun analogue located at a distance of 10 pc as simulated for HIRES assuming an atmosphere without temperature inversions (a) and an atmosphere with a temperature inversions (b). In both cases the surface pressure is assumed constant at 1 bar while the pressure in the atmosphere changes exponentially. The variation in transmission (R_p^2/R_s^2) of O_2 for temperatures of 250 K (yellow), 300 K (blue), 350 K (orange), 400 (purple), and 500 K (green) is shown. The residual plots below show the difference between the different temperatures and the reference temperature of 300 K as function of wavelength.

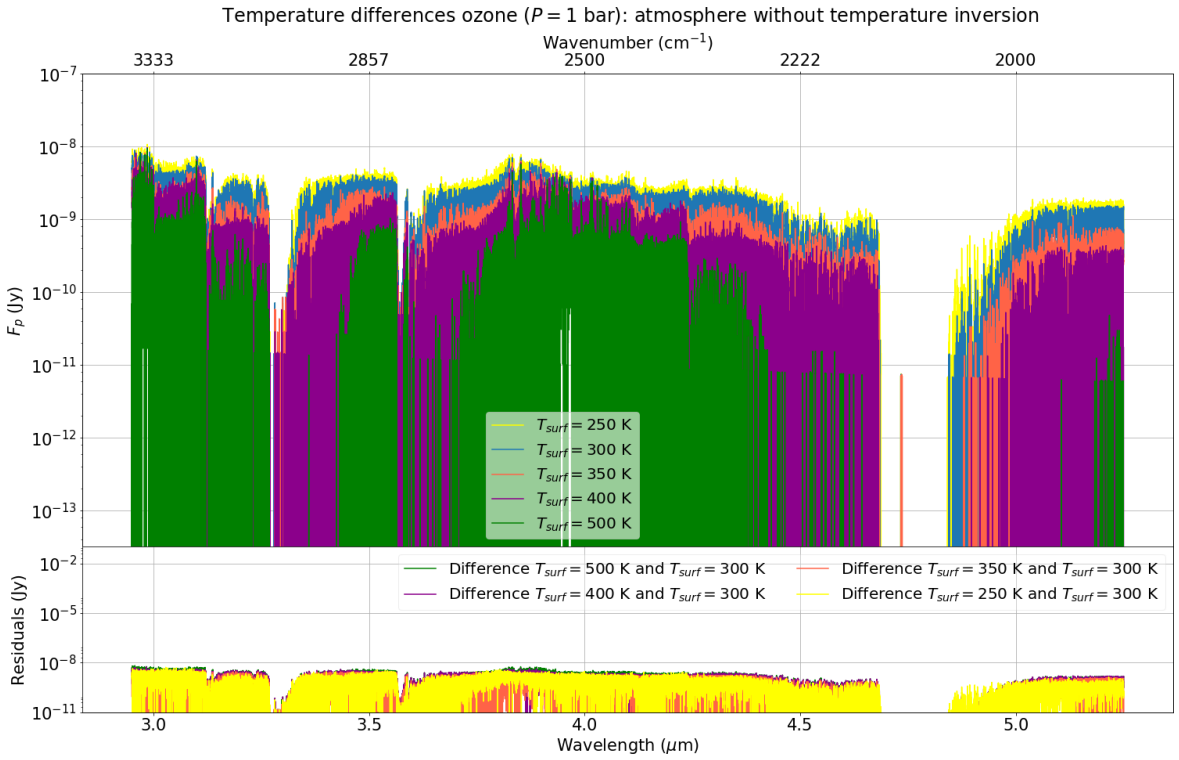

(a)

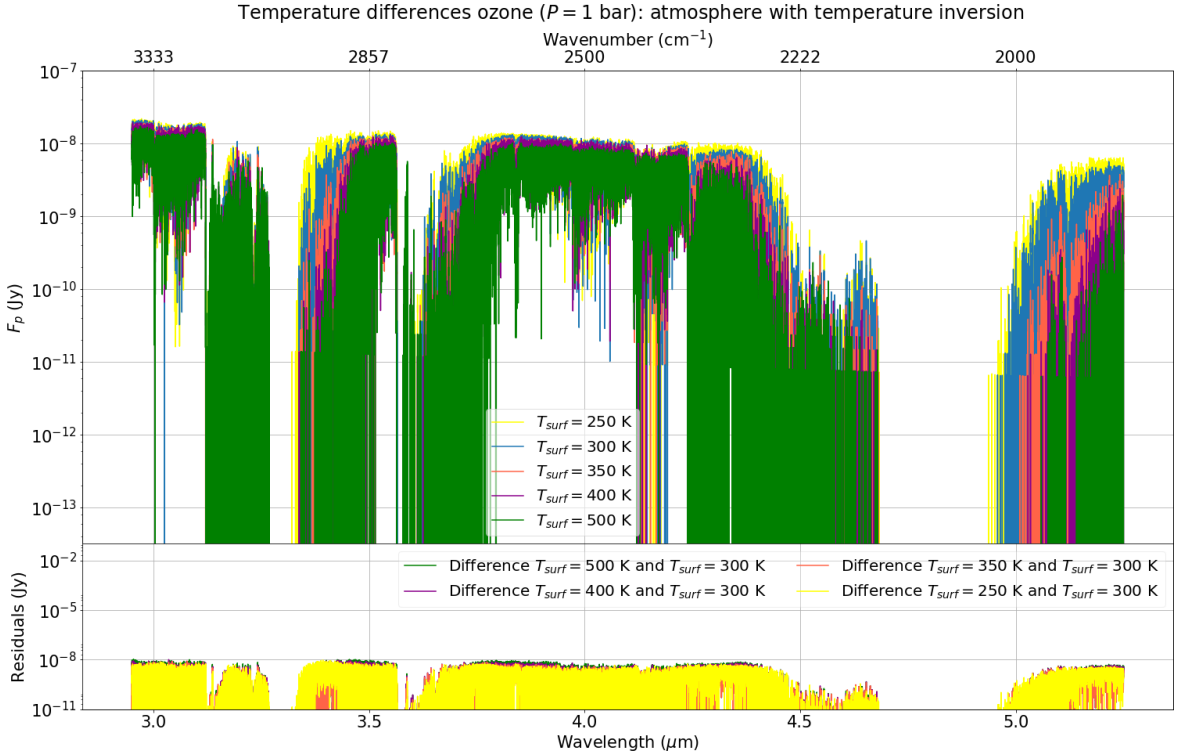

(b)

Figure 4.11: Synthetic transmission spectra of an 100% O_3 atmosphere showing the effect of the surface temperature for an Earth-Sun analogue located at a distance of 10 pc as simulated for METIS assuming an atmosphere without temperature inversions (a) and an atmosphere with a temperature inversions (b). In both cases the surface pressure is assumed constant at 1 bar while the pressure in the atmosphere drops exponentially. The variation in planetary flux of O_3 for temperatures of 250 K (yellow), 300 K (blue), 350 K (orange), 400 (purple), and 500 K (green) is shown. The residual plots below show the difference between the different temperatures and the reference temperature of 300 K as function of wavelength.

Molecular gas	Mixing ratio
N_2	0.21
O_2	0.78
CO_2	$4.09 \cdot 10^{-4}$
H_2O	10^{-3}
CH_4	$2 \cdot 10^{-6}$
N_2O	$4.5 \cdot 10^{-7}$
O_3	$7.5 \cdot 10^{-7}$
C_2H_6	$10^{-5} - 10^{-7}$
CH_3Cl	$10^{-5} - 10^{-7}$
NH_3	$10^{-5} - 10^{-7}$

Table 4.1: Assumed mixing ratios of an atmosphere consisting of a mixture of gases that are distributed in such a way that their abundance does not change as a function of altitude.

In this section, again an Earth-Sun analogue at 10 pc is assumed. The results assuming no vertical distribution of any of the molecules throughout the atmosphere are arranged such that for each gas that is varied the atmosphere without and with temperature inversion are shown below each other keeping the abundances of the other molecules constant. The P-T profile is not modified and is the same as displayed in Fig. (4.7). Instead of the assumed possible equilibrium temperatures and pressures taken in the previous sections, the synthetic spectra in this section are modelled assuming a planet with a fixed surface temperature of $T_{surf} = 288$ K and a surface pressure of 1 bar equivalent of the surface temperature and pressure of present day Earth.

The basis of each atmosphere is an atmosphere consisting of N_2, CO_2, H_2O, O_2, CH_4, N_2O, and O_3. C_2H_6, NH_3 and CH_3Cl are therefore not present in the basis of the atmosphere but are individually added to the spectrum in the abundances shown in Table 4.1. The abundance of each molecule is varied by a factor of 10 to investigate the effect of this on the spectrum and to inspect whether the abundance of a molecule in the planetary atmosphere can be inferred from the spectrum. For O_2, however, the abundances is changed by a factor of 3 instead of 10 since the mixing ratio of O_2 in the Earth's atmosphere is 0.21. Increasing this by a factor of 10 results in an nonphysical atmosphere containing 210% O_2. It has been taken into account that some molecules may not have any or very weak spectral features in the wavelength range of either HIRES or METIS. C_2H_6 and CH_3Cl both lack spectral features for wavelengths HIRES will be sensitive to. Therefore those molecules will have zero opacity and changing the abundance will not result in a change in the spectrum. Therefore C_2H_6 and CH_3Cl are not included in the analysis of HIRES. For the wavelength range of METIS, O_2 does not have any spectral features and for the same reasons as for C_2H_6 and CH_3Cl for HIRES is not included in the analysis of METIS.

All synthetic spectra modelled are assumed to be clear sky spectra without taking the Earth's atmosphere into account. From this section on also the transmission of the Earth's atmosphere is taken into consideration when observing other planets. The transmission spectrum of the Earth is taken from the European Southern Observatory (ESO) Sky Model Calculator [1]. In the figures the grey shaded area indicates the wavelength regions where radiation of other objects will penetrate through the Earth's atmosphere and be able to reach the detector. This is a first step concerning the detectability of biosignatures with the ELT. Another step to determine the detectability is the plotting a 'residual plot'. Spectra in the following section contain such a plot below the spectra of the molecules and their different abundances. In this plot the differences between the Earth abundances (i.e. the abundances in Table 4.1) and the spectrum that results from varying the abundance of one of the molecules by a factor of 10 (or a factor 3 in the case of O_2). This plot helps to see differences in

[1] http://www.eso.org/observing/etc/skycalc/skycalc.htm

the spectra that are not seen by inspection by eye and show the level of the difference which is useful when talking about detectability of the biosignature.

Fig. (4.12) shows synthetic transmission spectra of an Earth-Sun analogue at a distance of 10 pc of both an atmosphere without temperature inversions (Fig. (4.12a)) and one with a temperature increase in the stratosphere (Fig. (4.12b)) with the concept of HIRES. The main molecules that cause absorption features are indicated in the plots. H_2O, however, has spectral features over the whole wavelength region and is therefore not indicated in the plot but is causing the features not indicated in the plot. Both of these spectra have an decrease in the transmission with a higher abundance of O_2 due to the increase of the mean molecular weight in the atmosphere with a higher abundance of O_2. The O_2 molecule is relatively heavy. Since the scale height is inversely proportional to the mean molecular weight of the constituents of the atmosphere and the scale height is mainly responsible for setting the depth of the absorption features in the transmission spectrum, the overall spectrum shows a decrease in R_p^2/R_s^2. This results in an overall difference of about 10^{-7} of the transmission (see the residual plot). The differences in the strengths of the lines are also of the same order of magnitude, the strongest features being the O_2 1.3μm band and the O_2 A-band. Comparing the transmission spectra for an atmosphere without temperature inversions and the one with a temperature inversion, there is no change of the spectrum. This is again a result of the nature of a transmission spectrum: it is a pure absorption spectra and therefore insensitive to the vertical temperature profile of the atmosphere. The last point also holds for all other molecules considered in the analysis of transmission spectra.

The synthetic transmission spectra as observed with HIRES considering an Earth-Sun analogue at a distance of 10 pc for both an atmosphere with and an atmosphere without temperature inversions and changing the abundance of O_3 by a factor of 10 are shown in Fig. (4.13). The transmission spectra shown that changing the abundance of O_3 only has an effect of the spectrum between 2 μm and 2.5 μm. The difference between an abundance of $[O_3]$=$7.5 \cdot 10^{-7}$ (i.e. Earth abundance) by volume and an abundance of $7.5 \cdot 10^{-6}$ (i.e. $0.1 \cdot [O_3]_{Earth}$) does not show a significant change. The only difference seen is the feature at $\sim 2.2\mu$m but is about 10^{-8} of the transmission. For ten times $[O_3]_{Earth}$, however, there are a change up to 10^{-7} transmission, the most strongest being the feature at $\sim 2.2\mu$m. The O_3 2.05 band will not be detectable because of the Earth's atmospheric blocking.

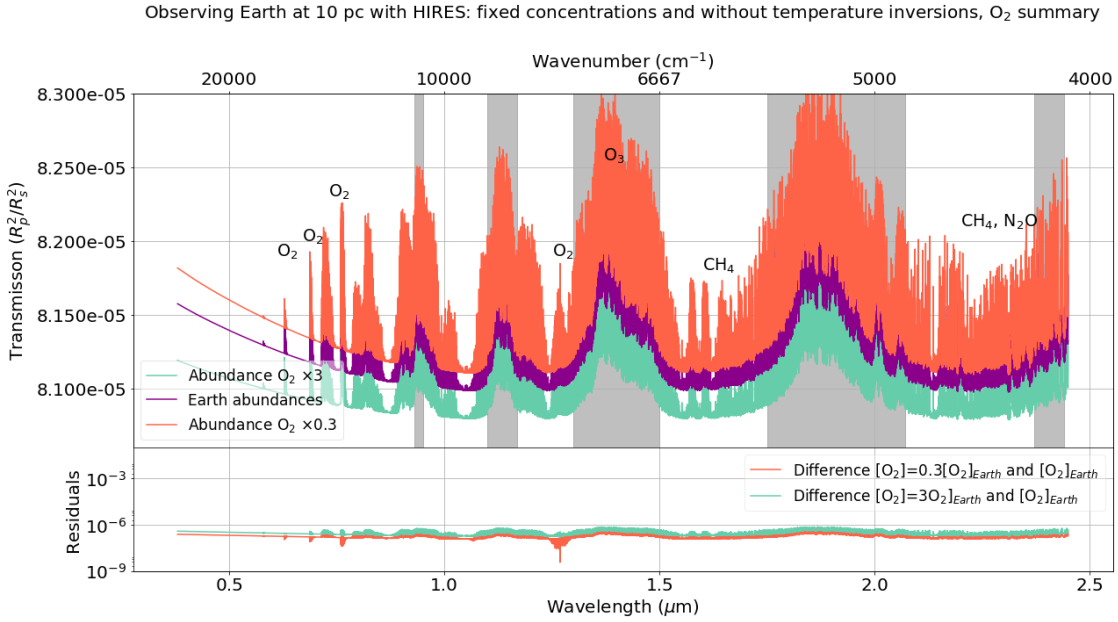

(a)

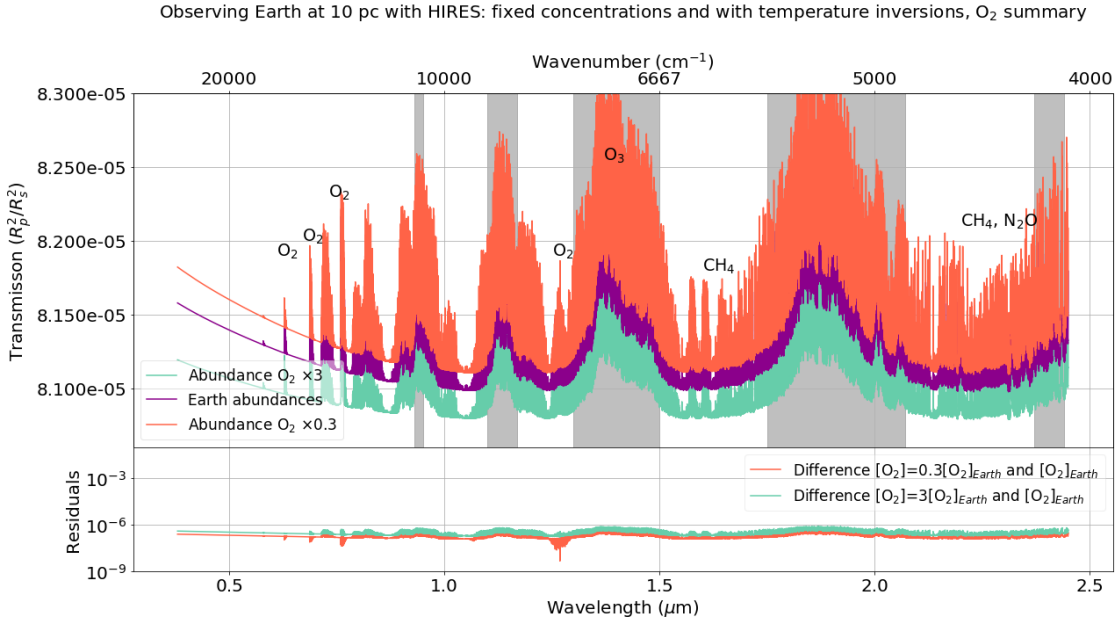

(b)

Figure 4.12: Synthetic transmission spectra of an atmosphere of a mixture of gases without varying the vertical abundance of any gas (i.e. as function of altitude) showing the effect of changing the overall abundance of O_2 by a factor of 10 for an Earth-Sun analogue located at a distance of 10 pc as simulated for HIRES assuming an atmosphere without temperature inversions (a) and an atmosphere with a temperature inversion (b). In both cases the surface temperature is assumed to be similar to Earth (i.e. 288 K) while the pressure in the atmosphere drops exponentially. The variation in transmission (R_p^2/R_s^2) is shown assuming Earth atmospheric abundances for all molecules (purple), 10 times more O_2 (green) and 10 times less O_2 (orange) keeping the other atmospheric abundances constant (i.e. the Earth abundances). The residual plots below show the difference between an atmosphere with ten times less O_2 (orange) and ten times more O_2 (green) compared to Earth's atmosphere. The grey shaded areas indicate wavelength regions where the Earth's atmosphere blocks light coming from other sources.

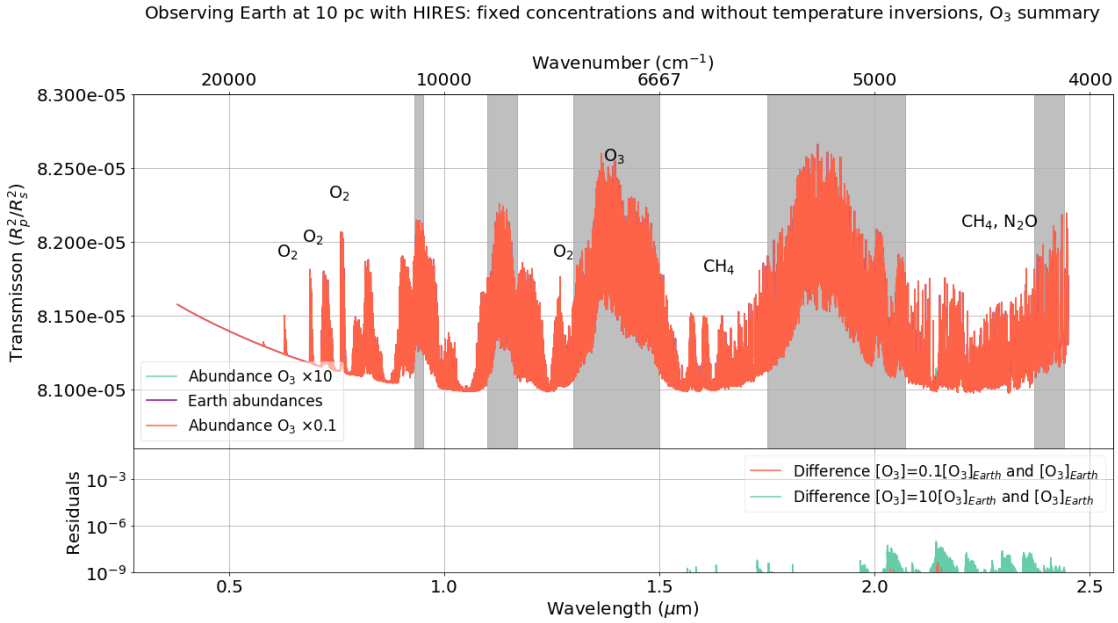

(a)

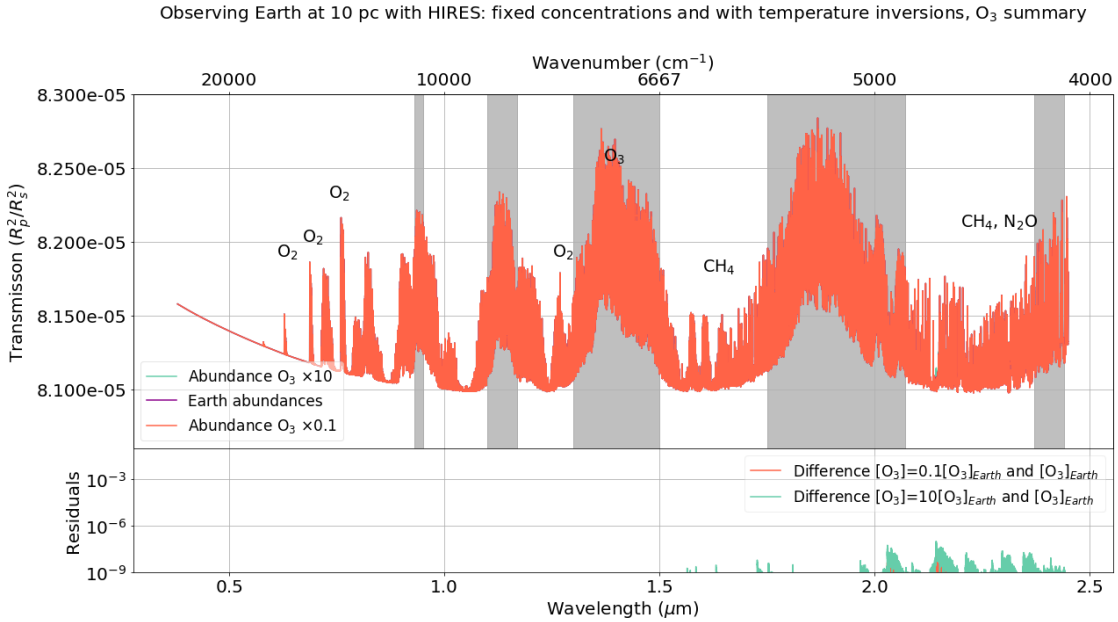

(b)

Figure 4.13: Synthetic transmission spectra of an atmosphere of a mixture of gases without varying the vertical abundance of any gas (i.e. as function of altitude) showing the effect of changing the overall abundance of O_3 by a factor of 10 for an Earth-Sun analogue located at a distance of 10 pc as simulated for HIRES assuming an atmosphere without temperature inversions (a) and an atmosphere with a temperature inversion (b). In both cases the surface temperature is assumed to be similar to Earth (i.e. 288 K) while the pressure in the atmosphere drops exponentially. The variation in transmission (R_p^2/R_s^2) is shown assuming Earth atmospheric abundances for all molecules (purple), 10 times more O_3 (green) and 10 times less O_3 (orange) keeping the other atmospheric abundances constant (i.e. the Earth abundances). The residual plots below show the difference between an atmosphere with ten times less O_3 (orange) and ten times more O_3 (green) compared to Earth's atmosphere. The grey shaded areas indicate wavelength regions where the Earth's atmosphere blocks light coming from other sources.

Fig. (4.14b) shows the synthetic transmission spectrum of an Earth-Sun analogue at 10 pc while varying the abundance of N_2O by a factor of 10 without varying the abundance as a function of altitude. Again, both an atmosphere with an and atmosphere without temperature inversions are considered and the wavelength regions the Earth's atmosphere blocks are indicated by the shaded grey regions.

The effect of changing the abundance such that $[N_2O]$=$4.5 \cdot 10^{-6}$ is visible by eye around 2.3 μm, where the difference between the Earth abundance of N_2O and 10 times this abundance is $\sim 10^{-7}$. In the residual plot it is shown that there are differences for 10 $[N_2O]_{Earth}$ at wavelengths $\sim$ 1.3 μm, 1.5-1.8 μm and 1.9-2.3 μm. The difference between $[N_2O]_{Earth}$ and $0.1 \cdot [N_2O]_{Earth}$ is, however, not significant in comparison with the former difference. The 1.3 μm band is not detectable because it is blocked by the Earth's atmosphere. To overcome this, convolution between lines of Earth and the observed planet need to be very good. Assuming this is not possible in the near-future, we do not consider this line in depth.

For H_2O, the results of synthetic transmission spectra of an Earth-Sun analogue at 10 pc are shown in Fig. (4.15). An atmosphere without any temperature inversion is shown in Fig. (4.15a) while an atmosphere including a temperature increase as function of altitude in the stratosphere is shown in Fig (4.15b). It can be seen that increasing the abundance of H_2O does not increase the overall spectrum as was the case for O_2 but the strength of the H_2O lines increases. This increase is over the wavelength region of 0.7 to 2.4 μm. Note that the strength of the O_2 features does not change when changing the abundance of H_2O by a factor of 10. Although O_2 bands are rather narrow, the abundance of O_2 and H_2O can be determined separately. Whether there is an increase in the abundance of N_2O or O_3 compared to an increase in the abundance of H_2O is hard to distinguish.

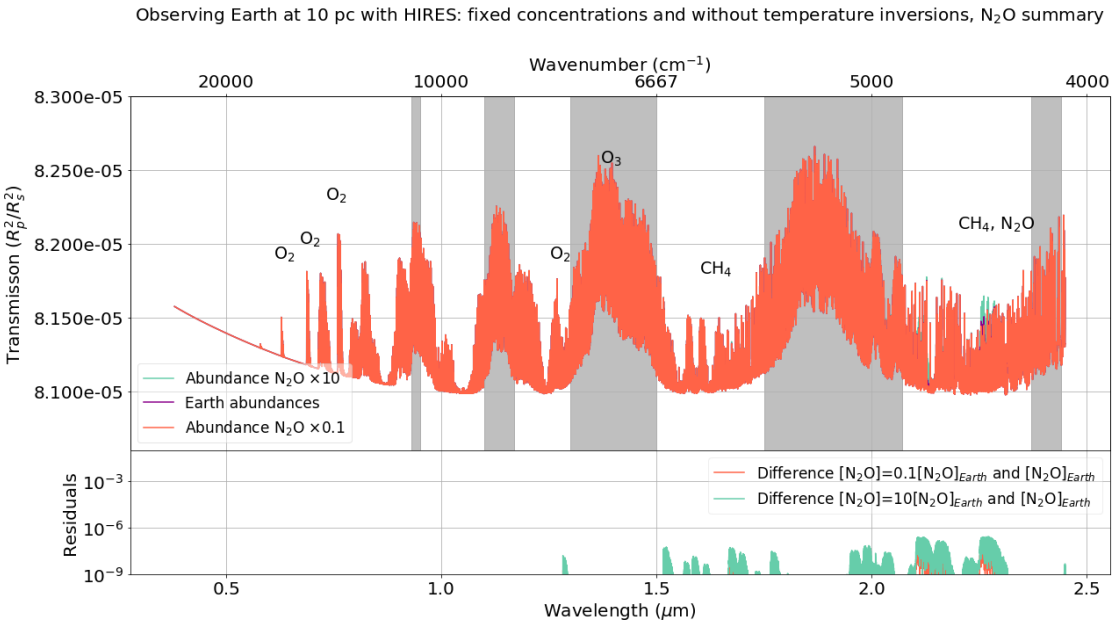

(a)

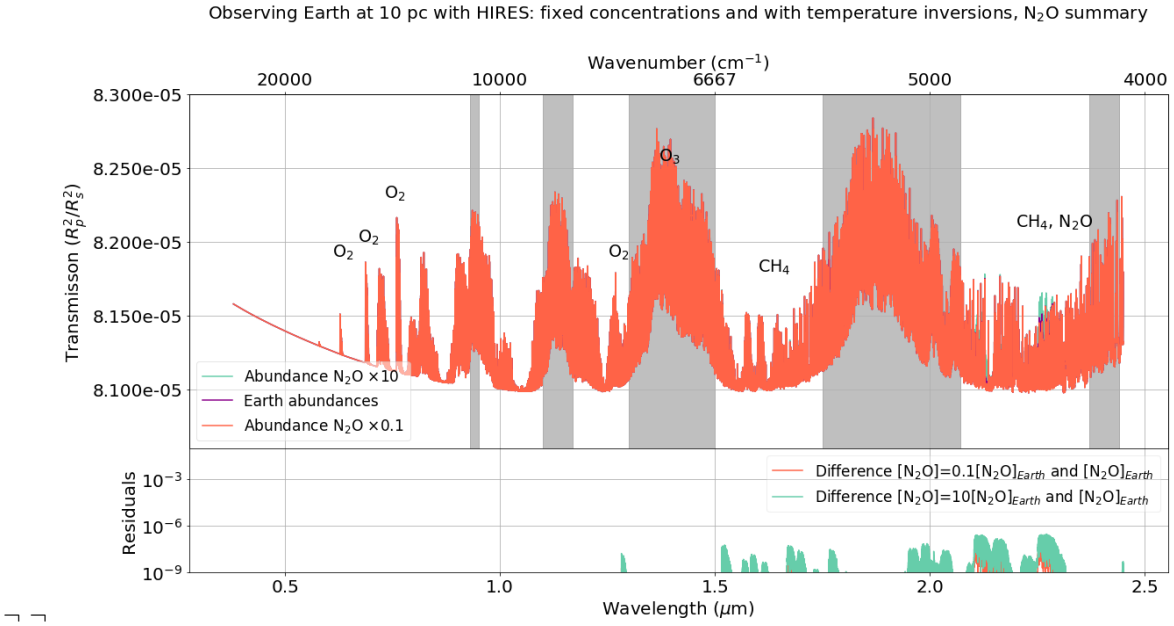

(b)

Figure 4.14: Synthetic transmission spectra of an atmosphere of a mixture of gases without varying the vertical abundance of any gas (i.e. as function of altitude) showing the effect of changing the overall abundance of N_2O by a factor of 10 for an Earth-Sun analogue located at a distance of 10 pc as simulated for HIRES assuming an atmosphere without temperature inversions (a) and an atmosphere with a temperature inversion (b). In both cases the surface temperature is assumed to be similar to Earth (i.e. 288 K) while the pressure in the atmosphere drops exponentially. The variation in transmission (R_p^2/R_s^2) is shown assuming Earth atmospheric abundances for all molecules (purple), 10 times more N_2O (green) and 10 times less N_2O (orange) keeping the other atmospheric abundances constant (i.e. the Earth abundances). The residual plots below show the difference between an atmosphere with ten times less N_2O (orange) and ten times more N_2O (green) compared to Earth's atmosphere. The grey shaded areas indicate wavelength regions where the Earth's atmosphere blocks light coming from other sources.

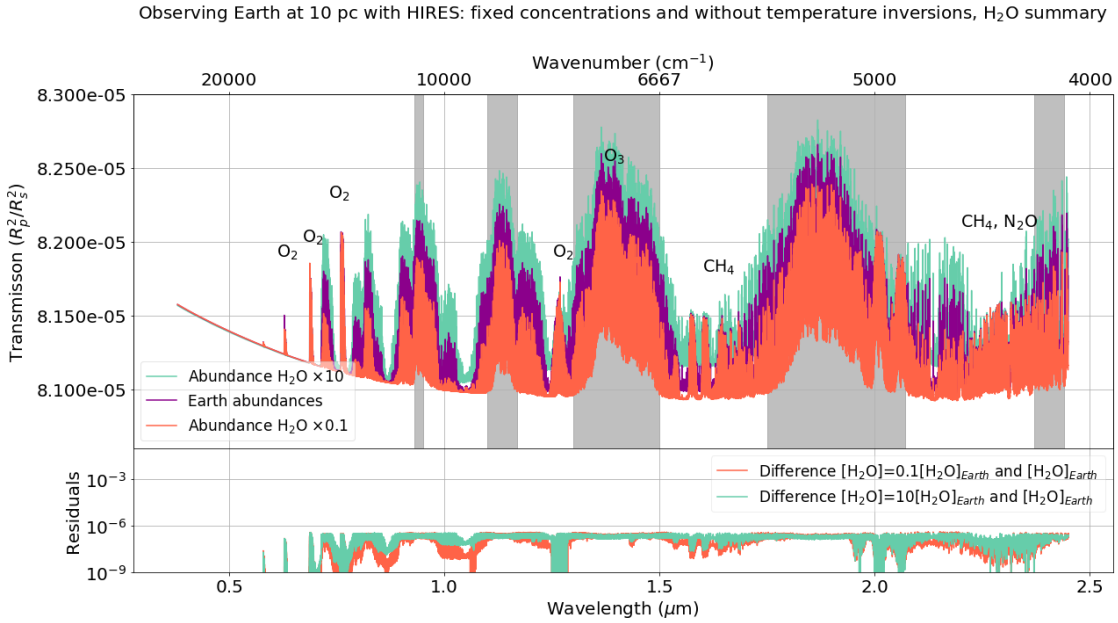

(a)

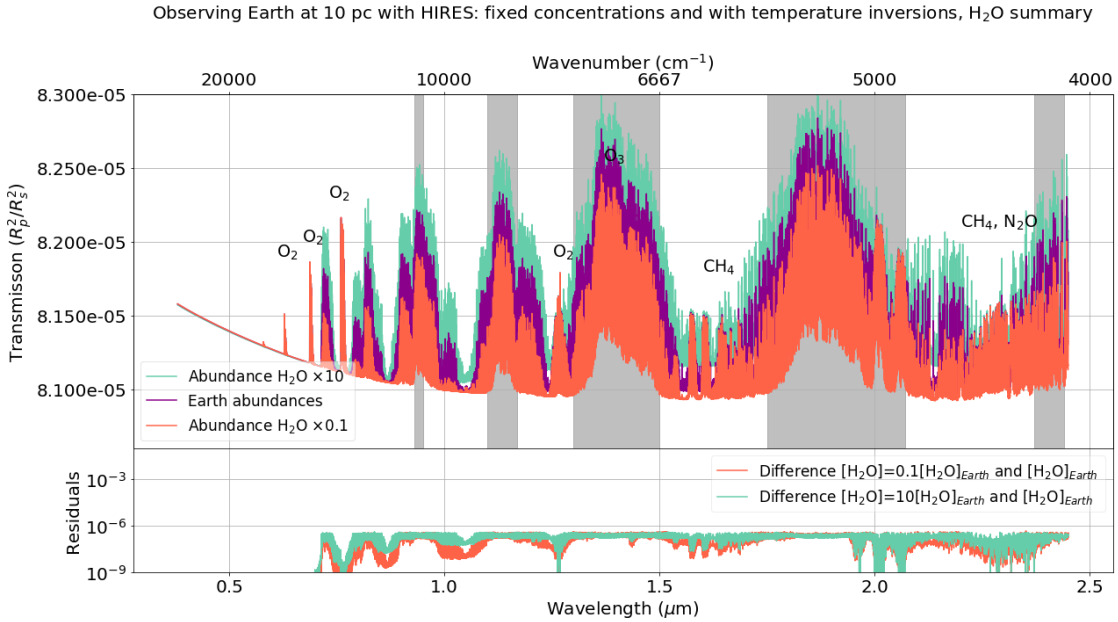

(b)

Figure 4.15: Synthetic transmission spectra of an atmosphere of a mixture of gases without varying the vertical abundance of any gas (i.e. as function of altitude) showing the effect of changing the overall abundance of H_2O by a factor of 10 for an Earth-Sun analogue located at a distance of 10 pc as simulated for HIRES assuming an atmosphere without temperature inversions (a) and an atmosphere with a temperature inversion (b). In both cases the surface temperature is assumed to be similar to Earth (i.e. 288 K) while the pressure in the atmosphere drops exponentially. The variation in transmission (R_p^2/R_s^2) is shown assuming Earth atmospheric abundances for all molecules (purple), 10 times more H_2O (green) and 10 times less H_2O (orange) keeping the other atmospheric abundances constant (i.e. the Earth abundances). The residual plots below show the difference between an atmosphere with ten times less H_2O (orange) and ten times more H_2O (green) compared to Earth's atmosphere. The grey shaded areas indicate wavelength regions where the Earth's atmosphere blocks light coming from other sources.

Fig. (4.16) shows the effect of changing the abundance of CH_4 by a factor of 10 in an atmosphere without changing the vertical distribution of any molecule for an Earth-Sun analogue at 10 pc taking HIRES as the instrument on the ELT. Again an atmosphere with and without a temperature inversion are considered. It can be seen that CH_4 has an effect on the spectrum at wavelengths between ~ 0.9

μ to 2.5 μm. The two band that cause the most significant change are the band around 1.6 μm and the one around 2.3 μm. In these two bands, the difference between $10 \cdot [CH_4]_{Earth}$ and $[CH_4]_{Earth}$ ($\sim 10^{-6}$) and $0.1 \cdot [CH_4]_{Earth}$ and $[CH_4]_{Earth}$ ($\sim 10^{-7}$) are about one order of magnitude or less apart. The presence of CH_4 for an atmosphere containing 10 times the Earth abundance will therefore more likely to be detection compared to 10 times less the Earth abundance. Note that besides the spectral regions of H_2O, the spectral regions of N_2O overlap with CH_4.

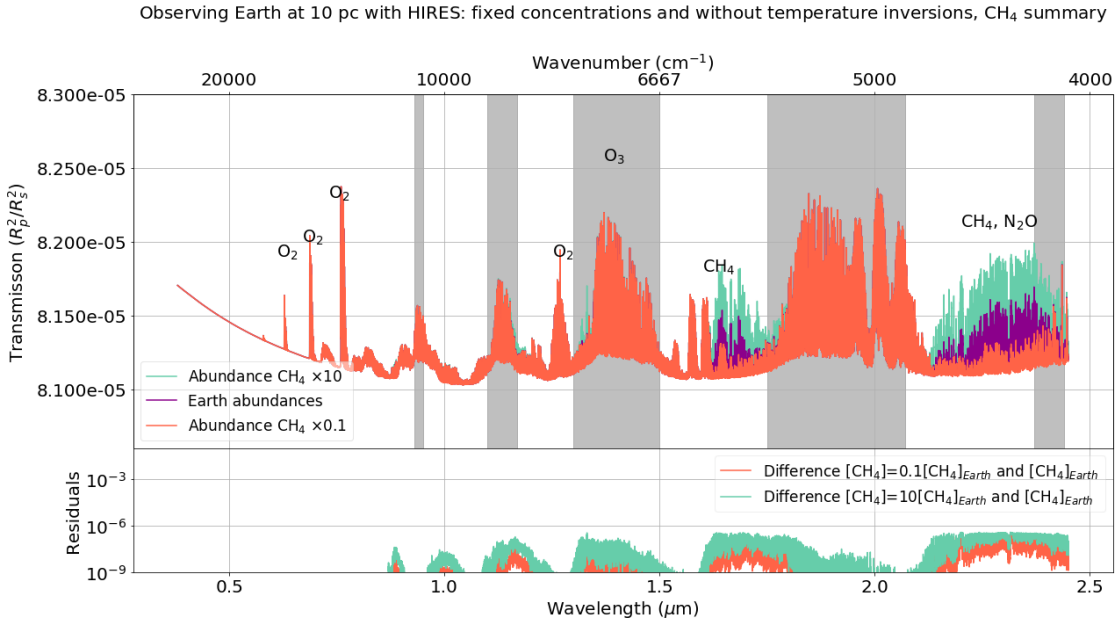

(a)

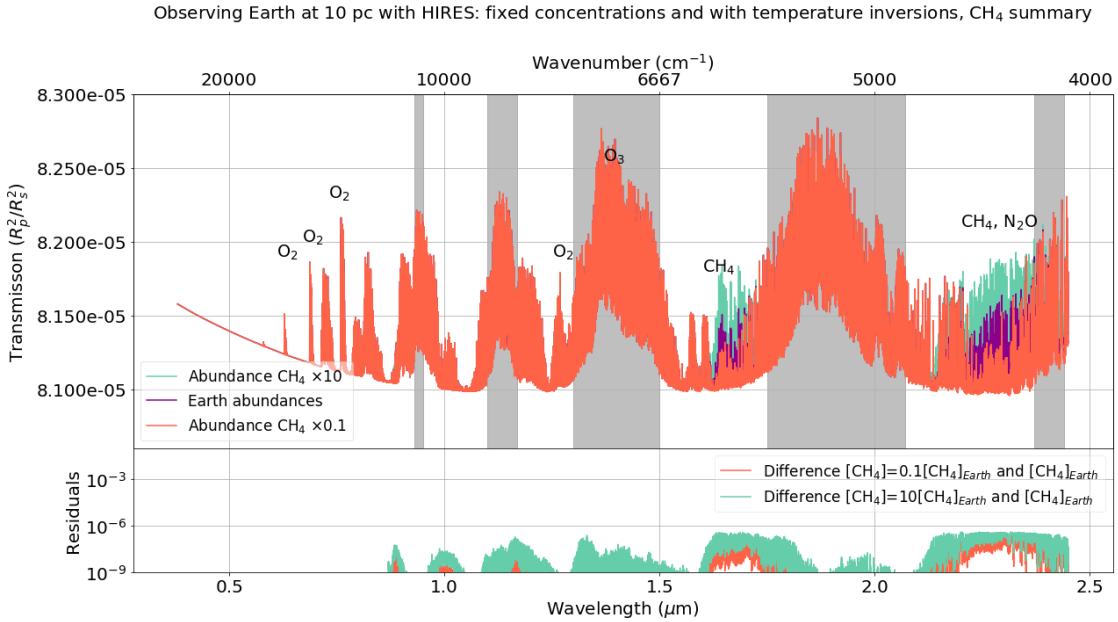

(b)

Figure 4.16: Synthetic transmission spectra of an atmosphere of a mixture of gases without varying the vertical abundance of any gas (i.e. as function of altitude) showing the effect of changing the overall abundance of CH_4 by a factor of 10 for an Earth-Sun analogue located at a distance of 10 pc as simulated for HIRES assuming an atmosphere without temperature inversions (a) and an atmosphere with a temperature inversion (b). In both cases the surface temperature is assumed to be similar to Earth (i.e. 288 K) while the pressure in the atmosphere drops exponentially. The variation in transmission (R_p^2/R_s^2) is shown assuming Earth atmospheric abundances for all molecules (purple), 10 times more CH_4 (green) and 10 times less CH_4 (orange) keeping the other atmospheric abundances constant (i.e. the Earth abundances). The residual plots below show the difference between an atmosphere with ten times less CH_4 (orange) and ten times more CH_4 (green) compared to Earth's atmosphere. The grey shaded areas indicate wavelength regions where the Earth's atmosphere blocks light coming from other sources.

In Fig. (4.17) synthetic transmission spectra of an atmosphere without changing the vertical distribution of any of gases adding NH_3 to the spectra of Earth abundances are shown. The atmospheric concentration of NH_3 is varied between 10^{-5}, 10^{-6} and 10^{-7} by volume. The gases that are present in the Earth's atmosphere by more than trace amounts (see. Table (4.1) are kept constant. Again

both an atmosphere with an Earth-like temperature decrease in the troposphere and an isothermal atmosphere thereafter is assumed (Fig. (4.17a) and an atmosphere where the temperature increases with altitude in the stratosphere (Fig. (4.17b)) are modelled. It can be seen that NH_3 has effect on the synthetic transmission spectrum at wavelengths of $\sim$ 1.1 μm, 1.3 μm, 1.5 μm, 2.0 μ and 2.3 μm. The band around 2.3 μm coincides with the bands of CH_4 and N_2O for bands of those molecules around 2.3 μm. The abundance of CH_4 should in that case be inferred from the 1.7 μm band while changing the abundance of N_2O does not show strong features in other wavelength regions. .

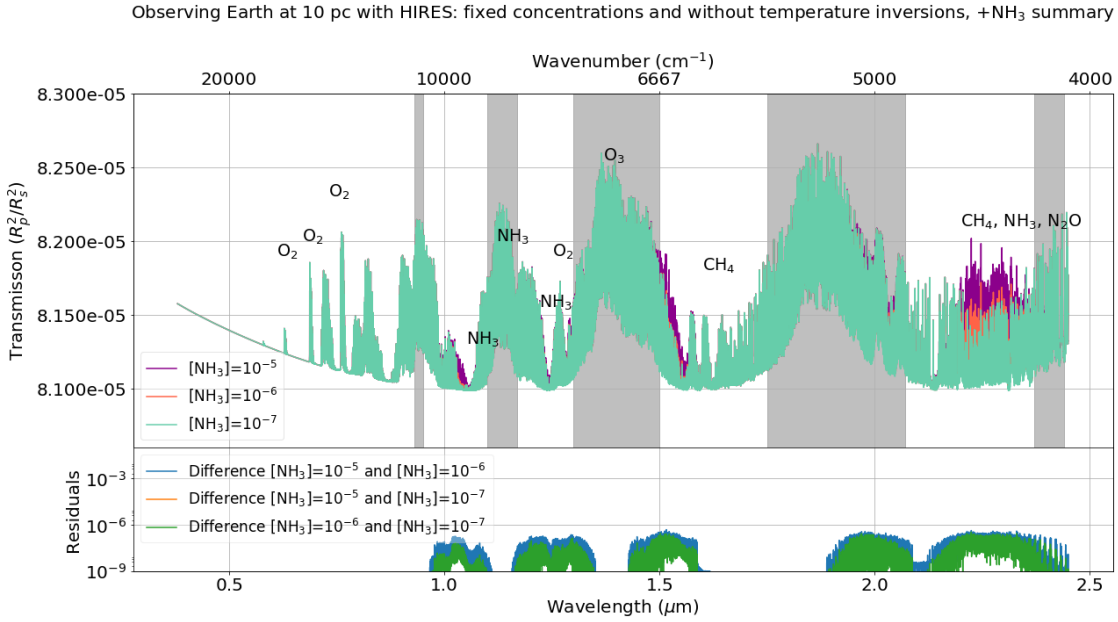

(a)

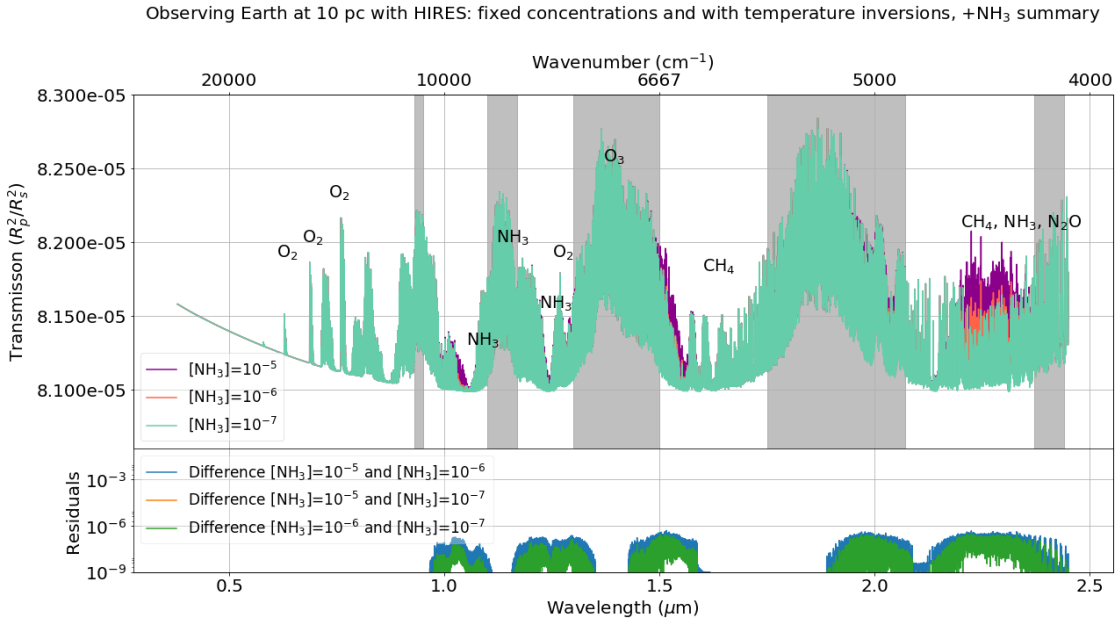

(b)

Figure 4.17: Synthetic transmission spectra of an atmosphere of a mixture of gases without varying the vertical abundance of any gas (i.e. as function of altitude) showing the effect of NH_3 to the atmosphere and changing the overall abundance of NH_3 by a factor of 10 for an Earth-Sun analogue located at a distance of 10 pc as simulated for HIRES assuming an atmosphere without temperature inversions (a) and an atmosphere with a temperature inversion (b). In both cases the surface temperature is assumed to be similar to Earth (i.e. 288 K) while the pressure in the atmosphere drops exponentially. The variation in transmission (R_p^2/R_s^2) is shown assuming Earth atmospheric abundances for the basis atmosphere plus a concentration of 10^{-5} of NH_3 (purple), 10 times this concentration (orange) and for an atmospheric concentration of 10^{-7} for NH_3 (green) keeping the other atmospheric abundances constant (i.e. the Earth abundances). The residual plots below show the difference between an atmosphere with an abundance of 10^{-5} and 10^{-6} (blue) of NH_3, an atmosphere with an abundance of 10^{-5} and 10^{-7} (orange) and an atmosphere with an abundance of 10^{-6} and 10^{-7} (blue). The grey shaded areas indicate wavelength regions where the Earth's atmosphere blocks light coming from other sources.

For the specifications of METIS the same analysis can be done taking the example of an Earth-sun analogue at a distance of 10 pc considering both atmospheres with an temperature inversion and without a temperature inversion. While the effect of the temperature inversion is not seen in transmission spectra, it may, although not significant, be uncovered in reflection spectra. Again, the

abundances of the molecules does not change as a function of altitude. Changing the abundance of O_3 by a factor of 10 while keeping all other abundances of the present gases constant results in synthetic reflection spectra with an almost constant change of about a factor of $\sim 10^{-8}$ Jy as is shown in Fig. (4.18). In the spectra the effect of changing the abundance of O_3 is greatest around 4.7 μm where the differences between $[O_3]$=$7.5 \cdot 10^{-6}$, $7.5 \cdot 10^{-7}$, and $7.5 \cdot 10^{-8}$ can be seen most clearly by inspection by eye. In this wavelength region the Earth's atmosphere, however, blocks light from other sources as indicated by the grey shaded region. For the detectability this means that a variation in the concentration of O_3 is not observable with METIS. Moreover, the distinction of an atmosphere with and without temperature inversions cannot be made when changing the abundances of O_3.

Fig. (4.19) shows synthetic reflection spectra of an Earth-Sun analogue at 10 pc demonstration the effect of changing the concentration of N_2O by a factor of 10 without changing the abundances of any molecule as a function of altitude. Again, the effect of temperature inversions is not noteworthy. Changing the abundances of N_2O by a factor of 10 results in a considerable change in the reflection spectra around wavelengths of 3.9 μm, 4.1 μm and 4.5 μm. The band around 4.5 μ is fully blocked by our own atmosphere while the other two bands are in the region where the atmosphere does not block light from other sources. These bands have a difference of $\sim 10^{-8}$ Jy between $[N_2O]$= $4.5 \cdot 10^{-7}$ and either $[N_2O]$= $4.5 \cdot 10^{-6}$ or $[N_2O]$= $4.5 \cdot 10^{-8}$ by volume.

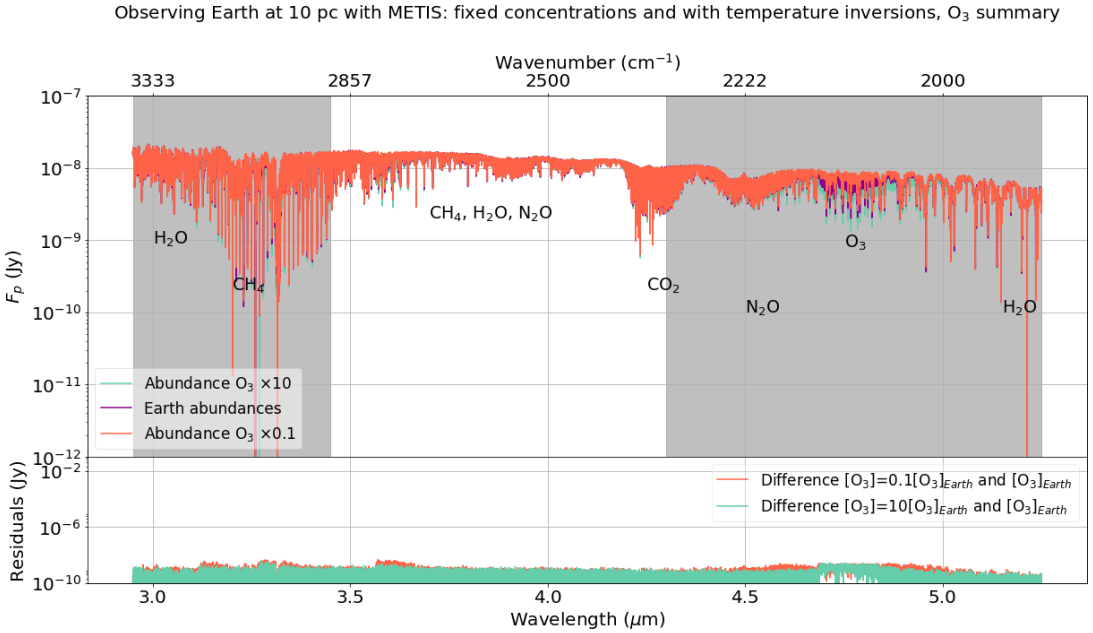

(a)

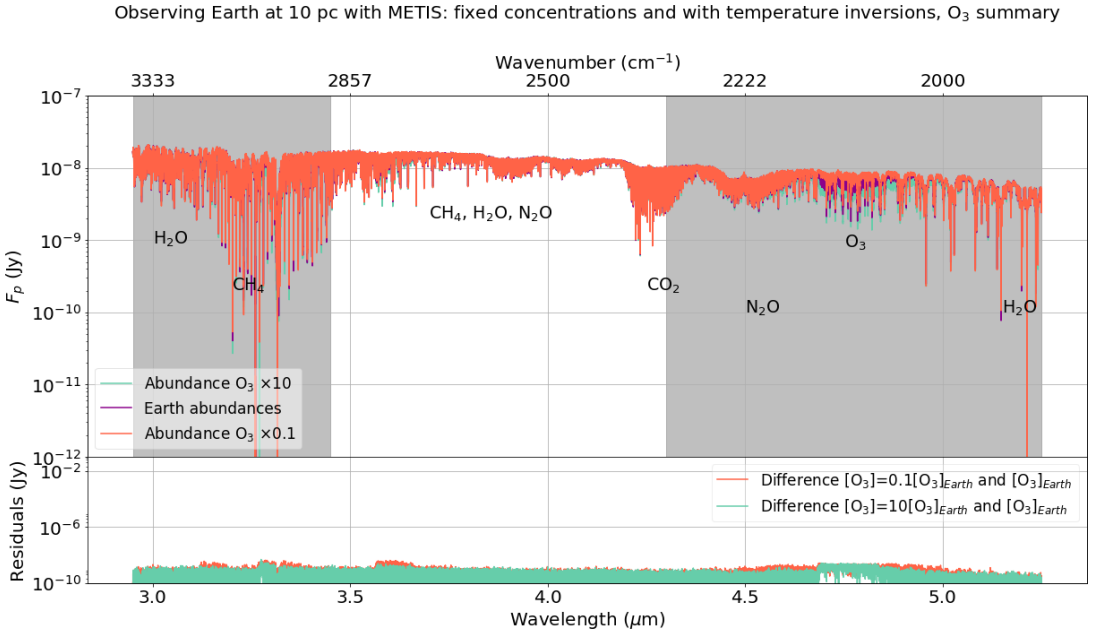

(b)

Figure 4.18: Synthetic reflection spectra of an atmosphere of a mixture of gases without varying the vertical abundance of any gas (i.e. as function of altitude) showing the effect of changing the overall abundance of O_3 by a factor of 10 for an Earth-Sun analogue located at a distance of 10 pc as simulated for METIS assuming an atmosphere without temperature inversions (a) and an atmosphere with a temperature inversion (b). In both cases the surface temperature is assumed to be similar to Earth (i.e. 288 K) while the pressure in the atmosphere drops exponentially. The variation in planetary flux is shown assuming Earth atmospheric abundances for all molecules (purple), 10 times more O_3 (green) and 10 times less O_3 (orange) keeping the other atmospheric abundances constant (i.e. the Earth abundances). The residual plots below show the difference between an atmosphere with ten times less O_3 (orange) and ten times more O_3 (green) compared to Earth's atmosphere.

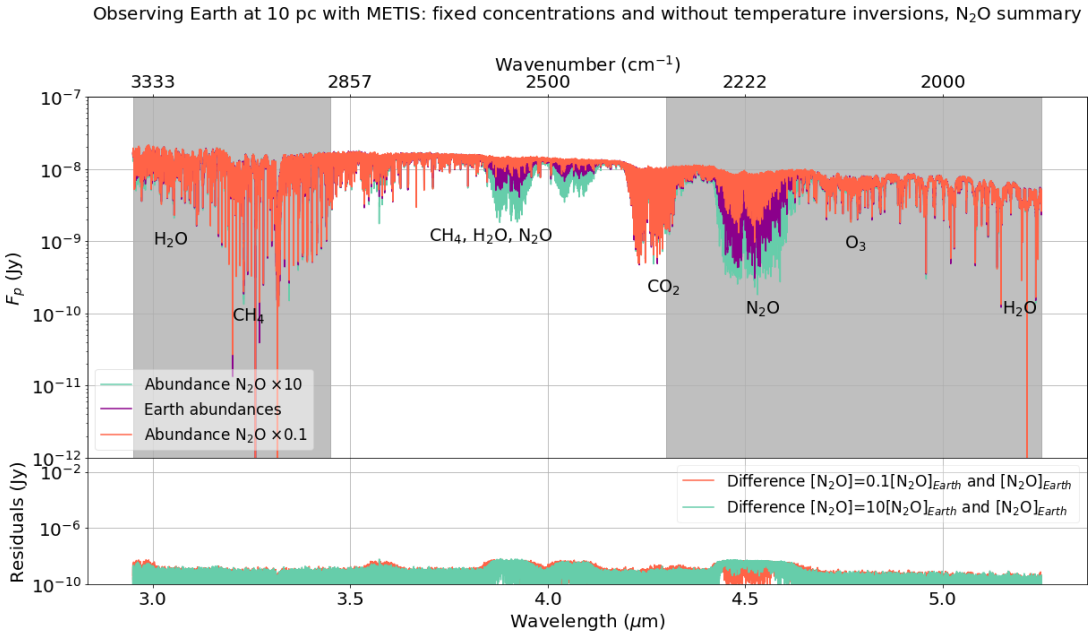

(a)

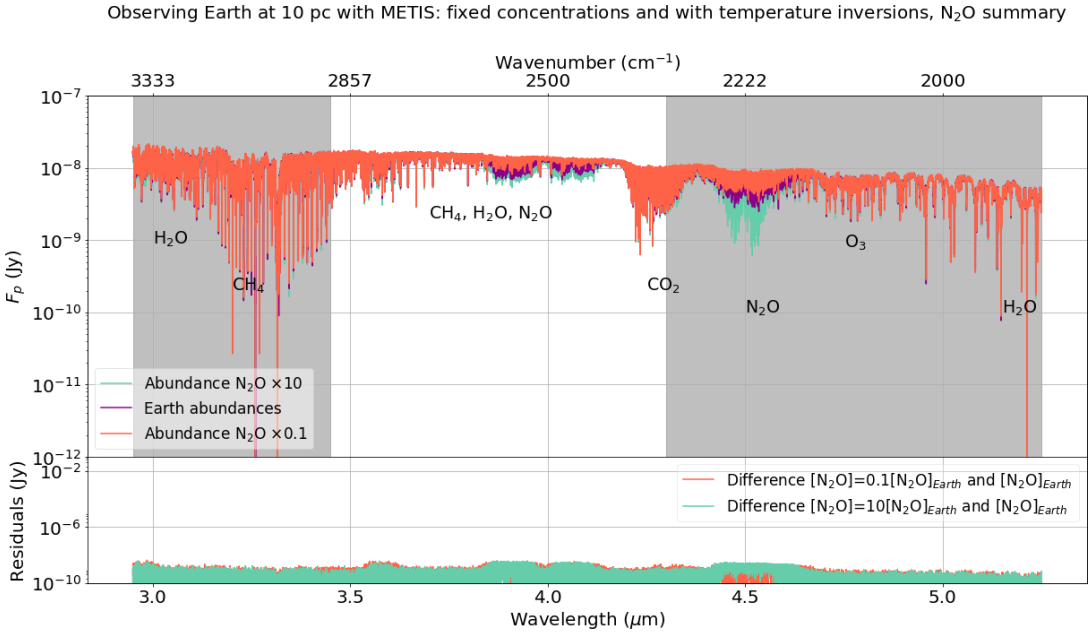

(b)

Figure 4.19: Synthetic reflection spectra of an atmosphere of a mixture of gases without varying the vertical abundance of any gas (i.e. as function of altitude) showing the effect of changing the overall abundance of N_2O by a factor of 10 for an Earth-Sun analogue located at a distance of 10 pc as simulated for METIS assuming an atmosphere without temperature inversions (a) and an atmosphere with a temperature inversion (b). In both cases the surface temperature is assumed to be similar to Earth (i.e. 288 K) while the pressure in the atmosphere drops exponentially. The variation in planetary flux is shown assuming Earth atmospheric abundances for all molecules (purple), 10 times more N_2O (green) and 10 times less N_2O (orange) keeping the other atmospheric abundances constant (i.e. the Earth abundances). The residual plots below show the difference between an atmosphere with ten times less N_2O (orange) and ten times more N_2O (green) compared to Earth's atmosphere.

By changing the concentration of atmospheric H_2O, the effect of one of the habitability markers is considered. Although H_2O is not a biosignature, it is the habitability marker used to define the HZ. Changing the abundances by a factor of 10 compared to the Earth atmospheric abundance of $[H_20]=10^{-3}$ per unit volume in the troposphere and assuming this concentration remains constant

throughout the atmosphere results in differences in the reflection spectra. This is shown in Fig. (4.20). The bands for 10 times the atmospheric H_2O content of Earth the spectral lines from 3.0-3.5 μm and from 4.9- 5.3 μm are saturated due to computational errors using ARCiS. This effect is caused by the high resolutions that are adopted while ARCiS was designed for modelling synthetic transmission spectra at resolutions up to a few 100. For $[H_2O]=10^{-3}$ and $[H_2O]=10^{-4}$ also some of these saturations are seen for both the case with and without temperature inversions. The overall change in the reflection due to a change in the H_2O abundance is about 10^{-8} Jy.

Fig. (4.21) shows synthetic reflection spectra for both an atmosphere without and with temperature inversions of a mixture of gases and varying the abundance of CH_4 by a factor of 10 taking an Earth-Sun analogue as an example and METIS as the instrument. Again, a saturation is present for the spectrum for 10 times more CH_4 in the atmosphere which is caused by the same reasoning as given above. CH_4 has a strong band in the wavelength region between 3.0 μm and 4.0 μm which results in a difference in reflection up to $\sim 10^{-8}$ Jy between $[CH_4]=2 \cdot 10^{-6}$ and either $2 \cdot 10^{-5}$ or $2 \cdot 10^{-7}$ as inferred from the residual plot.

Next, it was investigated whether adding CH_3Cl, C_2H_6 or NH_3 to the spectrum of the Earth abundances may resulted in (detectable) changes in reflection spectra of the Earth-Sun analogue at 10 pc. Although it is not very likely that these gases are present in the Earth's or an exo-Earth atmosphere, investigating whether these abundances result in detectable features in different atmospheres are useful. These molecules are added in concentrations of 10^{-5}, 10^{-6} and 10^{-7} per unit volume to the atmosphere of the Earth abundances. The results for CH_3Cl are shown in Fig. (4.22), while those for C_2H_6 and NH_3 are shown in Fig. (4.23) and Fig. (4.24) respectively. For both changing the abundance of CH_3Cl and the abundance of C_2H_6 there seems to be a discrepancy between an atmosphere which only decreases in temperature in the lower part of the atmosphere and changes to be isothermal at higher altitudes and an atmosphere with has a temperature inversion in the stratosphere. For C_2H_6 this difference is most likely caused by an error in the computation of $[C_2H_6]=10^{-5}$ per unit volume for an atmosphere without a temperature inversion. This error was, however, not resolved by running the model again or by recomputing the opacity tables. For CH_3Cl is seems that there is an overall increase in strength of the reflection of the reflection spectrum of the Earth-Sun analogue adding CH_3Cl for $[CH_3Cl]=10^{-6}$. Whether this results from computational errors is not clear. The most substantial effect CH_3Cl has on the spectrum is at wavelengths between 3.3 and 3.4 μm. This wavelength region is however contained in the grey shaded area and therefore blocked by our own atmosphere. The small differences in reflecting of the order of 10^{-9} Jy in the wavelength region of 3.4 to 4.3 μm will not be detectable. For NH_3 the change in reflection is overall on the order of 10^{-9} coming mostly from computation errors. Although NH_3 has some bands in the wavelength region of METIS those bands are not strong enough to alter the reflection spectra of the Earth-Sun analogue. Adding concentrations of 10^{-5}, 10^{-6} or 10^{-7} of NH_3 per unit volume will not be detectable with METIS.

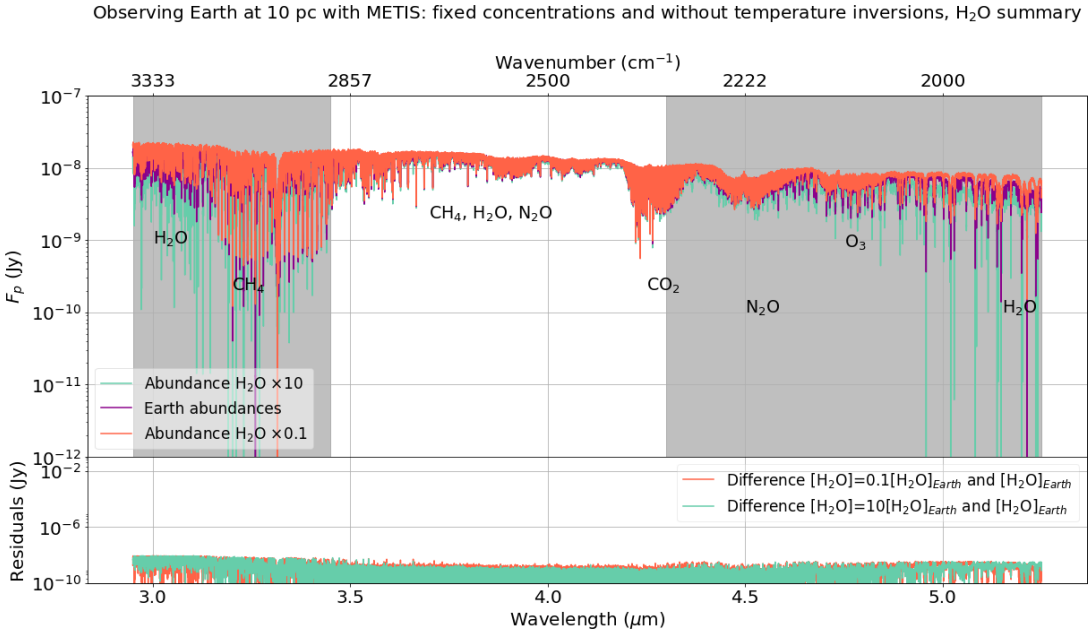

(a)

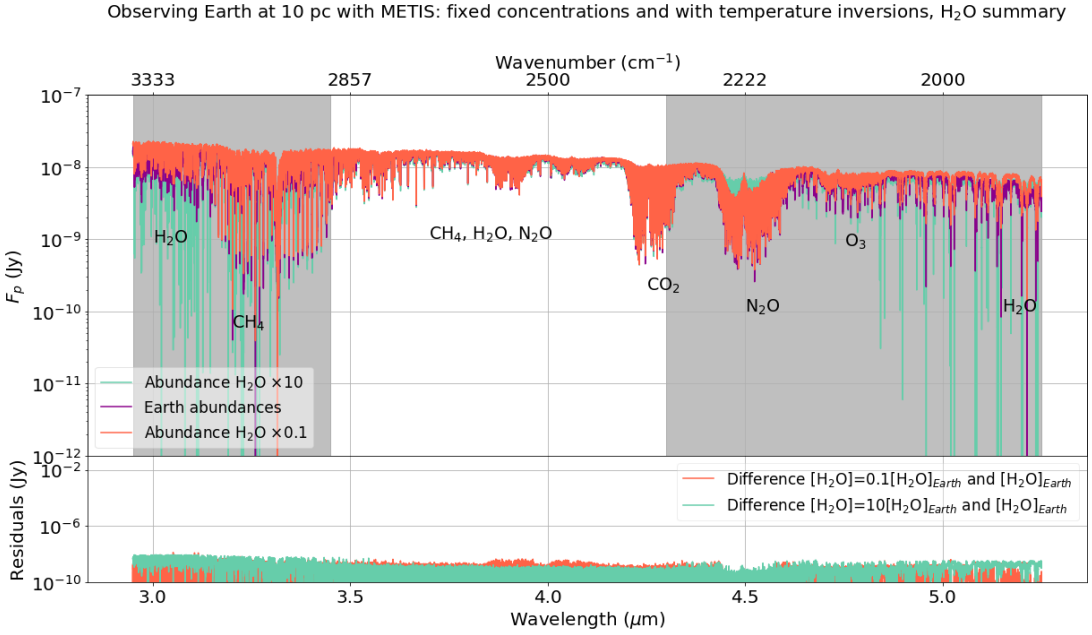

(b)

Figure 4.20: Synthetic reflection spectra of an atmosphere of a mixture of gases without varying the abundance of any gas as function of altitude showing the effect of changing the overall abundance of H_2O by a factor of 10 for an Earth-Sun analogue located at a distance of 10 pc as simulated for METIS assuming an atmosphere without temperature inversions (a) and an atmosphere with a temperature inversion (b). In both cases the surface temperature is assumed to be similar to Earth (i.e. 288 K) while the pressure in the atmosphere drops exponentially. The variation in planetary flux assuming Earth atmospheric abundances for all molecules (purple), 10 times more H_2O (green) and 10 times less H_2O (orange) keeping the other atmospheric abundances constant (i.e. the Earth abundances). The residual plots below show the difference between an atmosphere with ten times less H_2O (orange) and ten times more H_2O (green) compared to Earth's atmosphere

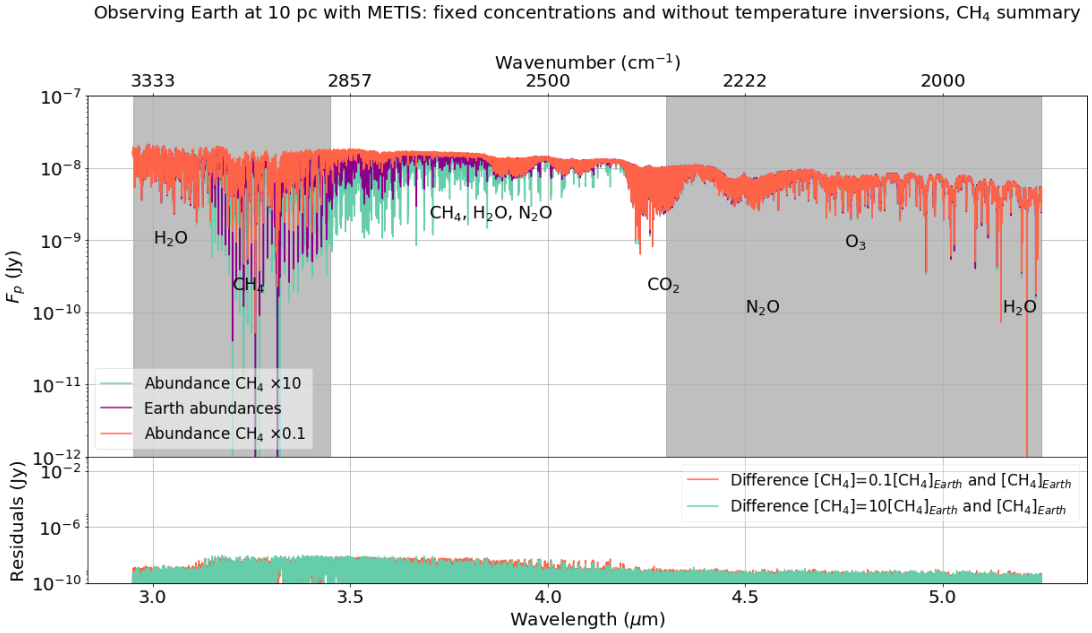

(a)

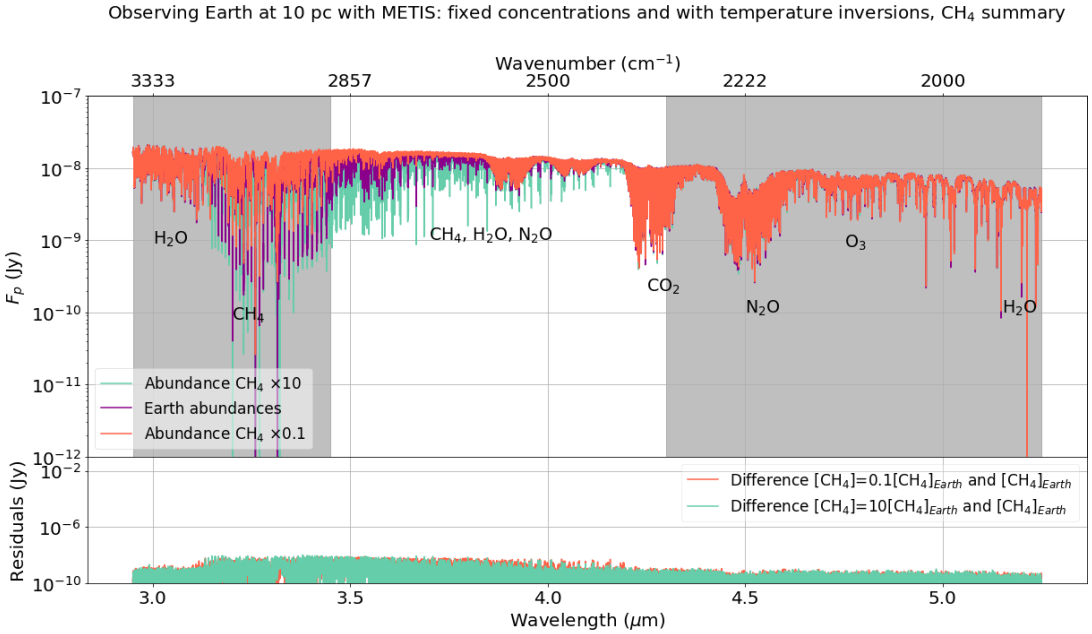

(b)

Figure 4.21: Synthetic reflection spectra of an atmosphere of a mixture of gases without varying the vertical abundance of any gas (i.e. as function of altitude) showing the effect of changing the overall abundance of CH_4 by a factor of 10 for an Earth-Sun analogue located at a distance of 10 pc as simulated for METIS assuming an atmosphere without temperature inversions (a) and an atmosphere with a temperature inversion (b). In both cases the surface temperature is assumed to be similar to Earth (i.e. 288 K) while the pressure in the atmosphere drops exponentially. The variation in planetary flux is shown assuming Earth atmospheric abundances for all molecules (purple), 10 times more CH_4 (green) and 10 times less CH_4 (orange) keeping the other atmospheric abundances constant (i.e. the Earth abundances). The residual plots below show the difference between an atmosphere with ten times less H_2O (orange) and ten times more H_2O (green) compared to Earth's atmosphere.

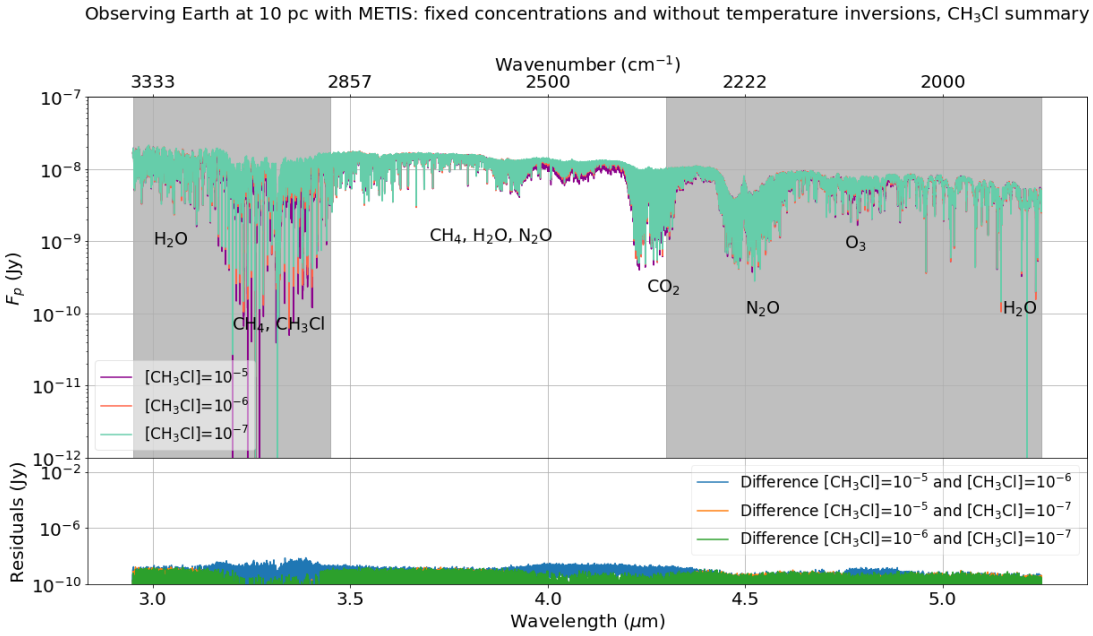

(a)

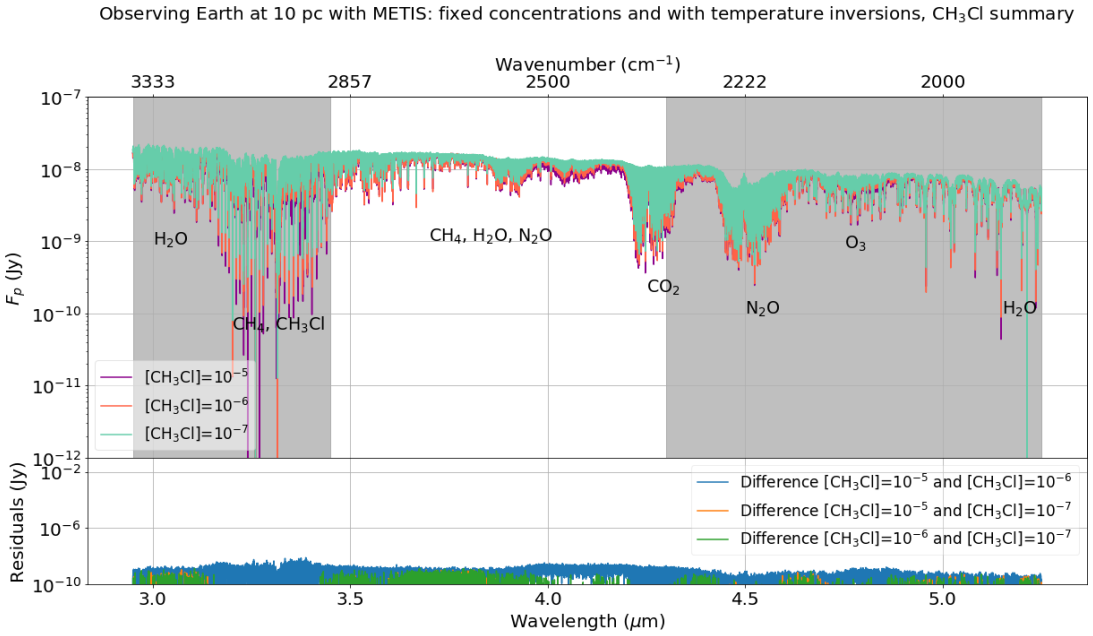

(b)

Figure 4.22: Synthetic reflection spectra of an atmosphere of a mixture of gases without varying the vertical abundance of any gas (i.e. as function of altitude) showing the effect of CH_3Cl to the atmosphere and changing the overall abundance of CH_3Cl by a factor of 10 for an Earth-Sun analogue located at a distance of 10 pc as simulated for METIS assuming an atmosphere without temperature inversions (a) and an atmosphere with a temperature inversion (b). In both cases the surface temperature is assumed to be similar to Earth (i.e. 288 K) while the pressure in the atmosphere drops exponentially. The variation in planetary flux is shown assuming Earth atmospheric abundances for the basis atmosphere plus a concentration of 10^{-5} of CH_3Cl (purple), 10 times this concentration (orange) and for an atmospheric concentration of 10^{-7} for CH_3Cl (green) keeping the other atmospheric abundances constant (i.e. the Earth abundances). The residual plots below show the difference between an atmosphere with an abundance of 10^{-5} and 10^{-6} (blue) of CH_3Cl, an atmosphere with an abundance of 10^{-5} and 10^{-7} (orange) and an atmosphere with an abundance of 10^{-6} and 10^{-7} (blue).

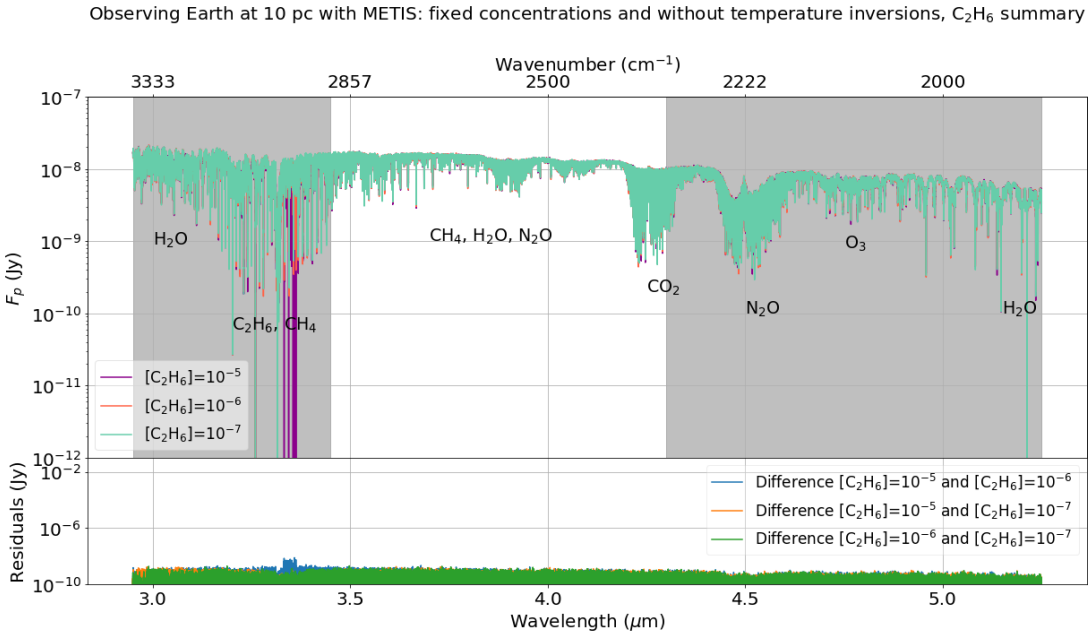

(a)

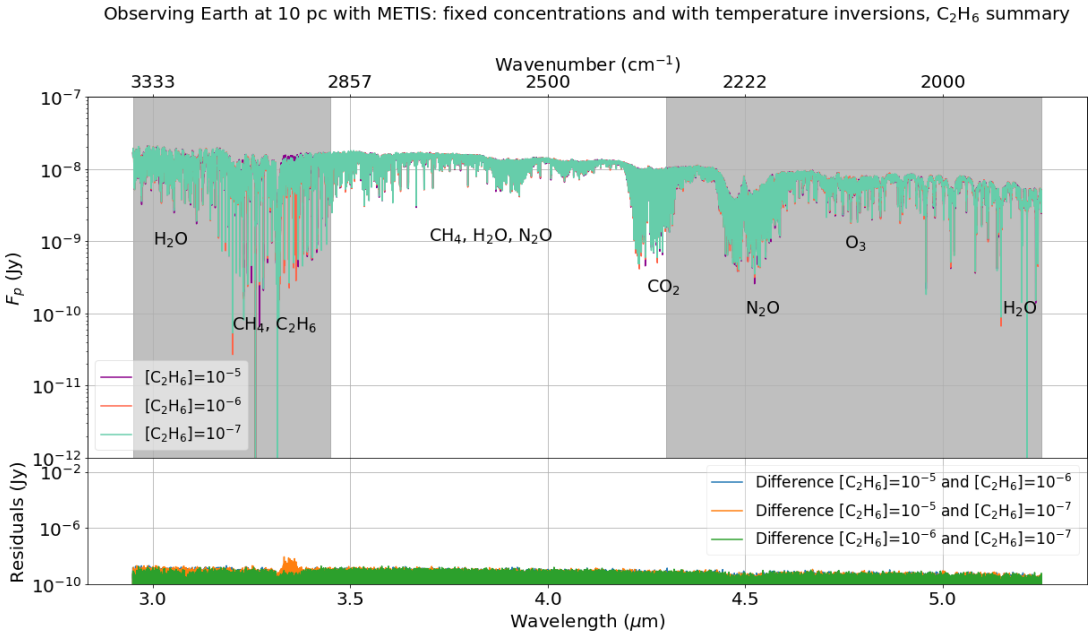

(b)

Figure 4.23: Synthetic reflection spectra of an atmosphere of a mixture of gases without varying the vertical abundance of any gas (i.e. as function of altitude) showing the effect of C_2H_6 to the atmosphere and changing the overall abundance of C_2H_6 by a factor of 10 for an Earth-Sun analogue located at a distance of 10 pc as simulated for METIS assuming an atmosphere without temperature inversions (a) and an atmosphere with a temperature inversion (b). In both cases the surface temperature is assumed to be similar to Earth (i.e. 288 K) while the pressure in the atmosphere drops exponentially. The variation in planetary flux is shown assuming Earth atmospheric abundances for the basis atmosphere plus a concentration of 10^{-5} of C_2H_6 (purple), 10 times this concentration (orange) and for an atmospheric concentration of 10^{-7} for C_2H_6 (green) keeping the other atmospheric abundances constant (i.e. the Earth abundances). The residual plots below show the difference between an atmosphere with an abundance of 10^{-5} and 10^{-6} (blue) of C_2H_6, an atmosphere with an abundance of 10^{-5} and 10^{-7} (orange) and an atmosphere with an abundance of 10^{-6} and 10^{-7} (blue).

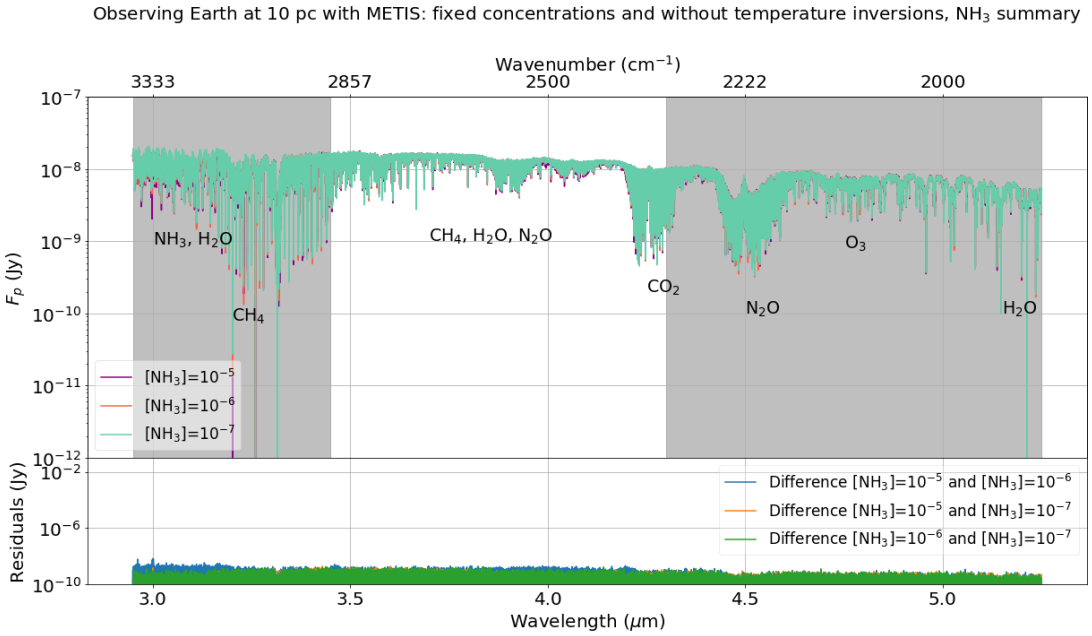

(a)

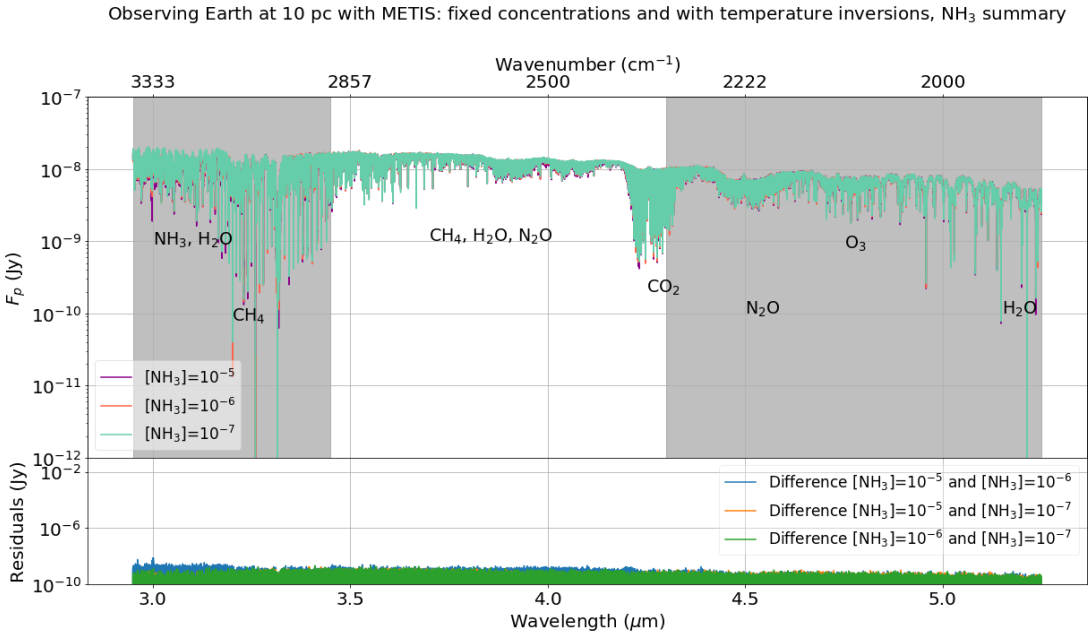

(b)

Figure 4.24: Synthetic reflection spectra of an atmosphere of a mixture of gases without varying the vertical abundance of any gas (i.e. as function of altitude) showing the effect of NH_3 to the atmosphere and changing the overall abundance of NH_3 by a factor of 10 for an Earth-Sun analogue located at a distance of 10 pc as simulated for METIS assuming an atmosphere without temperature inversions (a) and an atmosphere with a temperature inversion (b). In both cases the surface temperature is assumed to be similar to Earth (i.e. 288 K) while the pressure in the atmosphere drops exponentially. The variation in planetary flux is shown assuming Earth atmospheric abundances for the basis atmosphere plus a concentration of 10^{-5} of NH_3 (purple), 10 times this concentration (orange) and for an atmospheric concentration of 10^{-7} for NH_3 (green) keeping the other atmospheric abundances constant (i.e. the Earth abundances). The residual plots below show the difference between an atmosphere with an abundance of 10^{-5} and 10^{-6} (blue) of NH_3, an atmosphere with an abundance of 10^{-5} and 10^{-7} (orange) and an atmosphere with an abundance of 10^{-6} and 10^{-7} (blue).

4.3.2 Molecules distributed vertically throughout the atmosphere like Earth

In the atmosphere of the Earth some gases are distributed such that the concentration per unit volume does change with altitude, i.e. have a vertical distribution. Some gases are more abundance in the lower atmosphere compared to above the stratosphere (e.g. H_2O), while O_3 is more abundant in the lower stratosphere compared to other atmospheric layers where the O_3 layer is present. Moreover, CH_4 and N_2O are more abundant in the troposphere compared with altitudes above 40 km. The mixing ratios as a function of altitude are illustrated in Fig. (4.25). The mixing ratios as a function of height above the surface of Earth are taken from Brasseur et al. (1999) (see Fig. (4.25a)). Adapting these values and approximate the mixing ratios as a function of altitude from this figure resulted in mixing ratios as shown in Fig. (4.25b) which are used in further calculations. These are the potential biosignatures O_2, O_3, CH_4, and N_2O and the habitability markers N_2, CO_2 and H_2O. O_2 atoms, hydrogen atoms and argon are not taken into account since they do not have any spectral features in the wavelength range of interest in this thesis and therefore will not result in differences in the synthetic spectra. As discussed in section 3.1, the atmosphere is only modelled to an altitude of 80 km above the planetary surface.

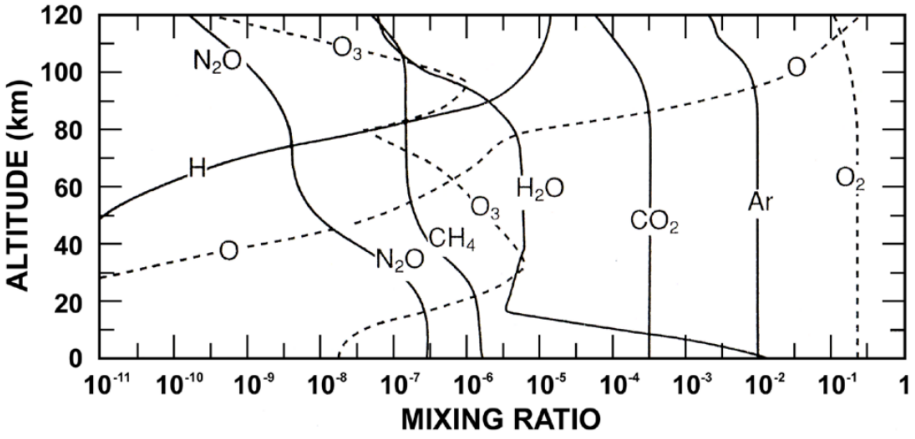

(a) Mixing ratios of the Earth as a function of altitude. N_2, the most abundant atmospheric gas, is not included but set to a mixing ratio of 0.78 for all altitudes. Moreover, rare noble gases are not shown but are well mixed up to altitudes of 100 km above the surface. Dashed lines are applied for clarity (Brasseur et al., 1999)

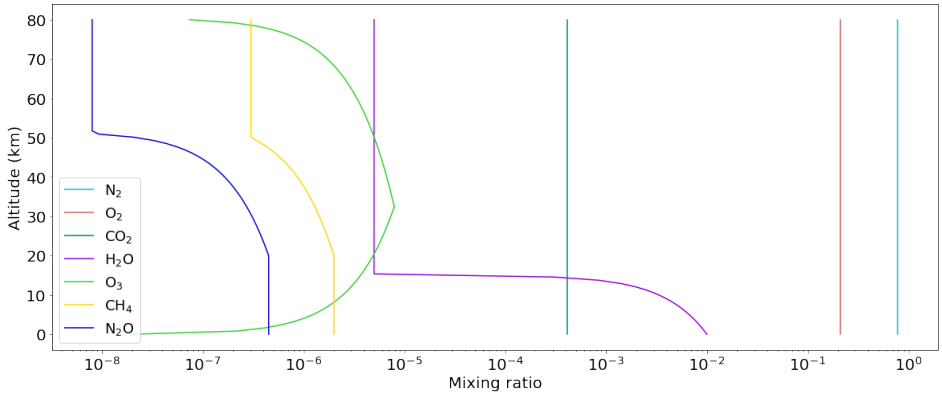

(b) Mixing ratios per unit volume of the Earth constructed from the plot by Brasseur et al., (1999). Only biosignature gases and habitability markers are considered. The mixing ratios are modelled up to an altitude of 80 km. The vertical distribution of N_2 (blue), O_2 (red), CO_2 (blue green), H_2O (purple), O_3 (green), CH_4 (yellow), and N_2O (dark blue) are shown.

Figure 4.25: Mixing ratios per unit volume of habitability markers and biosignatures of Earth as a function of height above the planetary surface. Mixing ratios are adapted from Brasseur et al., (1999) (a) and the applied mixing ratios are shown in (b)

In this section the vertical distribution of NH_3, CH_3Cl and C_2H_6 are kept constant and the abundances of these molecules are again assumed to vary between concentrations of 10^{-7} and 10^{-5} per unit volume. Again an Earth-Sun analogue at a distance of 10 pc with a surface temperature of 288 K is chosen as an example. The assumed temperature profile is such that it has one temperature inversion (i.e. the red profile in Fig. (4.7)). As previously, the pressure profile is assumed such that it drops exponentially with altitude. The synthetic transmission spectra for observing an atmosphere taking an Earth-Sun analogue at a distance of 10 pc as an example observed with HIRES are shown in Fig. (4.26). The abundance of O_2 is changed by a factor of 3 and the abundances of O_3, N_2O, H_2O, CH_4 and NH_3 are changed by a factor of 10. Comparing the plots in section 4.3.1 with Fig. (4.26) smaller 'bumps' appear in general in Fig. (4.26) compared to the figures in section 4.3.1 were it was assumed that molecules present in the atmosphere do not change their abundance with altitude. This difference is predominantly caused by the H_2O features. Transmission spectra probe primarily the upper parts of the atmosphere. Since H_2O is less abundant in the upper atmosphere compared to the troposphere the abundance of atmospheric H_2O is lower overall causing the decrease of transmission. This does not affect the strength of the O_2 lines (see Fig. (4.26a)). The residual plot now gives the difference in just the O_2 instead of also some overall difference between the spectra of the different abundances. The difference of strengths of the O_2 bands are $\sim 10^{-7}$ and is strongest for the B-band, the A-band, and the $a\ 1\delta_g$ band.

For O_3 the discrepancy between an atmosphere without a change abundance of any gas with altitude (Fig. (4.13)) and an atmosphere where a change in abundance is assumed of some molecules (Fig. (4.26b)) is bigger. For the latter case, the residual plot shows differences between 10 times more O_3 and Earth abundances of O_3 continuously over wavelengths between 0.7 and 2.5 μm while for the 1 concentration case this difference was limited to the region between 2.0 and 2.5 μm. This resulted from the difference in mixing ratio: O_3 is more abundant in the middle and upper atmosphere than in the troposphere.

N_2O is less abundant in the upper atmosphere compared to the troposphere. Therefore, the concentration of N_2O probed with transmission spectroscopy assuming an atmosphere with a vertical distribution of molecules will result in probing the lower abundance compared to the case assuming the abundances are equal to the Earth concentration in the troposphere. For N_2O the differences between Fig. (4.26c) and Fig. 4.14b) are primarily in the difference between the Earth abundances and 10% of this abundance. For the latter case, there is no notable change between these whereas for the former case, there is a difference of about 10^{-7} in transmission for almost the full wavelength range. Moreover, the concentration N_2O has an effect on the strength of the O_2 bands.

The concentration of H_2O changes by more than 3 orders of magnitude in the first 20 km measured from the surface. After that, the concentration stays approximately constant. Besides the overall change in the transmission spectrum, there is a change in the residuals for the case where there is 10 times more H_2O present in the atmosphere. The residuals show a more saturated behaviour if there is a vertical distribution of molecules (compare Fig. (4.26d) and Fig. (4.15b)) whereas for the case there is no vertical distribution of molecules in the atmosphere, the residual for 10 times more and 10 times less H_2O vapour have similar shapes. Similarly for CH_4, which is also less abundant at higher altitudes compared to tropospheric concentrations, the residuals are saturated.

As expected, besides the overall change of transmission spectra due to H_2O absorption features, there is no change in the transmission spectra for NH_3 adjusting the vertical distribution of other molecules since no assumed difference in vertical distribution was assumed in this section.

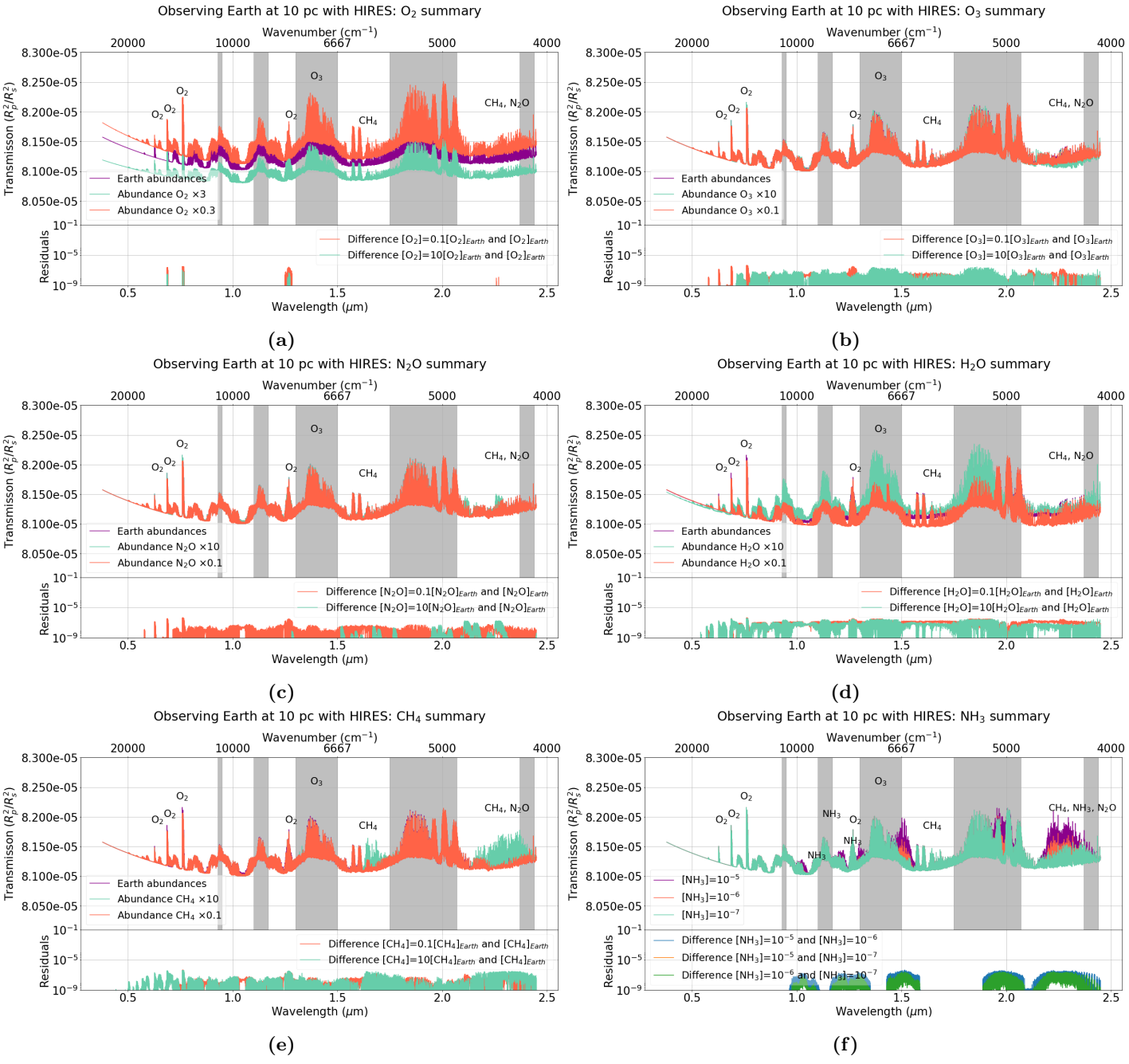

Figure 4.26: Results for an Earth-Sun analogue at 10 pc and investigating the effect of changing the abundances by a factor 10 assuming mixing ratios of molecules as of Earth's atmosphere (see Fig. (4.25)). Synthetic transmission spectra of an Earth-Sun analogue at a distance of 10 pc are presented where it is assumed that the surface temperature is 288 K, that the temperature increases with altitude in the stratosphere (i.e. with a temperature inversion), and that the pressure drops exponentially with altitude. The synthetic transmission spectra as modelled for HIRES contain each 3 spectra: one for an Earth-like abundance (purple), one with a factor times more of the gas (blue), and one with a factor less of the gas (orange). The gases for which the abundances are changed are (a) O_2 (by a factor of 3), (b) O_3 (by a factor of 10), (c) N_2O by a factor of 10, (d) H_2O (by a factor of 10), (e) CH_4 (by a factor of 10), and (f) NH_3 (by a factor of 10). NH_3 is present in trace amounts in Earth's atmosphere and only added in (f) assuming an abundance of 10^{-5} (purple), 10^{-6} (orange) and 10^{-7} (blue).

For METIS, or reflection spectra in general, the story is a bit different than for transmission spectra modelled for HIRES. Reflection depends on the temperature of the atmospheric layer. The temperature structure is not changed compared to the spectra shown in section 4.3. The abundance at a certain temperature is, however changed for layers above the troposphere. Therefore, the overall magnitude of the reflection is not changed if we assume an atmosphere where the mixing ratios of gases change

with altitude compared to an atmosphere where all constituent gases doe not change concentration as a function of altitude. Fig. (4.27) shows reflection spectra of O_3, N_2O, H_2O, CH_4, CH_3Cl, NH_3 and C_2H_6 when changing the atmospheric abundance by a factor of 10 assuming the Earth abundance reflection (purple) has abundances from Fig. (4.25).

Comparing the synthetic reflection spectra of O_3 in Fig. (4.18b) and Fig. (4.27a) no difference is seen although the abundance of O_3 has several abundances as a function altitude in the latter case. Comparing the spectra for N_2O, there is, however, a difference between an atmosphere for the case the mixing ratios were kept constant and for the case where those mixing ratios were subject to change. Comparing Fig. (4.19b) and Fig. (4.27b), the band a 4.6 μm shows a weakening in this N_2O band in the case there is a change in mixing ratio. The concentration of N_2O decreases with altitude. Although imaging planets can probe more of the atmosphere, they still encounter the upper atmosphere first. Therefore, the concentration of N_2O is lower. Note also that the H_2O bands do not show any lines going to zero because the H_2O abundance drops as a function of altitude. The same reasoning applies for the H_2O bands In Fig. (4.27c). The shaded regions in Fig. 4.20b are saturated, but not in the case that H_2O is present mostly in the lower atmosphere. The concentration of CH_4 is only slightly lower (i.e. less than one order of magnitude) in the case where the mixing ratio is assumed to vary with altitude compared to the case where the mixing ratio is assumed to be equal to the tropospheric mixing ratios. Comparing Fig. (4.21b) and Fig. (4.27d shows that increasing the abundance of CH_4 by a factor 10 results in weaker bands for the latter figure.

For the molecules that are added to the spectrum, CH_3Cl, C_2H_6 and NH_3, there is probably an inconsistency in the opacity tables used for calculating these synthetic spectra.

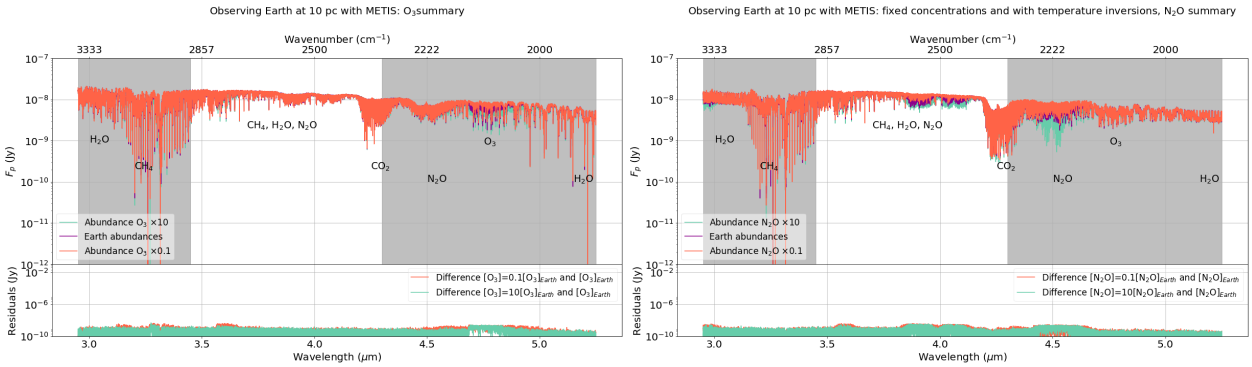

(a)

(b)

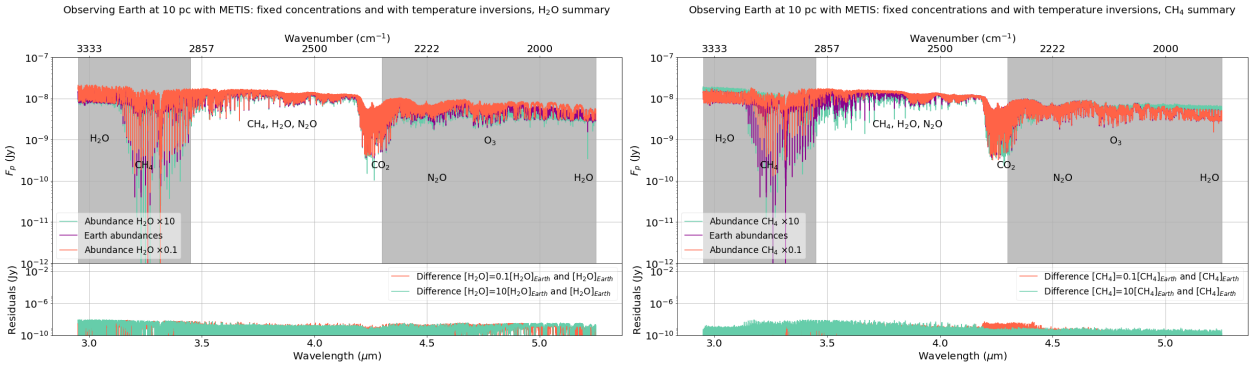

(c)

(d)

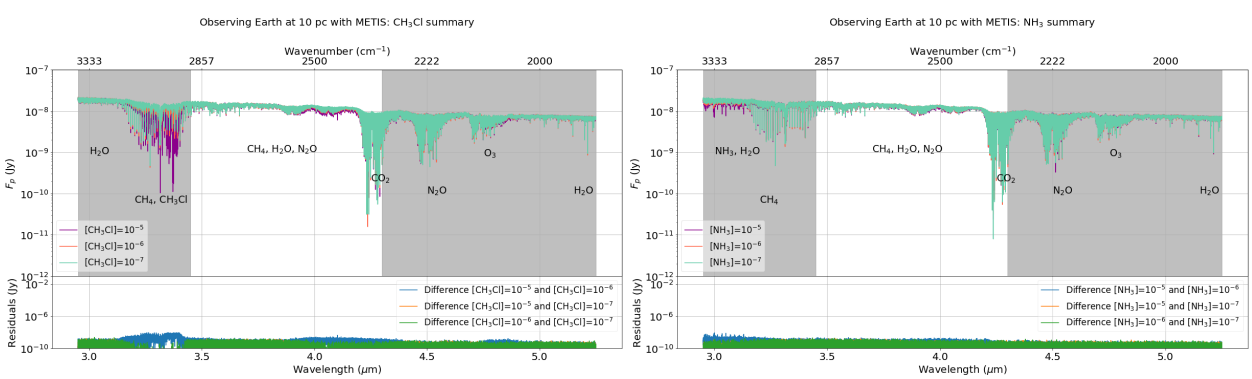

(e)

(f)

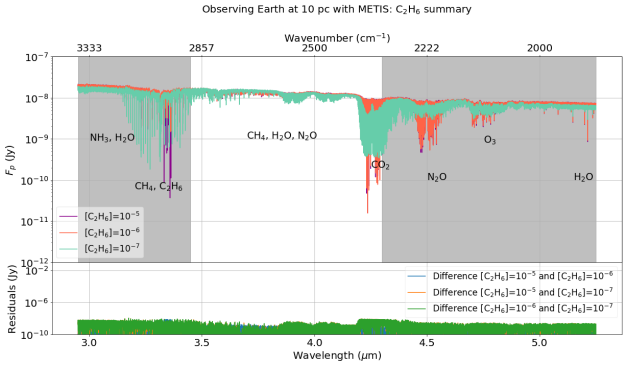

(g)

Figure 4.27: Results of changing the abundances by a factor 10 assuming mixing ratios of molecules with vertical distribution as of present day Earth's atmosphere (see Fig. (4.25)). Synthetic reflection spectra of an Earth-Sun analogue at a distance of 10 pc are presented where it is assumed that the surface temperature is 288 K, that the temperature increases with altitude in the stratosphere (i.e. with a temperature inversion), and that the pressure drops exponentially with altitude. The synthetic reflection spectra as modelled for METIS contain each 3 spectra: one for an Earth-like abundance (purple), one with a factor times more of the gas (blue), and one with a factor less of the gas (orange). CH_3Cl, NH_3, and C_2H_6, gases not present in more than trace amount in the Earth's atmosphere, abundances of 10^{-5} (purple), 10^{-6} (orange), and 10^{-7} (blue) per unit volume are assumed. The gases for which the abundances are changed are (a) O_3, (b) N_2O, (c) H_2O, (d) CH_4, (e) CH_3Cl, (f) NH_3, and (g) C_2H_6.

4.4 Atmospheres and detectability for some known planets

As described in section (3.2), 6 planets are investigated further which obey the criteria that these planets are included in the HEC and that both planetary mass and planetary radius are known from previous observations. To see whether the stellar- and planetary properties have an effect of the detectability, Trappist-1 d, Trappist-1 e, Trappist-1 f, Trappist-1 g, LHS 1140 b, and K2-18 b and their host stars will get some more in depth consideration. Stellar parameters of the Sun, Trappist-1, LHS 1140, and K2-18 are shown in Table 4.2. The equilibrium temperature, the radius, the mass, the distance between the star and the planet, the gravitational acceleration and the period of the planets of interest are presented in Table 4.3. For modelling these planets with ARCiS, the uncertainties of the parameters are not taken into account. The equivalent temperature is calculated from Eq. (1.8) assuming a fixed Bond albedo of $a = 0.3$ for all planets. The gravitational acceleration, g is calculated from:

$$g = \frac{GM_p}{R_p^2} \tag{4.1}$$

where G is the gravitational constant, M_p is the planetary mass and R_p is the planetary radius. The surface gravities of Trappist-1 e, Trappist-1 f, Trappist-1 g are similar to Earth. The surface gravity of Trappist-1 d is about a factor 2 lower compared to Earth's gravity while g for the two biggest planets is a factor $\sim$1.4 larger than Earth. Since the radii of these planets is known from transit observations, all considered planets are transiting the star from our point of view and therefore the inclination angle is about 90°.

The previous sections were devoted to the Earth-Sun analogue at 10 pc which is therefore considered in this section only as comparison material. For the six planets in this section, the goal is to examine whether or not biosignatures can be detectable for those planets. Those 6 planets all have an M-dwarf as host star. Trappist-1, LHS 1140 b, and K2-18 b have radii of 10%, 20% and 40% of the solar radius respectively. The planetary radii are within a factor of 3 of Earth's radius. Therefore, the planetary radius to stellar ratio should be larger by ~ 10. That means that the transmission (i.e. R_p^2/R_s^2) is larger and therefore should be easier to detect. For reflection, the planetary flux, F_p, depends on the radius of the planet. Since the considered Trappist-1 planets are similar to Earth in terms of size, the reflection is not very different for Trappist-1 d, Trappist-1 e, Trappist-1 f, Trappist-1 g and the Earth at 10 pc. For LHS 1140 b and K2-18 b, however, the size is 2.38 and 2.37 times the radius of the Earth respectively which gives an increase in the planetary flux. Note that the equilibrium temperatures of all 7 planets are below the 0 °C required for sustaining liquid H_2O on the surface. Again, the atmosphere may have a huge effect on the surface temperature. It has been suggested (e.g. Wolf 2017) that Trappist-1 e is the best candidate of the Trappist-1 system for having an habitable environment. These suggestions are based on the assumption that the Trappist-1 system has water world planets. Based on this assumption, models indicate that Trappist-1 b, c and d are too hot to have liquid water on the surface while the outer three planets are to cold to have liquid water on its surface. However, the assumption of those planets being water worlds implies that abundant water is present at the present time and location of the planet in the system. Because the Trappist-1 planets orbit an M-dwarf which had a long luminous pre-main sequence stage, H_2O may be lost. Therefore, Trappist-1 d, Trappist-1 f and Trappist-1 g will also be considered.

Moreover, due to observational limitations, only planets having a short period around their host star and orbit close to their host star are considered. This is not an additional assumption but an indication that planets are difficult to be detected and to be characterised if they have long periods and are farther away from they host star. One reason is that the transit method, the method with the most planet detection to date, one is able to observe the transits and therefore only a small part of

the orbit. The planet needs to transit multiple times from our point of view to be detected and to be characterised.

Star	T_{eff} (K)	R_{star} ($R_\odot$)	M_{star} ($M_\odot$)	d (pc)	spectral type
Sun	5777	1.0	1.0	10.0	G2V
Trappist-1	2559± 50 (1)	0.117 ± 0.0036 (1)	0.0802± 0.0073 (1)	12.1 ± 0.4 (1)	M8V(1)
LHS 1140	3216 ± 39 (4)	0.2139 ± 0.0041 (4)	0.179 ± 0.014 (4)	14.993 ± 0.015 (3)	M4.5V(3)
K2-18	3457 ± 39 (2)	0.411 ± 0.038 (2)	0.359± 0.047 (2)	34±4 (4)	M2.5V(4)

Table 4.2: Stellar parameters of the Sun, Trappist-1, LHS 1140 and K2-18.
(1) Parameters taken from Gillion et al. (2017)
(2) Parameters taken from Benneke et al. (2017)
(3) Parameters taken from the Gaia collaboration et al. (2018)
(4) Parameters taken from Ment et al. (2019)

Planet	T_{eq} (K)	R_p ($R_\oplus$)	M_p ($M_\oplus$)	d_{s-p} (AU)	g (cm s^{-2})	P (days)
Earth at 10 pc	255	1.0	1.0	1.0	981	365.25
Trappist-1 d	263.7 $^{+7.7}_{-7.6}$	0.772 ± 0.030 (1)	$0.297^{+0.039}_{-0.035}$ (2)	0.02145 $^{+0.00066}_{-0.00063}$ (1)	489 $^{+76.1}_{-70.3}$	$4.05\pm0.63 \cdot 10^{-4}$(1)
Trappist-1 e	230.1 ± 6.7	0.918 ± 0.039 (1)	$0.772^{+0.079}_{-0.075}$ (2)	0.02817 $^{+0.00083}_{-0.00087}$ (1)	899^{+121}_{-117}	$6.10\pm0.11 \cdot 10^{-4}$(1)
Trappist-1 f	200.5 ± 5.8	1.045 ± 0.038 (1)	$0.934^{+0.080}_{-0.078}$ (2)	0.0371 ± 0.0011 (1)	$839^{+95.5}_{-94.1}$	$9.21\pm0.15 \cdot 10^{-4}$(1)
Trappist-1 g	181.8 ± 5.3	1.127 ± 0.041 (1)	$1.148^{+0.098}_{-0.095}$ (2)	0.0451 ± 0.0014 (1)	887^{+101}_{-99}	$12.35\pm0.12 \cdot 10^{-3}$(1)
LHS 1140 b	214.5 ± 4.3	2.38 ± 0.22 (3)	7.96 ± 1.91 (3)	0.0936 ± 0.0024 (3)	1379 ±424	$24.7\pm0.63 \cdot 10^{-4}$ (3)
K2-18 b	258.6± 13.5	2.37 ± 0.22 (4)	$8.042^{+1.44}_{-1.35}$ (4)	$0.1429^{+0.0060}_{-0.0065}$ (5)	1405 $^{+365}_{-354}$	$32.9^{+1.0\cdot10^{-4}}_{-0.84\cdot10^{-5}}$ (4)

Table 4.3: Parameters of the planets considered including the example of an Earth-Sun analogue at 10 pc.
(1) Data from Gillion et al. (2017)
(2) Data from Grimm et al. (2018)
(3) Parameters taken from Ment et al. (2019)
(4) Data from Sarkis et al. (2018)
(5) Parameters taken from Benneke et al. (2017)

Since we do not have atmospheric characterisation of these 6 planets, assumptions of the atmospheric content of these planets need to be made. The atmospheres are assumed to have mixing ratios as in Fig. (4.25). Of course, it is very unlikely that these planets all have an atmospheric mixing ratios exactly the same as our Earth. Assuming Earth-like mixing ratios in the atmospheres of those planets makes sure that we consider a habitable environment. Note that stellar influences on these abundances are not taken into account. Moreover, the P-T profiles are chosen to have one temperature inversion. For the planets considered, including the Earth, the assumed P-T profiles are plotted in Fig. (4.28). All planets are modelled up to the assumed boundary of the atmosphere, 80 km. It can be seen that for the planet with the lowest equilibrium temperature, Trappist-1 g, the minimum pressure can become as low as $< 10^{-12}$ bar. For Earth, however, for which not the equilibrium temperature but the surface temperature is used, the pressure at the 'top' of the atmosphere is 10^{-6} bar.

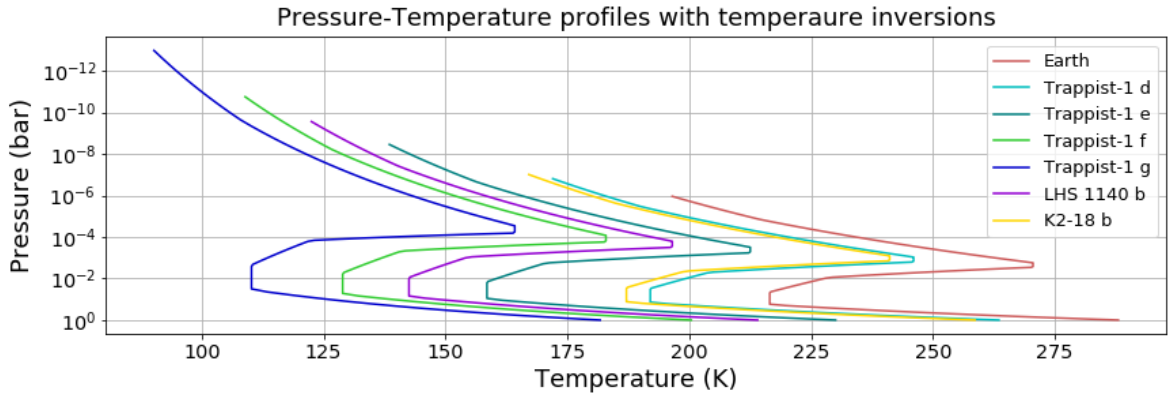

Figure 4.28: Pressure-Temperature profile for Earth (red), Trappist-1 d (light-blue), Trappist-1 e (cyan), Trappist-1 f (green), Trappist-1 g (blue), LHS 1140 b (purple), and K2-18 b (yellow) assuming an atmosphere with a temperature inversion. An atmosphere with temperature inversions has the same linear decrease in temperature in the troposphere, is isothermal in the tropopause, has a temperature increase in the stratosphere, an isothermal stratopause and a temperature decrease in the mesosphere.

This section is further divided in HIRES and METIS. The detectability of spectral features will be discussed.

4.4.1 HIRES

Transmission spectra for HIRES for the six planets are simulated assuming an atmosphere that has a vertical distribution of molecules as of Earth (Earth abundances) and changing again the mixing ratios by a factor of 3 for O_2 and 10 for O_3, N_2O, H_2O, CH_4 and NH_3. These effects are shown in Appendix 1 where the plots are shown per planet. For characterising planetary atmospheres of planets around M stars there is an advantage over characterizing those planets located in the habitable zone of G stars since their periods are smaller. Synthetic transmission spectra of Trappist-1 d, Trappist-1 e, Trappist-1 f, Trappist-1 g, LHS 1140 b and K2-18 b assuming Earth-like abundances are shown in Fig(4.29). Trappist-1 d is both the least massive and the smallest planet considered in the sample resulting in a transmission of the order of 3.33e−3 (see Fig. (4.29a)), a factor of 41 times the transmission of the Earth. Trappist-1 e, considered as the planet with the largest change to be habitable at at least portions of the planet, has a transmission of $\sim 5.0 \cdot 10^{-3}$, a factor ∼60 larger compared to the Earth-Sun analogue at 10 pc. Trappist-1 f is only slightly larger than the Earth and has a transmission of the order of $\sim 6.12 \cdot 10^{-3}$ (a factor $\sim$ 75. Trappist-1 g has a slightly larger transmission as Trappist-1 f: on the order of $7.06 \cdot 10^{-3}$. LHS 1140 b, being more than twice the size of the Earth and orbiting the star LHS 1140, an earlier type M star than Trappist-1, has a transmission of $\sim 9.98 \cdot 10^{-3}$ (a factor of $\sim 10^2$ compared to Earth). Out of the 7 planets (6 planets in the HEC and the Earth-Sun analogue at 10 pc), LHS 1140 b has the largest transmission of close to 0.01. K2-18 b, located at a distance of 34 pc, orbits the early type M dwarf K2-18 at a distance of 0.1429 AU has a transmission of about an order of magnitude less compared to LHS 1140 b: $R_p^2/R_s^2 \sim 1.425 \cdot 10^{-3}$.

Since the six planets all orbit around M stars, the stellar radiation emitted by their host star is shifted to the near-IR compared to the radiation emitted by the Sun. Since near-IR radiation is more easily absorbed by H_2O vapour and H_2O ice, radiative interactions are affected in the atmosphere and with the surface (Shield et al., 2013).

Are spectral features for these planets expected to be detectable with the planned HIRES instrument? The total integration times in seconds for Earth at 10 pc, Trappist-1 d, Trappist-1 e, Trappist-1 f, Trappist-1 g, LHS 1140 b, and K2-18 b to detect a signal for a SNR of 10 are shown in Table 4.4. For molecules whose absorption features are in the grey shaded areas, the regions blocked by our

own atmosphere, SNR calculations are not performed. H_2O has absorption bands from 0.5-2.5 μm in the wavelength HIRES is sensitive to. These absorption bands are not separated in our analysis. Therefore, H_2O the calculations are done for the highest wavelength for with HIRES is sensitive to. These largest integration times for a water detection at SNR= 10 are indicated with a '<' in Table 4.4. In Table 4.4 those molecular absorptions are indicated with a '-'. For the planets of interest, the corresponding duration of a transit and the time between two transits are displayed in Table 4.5.

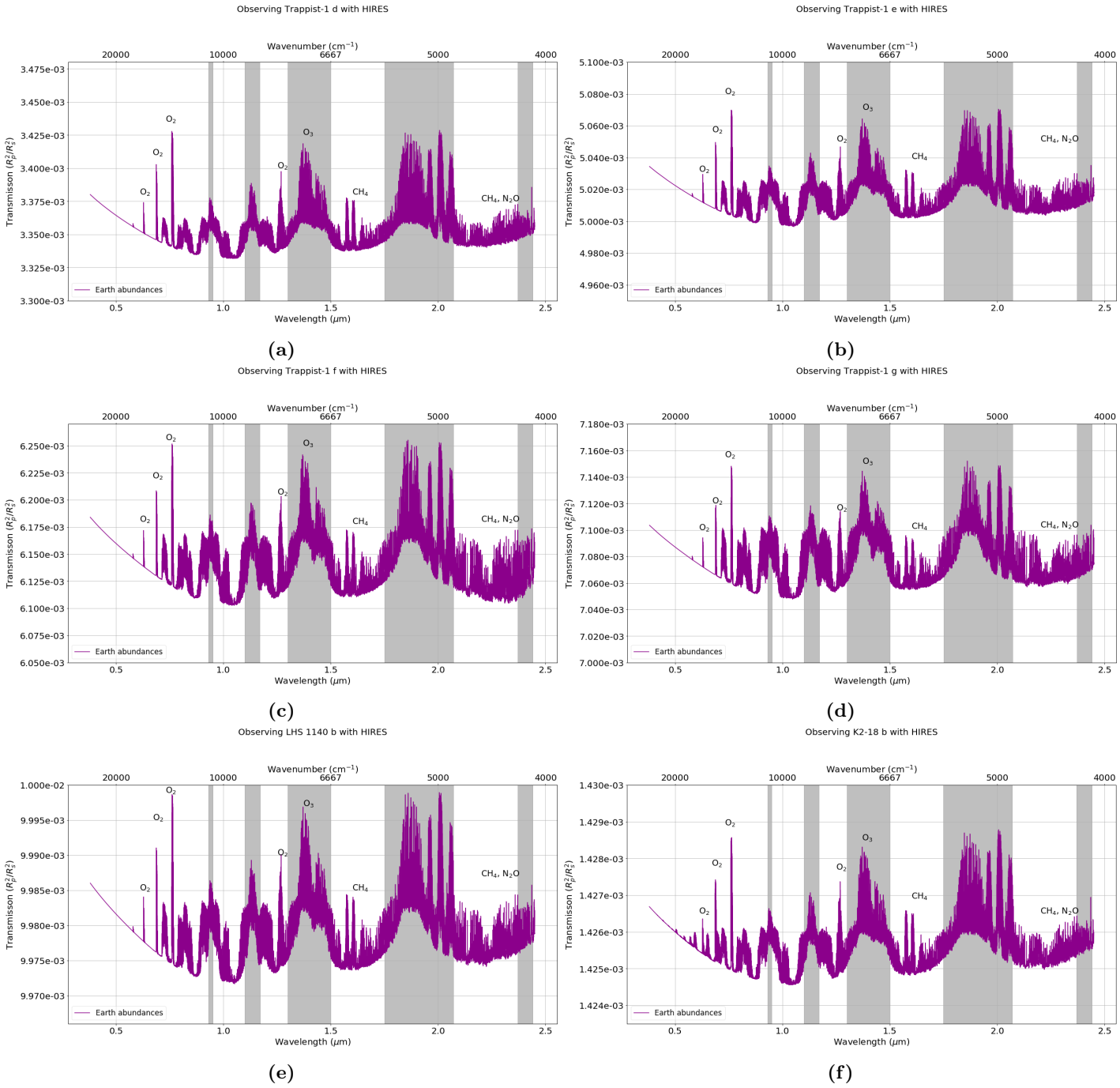

Figure 4.29: Synthetic transmission spectra of some known planets that orbit their host star in the habitable zone and are considered as likely candidates for habitability studies. Transmission spectra of Trappist-1 d (a), Trappist-1 e (b), Trappist-1 f (c), Trappist-1 g (d), LHS 1140 b (e), and K2-18 b (f) are modelled assuming the atmospheres of those planets have an Pressure-Temperature profile as Earth has and assuming that the atmosphere has the atmospheric abundances of Earth.

For a single transit of the Earth-Sun analogue at 10 pc the SNR of the O_2 A-band is about 0.1. One

transit of an Earth-Sun analogue takes ~ 13 hours. Therefore, $\sim 10^4$ transits are needed to achieve a SNR of 10. Since an exo-Earth will orbit its exo-Sun with the same period of the Earth around the Sun, this also means that $\sim 10^4$ years are needed to observe. Therefore, detecting the O_2 signal in an Earth-Sun analogue seems very unlikely with HIRES. Note that an Earth-Sun analogue at 10 pc requires the least amount of integration time in our analysis. However, an orbit around the star is longer compared to the other planets in our analysis. Therefore, it transits less often than the other planets, but reaches the highest SNR within one transit. As an example the SNR of the O_2 A band is 0.0001 for K2-18 b which is a factor 10^3 lower than for the Earth-Sun analogue. This difference results from a combination of the factors needed to calculate the SNR of the signal. The factor that contributes the most is the difference in stellar radii. This difference is about a factor 10, which gives a factor 10^2 in the calculation of the SNR (see Eq. (3.16)). This means that more transits are needed in order to be able to observe it. However, the time between subsequent transits is larger compared to Earth by a factor $\sim$10 and the transit duration is a factor 4 smaller compared to Earth. For the required SNR= 10, this will take $\sim 4 \cdot 10^9$ transits of K2-18 b from our point of view. This will take $\sim 10^8$ years of observation time. Detecting the O_2 A-band in the atmosphere of K2-18 b with transmission spectroscopy with HIRES is therefore unlikely. The observation time needed for LHS 1140 b is similar as for K2-18 b. The times needed to reach SNR=10 for the considered planets of the Trappist-1 system are a factor $\sim 10^3$ higher compared to K2-18 b. This means that for all 7 planets considered, it seems unlikely that HIRES will be able to detect the O_2 A band.

The reader may calculate the observation times necessary for all other spectral features using Table 4.4, Table 4.5, and the equations in section 3.4. By doing these computations, it is concluded that all molecular features shown in Table 4.4 for the 7 analysed planets in this thesis are unlikely to be detected with HIRES via transmission spectroscopy.

Molecule	λ (μm)	Earth	Trappist-1 d	Trappist-1 e	Trappist-1 f	Trappist-1 g	LHS 1140 b	K2-18 b
O_2	0.628	$3.8 \cdot 10^9$	$1.5 \cdot 10^{17}$	$1.3 \cdot 10^{17}$	$3.1 \cdot 10^{16}$	$1.3 \cdot 10^{16}$	$5.6 \cdot 10^{11}$	$4.0 \cdot 10^{13}$
	0.688	$3.2 \cdot 10^9$	$4.1 \cdot 10^{16}$	$3.6 \cdot 10^{16}$	$8.8 \cdot 10^{15}$	$3.6 \cdot 10^{15}$	$2.4 \cdot 10^{11}$	$2.0 \cdot 10^{13}$
	0.76	$3.2 \cdot 10^8$	$8.9 \cdot 10^{16}$	$2.6 \cdot 10^{16}$	$9.6 \cdot 10^{15}$	$5.2 \cdot 10^{15}$	$1.2 \cdot 10^{12}$	$1.4 \cdot 10^{13}$
	1.269	-	-	-	-	-	-	-
O_3	2.05	-	-	-	-	-	-	-
	2.15	$1.7 \cdot 10^9$	$1.4 \cdot 10^{15}$	$4.1 \cdot 10^{14}$	$1.5 \cdot 10^{14}$	$8.2 \cdot 10^{13}$	$2.3 \cdot 10^{11}$	$1.2 \cdot 10^{13}$
N_2O	1.3	-	-	-	-	-	-	-
	2.2	$1.5 \cdot 10^{10}$	$1.6 \cdot 10^{14}$	$1.4 \cdot 10^{14}$	$3.5 \cdot 10^{13}$	$1.4 \cdot 10^{13}$	$1.4 \cdot 10^{10}$	$2.3 \cdot 10^{12}$
H_2O	0.5-2.5	$< 2.4 \cdot 10^{10}$	$< 1.8 \cdot 10^{14}$	$< 1.6 \cdot 10^{14}$	$< 4.0 \cdot 10^{13}$	$< 1.6 \cdot 10^{13}$	$< 1.9 \cdot 10^{10}$	$< 3.1 \cdot 10^{12}$
CH_4	1.8	$8.3 \cdot 10^9$	$1.6 \cdot 10^{14}$	$1.4 \cdot 10^{14}$	$3.5 \cdot 10^{13}$	$1.4 \cdot 10^{13}$	$1.1 \cdot 10^{10}$	$1.8 \cdot 10^{12}$
	2.4	$2.1 \cdot 10^{10}$	$1.8 \cdot 10^{14}$	$1.5 \cdot 10^{14}$	$3.8 \cdot 10^{13}$	$1.5 \cdot 10^{13}$	$1.7 \cdot 10^{10}$	$2.9 \cdot 10^{12}$
NH_3	2.0	-	-	-	-	-	-	-
	2.3	$1.8 \cdot 10^{10}$	$1.7 \cdot 10^{14}$	$1.5 \cdot 10^{15}$	$3.6 \cdot 10^{13}$	$1.5 \cdot 10^{13}$	$1.5 \cdot 10^{10}$	$2.5 \cdot 10^{12}$

Table 4.4: Observation time (s) to detect a spectral feature with HIRES.

Taking the O_3 2.15 band as an example, the total amount of transits needed to reach a SNR of 10 are

Planet	Transit duration (h)	Time between two transits (h)
Earth at 10 pc	13	$8.7 \cdot 10^3$
Trappist-1 d	0.8	$9.6 \cdot 10^1$
Trappist-1 e	0.9	$1.5 \cdot 10^2$
Trappist-1 f	1.0	$2.2 \cdot 10^2$
Trappist-1 g	1.1	$3.0 \cdot 10^2$
LHS 1140 b	2.0	$5.9 \cdot 10^2$
K2-18 b	3.3	$7.9 \cdot 10^2$

Table 4.5: Approximate transit duration (h) and the time between two subsequent transits of the planets of interest.

4.4.2 METIS

Synthetic reflection spectra for atmospheres of the six planets assuming the atmosphere has the atmospheric abundances of Earth are shown in Fig. (4.30). The magnitude of the reflection depends on the radius of the planet, the stellar radius, the distance to the star, the stellar effective temperature, and the semi-major axis (see Eq. (2.5)) . Since the Trappist-1 planets are similar in size as the Earth, the stellar radius is about 1/10 of the Sun, the distance is also about the same as the example of the Earth-Sun analogue at 10 pc, the effective temperature of Trappist-1 is about half that of the Sun, and the distance between Trappist-1 and the considered planets is about 1/50 that of 1 AU, the reflection is not shifted significantly compared to Earth. All these parameters enter Eq. (2.5) and calculating the difference in planetary flux for the Trappist-1 planets and the example of an Earth-Sun analogue at 10 pc, this results of about a factor 1. Comparing LHS 1140 b and an Earth-Sun analogue at 10 pc, however, the planetary radius is about a factor 2 larger compared to Earth, the stellar radius is about a factor of 5 smaller compared to the Sun, the distance is about a factor 1.5 larger, the effective temperature of LHS 1140 is slightly more than half the solar effective temperature, and the semi-major axis is about a tenth of an AU resulting in a factor of about 10. LHS 1140 b has ~ 10 times the reflection of the Earth-Sun analogue at 10 pc. Similarly, the reflection for K2-18 b, which is located at a distance of 34 pc, is enhanced by about a factor 2 compared to an Earth-Sun analogue at 10 pc.

Results for the sensitivity calculations for METIS and are shown in 4.6. All regions blocked by our atmosphere are excluded from the analysis. Molecules that absorb in these wavelength regions are indicated with a '-' in Table 4.6. Only for three remaining absorption bands the integration time (in seconds) can be measured. Both LHS 1140 b and K2-18 b are relatively far away in terms of near-future exoplanet characterisation. Therefore, their observation times are large compared to the Earth-Sun analogue at 10 pc and the considered planets in the Trappist-1 system. Integration times for biosignature research for the four considered planets in Trappist-1 system and the Earth-Sun analogue at 10 pc are reasonable. It may be reached within ~ 270 observation hours, equivalent of 27 nights of observation for Earth at 10 pc and the Trappist-1 system planets. LHS 1140 b and K2-18 b need much longer observation times. These observation times are on the order of ~ 5 yr for the N_2O 3.7 μm band. Since METIS is able to both directly image planets and high resolution spectroscopy, observations aren't limited to the time the planet transits the planet and observations can be carried out for several nights in a row. It is very unlikely that METIS will be able to detect differences in mixing ratio structures for gases in the atmosphere.

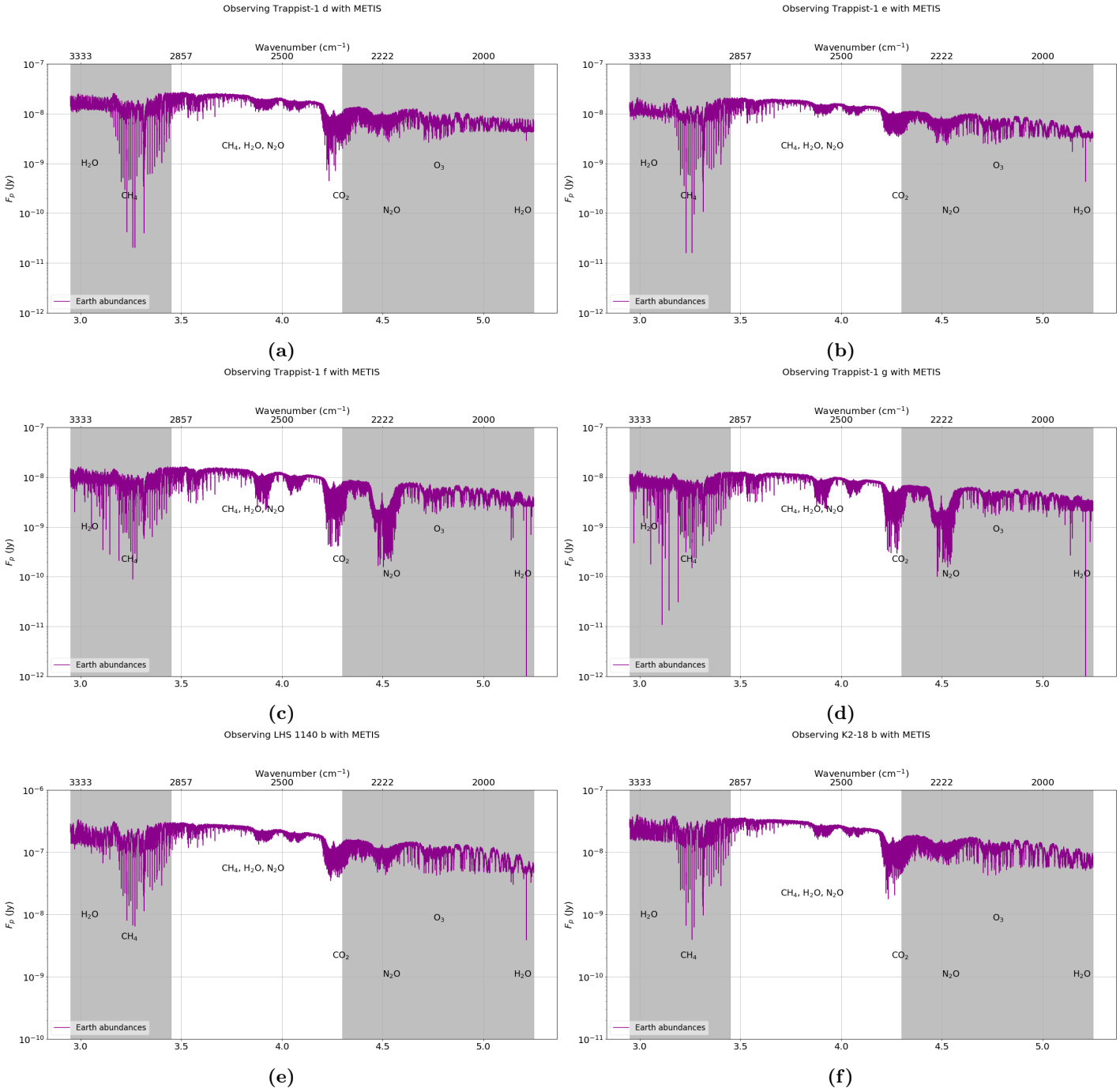

Figure 4.30: Synthetic reflection spectra of some known planets that orbit their host star in the habitable zone and are considered as likely candidates for habitability studies. Reflection spectra of Trappist-1 d (a), Trappist-1 e (b), Trappist-1 f (c), Trappist-1 g (d), LHS 1140 b (e), and K2-18 b (f) are modelled assuming the atmospheres of those planets have an Pressure-Temperature profile as Earth has and assuming that the atmosphere has the atmospheric abundances of Earth.

Molecule	λ (μm)	Earth	Trappist-1 d	Trappist-1 e	Trappist-1 f	Trappist-1 g	LHS 1140 b	K2-18 b
O_3	3.6	$9.2 \cdot 10^4$	$5.8 \cdot 10^5$	$5.8 \cdot 10^5$	$5.8 \cdot 10^5$	$5.8 \cdot 10^5$	$3.7 \cdot 10^8$	$9.2 \cdot 10^6$
	4.6	-	-	-	-	-	-	-
	4.8	-	-	-	-	-	-	-
N_2O	3.7	$9.7 \cdot 10^5$	$9.7 \cdot 10^5$	$9.7 \cdot 10^5$	$9.7 \cdot 10^5$	$9.7 \cdot 10^5$	$1.5 \cdot 10^6$	$1.5 \cdot 10^6$
	4.5	-	-	-	-	-	-	-
H_2O	3.5-4.3	$2.1 \cdot 10^6$- $3.9 \cdot 10^3$	$2.1 \cdot 10^6$- $3.9 \cdot 10^3$	$2.1 \cdot 10^6$- $3.9 \cdot 10^3$	$2.1 \cdot 10^6$- $6.1 \cdot 10^2$	$3.4 \cdot 10^8$- $1.5 \cdot 10^6$	$3.4 \cdot 10^9$- $9.7 \cdot 10^4$	$1.1 \cdot 10^9$- $5.2 \cdot 10^4$
CH_4	3.3	-	-	-	-	-	-	-
NH_3	3.0	-	-	-	-	-	-	-
C_2H_6	3.3	-	-	-	-	-	-	-
CH_3Cl	3.3	-	-	-	-	-	-	-

Table 4.6: Observation time (s) to detect a spectral feature with METIS.

4.5 Photon noise and Optimal resolution for characterising atmospheres with the ELT

The photon noise for an Earth-Sun analogue at 5 pc as observed in the optical with a 10m telescope with a spectral resolution of $R = 100$ is about 1 photon/s/resolution element (M. Min, private communication). Based on this estimate, results from the analysis technique described in section 3.3 were checked. In photon noise calculations the efficiency of the ELT ($q = 0.5$) was taken into account. The factor 1.2 for the total assumed noise budget is not taken into account for the photon noise calculations in this section. Table 4.7 shows the estimates of the photon noises for the wavelength boundaries for HIRES (i.e. 0.37 μm and 2.5 μm) and METIS (i.e. 2.9 μm and 5.3 μm for the 7 considered planets. Photon noises, $1/\sqrt{n}$, are shown where n is given in photons per second. Therefore, in the calculations, the observation time was set to 1 s. It can be seen that the optical has the lowest photon noise for all planets compared with the wavelengths in the IR. Moreover, the Trappist-1 planets have an overall higher photon noise compared with an Earth-Sun analogue at 10 pc (∼1% of photon noise of Trappist-1 planets), LHS 1140 b (∼ 15%) and K2-18 b (∼ 10%). The lower the photon noise, or at least the total noise budget, the easier would it be to observe the features. Therefore, at wavelengths in the near-IR, it would be easier to observe features because it can be considered as the photon noise limited regime.

Planet	Wavelengths			
	0.37 μm	2.5 μm	2.9 μm	5.3 μm
Earth at 10 pc	0.00086	0.00068	0.00076	0.0012
Trappist-1 d	0.61	0.016	0.016	0.023
Trappist-1 e	0.61	0.016	0.016	0.023
Trappist-1 f	0.61	0.016	0.016	0.023
Trappist-1 g	0.61	0.016	0.016	0.023
LHS 1140 b	0.088	0.0082	0.0088	0.013
K2-18 b	0.068	0.0089	0.0097	0.014

Table 4.7: Photon noise (i.e. $\frac{1}{\sqrt{n}}$, where n has units of photons per second) estimates for an Earth-Sun analogue at 10 pc, Trappist-1 d, Trappist-1 e, Trappist-1 f, Trappist-1 g, LHS 1140 b and K2-18 b for the boundaries of the wavelength ranges for which HIRES and METIS are sensitive to.

For determining the optimal resolution for both HIRES and METIS, some parameters need to be considered. The optical resolution depends on the intrinsic width of the stellar lines (Snellen et al., 2015). A high resolution is proposed because telluric lines need to be distinguished from planetary absorption lines in order to do characterisation of the atmosphere. However, because of the high

spectral resolution, fewer photons will be collected by the telescope. Moreover, the SNR for a single transit is smaller for higher resolutions because it depends on the resolution (see e.g. Rauer et al., 2011). Is a lower R maybe better for HIRES when considering atmospheric characterisation? Snellen et al. (2015) come to a spectral resolution of 75.000 for the optical for HDS and HCL (i.e. a METIS like instrument in the optical). This can be deduced from the turbulent velocity, Δv of the star and the speed of light, c in:

$$R = \frac{c}{\Delta v} \tag{4.2}$$

Depending on the star, the optimal resolution will be between 75.000 and 100.000. For HIRES, the proposed $R = 120.000 - 130.000$ and is not needed for characterisation of planetary atmospheres. This resolution was proposed to be able to cover all science cases proposed for HIRES. Similarly, for sensitivity calculations of METIS, the sensitivity also depends on $1/R$. For higher R the sensitivity will be higher. The optimal resolution depends on the velocity in the Mid-IR.

Chapter 5

Discussion

In this thesis the detectability of the frequently proposed biosignature gases O_2, O_3, N_2O, CH_4, NH_3, C_2H_6, and CH_3Cl and the habitability marker H_2O was examined. This was done by building atmospheres with the exoplanet modelling code ARCiS. First, simple isothermal atmospheres with only one gas (O_2 for HIRES, O_3 for METIS) were modelled and the effect of different temperatures and pressures was examined. It was seen that pressure differences only have a small contribution to both transmission and reflection spectra. The effect of pressure broadening is, however, present in both transmission and reflection spectra. Increasing the temperature of the atmosphere resulted in increasing the transmission. This is consistent with the concept of the atmospheric scale height. For the reflection spectra modelled with the characteristics of METIS, the O_3 band at 4.8 μm changes location with different atmospheric temperatures.

Next, the effects of those temperatures and pressures on Earth-like atmospheres were examined. P-T profiles considered were (1) a temperature profile with one temperature inversion in the stratosphere and (2) a temperature profile in which the temperature dropped in the troposphere and was isothermal at higher altitudes. The pressure profile for both these atmospheres was assumed to follow an exponential profile. It was concluded that for transmission spectra for the optical and near-IR the pressure profile had a small influence on the transmission because of the atmospheric scale height. The temperature profile, however, had no effect on the transmission. This was expected since transmission spectra are not sensitive to the temperature profile of an atmosphere. For reflection spectra, both the pressure profile and the temperature profile had an effect on the the flux of the planet and therefore on the reflection spectra. Reflection spectra can probe deeper into atmospheres while the upper atmosphere is probed with transmission spectra.

In the next steps the atmospheres were modelled with O_2, O_3, N_2O, CH_4, CO_2, H_2O, and N_2. Also NH_3, CH_3Cl and C_2H_6 were added to the spectrum. The effect of changing the abundances by a factor 3 for O_2 and 10 for all other molecules was discussed. The goal here was to understand what caused the changes in both the transmission and reflection spectra and to infer whether these would be detectable. For HIRES, changes in the absorbance of CH_4, H_2O and NH_3 may be observed through our own atmosphere, while for METIS those are for NH_3, H_2O and, although weak, O_3. For HIRES, it will be extremely difficult to detect the atmospheric gases since transmission spectroscopy can only be done in the time the planet transits the star. In the wavelength range of METIS, most molecular spectral features are blocked by our own atmosphere and only the O_3 3.6 μm band, the H_2O bands, and the N_2O 3.7 μm band will be detectable. For Earth, Trappist-1 d, e, f and g these features can be seen in a reasonable observation time of about 27 observation nights. For LHS 1140 b and K2-18 b, however, the observation times will be about a factor 10^4 times larger for the 3.6 μm O_3 band and the 3.7 μm N_2O band. Therefore, it will be unfeasible to detect those signatures in the atmospheres

of LHS 1140 b and K2-18 b. LHS 1140 b and K2-18 b are also those planets that are in the optimistic sample of the HEC while the four Trappist-1 planets considered in this thesis are in the conservative sample.

The detectability of biosignatures in planetary atmospheres has been modelled by numerous authors (e.g. Rauer et al., 2011; Snellen et al., 2015; Krissansen-Totton et al., 2018; Serindag & Snellen, 2019) considering different telescopes. Research in the characterisation of exoplanetary atmospheres rely necessarily on assumptions since no other planet than Earth is found to host life. In this section the assumptions made are discussed and the results are compared to previous work related to the detectability of biosignatures with the ELT.

One assumption in each work considering biosignatures in exoplanetary atmosphere is the temperature and pressure structure in the atmosphere. In this work temperature structures were assumed to be completely isothermal, having a linear decrease in the troposphere followed by isothermal layers at higher altitudes or a profile with a linear decrease in the temperature in the troposphere and a temperature inversion in the stratosphere (which is caused by ozone heating on Earth). The effect of surface gravity on the temperature structure was neglected and the planetary equilibrium temperature was the only factor that changed the temperature structure. Rauer et al. (2011), however, did include the effect of the surface gravity. They considered two planets with the same incident radiation. For a higher surface gravity, the surface temperature decreases because of the lower vertical column mass. If there is less mass, there is less absorption and therefore less greenhouse effect and therefore a lower surface gravity (Rauer et al., 2011). Moreover, they considered a temperature structure where the maximum temperature in the stratosphere decreases at higher pressures for higher surface gravities because O_3 heating occurs at higher pressures. Also the effect of the surface gravity was shown in the vertical chemical profiles. For the same surface pressure, the tropospheric H_2O number density was decreased for the higher surface gravity case compared to the lower surface gravity case. Because H_2O has a relatively high mean molecular weight, this leads to a decrease in overall column mass.

Ohter properties not taken into account are the effect of the host star on the abundance of any atmospheric gas and the effect of clouds on the synthetic transmission and reflection spectra. This was beyond the scope of this thesis because of the lack in knowledge regarding the effects of the host star. Rauer et al. (2011) took into account the increase in N_2O abundance for increasing M-star class, the decrease in O_3 abundance for M-dwarfs (Segura et al., 2005; Rauer et al., 2011) and an increase in CH_3Cl for cooler M-stars.

Snellen et al. (2015) simulated results of combining the techniques of high-resolution spectroscopy and high-contrast imaging for O_2. They assumed an 1-1.5 $R_\oplus$ planet orbiting around α Cen ($d = 1.3$ pc) and concluded that a planet with $T_{eq} = 300$ K around this star could be detected at a wavelength of 4.8 μm at a S/N=5 within one observation night (i.e. 10 h). In this observation night, also reflected light in the optical of planet of the same size in the HZ of Proxima Centauri ($d = 1.3$ pc) may be detected with S/N=10. These stars are located at a distance of a factor 7 to 26 times closer than the host stars considered in this thesis. Since the detectability depends on the distance of the star squared, our values are expected to be a factor 50-700 higher than those of Snellen et al. (2015). However, since also properties of the stars and the size of the planets assumed in both works are different, this estimation of the factor is not reliable.

Serindag and Snellen (2019) investigated the detectability of O_2 in exoplanetary atmospheres using HRS with the Extremely Large Telescopes (ELTs). They have found that O_2 would be detectabile for an Earth-twin transiting an M5V star at a distance of 7 pc in 70-175 hours observation time. This time is similar to 4-10 years when the transit time and the planetary period is taken into account. They used data from the VLT and the characteristics of the VLT and the ELT to simulate real noise. Our result was that the strongest O_2 band can be detected in $3.8 \cdot 10^9$ s, equivalent to 10^6 h. This discrepancy is

due to the fact that they considered a METIS-like instrument (i.e. an instrument combining HRS and HCI) assumed to be sensitive to optical wavelengths while we assumed HIRES (i.e. only HRS) as an instrument for optical wavelengths. For METIS, most features in the IR can be distinguished within ~ 30 h, more consistent with the results of Snellen et al. (2015).

Krissansen-Totton et al. (2018) investigated the detectability of biosignatures with the James Webb Space Telescope (JWST) considering anoxic atmospheres. In particular, they examined whether an atmosphere with both CH_4 and CO_2 in disequilibrium would be detectable with transmission spectroscopy. This CH_4/CO_2 combination is proposed as a biosignature for anoxic atmospheres (Krissansen-Totton et al., 2018). Instead of assuming a modern Earth atmosphere, they assumed an atmosphere atmosphere more like early Earth. In particular, during the Archean eon the Earth's atmosphere likely had an disequilibrium between those two gases. They simulated synthetic transmission spectra and concluded that the CH_4-CO_2 disequilibrium biosignature would be detectable in about 10 transits for Trappist-1 e assuming an Archean-like atmosphere. Based on the low number of transits needed, the CH_4-CO_2 disequilibrium biosignature should be easier detectable than O_2 or O_3 with JWST. However, there is a probability of $\sim 9\%$ that the observed CH_4 abundance is abiotic in origin. This probability decreases with the number of transits. They assumed similar temperature structures as this work. Moreover, their assumed abundances, although different, are similarly assumed to not vary with height.

Chapter 6

Conclusion

We analysed whether the commonly proposed gaseous biosignature O_2, O_3, N_2O, CH_4, CH_3Cl, C_2H_6, and NH_3 and the habitability marker H_2O will be detectable with planned instruments on the ELT. Synthetic transmission and reflection spectra were modelled for HIRES and METIS respectively using the exoplanetary modelling code ARCiS. We considered a hypothetical Earth-Sun analogue at a distance of 10 pc and built a realistic atmosphere. First, the effect of the pressure and temperature were examined considering a simple isothermal atmosphere in which only one gas is present. This was followed by investigating the effect of temperature profiles and subsequently the distributions of molecules. Additionally, properties of six planets that were discovered in previous years using the transit method and the radial velocity method were taken from the HEC. These planets were examined to determine the detectability for these planets orbiting cool stars. For an Earth-Sun analogue at 10 pc it would not be possible to detect biosignatures with transmission spectroscopy in the wavelength range of HIRES for a SNR of 10 within the lifetime of a human. Therefore, it was concluded that detecting biosignatures present in the atmosphere of an Earth-Sun analogue at 10 pc will not be detectable with HIRES.

Considering METIS as an instrument, it can be concluded that most molecules absorbing in this region are not detectable because of blocking by our own atmosphere. For the case of Earth at 10 pc and Trappist-1 d, Trappist-1 e, Trappist-1 f, and Trappist-1 g the observation times for detecting the O_3 3.6 μm band, the N_2O 3.7 μm band and water features in the wavelength range of 3.5-4.3 μm are detectable within 27 observation nights. Biosignatures of habitability markers for LHS 1140 b and K2-18 b require much higher observation times that are considered as unreasonable and are therefore not able to be detected.

The optimal resolution concerning the characterisation of exoplanetary atmospheres, the proposed resolutions are higher than needed. Optimal resolutions for this science case will be $R = 75,000 - 100,000$ in both the optical and the IR. The value depends on the intrinsic width of the stellar lines which is also wavelength dependent. Photon noises are smallest in the near-IR and are on the order of 10^{-2} for planets in the Trappist-1 system. This photon noise was calculated using number of photons per second as units for n.

6.1 Plans for the near future

The search of biosignatures in exoplanetary atmospheres goes far beyond the investigation of the effect of surface pressures and temperatures, the effect of temperature inversions and the effect of changing the abundance of a biosignature or a habitability marker. One important suggestion to examine in the near future is the effect of clouds. Cloud chemistry is included in ARCiS but was not taken into

account in this thesis. Understanding clouds would help to interpret spectra obtained with near-future telescopes. One frequently cited example is GJ 1214 b which has a flat transmission spectrum (e.g. Berta et al., 2012). The flat spectrum is suggested to be caused by clouds high in the atmosphere. Most of the solar system planets have clouds. Earth has water clouds but Venus has sulphuric acid clouds. With a better understanding of clouds it would be possible to constrain the planetary albedo which in turn ensures that the surface temperature can be better estimated. This in turn will give us insight into whether we could expect liquid water on the surface. For future work in atmospheric characterisations it would be better to include or understand both the theoretical side of clouds and the effect of clouds on the spectrum.

Besides the gaseous biosignatures investigated in this thesis, there are two other categories of biosignatures mentioned in section 1.3. Temporal biosignatures need more theoretical work in order to be able to be modelled with significance. Surface biosignatures, in particular the VRE, can be modelled in exoplanetary spectra. ARCiS is not the appropriate code for this because the surface is modelled in such a way that it is fully reflective. If the VRE is considered, care should be taken with respect to where the reflection will be present in the reflection spectrum since the VRE could be shifted with respect to 'our' VRE due to differences in stellar flux and stellar activity.

ARCiS gave some limitations to our work. Besides the planetary surface is assumed to be a fully reflective surface, the resolution for calculating opacity tables could not be set to higher resolutions necessary to model synthetic reflection and transmission spectra for HIRES and METIS in the search for biosignatures. In future work, a modelling code that is able to sustain such resolutions would work. One example in Exo-Transmit for modelling synthetic transmission spectra.

Besides planned telescopes having as a science goal the characteristion of exoplanetary atmospheres such as the ELT and James Webb Space Telescope (JWST), the Atmospheric Remote-sensing Infrared Exoplanet Large-survey (Ariel[1]) is proposed as the first space-based telescope fully dedicated to measuring the chemical composition and thermal structures of exoplanets. Ariel is scheduled for launch in 2028. During its mission, Ariel will study 1,000 exoplanets in both the optical and IR. Not only planets in the HZ, but planets of all sizes and at all distances from the host star are subject of Ariel. Moreover, Luvoir and HabEx are proposed as large space based facilities to be launched in the 2030's. These space-based instruments are interesting for exoplanetary science because data obtained is not contaminated by our own atmosphere. That means that the resolution needed is also lower. Since these telescopes will be about 2.5 times smaller than the ELT, but probably have a lower R, about the same order of photons will be detected.

[1] https://arielmission.space/

Bibliography

Arnold L., Gillet S., Lardière O., Riaud P. and Schneider J. (2002). Airborne spectral measurements of surface–atmosphere anisotropy for arctic sea ice and tundra, int. j. remote sensing, 23, 18, 3763–3781.

Barnes, R. (2017). Tidal locking of habitable exoplanets. Celestial Mechanics and Dynamical Astronomy, 129(4), pp.509-536.

Benneke, B., Werner, M., Petigura, E. et al. (2017). Spitzer Observations Confirm And Rescue the Habitable zone super-Earth K2-18 b For Future Characterization. The Astrophysical Journal, 834(2), p.187.

Benner S,. A., Ricardo, A., Carrigan, M. A. (2004). Is there a common chemical model for life in the universe? Curr Opin Chem Biol, 8:672–689.

Berta, Z., Charbonneau, D., Désert, J., Miller-Ricci Kempton, E., McCullough, P., Burke, C., Fortney, J., Irwin, J., Nutzman, P. and Homeier, D. (2012). THE FLAT TRANSMISSION SPECTRUM OF THE SUPER-EARTH GJ1214b FROM WIDE FIELD CAMERA 3 ON THEHUBBLE SPACE TELESCOPE. The Astrophysical Journal, 747(1), p.35.

Borucki, W. and Summers, A. (1984). The photometric method of detecting other planetary systems. Icarus, 58(1), pp.121-134.

Brandl, B. R., Markus, F., Alistair, G. et al., (2014). METIS: the mid-infrared E-ELT imager and spectrograph. Proceedings of the SPIE. 9147, 914821

Brasseur, G. P., Orlando, J. J. and Tyndall, G.S. (1999). Atmospheric Chemistry and Global Change. Oxford University Press, Oxford. 654.

Canfield, D. E. (2005). The early history of atmospheric oxygen: homage to Robert M. Garrels. Ann Rev Earth Planet Sci 33: 1–36.

Catling, D. C., Zahnle, K. J., and McKay, C. P. (2001). Biogenic methane, hydrogen escape, and the irreversible oxidation of early Earth. Science 293:839–843.

Catling, D. C., Krissansen-Totton, J., Kiang, N. Y., et al. (2018). Exoplanet Biosignatures: A Framework for Their Assessment. Astrobiology, 18, 709

Chapman, S. (1930). A theory of atmospheric ozone. R Meteorol Soc Memoir 3:103–125.

Clark, R. N., Swayze, G. A., Gallagher, A. J., King, T. V. V., and Calvin, W. M. (1993). The U.S. Geological Survey, Digital Spectral Library: Version 1: 0.2 to 3 Microns. U.S. Geological Survey Open File Report 93–592, U.S. Geological Survey, Reston, VA

Cockell, C. (2014). Habitable worlds with no signs of life. Philosophical Transactions of the Royal Society A: Mathematical, Physical and Engineering Sciences, 372(2014), pp.20130082-20130082.

Cockell, C. S., Bush, T., Bryce, C. et al. (2016). Habitability: A Review. Astrobiology 16, 89–117

Cocconi, G. and Morrison, P. (1959). Searching for Interstellar Communications. Nature, 184(4690), pp.844-846.

Czaja, A. D., Johnson, C. M., Roden, E. E., et al. (2012). Evidence for free oxygen in the Neoarchean ocean based on coupled iron-molybdenum isotope fractionation. GeochimCosmochim Acta 86:118–137.

De Pater, I. and Lissauer, J. (2010). Planetary sciences. Cambridge: Cambridge University Press.

Des Marais, D. J. and Walter, M. R. (1999). Astrobiology: Exploring the Origins, Evolution, and Distribution of Life in the Universe. Ann. Rev. Ecol. syst. 30:397-420

Des Marais, D., Harwit, M., Jucks, K., et al. (2002). Remote Sensing of Planetary Properties and Biosignatures on Extrasolar Terrestrial Planets. Astrobiology, 2(2), pp.153-181.

Des Marais, D. J., Nuth, J. A., Allamandola, L. J. et al. (2008). The NASA Astrobiology Roadmap. Astrobiology 8:715-730.

Domagal-Goldman, S., Meadows, V., Claire, M. and Kasting, J. (2011). Using Biogenic Sulfur Gases as Remotely Detectable Biosignatures on Anoxic Planets. Astrobiology, 11(5), pp.419-441.

Domagal-Goldman, S. D., Segura, A., Claire, M. W., Robinson, T. D., and Meadows, V. S. (2014). Abiotic ozone and oxygen in atmospheres similar to prebiotic earth. ApJ 792:43.

Donahue, T., Hoffman, J., Hodges, R. and Watson, A. (1982). Venus Was Wet: A Measurement of the Ratio of Deuterium to Hydrogen. Science, 216(4546), pp.630-633.

Etiope, G. and Sherwood-Lollar, B. S. (2013). Abiotic methane on earth. Rev Geophys, 51:276–299.

Farquhar, J. (2000). Atmospheric influence of earth's earliest sulfur cycle. Science 289:756–758

Fayolle, E., Oberg, K., Jorgensen, J., et al. (2017). Protostellar and cometary detections of organohalogens. Nature Astronomy, 1(10), pp.703-708.

Frische, M., Garofalo, K., Hansteen, T. and Borchers, R. (2006). Fluxes and origin of halogenated organic trace gases from Momotombo volcano (Nicaragua). Geochemistry, Geophysics, Geosystems, 7(5)

Gaia Collaboration, Brown, A. G. A., Vallenari, A., Prusti, T. et al. (2018). Gaia Data Release 2. Summary of the contents and survey properties, Astronomy & Astrophysics, 616, A1

Gao, P., Hu, R., Robinson, T. D., et al. 2015, ApJ, 806, 249

Gillon, M., Jehin, E., Lederer, S., Delrez, L., de Wit, J., Burdanov, A., Van Grootel, V., Burgasser, A., Triaud, A., Opitom, C., Demory, B., Sahu, D., Bardalez Gagliuffi, D., Magain, P. and Queloz, D. (2016). Temperate Earth-sized planets transiting a nearby ultracool dwarf star. Nature, 533(7602), pp.221-224.

Gordon, I. E., Rothman, L. S., Hill, C. (2017). The HITRAN2016 Molecular Spectroscopic Database. Journal of Quantitative Spectroscopy and Radiative Transfer, 203, pp: 3-69.

Grenfell, J.L., Stracke, B., von Paris, P., et al. (2007). The response of atmospheric chemistry on earthlike planets around F, G and K Stars to small variations in orbital distance. Planet Space Sci, 55:661–671.

Grimm, S, Demory, B.-O., Gillon, M., Dorn, C., Agol, E., Burdanov, A., Delrez, L., et al. (2018). The nature of the TRAPPIST-1 exoplanets. Astronomy & Astrophysics, 613, A68

Hall, A. and Kaufmann, M. (1975). Stomatal Response to Environment with Sesamum indicum. L. Plant Physiology, 55(3), pp.455-459.

Hamilton, J. T. G., McRoberts, W. C., Keppler, F., Kalin, R. M., and Harper, D. B. (2003). Chloride methylation by plant pectin: an efficient environmentally significant process. Science, 301:206–209.

Harper, D. B. (1985). Halomethane from halide ion—a highly efficient fungal conversion of environmental significance. Nature, 315:55–57.

Hitchcock, D. R. and Lovelock, J. E. (1967). Life detection by atmospheric analysis. Icarus, 7:149–159.

Huang, S. -S. (1959) The problem of life in the universe and the mode of star formation. PASP 71: 421-424

ISO. (1975). Standard Atmosphere. Ref. No. ISO 2533-1975

Khalil, M. and Rasmussen, R. (1983). Sources, sinks, and seasonal cycles of atmospheric methane. Journal of Geophysical Research: Oceans, 88(C9), pp.5131-5144.

Kaltenegger, L. (2017). How to Characterize Habitable Worlds and Signs of Life. Annual Review of Astronomy and Astrophysics, 55(1), pp.433-485.

Kasper, M., Beuzit, J-L., Verinaud, C. et al. (2010). EPICS: direct imaging of exoplanets with the E-ELT. SPIE 7735, 84

Kasting, J. F., Whitmire, D. P., and Reynolds, R. T. (1993). Habitable zones around main sequence stars. Icarus, 101, pp.108-128

Kasting, J.F. (2001). Earth history: the rise of atmospheric oxygen. Science 293:819–820.

Kasting, J., Kopparapu, R., Ramirez, R. and Harman, C. (2013). Remote life-detection criteria, habitable zone boundaries, and the frequency of Earth-like planets around M and late K stars. Proceedings of the National Academy of Sciences, 111(35), pp.12641-12646.

Keeling, C., Chin, J. and Whorf, T. (1996). Increased activity of northern vegetation inferred from atmospheric CO2 measurements. Nature, 382(6587), pp.146-149.

Keppler, F., Eiden, R., Niedan, V., Pracht, J., and Scholer, H. F. (2000). Halocarbons produced by natural oxidation processes during degradation of organic matter. Nature, 403:298–301.

Khalil, M. A. K. and Rasmussen, R. A. (1999). Atmospheric methyl chloride. Atmos Environ, 33:1305–1321.

Kleidon, A. (2012). How does the Earth system generate and maintain thermodynamic disequilibrium and what does it imply for the future of the planet?. Philosophical Transactions of the Royal Society A: Mathematical, Physical and Engineering Sciences, 370(1962), pp.1012-1040.

Kochanov, R., Gordon, I., Rothman, L., Wcisło, P., Hill, C. and Wilzewski, J. (2016). HITRAN Application Programming Interface (HAPI): A comprehensive approach to working with spectroscopic data. Journal of Quantitative Spectroscopy and Radiative Transfer, 177, pp.15-30.

Kohn, M. P., Castaldi, M. J., and Farrauto, R. J. (2014), Biogas reforming for syngas production: the effect of methyl chloride. Applied Catalysis B: Environmental, 144:353–361

Kopparapu, R., Ramirez, R., Kasting, J., Eymet, V., Robinson, T., Mahadevan, S., Terrien, R., Domagal-Goldman, S., Meadows, V. and Deshpande, R. (2013). HABITABLE ZONES AROUND MAIN-SEQUENCE STARS: NEW ESTIMATES. The Astrophysical Journal, 765(2), p.131.

Krissansen-Totton, J., Garland, R., Irwin, P. and Catling, D. (2018). Detectability of Biosignatures in Anoxic Atmospheres with the James Webb Space Telescope: A TRAPPIST-1e Case Study. The Astronomical Journal, 156(3), p.114.

Kreidberg, L. (2017). Exoplanet Atmosphere Measurements from Transmission Spectroscopy and other Planet-Star Combined Light Observations. Handbook of Exoplanets, eds. Hans J. Deeg and Juan Antonio Belmonte (Springer-Verlag).

Lederberg, J. (1965). Signs of Life: Criterion-System of Exobiology. Nature, 207(4992), pp.9-13.

Léger, A., Pirre, M., and Marceau, F. J. (1993). Search for primitive life on a distant planet: relevance of O2 and O3 detections. Astron Astrophys 277:309.

Léger, A., Fontecave, M., Labeyrie, A., Samuel, B., Demangeon, O., and Valencia, D. (2011). Is the presence of oxygen on an exoplanet a reliable biosignature? Astrobiology 11:335–341.

Levine, J. S., Hughes, R. E., Chameides, W. L., and Howell, W. E. (1979). N2O and CO production by electric discharge: atmospheric implications. Geophys Res Lett, 6:557–559.

Lippincott, E., Eck, R., Dayhoff, M. and Sagan, C. (1967). Thermodynamic Equilibria in Planetary Atmospheres. The Astrophysical Journal, 147, p.753.

Lobert, J. M., Keene, W. C., Logan, J. A., and Yevich, R. (1999). Global chlorine emissions from biomass burning: reactive Chlorine Emissions Inventory. J Geophys Res Atmos, 104:8373–8389.

Lovelock, J. (1965). A Physical Basis for Life Detection Experiments. Nature, 207(4997), pp.568-570.

Lovelock, J. (1975). Thermodynamics and the recognition of alien biospheres. Proceedings of the Royal Society of London. Series B. Biological Sciences, 189(1095), pp.167-181.

Lovis, C. and Fischer, D., Radial Velocity, Yale University Press, 2010.

Luger, R. and Barnes, R. (2015). Extreme Water Loss and Abiotic O2 Buildup on Planets Throughout the Habitable Zones of M Dwarfs. Astrobiology, 15(2), pp.119-143.

Lyons, T., Reinhard, C. and Planavsky, N. (2014). The rise of oxygen in Earth's early ocean and atmosphere. Nature, 506(7488), pp.307-315.

Maiolino, R., Haehnelt, M., Murphy, M. T. et al. (2013). A Community Science Case for E-ELT HIRES. arXiv:1310.3163

Mayor, M. and Queloz, D. (1995). A Jupiter-mass companion to a solar-type star. Nature, 378(6555), pp.355-359.

Meadows, V.S. (2006). Modelling the diversity of extrasolar terrestrial planets. Proc Int Astron Union 1:25.

Meadows, V.S. (2008). Planetary environmental signatures for habitability and life. In: Exoplanets, edited by J.W. Mason, Springer Berlin Heidelberg, Berlin, Heidelberg, pp 259–284.

Meadows, V. and Seager, S. (2010). Terrestrial Planet Atmospheres and Biosignatures. Exoplanets, edited by S. Seager. Tucson, AZ: University of Arizona Press, 526 pp. ISBN 978-0-8165-2945-2., p.441-470.

, v. S., Reinhard, C. T., Arney, G. N. et al. (2018). Exoplanet Biosignatures: Understanding Oxygen as a Biosignature in the Context of Its Environment. Astrobiology, 18(6).

Ment, K., Dittmann, J., Astudillo-Defru, N., et al. (2019). A Second Terrestrial Planet Orbiting the Nearby M Dwarf LHS 1140. The Astronomical Journal, 157(1), p.32.

Myhre, G., Shindell, D., Breon, F.-M., et al. (2013). Anthropogenic and natural radiative forcing. In Climate Change 2013—The Physical Science Basis, edited by Intergovernmental Panel on Climate Change (Ed.), Cambridge University Press, Cambridge, pp 659–740.

Pallé, E., Osorio, M., Barrena, R., Montañés-Rodríguez, P. and Martín, E. (2009). Earth's transmission spectrum from lunar eclipse observations. Nature, 459(7248), pp.814-816.

PHL. (2019). The Habitable Exoplanets Catalog - Planetary Habitability Laboratory @ UPR Arecibo. [online] Available at: http://phl.upr.edu/projects/habitable-exoplanets-catalog [Accessed 24 Jun. 2019].

Pierrehumbert, R. and Gaidos, E. (2011). Hydrogen Greenhouse Planets Beyond The Habitable Zone. The Astrophysical Journal, 734(1), p.L13.

Pilcher, C. B. (2003). Biosignatures of early earths. Astrobiology, 3:471–486.

Quanz, S., Amara, A., Meyer, M., Girard, J., Kenworthy, M. and Kasper, M. (2015). CONFIRMATION AND CHARACTERIZATION OF THE PROTOPLANET HD 100546 b—DIRECT EVIDENCE FOR GAS GIANT PLANET FORMATION AT 50 AU. The Astrophysical Journal, 807(1), p.64.

Quintana, E. V., Barclay, T., Raymond, S. N. et al. (2014). An Earth-sized planet in the habitable zone of a cool star. Science 344(6181):277–280 .

Ragsdale, S. W. (2004). Life with carbon monoxide. Crit. Rev. Biochem. Mol. Biol., 39, 165.

Rasmussen, R. A. (1974). Emission of biogenic hydrogen sulfide. Tellus, 26:254–260.

Rauer, H., Gebauer, S., Paris, P., Cabrera, J., Godolt, M., Grenfell, J., Belu, A., Selsis, F., Hedelt, P. and Schreier, F. (2011). Potential biosignatures in super-Earth atmospheres. Astronomy & Astrophysics, 529, p.A8.

Reinhard, C., Olson, S., Schwieterman, E. and Lyons, T. (2017). False Negatives for Remote Life Detection on Ocean-Bearing Planets: Lessons from the Early Earth. Astrobiology, 17(4), pp.287-297.

Rhew, R. C., Whelan, M. E., and Min, D. H. (2014). Large methyl halide emissions from south Texas salt marshes. Biogeosciences, 11:6427–6434.

Ricker G. R., Winn J. N., Vanderspek R. et al. (2015) Transiting Exoplanet Survey Satellite, J. Astron. Telesc. Instrum. Syst., 1(1), 014003.

Riding, R., Fralick, P., and Liang, L. (2014). Identification of an Archean marine oxygen oasis. Precambrian Res 251:232–237

Roberson, A .L., Roadt, J., Halevy, I., and Kasting, J. F. (2011). Greenhouse warming by nitrous oxide and methane in the Proterozoic Eon. Geobiology, 9:313–320.

Rodler, F. and López-Morales, M. (2014). Feasibility studies for the detection of O2 in an Earth-like exoplanet. The Astrophysical Journal, 781(1), p.54.

Rugheimer, S., Kaltenegger, L., Zsom, A., Segura, A. and Sasselov, D. (2013). Spectral Fingerprints of Earth-like Planets Around FGK Stars. Astrobiology, 13(3), pp.251-269.

Rugheimer, S., Segura, A., Kaltenegger, L., and Sasselov, D. (2015). UV surface environment of Earth-like planets orbiting FGKM stars through geological evolution. Astrophysical Journal, 806:137.

Sagan, C., Thompson, W., Carlson, R., Gurnett, D. and Hord, C. (1993). A search for life on Earth from the Galileo spacecraft. Nature, 365(6448), pp.715-721.

Saini, H. S., Attieh, J. M., and Hanson, A. D. (1995). Biosynthesis of halomethanes and methanethiol by higher-plants via a novel methyltransferase reaction. Plant Cell Environ, 18: 1027–1033.

Saito, T. and Yokouchi, Y. (2006). Diurnal variation in methyl halide emission rates from tropical ferns. Atmos Environ, 40:2806–2811.

Samarkin, V. A., Madigan, M. T., Bowles, M. W. et al. (2010). Abiotic nitrous oxide emission from the hypersaline Don Juan Pond in Antarctica. Nat Geosci, 3:341–344.

Sarkis, P., Henning, T., Kürster, M. et al. (2018). The CARMENES Search for Exoplanets around M Dwarfs: A Low-mass Planet in the Temperate Zone of the Nearby K2-18. The Astronomical Journal, 155(6), p.257.

Schiaparelli, G. V. Considerazioni sul Moto Rotatorio del Pianeta Venere. Memorie della Societa Degli Spettroscopisti Italiani, 19:220–221, 1891.

Schulze-Makuch, D. and Irwin, L. (2006). The prospect of alien life in exotic forms on other worlds. Naturwissenschaften, 93(4), pp.155-172.

Schulze-Makuch, D., Méndez, A., Fairén, A., von Paris, P., Turse, C., Boyer, G., Davila, A., António, M., Catling, D. and Irwin, L. (2011). A Two-Tiered Approach to Assessing the Habitability of Exoplanets. Astrobiology, 11(10), pp.1041-1052.

Schwandner, F., Seward, T., Gize, A., Hall, P. and Dietrich, V. (2004). Diffuse emission of organic trace gases from the flank and crater of a quiescent active volcano (Vulcano, Aeolian Islands, Italy). Journal of Geophysical Research: Atmospheres, 109(D4).

Schwieterman, E. W. (2018). Surface and temporal biosignatures. Handbook of Exoplanets, ISBN 978-3-319-55332-0. Springer International Publishing AG, part of Springer Nature, id.69

Schwieterman, E., Kiang, N., Parenteau, M., Harman, C., DasSarma, S., Fisher, T., Arney, G., Hartnett, H., Reinhard, C., Olson, S., Meadows, V., Cockell, C., Walker, S., Grenfell, J., Hegde, S., Rugheimer, S., Hu, R. and Lyons, T. (2018). Exoplanet Biosignatures: A Review of Remotely Detectable Signs of Life. Astrobiology, 18(6), pp.663-708.

Schwieterman, E., Reinhard, C., Olson, S., Ozaki, K., Harman, C., Hong, P. and Lyons, T. (2019). Rethinking CO Antibiosignatures in the Search for Life Beyond the Solar System. The Astrophysical Journal, 874(1), p.9.

Seager, S., Turner, E., Schafer, J. and Ford, E. (2005). Vegetation's Red Edge: A Possible Spectroscopic Biosignature of Extraterrestrial Plants. Astrobiology, 5(3), pp.372-390.

Seager, S. and Deming, D. (2010). Exoplanet Atmospheres. Annual Review of Astronomy and Astrophysics, 48(1), pp.631-672.

Seager, S., Bains, W. and Hu, R. (2013). Biosignature Gases in H2-dominated Atmospheres On Rocky Exoplanets. The Astrophysical Journal, 777(2), p.95.

Seager, S., Bains, W. and Petkowski, J. (2016). Toward a List of Molecules as Potential Biosignature Gases for the Search for Life on Exoplanets and Applications to Terrestrial Biochemistry. Astrobiology, 16(6), pp.465-485.

Segura, A., Kasting, J., Meadows, V., Cohen, M., Scalo, J., Crisp, D., Butler, R. and Tinetti, G. (2005). Biosignatures from Earth-Like Planets Around M Dwarfs. Astrobiology, 5(6), pp.706-725.

Singh, H. B., Salas, L. J., and Stiles, R. E. (1983). Methyl halides in and over the eastern Pacific (40-degrees-N-32-degrees-S). J Geophys Res Oceans Atmos, 88:3684–3690.

Serindag, D. and Snellen, I. (2019). Testing the Detectability of Extraterrestrial O2 with the Extremely Large Telescopes Using Real Data with Real Noise. The Astrophysical Journal, 871(1), p.L7.

Snellen, I., de Kok, R., le Poole, R., Brogi, M. and Birkby, J. (2013). FINDING EXTRATERRESTRIAL LIFE USING GROUND-BASED HIGH-DISPERSION SPECTROSCOPY. The Astrophysical Journal, 764(2), p.182.

Snellen, I., de Kok, R., Birkby, J., Brandl, B., Brogi, M., Keller, C., Kenworthy, M., Schwarz, H. and Stuik, R. (2015). Combining high-dispersion spectroscopy with high contrast imaging: Probing rocky planets around our nearest neighbors. Astronomy & Astrophysics, 576, p.A59.

Sparks, W., Hough, J., Germer, T. A., et al. (2009). Detection of circular polarization in light scattered from photosynthetic microbes. Proceedings of the National Academy of Sciences, 106 (19), 7816-7821

Stathopoulou, E., Mihalakakou, G., Santamouris, M. and Bagiorgas, H. (2008). On the impact of temperature on tropospheric ozone concentration levels in urban environments. Journal of Earth System Science, 117(3), pp.227-236.

Stevenson, D. J. (1999). Life-sustaining planets in interstellar space?. Nature, 400, 32.

Thornton, B. F., Horst, A., Carrizo, D., and Holmstrand, H. (2016). Methyl chloride and methyl bromide emissions from baking: an unrecognized anthropogenic source. Sci Total Environ, 551-552:327–333.

Tinetti, G., Cash, W. C., Glassman, T. M. et al. (2009). Characterization of Extra-Solar Planets with Direct-Imaging Techniques. Science White Paper Submitted to Astro2010.

Traub, W. A. and Oppenheimer, B. R. (2010). Direct Imaging of Exoplanets. Exoplanets, edited by S. Seager. Tucson, AZ: University of Arizona Press, 2010, 526 pp. ISBN 978-0-8165-2945-2., p.111-156

Turnbull, M., Traub, W., Jucks, K., et al. (2006). Spectrum of a Habitable World: Earthshine in the Near-Infrared. The Astrophysical Journal, 644(1), pp.551-559.

Vogt, S. S., Radovan, M., Kibrick, R. et al. (2014). APF - The Lick Observatory Automated Planet Finder. Publications of the Astronomical Society of the Pacific, 126, 938, pp. 359-379

Walker, S.I. and Davies, P.C.W. (2013). The algorithmic origins of life. J R Soc Interface 10:20120869

Watling, R. and Harper, D. B. (1998). Chloromethane production by wood-rotting fungi and an estimate of the global flux to the atmosphere. Mycol Res, 102:769–787.

Wolf, E. (2017). Assessing the Habitability of the TRAPPIST-1 System Using a 3D Climate Model. The Astrophysical Journal, 839(1), p.L1.

Wolszczan, A. and Frail, D. (1992). A planetary system around the millisecond pulsar PSR1257 + 12. Nature, 355(6356), pp.145-147.

Woolf, N., Smith, P., Traub, W. and Jucks, K. (2002). The Spectrum of Earthshine: A Pale Blue Dot Observed from the Ground. The Astrophysical Journal, 574(1), pp.430-433.

Yokouchi, Y., Ikeda, M., Inuzuka, Y., and Yukawa, T. (2002). Strong emission of methyl chloride from tropical plants. Nature, 416:163–165.

Zhao, F. and Zeng, N. (2014). Continued increase in atmospheric CO2; seasonal amplitude in the 21st century projected by the CMIP5 Earth system models. Earth System Dynamics, 5(2), pp.423-439.

Appendix 1

Trappist-1 d: HIRES

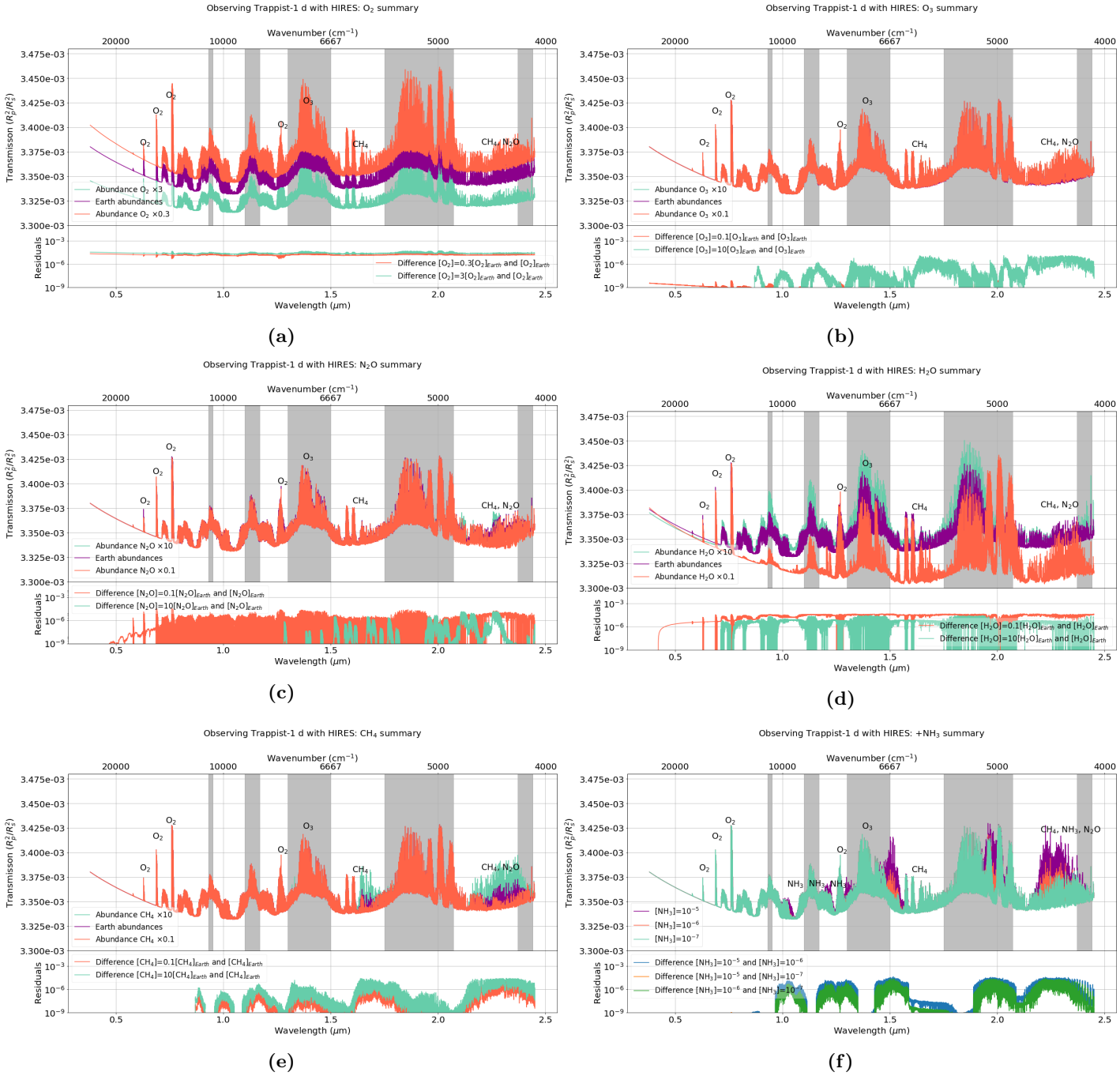

Figure 1: Results of changing the abundances by a factor 10 assuming mixing ratios of molecules with vertical distribution as of present day Earth's atmosphere (see Fig. (4.25)). Synthetic reflection spectra of Trappist-1 d pc are presented. The synthetic reflection spectra as modelled for HIRES contain each 3 spectra: one for an Earth-like abundance (purple), one with a factor times more of the gas (blue), and one with a factor less of the gas (orange). Methyl chloride, ammonia, and ethane, gases not present in more than trace amount in the Earth's atmosphere, abundances of 10^{-5} (puple), 10^{-6} (orange), and 10^{-7} (blue) per unit volume are assumed. The gases for which the abundances are changed are (a) ozone, (b) nitrous oxide, (c) water, (d) methane, (e) methyl chloride, (f) ammonia, and (g) ethane.

Trappist-1 e: HIRES

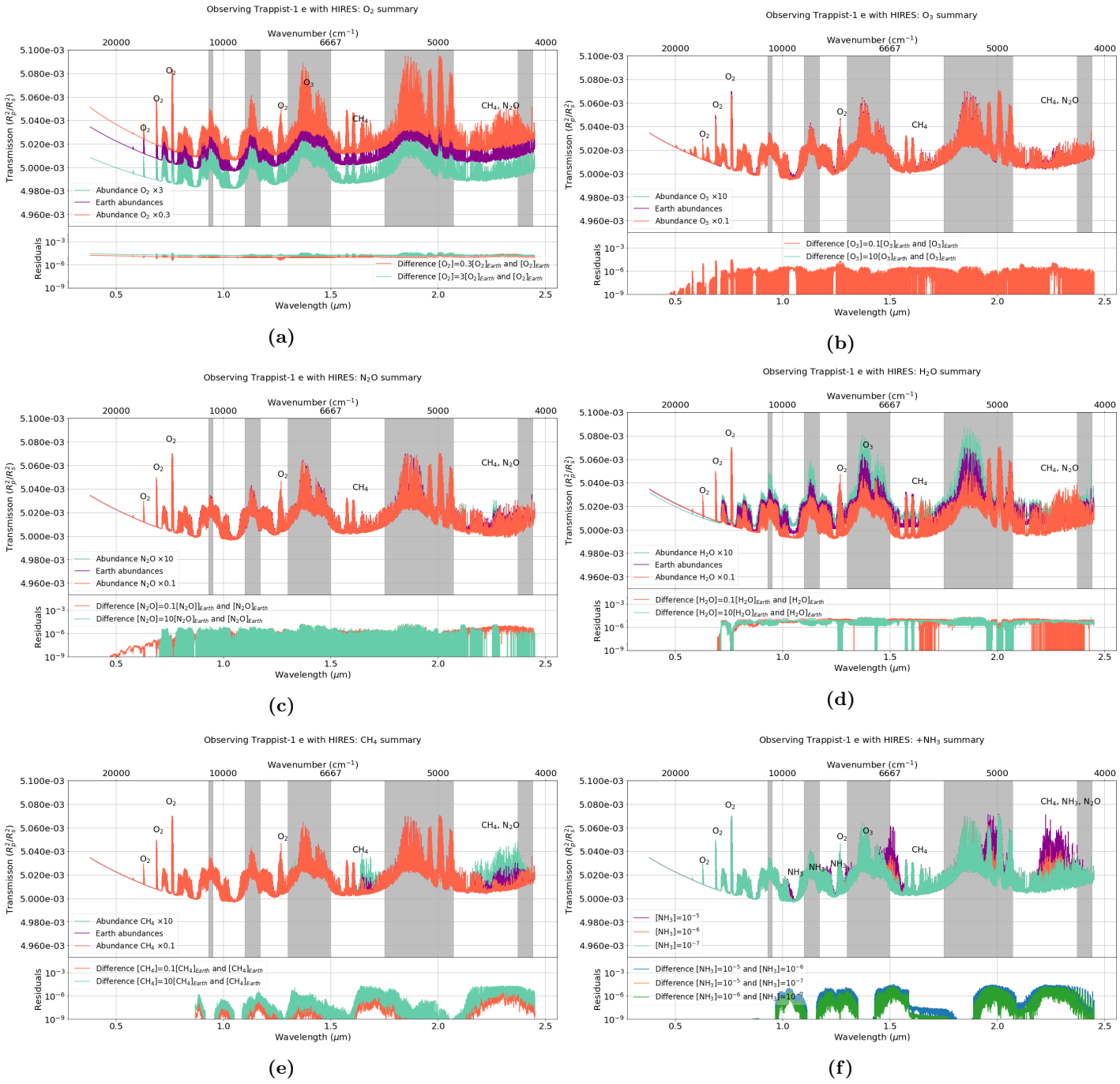

Figure 2: Results of changing the abundances by a factor 10 assuming mixing ratios of molecules with vertical distribution as of present day Earth's atmosphere (see Fig. (4.25)). Synthetic reflection spectra of an Earth-Sun analogue at a distance of 10 pc are presented where it is assumed that the surface temperature is 288 K, that the temperature increases with altitude in the statosphere (i.e. with a temperature inversion), and that the pressure drops exponentially with altitude. The synthetic reflection spectra as modelled for HIRES contain each 3 spectra: one for an Earth-like abundance (purple), one with a factor times more of the gas (blue), and one with a factor less of the gas (orange). Methyl chloride, ammonia, and ethane, gases not present in more than trace amount in the Earth's atmosphere, abundances of 10^{-5} (puple), 10^{-6} (orange), and 10^{-7} (blue) per unit volume are assumed. The gases for which the abundances are changed are (a) ozone, (b) nitrous oxide, (c) water, (d) methane, (e) methyl chloride, (f) ammonia, and (g) ethane.

Trappist-1 f: HIRES

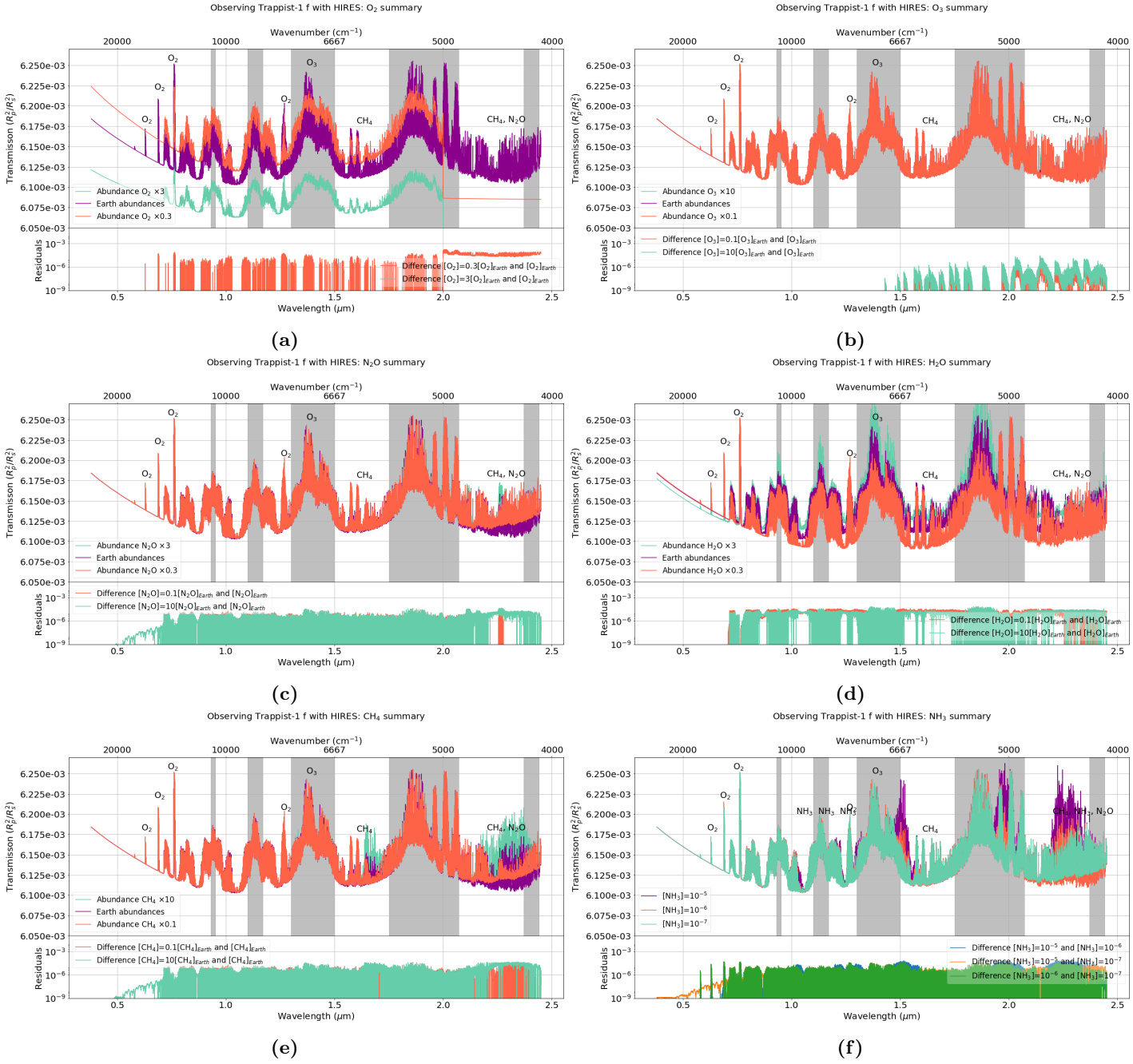

Figure 3: Results of changing the abundances by a factor 10 assuming mixing ratios of molecules with vertical distribution as of present day Earth's atmosphere (see Fig. (4.25)). Synthetic reflection spectra of an Earth-Sun analogue at a distance of 10 pc are presented where it is assumed that the surface temperature is 288 K, that the temperature increases with altitude in the statosphere (i.e. with a temperature inversion), and that the pressure drops exponentially with altitude. The synthetic reflection spectra as modelled for HIRES contain each 3 spectra: one for an Earth-like abundance (purple), one with a factor times more of the gas (blue), and one with a factor less of the gas (orange). Methyl chloride, ammonia, and ethane, gases not present in more than trace amount in the Earth's atmosphere, abundances of 10^{-5} (puple), 10^{-6} (orange), and 10^{-7} (blue) per unit volume are assumed. The gases for which the abundances are changed are (a) ozone, (b) nitrous oxide, (c) water, (d) methane, (e) methyl chloride, (f) ammonia, and (g) ethane.

Trappist-1 g: HIRES

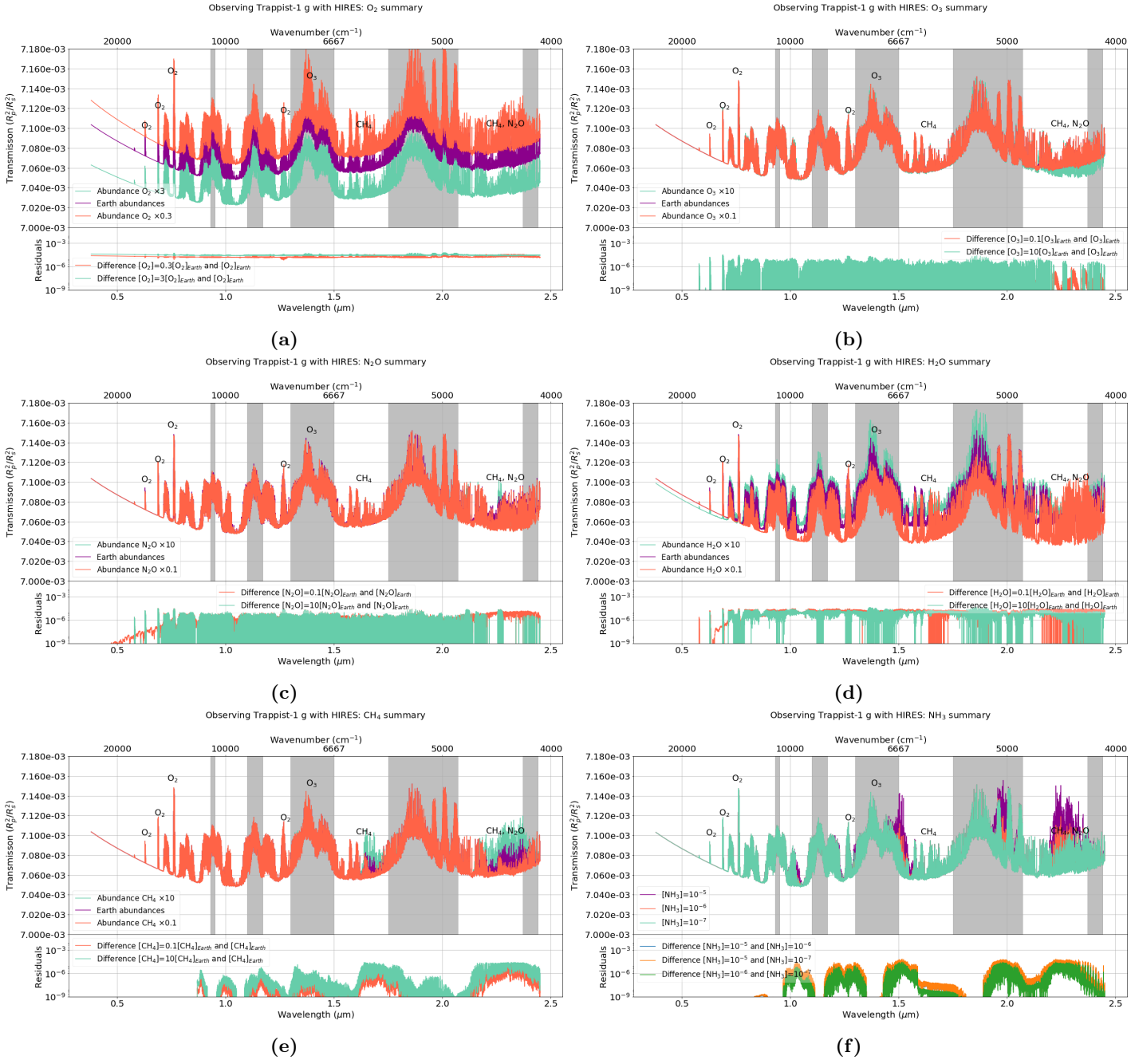

Figure 4: Results of changing the abundances by a factor 10 assuming mixing ratios of molecules with vertical distribution as of present day Earth's atmosphere (see Fig. (4.25)). Synthetic reflection spectra of an Earth-Sun analogue at a distance of 10 pc are presented where it is assumed that the surface temperature is 288 K, that the temperature increases with altitude in the statosphere (i.e. with a temperature inversion), and that the pressure drops exponentially with altitude. The synthetic reflection spectra as modelled for HIRES contain each 3 spectra: one for an Earth-like abundance (purple), one with a factor times more of the gas (blue), and one with a factor less of the gas (orange). Methyl chloride, ammonia, and ethane, gases not present in more than trace amount in the Earth's atmosphere, abundances of 10^{-5} (puple), 10^{-6} (orange), and 10^{-7} (blue) per unit volume are assumed. The gases for which the abundances are changed are (a) ozone, (b) nitrous oxide, (c) water, (d) methane, (e) methyl chloride, (f) ammonia, and (g) ethane.

LHS 1140 b: HIRES

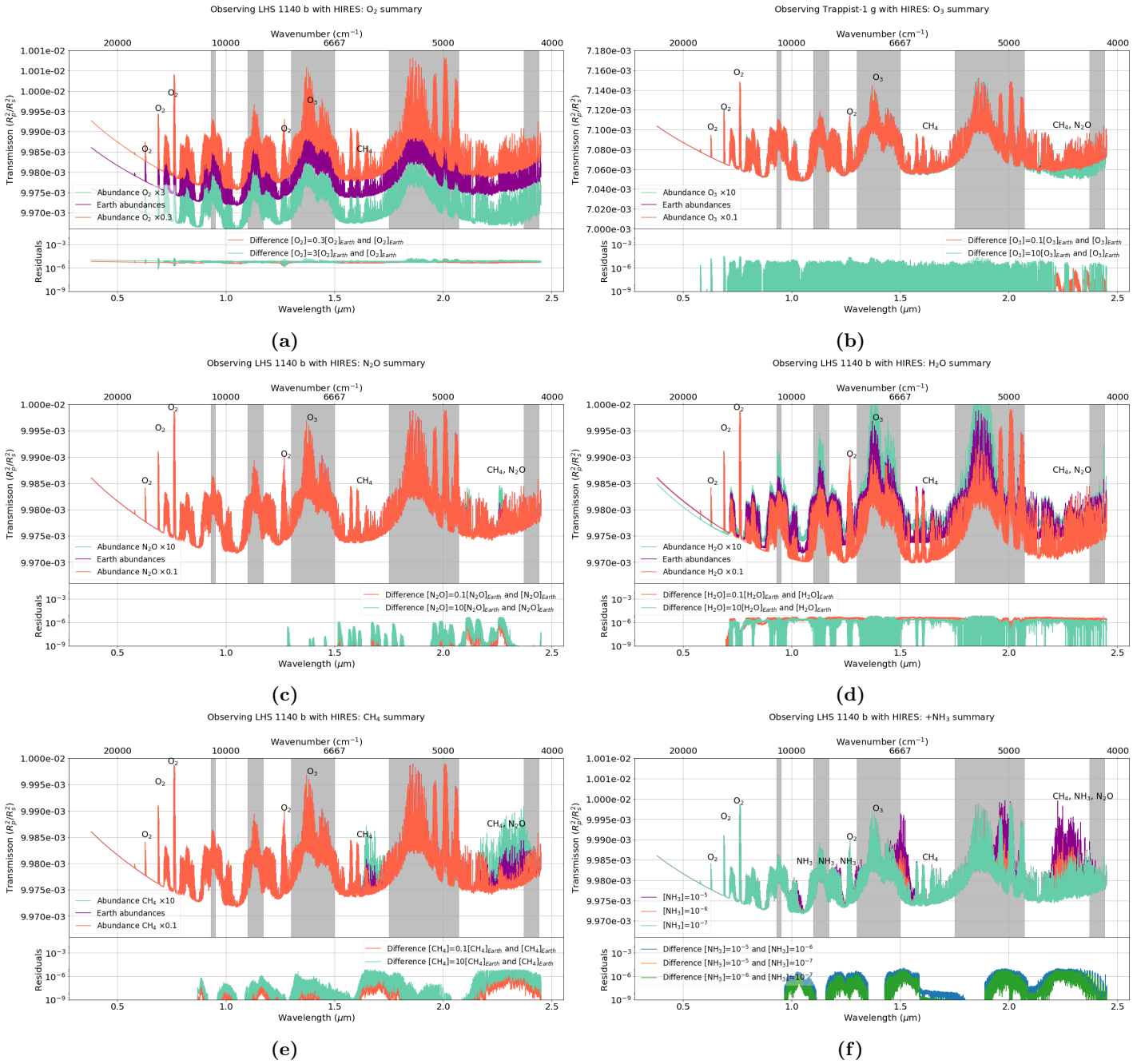

Figure 5: Results of changing the abundances by a factor 10 assuming mixing ratios of molecules with vertical distribution as of present day Earth's atmosphere (see Fig. (4.25)). Synthetic reflection spectra of an Earth-Sun analogue at a distance of 10 pc are presented where it is assumed that the surface temperature is 288 K, that the temperature increases with altitude in the statosphere (i.e. with a temperature inversion), and that the pressure drops exponentially with altitude. The synthetic reflection spectra as modelled for HIRES contain each 3 spectra: one for an Earth-like abundance (purple), one with a factor times more of the gas (blue), and one with a factor less of the gas (orange). Methyl chloride, ammonia, and ethane, gases not present in more than trace amount in the Earth's atmosphere, abundances of 10^{-5} (puple), 10^{-6} (orange), and 10^{-7} (blue) per unit volume are assumed. The gases for which the abundances are changed are (a) ozone, (b) nitrous oxide, (c) water, (d) methane, (e) methyl chloride, (f) ammonia, and (g) ethane.

K2-18 b: HIRES

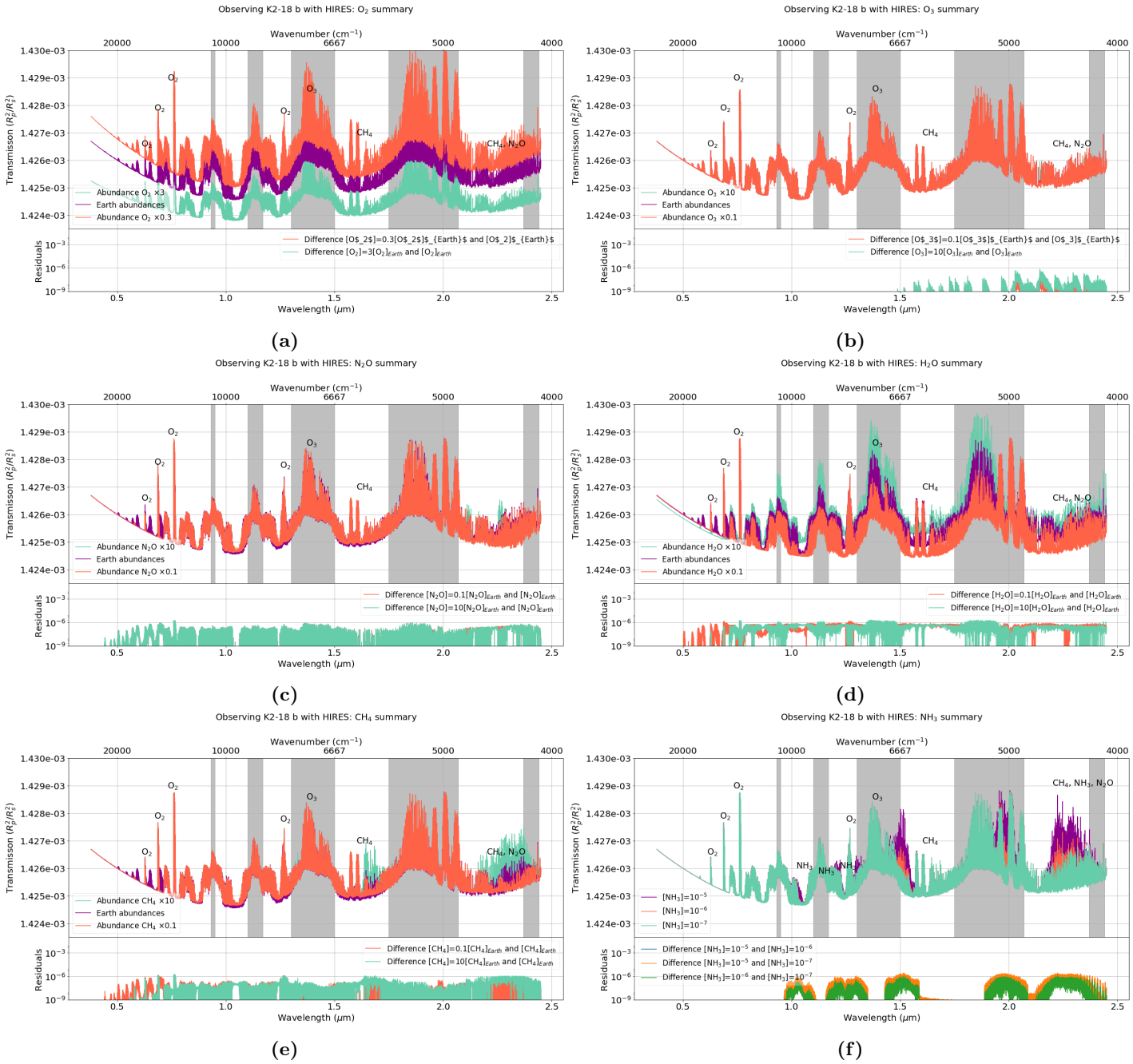

Figure 6: Results of changing the abundances by a factor 10 assuming mixing ratios of molecules with vertical distribution as of present day Earth's atmosphere (see Fig. (4.25)). Synthetic reflection spectra of an Earth-Sun analogue at a distance of 10 pc are presented where it is assumed that the surface temperature is 288 K, that the temperature increases with altitude in the statosphere (i.e. with a temperature inversion), and that the pressure drops exponentially with altitude. The synthetic reflection spectra as modelled for HIRES contain each 3 spectra: one for an Earth-like abundance (purple), one with a factor times more of the gas (blue), and one with a factor less of the gas (orange). Methyl chloride, ammonia, and ethane, gases not present in more than trace amount in the Earth's atmosphere, abundances of 10^{-5} (puple), 10^{-6} (orange), and 10^{-7} (blue) per unit volume are assumed. The gases for which the abundances are changed are (a) ozone, (b) nitrous oxide, (c) water, (d) methane, (e) methyl chloride, (f) ammonia, and (g) ethane.

Appendix 2

Trappist-1 d: METIS

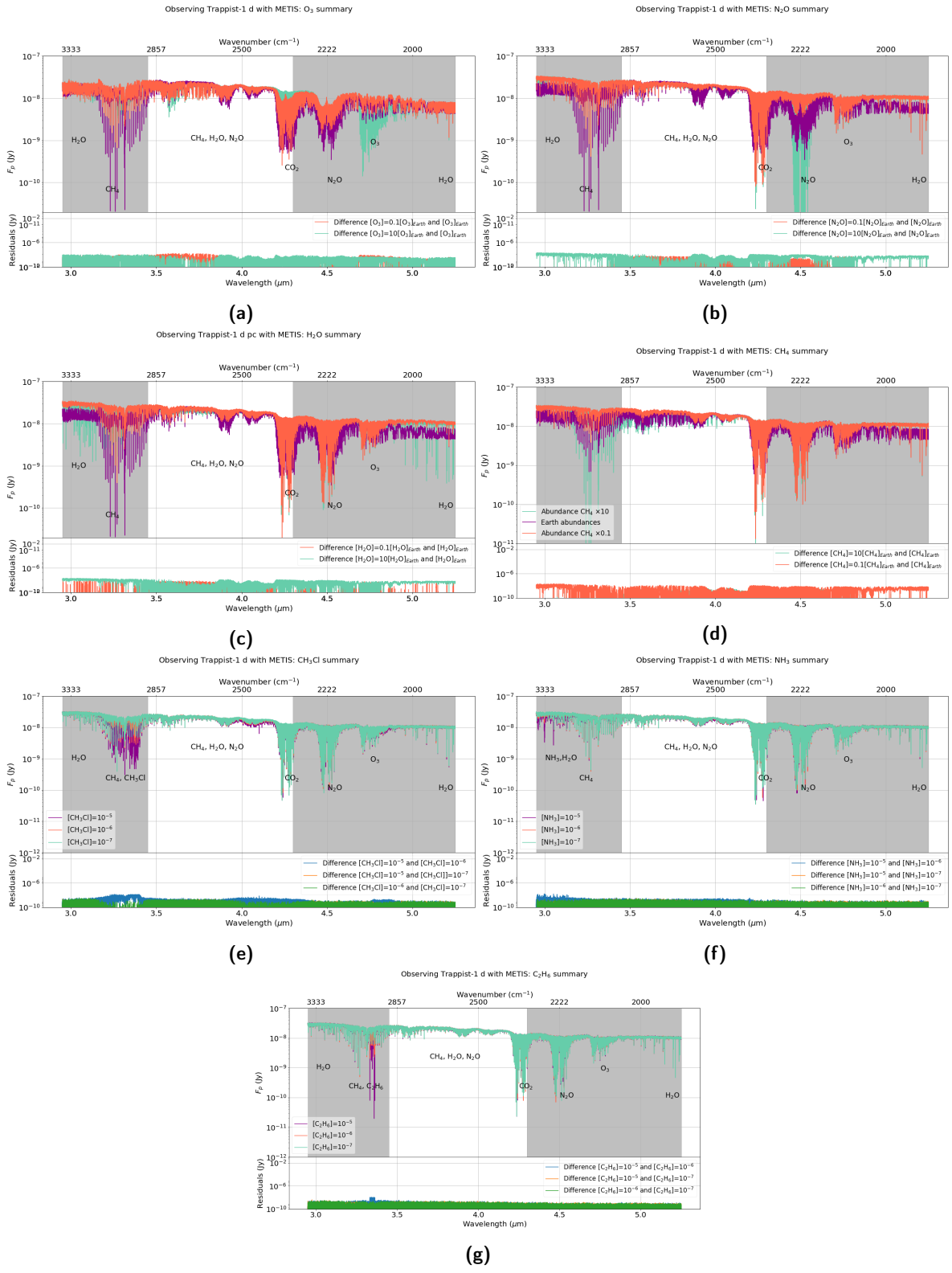

Figure 1: Synthetic reflection spectra of Trappist-1 d are presented. The synthetic reflection spectra as modelled for METIS contain each 3 spectra: one for an Earth-like abundance (purple), one with a factor times more of the gas (blue), and one with a factor less of the gas (orange). CH_3Cl, NH_3, and C_2H_6, gases not present in more than trace amount in the Earth's atmosphere, abundances of 10^{-5} (purple), 10^{-6} (orange), and 10^{-7} (blue) per unit volume are assumed. The gases for which the abundances are changed are (a) O_3, (b) N_2O, (c) H_2O, (d) CH_4 (e) CH_3Cl, (f) NH_3, and (g) C_2H_6.

Trappist-1 e: METIS

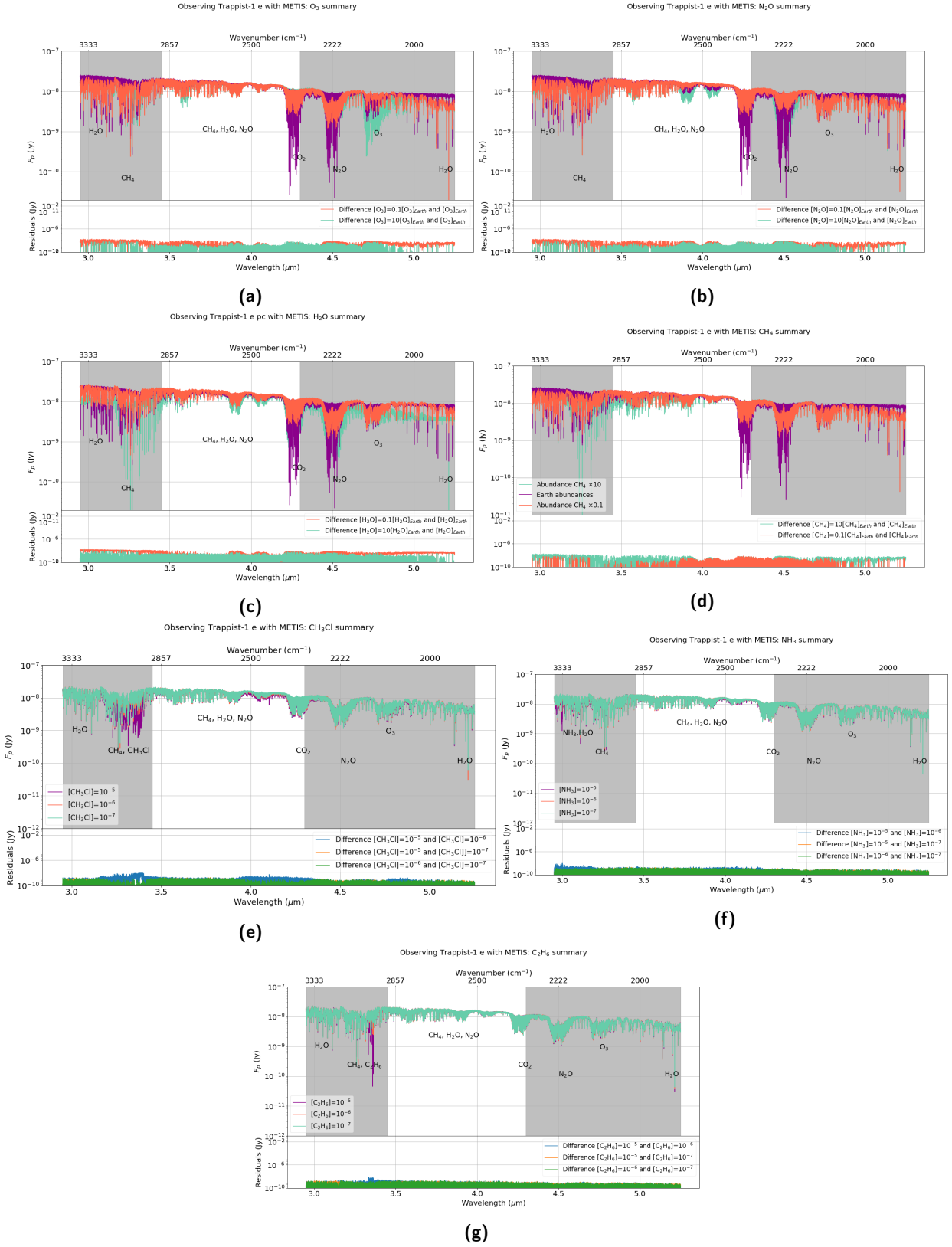

Figure 2: Synthetic reflection spectra of Trappist-1 e are presented. The synthetic reflection spectra as modelled for METIS contain each 3 spectra: one for an Earth-like abundance (purple), one with a factor times more of the gas (blue), and one with a factor less of the gas (orange). CH_3Cl, NH_3, and C_2H_6, gases not present in more than trace amount in the Earth's atmosphere, abundances of 10^{-5} (purple), 10^{-6} (orange), and 10^{-7} (blue) per unit volume are assumed. The gases for which the abundances are changed are (a) O_3, (b) N_2O, (c) H_2O, (d) CH_4 (e) CH_3Cl, (f) NH_3, and (g) C_2H_6.

Trappist-1 f: METIS

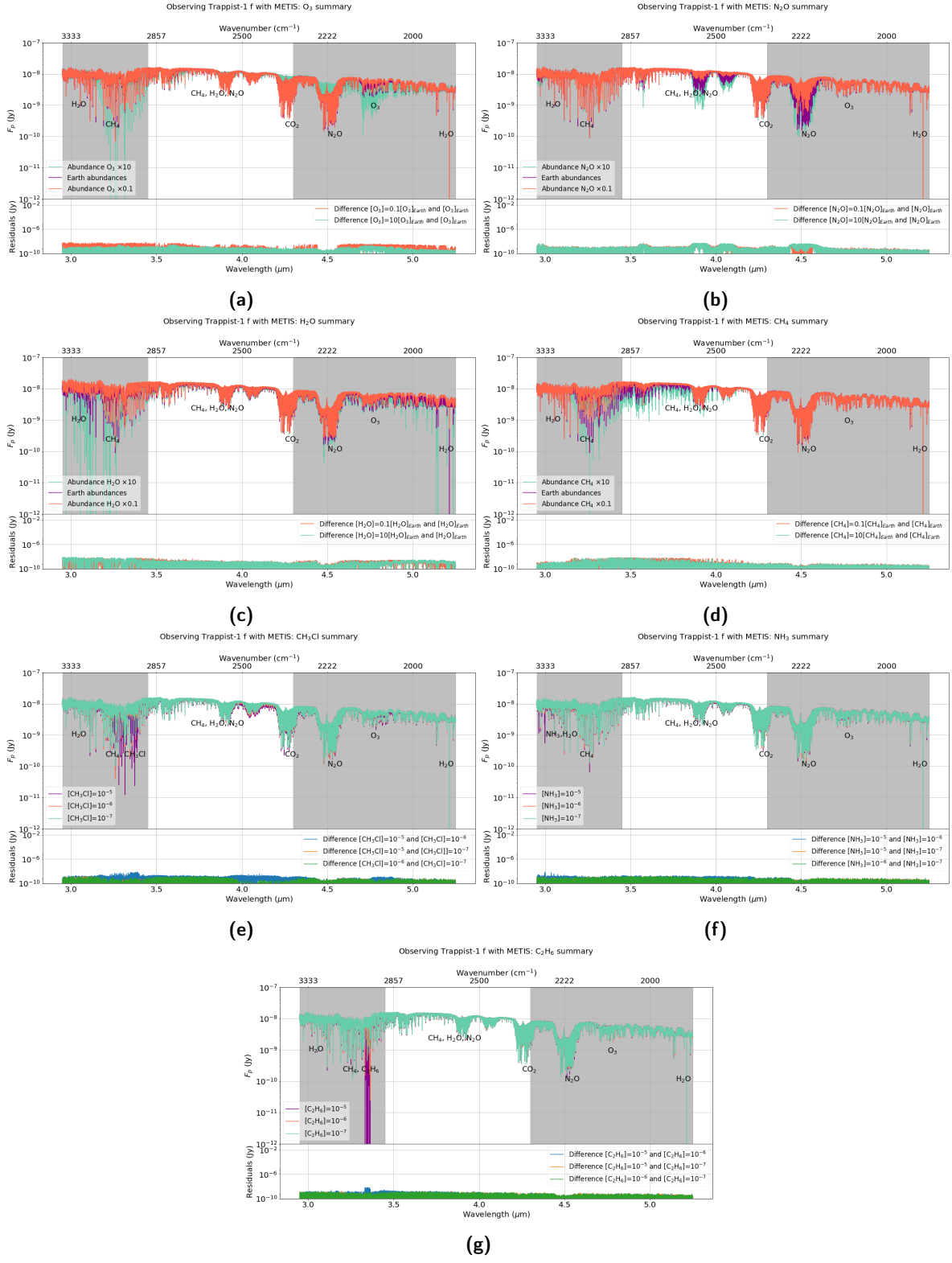

Figure 3: Synthetic reflection spectra of Trappist-1 f are presented. The synthetic reflection spectra as modelled for METIS contain each 3 spectra: one for an Earth-like abundance (purple), one with a factor times more of the gas (blue), and one with a factor less of the gas (orange). CH_3Cl, NH_3, and C_2H_6, gases not present in more than trace amount in the Earth's atmosphere, abundances of 10^{-5} (purple), 10^{-6} (orange), and 10^{-7} (blue) per unit volume are assumed. The gases for which the abundances are changed are (a) O_3, (b) N_2O, (c) H_2O, (d) CH_4 (e) CH_3Cl, (f) NH_3, and (g) C_2H_6.

Trappist-1 g: METIS

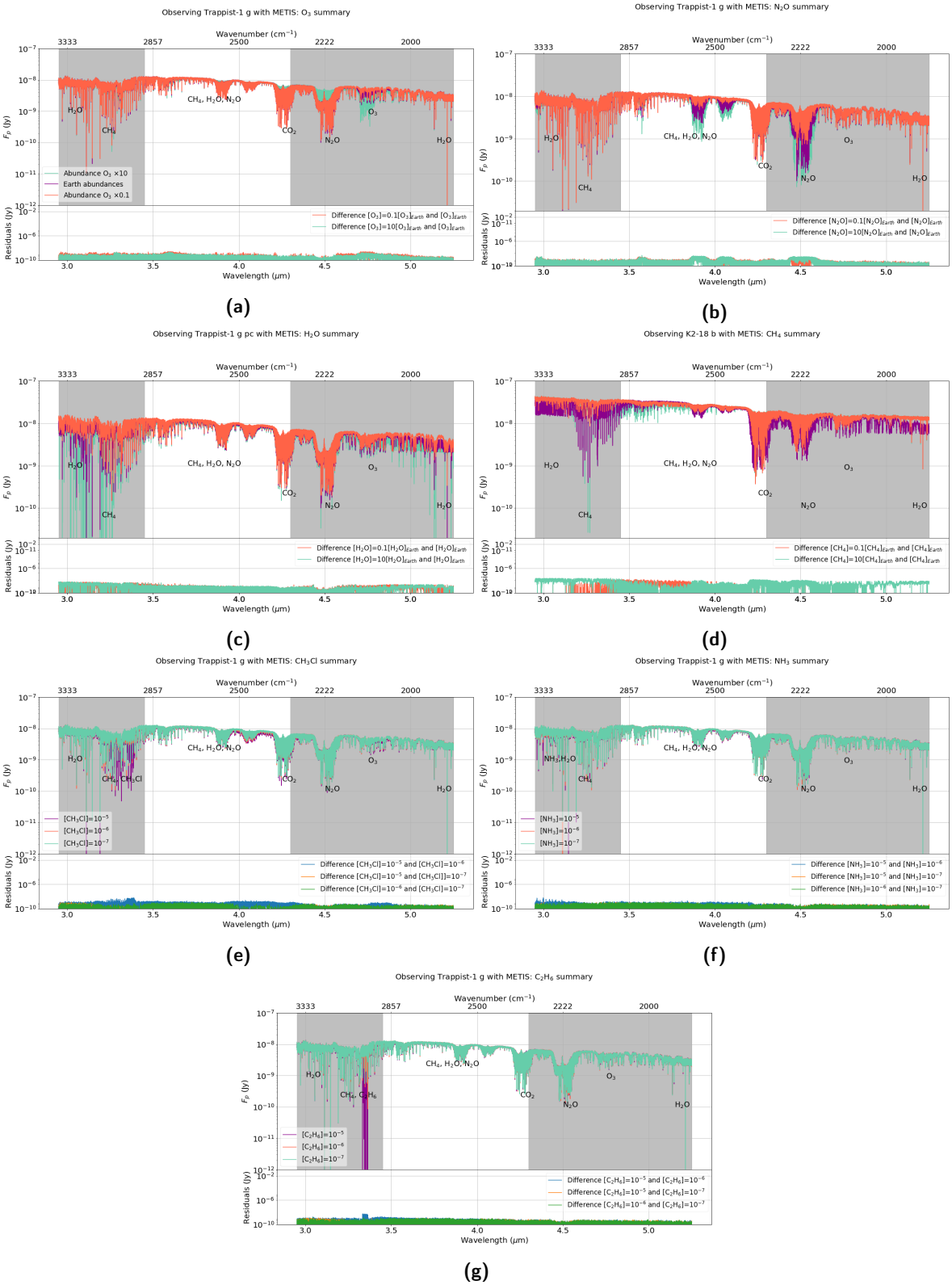

Figure 4: Synthetic reflection spectra of Trappist-1 g are presented. The synthetic reflection spectra as modelled for METIS contain each 3 spectra: one for an Earth-like abundance (purple), one with a factor times more of the gas (blue), and one with a factor less of the gas (orange). CH_3Cl, NH_3, and C_2H_6, gases not present in more than trace amount in the Earth's atmosphere, abundances of 10^{-5} (purple), 10^{-6} (orange), and 10^{-7} (blue) per unit volume are assumed. The gases for which the abundances are changed are (a) O_3, (b) N_2O, (c) H_2O, (d) CH_4 (e) CH_3Cl, (f) NH_3, and (g) C_2H_6.

LHS 1140 b: METIS

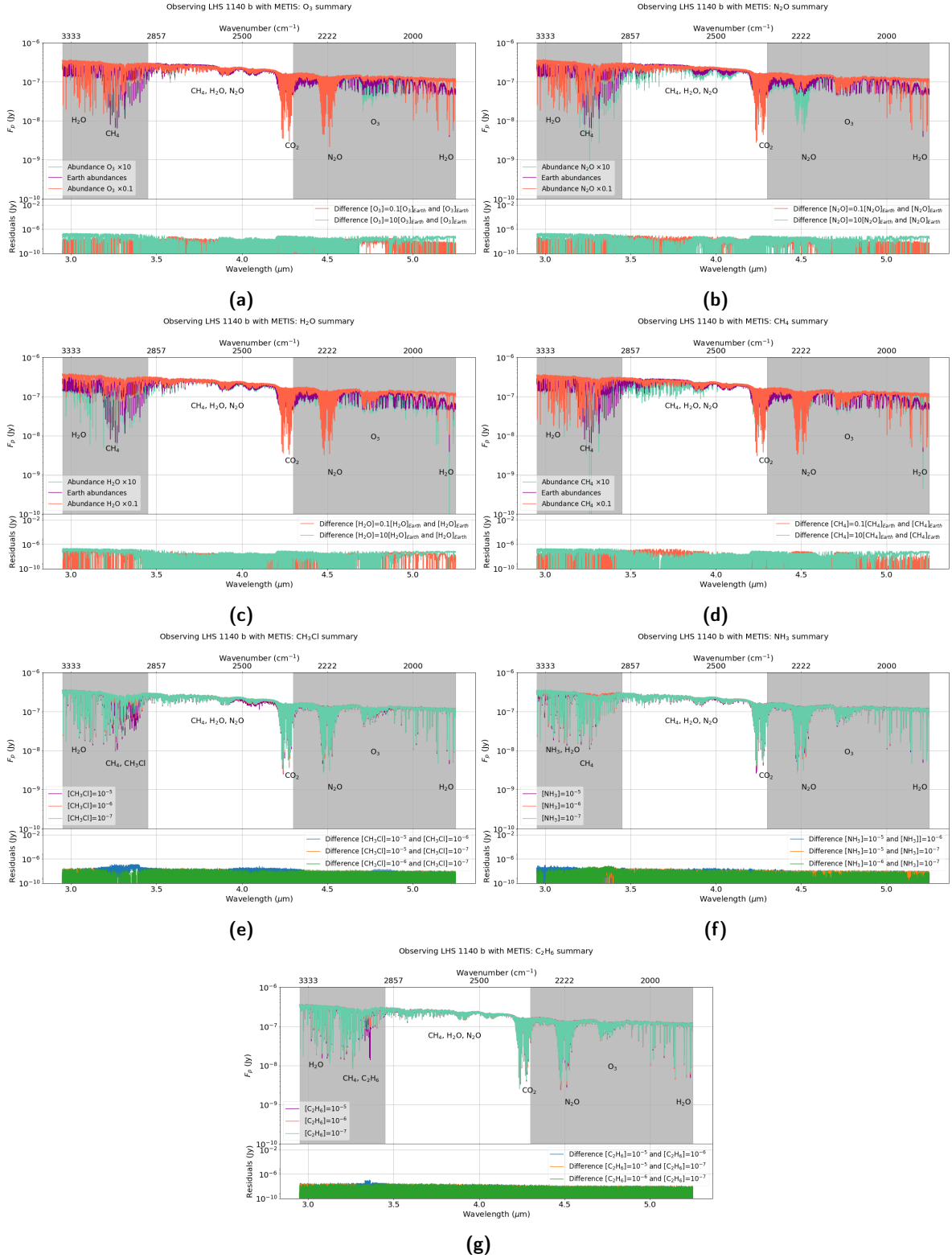

Figure 5: Synthetic reflection spectra of LHS 1140 b are presented. The synthetic reflection spectra as modelled for METIS contain each 3 spectra: one for an Earth-like abundance (purple), one with a factor times more of the gas (blue), and one with a factor less of the gas (orange). CH_3Cl, NH_3, and C_2H_6, gases not present in more than trace amount in the Earth's atmosphere, abundances of 10^{-5} (purple), 10^{-6} (orange), and 10^{-7} (blue) per unit volume are assumed. The gases for which the abundances are changed are (a) O_3, (b) N_2O, (c) H_2O, (d) CH_4 (e) CH_3Cl, (f) NH_3, and (g) C_2H_6.

K2-18 b: METIS

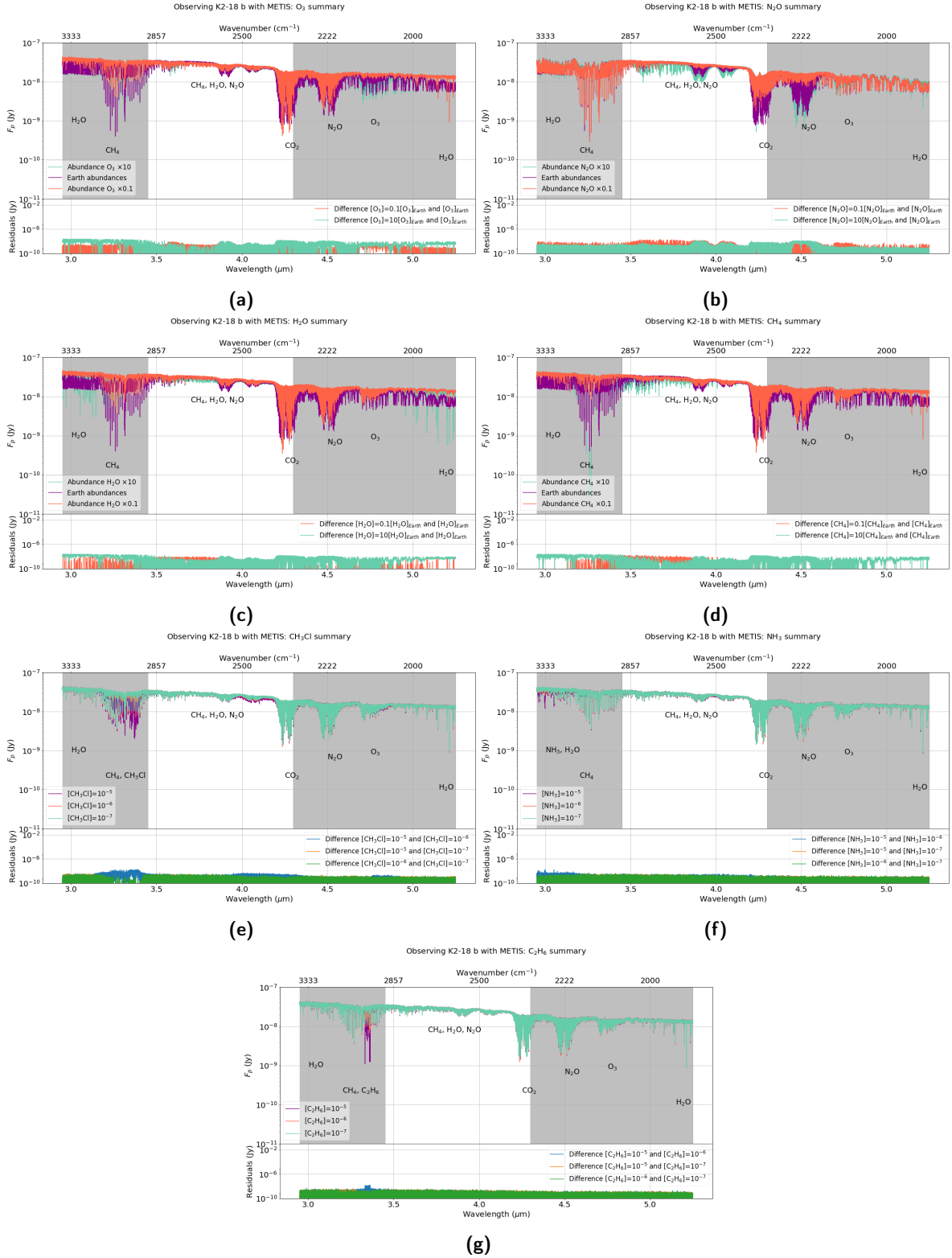

Figure 6: Synthetic reflection spectra of K2-18 b are presented. The synthetic reflection spectra as modelled for METIS contain each 3 spectra: one for an Earth-like abundance (purple), one with a factor times more of the gas (blue), and one with a factor less of the gas (orange). CH_3Cl, NH_3, and C_2H_6, gases not present in more than trace amount in the Earth's atmosphere, abundances of 10^{-5} (purple), 10^{-6} (orange), and 10^{-7} (blue) per unit volume are assumed. The gases for which the abundances are changed are (a) O_3, (b) N_2O, (c) H_2O, (d) CH_4 (e) CH_3Cl, (f) NH_3, and (g) C_2H_6.